UNIVERSITÀ
DEGLI STUDI
FIRENZE

DOTTORATO DI RICERCA IN SCIENZE CHIMICHE

CICLO XXXI
COORDINATORE Prof. PIERO BAGLIONI

STONE ARTIFACTS CONSERVATION: SYNTHESIS AND STUDY OF NEW PARTIALLY FLUORINATED COMPOUNDS

Settore Scientifico Disciplinare CHIM/04

Dottorando
Dott. YIJIAN CAO

Tutore
Prof.ssa Mara Camaiti

Co-tutore
Prof.ssa Antonella Salvini

Coordinatore
Prof. Piero Baglioni

Anni 2015/2018

Acknowledgement

First and foremost, I would like to express my deepest gratitude to my supervisor Dr. Mara Camaiti. She has been my academic supervisor for nearly five years, since May 2014 when I started to work with her for my Master thesis. I really appreciate her immense knowledge and experience in the field of heritage conservation. Honestly speaking, the working conditions we have been experiencing are not very satisfactory, in terms of funding, equipment, lab environment etc. However, she has always been a good model, showing me how to overcome difficulties, how to work with great enthusiasm and patience and how to exploit what we have to create the maximum outcomes possible. Without her contributions of time, ideas and funding, I would not have accomplished my Ph.D. study or have published several papers. Moreover, what I admire her most is her working attitude, e.g. patient, professional, objective, precise, optimistic, helpful etc. which encourages me to be a good researcher like her in my future academic life.

I want to thank my co-supervisor Professor Antonella Salvini sincerely as well. Since the research for my Master thesis, she has always been helping me with NMR analysis, photocatalytic study and colorimetric measurement. Regarding the papers I have published, every time she reviewed the draft patiently and critically, and sometimes she worked even during the holidays.

My thanks also go to Prof. Rodorico Giorgi and the Department of Chemistry of University of Florence and Consorzio per lo Sviluppo dei Sistemi a Grande

Interfase (CSGI) for their help with the contact angle measurement.

I gratefully acknowledge CNR-Institute of Geosciences and Earth Resources and the Ministry of Foreign Affairs and International Operation of Italian government for providing me research grants during the three-year Ph.D. career.

Last but not least, I would also like to thank my beloved family for their unconditional support, both spiritually and physically. I was raised in a family that has been considered as the perfect combination of two occupations i.e., a teacher and a doctor (a surgeon specifically), in China. My mother began to teach me English since when I was six years old, and this allows me to study in a foreign country later. Yet, my father has always been a spiritual model in enlightening me how science could change people's life, and hence encouraging me to pursue science. Although I have got some sorts of financial support, I unfeignedly thank his hard work which affords my expense abroad which sometimes, has to include the purchasing of chemical reagents, small instruments etc. Thanks to my parents, I was able to overcome emotional, academic, economic and healthy problems. To a large extent, it was my parents who made this Ph.D. thesis possible. And also, for my loving, supportive, encouraging girlfriend Cong whose faithful support during the Ph.D. is so appreciated. Thank you.

Contents

Chapter I

Introduction

1.1 Stone degradation: causes and mechanisms

Ahead of taking any action to prevent or to remedy the deterioration of stone, a good understanding of what the conservation problem is, how and to what extent decay takes place is of paramount importance.

1.1.1 Terminology clarification

The ICOMOS International Scientific Committee for Stone (ISCS) has set up a scientific, systematic and simplified glossary for the benefits of scientists, conservators and practitioners [1]. General terms, such as alteration, degradation, decay and deterioration are well-defined and distinguished.

- **Alteration** is the modification of the material that does not necessarily imply a worsening of its characteristics from the point of view of conservation. One good example of prevention is a reversible protective coating applied on the stone surface for conservation purposes.

- **Decay** signifies any chemical or physical modification of the intrinsic

stone properties leading to a loss value—historical, artistic and scientific value, or to the impairment of use. Blurring of a tombstone resulted from defective rainfall is a typical decay phenomenon.

- Furthermore, process of making or becoming worse or lower in quality, value, character, etc. is assigned to **deterioration** or depreciation, e.g. fungi colonization on outdoor stone architecture [1, 2].

1.1.2 Causes and mechanisms

Stone decay is a complex phenomenon, no single cause can be ascribed as the culprit, no single mechanism can be attributed, and no single investigation technique can disentangle and quantify the causes and effects. Despite of the intrinsic differences—mineralogical composition, textures, porosity, pore size distribution, etc., decay patterns may differ from one another largely owing to the extrinsic conditions, e.g. climate (temperature, humidity, rainfall), specific functions (as columns or pavement slabs), position within an area (urban or rural areas), previous conservation treatment, other anthropogenic activities.

Consensus is achieved on the general mechanisms of stone degradation, as following.

1.1.2.1 Chemical causes

Many factors such as chemical-mineralogical composition, water content,

porosity, environmental condition and air pollution have significant influence on the chemical degradation of stone materials. Among all the factors above mentioned, the chemical essence of deteriorating agents determines the decay pathway to the greatest extent. Consequently, chemical decay is further discriminated.

- Carbon dioxide (CO_2) induced degradation

Carbon dioxide, the universally recognised chief culprit for greenhouse effect, has a concentration of more than 400 ppm in 2018. It is not surprising that when gaseous CO_2 is dissolved, for example in raindrops, and precipitated on stone surfaces, it erodes the materials by means of chemical reactions.

$$CO_2 + 2\ H_2O \leftrightarrows HCO_3^- + H_3O^+ \qquad (R1)$$

Typical stones, e.g. limestone (mainly calcite: $CaCO_3$), sandstone (metal silicates predominate) are hardly soluble in neutral water at environment temperature, but become more soluble in CO_2 water solution (pH=5.67).

$$CaCO_3 + 2\ HCO_3^- \leftrightarrows Ca(HCO_3)_2 \qquad (R2)$$

As indicated by the formula, calcium carbonate is transformed to calcium bicarbonate via this reversible reaction which will occur automatically when the environment conditions e.g. wet precipitation, temperature and relative humidity, are favorable. The damage is observed when the resultant soluble parts of the material is washed away by the rainfall which is strong enough to cause the so called—*leaching* effect. Additionally, stone substrate will

undergo the crystallization and re-crystallization cycles of these two mineralogically and crystallographically different minerals, hence creating internal stress which may promote mainly physical deterioration events inside substrates.

- Sulfurous oxides (SO_x) induced degradation

Even though the decreasing trend in the combustion of fossil fuel has contributed to the reduction of sulfur compounds emission in atmosphere, there are still some indispensable natural and biogenic sources, for instance, volcano eruption, vegetation emission, ocean emission. Primary sulfurous compounds emitted directly by the sources into atmosphere will react with each other or other atmospheric components (OH radicals, O_3), giving rise to new species, for instance some secondary pollutants.

$$S + O_2 \rightarrow SO_2 \quad \text{(R3)}$$

$$2\,S + 3\,O_2 \rightarrow 2\,SO_3 \quad \text{(R4)}$$

$$SO_2 + \bullet OH + O_2 \rightarrow SO_3 + HOO^- \quad \text{(R5)}$$

$$SO_2 + O_3 \rightarrow SO_3 + O_2 \quad \text{(R5b)}$$

Through dry deposition and wet deposition, sulfurous oxides has introduced damaging effects to our stone relics.

$$SO_2 + H_2O \rightarrow H_2SO_3 \quad \text{(R6)}$$

$$SO_3 + H_2O \rightarrow H_2SO_4 \quad \text{(R7)}$$

$$SO_3^{2-} \xrightarrow{catalyst} SO_4^{2-} \quad \text{(R8)}$$

$$CaCO_3 + H_2SO_4 \rightarrow CaSO_4 + CO_2 + H_2O \quad \text{(R9)}$$

$$CaSO_4 + 2\ H_2O \rightarrow CaSO_4 \cdot 2\ H_2O \quad \text{(R10)}$$

In (R8), H_2SO_3 formed by dry deposition of SO_2 on stone surface is oxidized to H_2SO_4 by other atmospheric pollutants, e.g. elemental particles (Pb, Ni, C) from gasoline, diesel, coal combustion, aerosols of pollutants.

Calcium carbonate is transformed to calcium sulfate (R9) by wet precipitation—acid rain normally, calcium sulfate grows on the surface of calcite crystals. Sulfates are soluble in neural and acidic water, so they could be washed away by raindrops if it is in an unsheltered position, causing material losing. They crystallize to form gypsum crystals by combing two molecules of water (R10) in suitable conditions. Gypsum crystals have dissimilar crystallographic properties from carbonate and silicate crystals, e.g. morphology, dimension, contraction-expansion coefficient, deliquescent point that will develop internal stress within substrates. Moreover, when soot, especially carbonaceous particles, derived from all processes of fuel combustion deposit on gypsum, gradually, the so notorious *black crust* (Figure 1.9, Figure 1.10) is formed, partially due to the peculiar morphology of gypsum crystals.

Figure 1.9 Black crust (sheltered area)

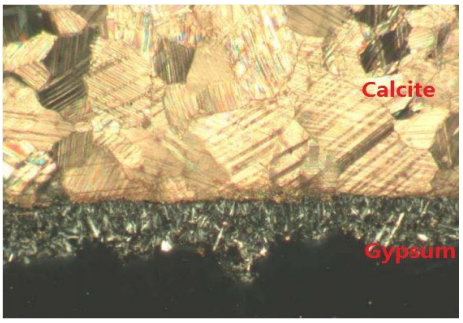

Figure 1.10 Black crust (OM image)

- Nitrogen oxides (NO_x) induced degradation

Nitrogen oxides, i.e. NO, NO_2, N_2O have both anthropogenic and natural sources, e.g. fuel combustion, biomass burning, lightening, soil (bacteria), NH_3 oxidation, among which combustion process inside vehicle engines (N_2 reacts with O_2 directly in high temperature) accounts for more than 50% of total NO_x emission. Once emitted, NO_x are prone to react with other atmospheric components, for instance, oxygen (O_2), hydroxyl radical (•OH), ozone (O_3) and even ultraviolet light.

$$2\ N_2 + O_2 \xrightarrow{\Delta} 2\ N_2O \qquad \text{(R11)}$$

$$2\ N_2O + O_2 \xrightarrow{\Delta} 4\ NO \qquad \text{(R12)}$$

$$2\ NO + O_2 \xrightarrow{\Delta} 2\ NO_2 \qquad \text{(R13)}$$

$$NO_2 + h\nu \xrightarrow{O2} NO + O_3 \qquad \text{(R14a)}$$

$$NO_2 + O_3 \rightarrow NO_3 + O_2 \qquad \text{(R14b)}$$

$NO_2 + OH \rightarrow HNO_3$ (R14c)

$NO_3 + NO_2 \rightarrow N_2O_5$ (R15)

$N_2O_5 + H_2O \rightarrow 2\ HNO_3$ (R16)

$2\ NO_2$ (or N_2O_4) $+ H_2O \rightarrow HNO_2 + HNO_3$ (R17)

$3\ NO_2 + H_2O \rightarrow 2\ HNO_3 + NO$ (R18)

As illustrated, NO_x are principally removed from atmosphere through wet deposition (R16, R17 and R18) in the form of nitrous acid and nitric acid that both are strong acids. Apparently, calcium carbonate will be dissolved and washed away gradually (R19).

$CaCO_3 + HNO_3 \rightarrow Ca(NO_3)_2 + H_2O + CO_2$ (R19)

Nitric acid, together with sulfuric acid, formed in the atmosphere and deposited onto the ground, are the major constituents in *acid rain* (pH< 5.7) which precipitates in two distinct ways: (i) wet deposit—in the form of rain, snow, sleet, fog, dew, etc.; (ii) dry deposit—in the form of particles, gases, aerosols. Therefore, acid precipitations are not only damaging to our human health, forests, groundwater, soil, animals, but also detrimental to our cultural properties, especially outdoor stone artifacts.

1.1.2.2 Physical causes

Physical damages, as the term indicated, the physical changes occurred within substrate are blamed for stone decay. To a considerable degree, the physical

reactions are induced, facilitated, or promoted by the intrinsic properties of stone materials in a given environment. A brief classification is followed.

- Salts crystallization

Among all the factors, soluble salts represent one of the most important causes of physical degradation. Air pollution is a major source of salts like sulfates and nitrates. Other sources include the soil, from which salts may be carried into masonry by rising damp, salts blown by the wind from the sea or the desert, deicing salt, unsuitable conservation treatments, incompatible building materials, garden fertilizers [3].

Salts cause damage to stone in several ways. The most widely acknowledged is the growth of salt crystals in the pores of a stone, which can generate stresses that are sufficient to overcome the tensile strength of stone and crack the material. This process is usually attributed to crystallization, caused by environmental changes. Differences between the chemical potentials of ions in solution and nuclei, supersaturation of salt solution are two essential factors that determine the damaging pattern and rate. When water evaporates from a salt-bearing stone, the salt concentration increases until it precipitates. A change of temperature, generally a decrease, may also lead to supersaturation of the solution, resulting in crystallization of salts. When supersaturation exceeds the threshold for a certain salt, nucleation initiates, thereby leading to the growth of crystals. To permit the diffusion of ions to crystals, a nanometric aqueous thin film is formed between the pore wall and crystal as

a result of repulsive forces (electrostatic interaction or structural forces) [4]. It is the pressure exerted by this liquid film—*crystallization pressure*—that causes major damages to stone during salt crystallization. In the real scenarios, the decay severity and rate varies. If water evaporation occurs on the surface of the stone, then the crystals form a structurally harmless but aesthetically impairing deposit on the surface called "*efflorescence*" (Figure 1.11). However, if water evaporates fast before arriving the stone surfaces, salts precipitate inside the porous structures (a phenomenon called "*subflorescence"* or "*cryptoflorescence"*) (Figure 1.12), severe damage can result [3, 4].

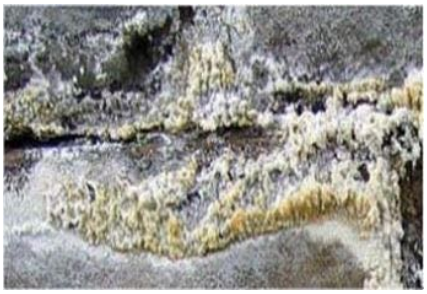

Figure 1.11 Efflorescence

Figure 1.12 Subflorescence

Sodium sulfate (Na_2SO_4) is one of the most damaging soluble salts. When salt solution evaporates or cools, the anhydrous salt thenardite (Na_2SO_4) crystallizes, and decahydrate mirabilite ($Na_2SO_4 \cdot 10H_2O$) or a metastable hepthydrate ($Na_2SO_4 \cdot 7H_2O$) salt may form in some circumstances, producing great volume change and crystallization pressure.

- Differential stress

Recently, a trend in decay mechanism research has been focusing on the so-called "*differential stress*". It is a collective term which includes the effects

of wet/dry cycling, clay swelling, differential hygric stress, differential thermal stress, and stress from differential expansion rates of materials in pores (e.g. salts, organic materials) versus the stone. The essentia is that treatments, salts, water films, or biofilms—anything that causes different reactions between the stone surface and the interior—can result in a shear stress, crack propagation, and eventually, surface parallel detachment (e.g. flaking) [3].

Significant shear stress is generated when, during a brief afternoon rain, the surface of a clay-containing stone swells, while the interior of the stone remains dry (clay minerals containing hydrous aluminum phyllosilicates with variable amounts of iron, magnesium, alkaline metals etc. are commonly present in fine-grained sedimentary rocks; examples are kaolinites, smectites, illites that have large concentration of structural water intrinsically). This is considered an example of differential hygric stress and is typically found on the corners of stones such as Sydney sandstone and Portland brownstone [3, 5]. Researchers at Princeton University have advanced the research on clay swelling, where it was found that shear forces can cause buckling of wetted stone surfaces and that intracrystalline swelling of clay is the primary mode of swelling for Portland brownstone, despite the proportion of swellable clay being only 1% of the stone [6, 7]. Another example is sodium chloride (NaCl) which expands at approximately five times the rate of calcite at surface temperature, so decay in limestone from this mechanism would exemplify the stress induced by differential thermal expansion [8]. Some scholars also

found that differential thermal expansion stress may also derive from color difference at the interface, for example minerals with different colors in granites when exposed to direct sunlight. Special attention is needed that organic compounds, protective agents, consolidants or biological materials may expand significantly faster than stones on wetting conditions [10, 11].

- Freeze – thaw cycle

Stones in cold regions suffer at least one freeze–thaw cycle that could seriously damage the material every year.

Freeze–thaw cycling deteriorates stones directly through ice crystallization, precisely crystallization pressure. Natural stones are porous materials that have a total porosity ranging from 2% (e.g. dolomitic marble, serpentinite) to 50% (e.g. tuff, Lecce stone), with average pore-size being 20 nm to 50 um. As a consequence, water is imbibed and accumulated inside the porous structure via various ways such as capillary absorption, moisture capture, and raindrops penetration. When the environmental temperature reaches the ice-point, water crystallizes with a 9% volume expansion. Tensile stress is exerted directly on the pore structure, damaging stones in the same mechanism as salt crystallization. The extent of damage by water crystallization is closely related to the saturation of the material. Chen et al. (2004) studied the effect of water saturation on highly porous welded tuff due to freeze–thaw action and they found that rock damage significantly increases when the initial degree of saturation exceeds 70% [11].

Furthermore, water flow may act as precursor for successive decay phenomena or facilitate some specific damages when the frozen rock is thawed [12]. Water is generally recognized as the culprit for stones degradation due to its multi-damaging effects. Firstly, water flows through the fractured pores, introducing extra problems. If the network of pore structure has been broken down during previous frozen period, then water could wet almost the entire stone. Wetted clay minerals, wetted soluble salts are important causes for stone degradation when interact with temperature, humidity fluctuations. Potential decay patterns may be swelling of clay minerals and salt crystallization. Secondly, water, although it is precipitated from the atmosphere or absorbed from groundwater (or environment moisture) is itself a heterogeneous mixture, containing pollens, spores, particles and aerosols from air pollution which are all potential deteriorating agents. Water flow within stones promotes the development of all kinds of degradation resulting from chemical, physical and biological causes.

1.1.2.3 Biological causes

Stone deterioration originates from biological agents was first defined as *Biodeterioration* by Hueck (1965), stating “any undesirable change in the properties of a given material caused by the activity of organisms”. The degree of change varies greatly, from disintegration and irreversible transformation of the substrate to the presence of unwanted organisms that do not cause material damage but that do create aesthetic damage [13].

Before identifying and characterizing the main biological species and their detrimental effects, it is important to understand the properties of the stone substrate—which has been defined as *bioreceptivity* by Guillitte in 1985. Its significance is threefold. A primary bioreceptivity indicates the likely of a material to being colonized whereas a secondary bioreceptivity is the result of the activity of organisms and other exogenous factors as well. Finally, the tertiary bioreceptivity is caused by any human activity on the materials (e.g. protective and consolidation treatments, use of biocides, etc.) leading to possible changes of the substrates [3, 13, 14].

The term *Biodeteriogen* refers to any organism that causes damage to the materials, although the term is often applied to any organism discovered on object, whether or not its capacity to damage the substrate is not known [13]. Biological species commonly found on or inside stones are lichens, fungi, bacteria (autotrophic, heterotrophic), algae, mosses (or non-vascular plants) and vascular plants. Their deleterious impacts include both physical and chemical actions, and to a certain extent, having synergistic effects with abiotic factors such as air pollution, temperature, moisture.

Different mechanisms may result in the biodeterioration of stone materials. However generally, there are physical and chemical processes. Physical processes could lead to phenomena such as disintegration, rupture, loss of cohesion. These include all mechanisms that effect a micro or macroloss of cohesion in the substrate due to mechanical actions, e.g. movement or growth.

The fragments thus produced have the same chemical composition as the original parts but are more prone to be detached by pressure exerted by growing organism [fungal hyphae or roots of vascular plants (Figure 1.13) [13]. The detached parts provide a larger surface area for other deteriorating agents, especially in outdoor environment, i.e. rain, wind, freeze/thaw cycle, air pollutants. Actually, there is no clear distinction between physical mechanism and chemical mechanism, as in the majority cases, these two processes act simultaneously and synergistically. The so infamous black meristematic fungi offer an excellent example, where hyphae penetrate into marble substrates and provoke the chemical damage of inner parts by black pigments excreted (Figure 1.14). Additionally, the presence of the colored patinas formed by microorganisms on stone in outdoor environment can induce physical stresses on substrate, by means of increasing thermal retention, water retention and changing thermohydric expansion rates.

Figure 1.13 Plant roots

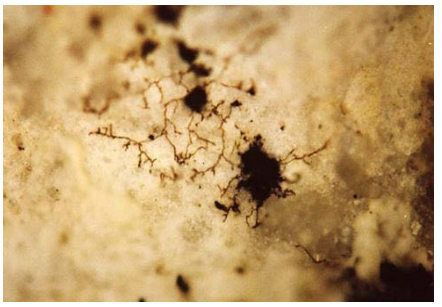

Figure 1.14 Black meristematic fungi

In some circumstances, e.g. in favorable environmental conditions, chemical processes that lead to transformation, degradation or decomposition of substrates may predominate over the coexisting physical processes. The

chemical alteration of substrates caused by microbial communities begins at the moment when adhesion and the subsequent development of biofilm take place. Once adhered to a surface, microorganism, i.e. cyanobacteria, green and red algae, diatoms, chemoorganotrophic bacteria, fungi form complex communities structured in *biofilm*s or microbial mats—assemblages of microbial cells embedded in a complicated matrix of extra cellular polymeric substances (EPS). EPS, which represent the cement that bind microbial development and ensure its adhesion to the substrate, protect cells against dehydration, and represent storage of organic carbon, enables the successive deterioration, especially through chemical mechanisms.

Chemical alteration, transformation of substrates, is essentially due to the effects of metabolic processes of microorganisms. Intermediate metabolic products, substances with an inhibitory or waste function, substances of assimilatory processes and their subsequent extracellular enzymes are all damaging substances excreted by microorganisms [15, 16].

Principally, the chemical processes of biodeterioration are the following:

- the production of inorganic and organic acids;
- the production of CO_2;
- the chelation of elements;
- the production of alkalis;
- selective mobilization and accumulation of elements;
- cationic exchange;

- the production of enzymes;
- the production of pigments [13].

A conclusion that could be drawn here is that stone decay is a complex phenomenon, the synergistic effects of chemical, physical and biological factors account for stone deterioration. The large varieties of scientific techniques available nowadays are certainly useful, but the methodical measurements of decay i.e. decay extent, decay processes, rates over time, have not yet satisfied. Advances in experimental work, field measurements, and theory are still needed.

1.2 Materials for stone conservation

When confronted with decaying stone artefacts, after performing materials characterization, degradation mechanism and extended identification, evaluation by exploiting non-invasive and non-destructive scientific techniques, it is the responsibility of conservation scientists to propose conservation actions in order to stop or slow down the deterioration processes. Primarily, conservation treatment is divided into two categories: preventive conservation (or "Preservation") and active conservation. Preservation, defined as "the activities that avoid something alteration over time" or "Treatment procedures intended to maintain the integrity of cultural property and to minimize deterioration" by AIC (American Institute for Conservation of historic and artistic works) [17], is generated and developed based on the

principal of minimum intervention. Routine maintenance such as temperature, relative humidity, pollution, traffic and visitor management for indoor artworks, and groundwater control, shelters, wind fences, reburial for immovable stone heritage are of vitally importance. In the meanwhile, with the advance of scientific methodologies and techniques, there is a better understanding of decay mechanisms. Active conservation treatments—deliberate intervention operated on objects are designed specifically to reduce the rate of damage by focusing on points of leverage that can mitigate some decay processes. Surface cleaning, desalination, consolidation and protection are the major treatments for stone conservation. Here in the thesis, the focus will be on stone protection treatment, squarely on surface water-repellent coating.

In general, water inhibition treatments can be divided into broad categories considering whether they are completely impermeable to water or whether they are only impermeable to liquid water. The former treatment is called waterproofing while the later one is water-repelling or hydrophobization. This thesis addresses water-repelling treatments which prevents water from entering the treated surface but permits the migration of water vapor through the stone.

By definition, protection is an active treatment that operates directly on objects, rendering hydrophobic properties as well as resistance to deterioration agents (pollution, micro-organisms etc.) to an inorganic material

without reducing the original vapor permeability. The product used—"Protective" may not penetrate into the substrates. As nowadays there are extensively large quantities of polymeric substances, conservation scientists or conservators are ought to select the best product/s meeting a series of criteria in advance of application. According to Recommendation Norm 20/85 [18], the essential requirements for a substance to be used as protective are:

- Water insolubility;
- Good wettability, good adhesion to substrates;
- Compatibility with stone materials;
- Durability;
- Absence of harmful by-products even long time after application;
- Chemical inertness to atmospheric pollutants;
- Good resistance to photo-oxidation;
- Good thermal stability;
- Hydrophobicity;
- Good permeability to water vapor;
- Good solubility in non-toxic and environmentally benign solvents during polymerization and coating, with a pH between 6 and 8 even after ageing;
- Temperature of polymerization or cross-linking reaction near the temperature on the surface of the monument;
- Possible cure without air retention;
- Reversibility;
- Controlled thickness with the maximum hydrophobicity and durability

while maintaining transparency;

- Thermal expansion coefficient does not generate craquele;
- Ability to preserve the original gloss and color.

1.2.1 Traditional materials

The quality of building materials and their protection towards external deteriorating agents have been of concerns since ancient. Dating back to as far as Greek and Roman periods, surface treatment was conducted on stone surfaces for aesthetic and protective reasons by applying natural materials, e.g. waxes, oils. In the Middle Ages, the practice of painting of stone sculptures became widespread, especially in Northern Europe. During the Renaissance and the Baroque periods, shining and polishing marble by waxes, oils (e.g. bees wax, olive oil etc.) were very popular. In 1567, Public Palace of Louvain was painted with oil, and this was formally called a protection treatment. This practice continued until 1829, when some stones were coated with colored stucco [19]. Oil (walnut oil; linseed oil etc.), wax (bees wax; ceresin wax etc.), natural resins (rosin; dammar; mastic etc.) and their mixtures had been prevailing as water repellents until the advent of 19th century when the petroleum industry revolution broke out. Beeswax, paraffin wax and its modern equivalent micro-crystalline wax were widely applied as water repellents for sculptures in the 19th century and early 20th century. Meanwhile, other traditional methods such as the use of sacrificial layers like plasters, stucco or paint also existed for surface maintenance. Since the

second half of the 20th century, large varieties of synthetic polymeric materials which were originally manufactured for industrial applications have almost completely replaced natural resins in stone protection. The main reasons for their popularity are their diversity in types and range of applications, and the possibility of individualised or performance-oriented adjustment during production. Acrylic resins, silicon based resins, microcrystalline waxes, perfluoropolyethers (PFPEs), polyfluorourethanes, fluorinated polymers and fluoroelastomers are representative in this era. Recently, starting from the 21st century, some innovative materials such as structurally modified acrylic polymers and PFPEs, organic-inorganic hybrids, nano-scaled and micro-emulsions of some polymers, nanoparticle composites etc. are being proposed and tested.

1.2.1.1 Representative polymers

- **Acrylic polymers**

Derived from acrylic [CH_2=CH_2-COOH] and methacrylic acid [CH_2=$CHCH_3$-COOH] with varied alcohols, acrylic polymers used in stone conservation have two branches, i.e. acrylates and methacrylates in the form of homopolymers and copolymers. The nature of alcohols that combining with acids affects the chemical-physical properties of acrylic and methacrylic polymers. As a general rule, the lower molecular weight of the alcohol, the harder and more brittle will be the corresponding acrylates or methacrylates. This trend is confirmed by the data of mechanical strength and glass transition

temperature (T_g). Besides, when the alcoholic group is short the resin is soluble in polar solvents such as ketones, esters or alcohols. Instead, when the alcohol group is longer and less polar, aliphatic hydrocarbons will become good solvents [20].

A clear difference between the structures of the two monomers (i.e. methacrylates, acrylates) is the methyl group in methacrylic acid which makes methacrylates less vulnerable than acrylates. There are two individual degradation mechanisms for acrylates and methacrylates, cross-linking and chain-scission, respectively (Figure 1.15; Figure 1.16) [21, 22].

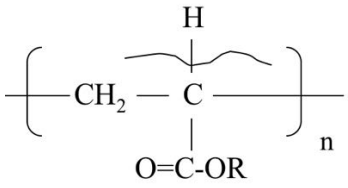

Figure 1.15 Cross-linking of acrylates

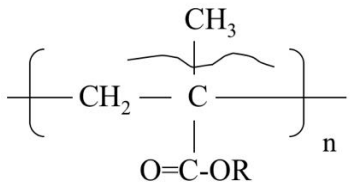

Figure 1.16 Chain scission of methacrylates

The most widespread commercial acrylics and methacrylics are mostly copolymers and terpolymers under the trade mark Paraloid^{TM} (Table 1.1). In general, acrylics and methacrylics have moderate hydrophobicity, good adhering property, good solubility in common organic solvents, transparency, compatibility with stone materials etc. They are predominant in the late 20th century and early 21st century for the conservation of stone, ceramics, glass, wood and other materials, in terms of protection, adhesion and consolidation treatment.

Table 1.1 Chemical composition of commercial Paraloid resins (mol%)

Paraloid	MA	EA	MMA	EMA	BMA	iBMA	Molecular weight
B44		28	70.3		1		105000
B66			47.6		52.4		55000
B67						100	44000
B72	32			65.8	2.2		88000
B82		43	56.1		1		96000

MA: methyl acrylate, EA: ethyl acrylate, MMA: methy methacrylate, EMA: ethyl Methacrylate, iBMA: isobutyl methacrylate.

However, acrylic resins have low resistance to environmental agents, e.g. UV radiation, heat, undergoing de-polymerization and/or cross-linking reactions as stated above. Their low T_g also makes them vulnerable to temperature fluctuations, sunlight moisture and air pollution agents in long term use. Paraloid B72, the most widely employed product in conservation has been proved to have low photo-oxidative stability [23]. Upon exposure to UV radiation for 2000h, chain fragmentation and cross-linking happens simultaneously, giving rise to weight loss, solubility decrease and yellowish color [23]. Aged acrylates have decreased protection effect and solubility that cause difficulties for removal. Apart from this, some researchers found P B72 is susceptible to biodegradation [24]. To improve the protective and physical properties, acrylics are usually blended or copolymerized. An example of

blending is dissolving B72 in an alkoxysilane (e.g. MTMOS), which induces high adhesive properties for consolidation applications [3]. On the other hand, to copolymerize, polyacrylic esters containing variable amounts of fluorine at the α-position of the main chain were synthesized by Salvini et al [25]. The partially fluorinated acrylic polymers were proposed as protective agent for stone surfaces. Besides, a series of methacrylates random copolymers containing fluorinated groups were prepared by Yoshida et al., the random copolymers showed high hydrophobicity and mechanical durability [26]. Fassina and co-workers reported a range of fluorinated acrylic polymers which intended to improve the water repellency and photo-oxidative stability [27]. Their chemical and physical properties were found unaltered after 1000h artificial ageing test. Other modifications were also done by grafting PFPE blocks to acrylic polymers [28]. The perfluorinated block introduces excellent water repellence, chemical, thermal and photo-oxidative property to acrylic polymers, while it also maintains the original vapor permeability of substrates [29].

Nowadays, acrylic resins are no longer preferred from the scientific point of view, yet they are still frequently employed worldwide by restores who are accustomed to doing so.

- **Silicon based compounds**

In 1861, ethyl silicates were first proposed as a primer for stone. While it was not widely used until 1940s, when the synthesis of silicon resins was

developed, and afterwards these resins appeared in the field of restoration in the 60s.

Silicon based resins derive from step-growth polymerization, during which water molecules are usually eliminated, causing volume changes. The commercial products vary, depending on the polymerization degree, e.g. monomers (alkyl alkoxy silanes), oligomers (poly alkyl alkoxy silanes) and polymers (polysiloxanes). They have stronger resistance to atmospheric deteriorating agents (e.g. solar radiation, heat, humidity) in comparison with acrylic resins, ascribing to the stronger Si-O bond (110kcal/mol) than C-O bond (80kcal/mol).

For protection treatment, silicon based resins are either applied as pure or as solution, relying on the polymerization degree: monomers, oligomers and polymers. Among them oligomers are frequently employed as protective agents. Generally, they are transparent polymers, showing good adhesive properties, excellent water repellence and good chemical, thermal, photo-oxidative stability. They also have high penetration ability in porous substrate. There are two types of silicon oils for protection, one has a structure as $[SiCH_3\text{-}(OH)_3]$, and the other is $[Si(CH_3)_2\text{-}(OH)_2]$. To work as water repellents, these products form hydrogen bonding with substrates and expose their methyl group to solid/air interface in order to give the desired hydrophobicity (by changing surface wettability) [30]. The latter one is also called “reactive oil”, since its polymerization or poly-condensation happens

in-situ between molecules or with hydroxyl groups of some specific stones, e.g. sandstone, forming poorly branched polymer chain with a consistence of oil. The in-situ polymerization may cause great problems for removal and reapplication. The poor reversibility is indicated by the significant reduction of their solubility after complete polymerization. Besides, it lacks ability to inhibit the growth of biologic agents (such as fungi) on treated stones. Biocides at long duration are necessary. Although it is a common problem to many products used as protective for stone materials, studies have been devoted to improving the biological resistance. Some research demonstrated that previously applied biocide may decrease the hydrophobicity of siloxanes treatment [29].

In addition to the use of silicon products for consolidation or protection, they also have been suggested to use as chemical barriers rising damp in masonry due to their excellent water repellency. In the recent decade, owing to their diverse types and forms, wide availability, low cost and easy to handle, silanes, silicones and nano silica are extensively exploited in the fabrication of bioinspired superhydrophobic and superoleophobic materials, among which some are also suggested as protective agents for stone artworks. Detailed information will be given in next section “Bioinspired smart materials”.

- **Fluorinated Polymers**

The low surface tension—high water and oil repellency, high chemical and photo-oxidative stability, anti-fouling features, compatibility with stone

materials, good reversibility etc. make fluoropolymers good candidates for stone protection. The high stability and low surface tension are derived from C-F bond which has high dissociation energy (116 Kcal/mol) while very low free surface energy. It has been reported that the hexagonal closed alignment of -CF_3 groups of *n*-perfluoroeicosane shows the lowest surface free energy of any solid—6.7 mJ/m^2 (water: 72.8 mJ/m^2) [31].

There are mainly two classes of fluoropolymer used for heritage conservation: fluoroelastomers and perfluoropolyethers (PFPEs). Fluoroelastomers e.g. Tecnolflon® N215, NM etc., are primarily used as binder and filler for fractures, joints, but sometimes they are also blended with other polymers e.g. acrylic polymers and used as water repellents. Copolymers or terpolymers of vinylidene fluoride-hexafluoropropene and tetrafluoroethylene with molecular weight ranging from about 100,000 to about 500,000 a. m. u. have been employed for stone conservation. Examples are commercial products like -$(CH_2\text{-}CF_2)_m$-$[CF_2\text{-}CF(CF_3)\text{-}CH_2\text{-}CF_2\text{-}]_n$ (Akeogard CO) and –$[CF_2\text{-}CF(CF_3)\text{-}CH_2\text{-}CF_2]_m$-$(CH_2\text{-}CF_2)_n$-$(CF_2\text{-}CF_2\text{-})_p$ (Akeogard LTX). The presence of hydrogen in the molecules makes them soluble in medium polar solvents e.g. acetone, ketones and esters in which form viscous solutions even at low concentrations (5-7% by weight). They have great stability to UV radiation, weathering and chemical agents, and good water repellency. But they have problems of storage and safety problems, when stored as solution in organic solvents, due to inflammability.

One of the drawbacks of fluoroelastomers is the lack of penetration inside the stone due to the high molecular weight, since the size of these molecules are often much larger than the pores of the stone. They tend to concentrate on the surface, forming superficial films which dramatically reduce the original vapor permeability of substrates. This phenomenon not only reduce the natural water vapor permeability, but also induces chromatic variations since the film tends to pick up dirt, dust. Especially on treated marble, surface becomes dark and dirty.

PFPEs are oils with relatively low molecular weights (5000-7000 a. m. u.). The ether linkage (C-O-C) endows high flexibility to polymer chains, and they have low T_g (T_g< -90 °C). They show different viscosity depending on the molecular weight, the type of monomer and the presence or absence of functional groups [32]. PFPES are easy to apply, either by spray or by brush, and they are absorbed by the support without forming superficial film. PFPEs (Scheme 1) and their derivatives have been suggested and applied as water repellents for stone conservation since 1980s [33-35].

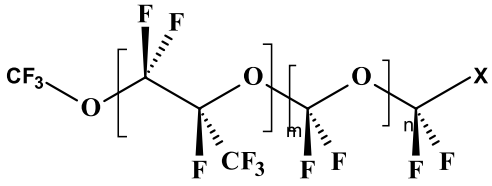

Scheme 1

where X= -CF_3 (named YR), -COOH, -$COOCH_2$-CH-$(CH_2)_2$, -CONH-CH_2-CH-$(CH_3)_2$ (named IBA).

Owing to high bond energy of C-F bond and to highly electronegative fluorine atoms, PFPEs possess high hydrophobicity, high chemical, thermal and photo-oxidative stability. Fomblin YR®, the non-functionalized oil (X= -CF_3 in scheme 1), derived from photo-oxidation of hexafluoropropene, was the first PFPE compound used for stone protection [33]. However, it has poor adhesion to stone substrates, which is insufficient to maintain the oil in place, leading to surface migration or absorption by the porous substrate. This phenomenon results from the inadequate intermolecular interaction provided by the lone pair of electrons on oxygen atoms. As a consequence, the treatment efficacy (hydrophobic properties) decreases dramatically with time. Later, a significant improvement in application was accomplished by introducing functional derivatives of PFPEs, among which the amide derivatives (IBA in Scheme 1 and hexamethylenediamide) have manifested the best performance [34, 35], as a consequence of hydrogen bonding formed between amidic groups and stone substrates. The problem of poor adhesion was addressed, and satisfying protective effects were achieved. Whereas, the limited solubility of mono- or di-amide in chlorofluorocarbons (CFCs), i.e. 1,2,2-trichloro-1,1,2 trifluoroethane (A113) has stopped their wide application, since CFCs have been banded worldwide for inducing ozone depletion. Eligible protective materials for artworks are required to have good solubility in non-toxic, environmentally benign solvents.

As mentioned in the section of “Acrylic polymers”, some researchers tried to introduce PFPE segments into acrylic polymers aiming to obtain properties

of fluoropolymers, e.g. high photo-oxidative stability [36, 37]. Copolymerisation of acrylates or methacrylates with fluorinated acrylic-based monomer derivatives (e.g. trifluoroethyl methacrylate) were conducted to produce fluorinated molecules with improve stability and protective effect [38, 39]. Similar attempts were also done by adding fluorine atoms into the backbones or side chains of silicon based polymers. Despite of all their good properties, the dangers and the specific operating conditions of the synthesis, the high cost of PFPEs have induced a high cost and hard work for manufactures, thus discouraging industrial production and large area application.

Recently, we have reported a series of partially fluorinated oliogomers incorporating pendant PFPE segments [40, 41]. These compounds have good solubility in common organic solvents e.g. alcoholic and hydro-alcoholic solvents. Application can be done by simply brushing or deposing their solutions on stone surface. By properly control the amount of coating materials applied, near superamphiphobic surfaces were created on highly porous Lecce stone surfaces which show water contact angle (CA) CA> 150° and oil CA> 140°. As-prepared coatings manifest high water inhibition efficacy (WIE) while maintain the original vapor diffusivity and chromatic features of substrates. Moreover, water droplets can pin tightly on the coated substrate even when the substrate is turned upside down, resembling “rose petal effect”. In addition to acting as water repellents for stone materials, the sticky near superamphiphobic property offers practical applications in other

important fields such as no-loss or no-contamination liquid transport, sticky tape etc.

1.2.2 Bioinspired, smart materials

1.2.2.1 Introduction

Nature is an inexhaustible source of science and technology. Inspired by the unique wetting and antiwetting phenomena in nature, e.g. water rolling off on lotus leaves [42], dew, rain nonwettable and dust-free cicada wings [43], dirt-free gecko feet [44], water pinning on rose petals [45], etc. ultra repellent surfaces have attracted great interests in academic and industrial fields. Super-antiwetting surfaces with water CA> 150° and low CA hysteresis (CAH) or sliding angle (SA) were firstly reported by Ollivier a century ago [46]. The development of artificial superhydrophobic surfaces was slowly until in 1997 when the "lotus effect" was interpreted by Barthlott and Neinhus [42]. Thereafter, bioinspired ultra liquid repellent surfaces have attracted much attention from researchers in the field of chemistry, material sciences, biology, engineering, physics etc.

Over the last two decades, artificial surfaces with "lotus effect" or "rose petal effect" properties, which have vast application in daily life, industrial and agriculture, have attracted great interest, and extensively successful biomimic surfaces have been developed and studied [47-50]. With static water CA

higher than 150° and low CAH (< 10°), water droplets on lotus leaf could easily roll off ("self-cleaning" effect). Droplets in "lotus effect" are in the Cassie-Baxter state as they suspend on the air-pockets trapped by the microstructure [42, 51]. Such surfaces have great value in both theoretical research and functional application in self-cleaning, anti-biofouling, anti-icing, oil/water separation fields etc.[52] Recently, much efforts have also been devoted to designing "sticky" superhydrophobic surfaces, where droplets are in the Cassie impregnating wetting state (water droplet penetrates into cavities), water droplets are tightly pinned at the interface due to the strong adhesive force ("rose petal effect")[45, 53-57]. These sticky surfaces are potentially applicable in many significant fields that include liquid transport without loss or contamination in microsample analysis [58], dew collection [59] etc.

On a globe scale, many research groups have made contribution to research on bioinspired superhydrophobic and superoleophobic surfaces, and their work mainly focuses on three aspects: 1) the techniques and methods for the fabrication of these materials, (2) the theories behind the unique wettability towards water and oils, and (3) their applications.

1.2.2.2 Basics of superhydrophobicity

- **Smooth surface**

Contact angle quantifies the wettability of a solid surface by a liquid via the

Young's equation (Figure 1.17a, Equation 1.1) where γ is interfacial tension, subscripts SV, SL, LG denote the solid-vapor (gas) interface, solid-liquid interface and liquid-vapor (gas) interface respectively and θ_Y is the equilibrium contact angle at three-phase point.

$$\gamma_{LG}\cos\theta_Y = \gamma_{SV} - \gamma_{SL} \quad \text{(Eq. 1.1)}$$

Surfaces are defined as hydrophilic when the water CA is less than 90°. If the CA ranges from 90° to 150°, the surface are hydrophobic, while surfaces are superhydrophobic when CA>150°. *Young's equation*, in fact, neglects the influences of roughness, chemical heterogeneity, surface reconstructions swelling and dissolution etc. which do affect the wetting phenomena. Among these factors, surface roughness is regarded as one of the most influential parameters for CA. Two models i.e. Wenzel model and Cassie model are generally employed to correlate surface roughness with apparent CA.

- **Rough surface**

In the Wenzel cases (Equation 1.2), surface roughness factor r is taken into account (Equation 1.3), since it assumes the droplet follows the roughness surface and fills in the asperities (Figure 1.17b). The roughness factor amplifies the effect of surface chemistry determined by $\cos\theta$. When $\theta_Y < 90°$, an increase of r reduces θ_w, while if $\theta > 90°$, an increase in r results in an increase of θ_w. These means, a hydrophilic surface will become more hydrophilic when its surface is rougher, whereas a hydrophobic surface will be more hydrophobic when its surface is roughened. In general, droplets in

the Wenzel state have large CAH, showing strong adhesion to surface. Yet, for some surfaces, such as high roughness or porous structures, the absolute value of the right side in Eq. 1.2 might be larger than 1. In such cases, the Wenzel model is not valid, and the Cassie model will be used.

$$\cos\theta_w = r\cos\theta_Y \quad \text{(Eq. 1.2)}$$

$$\mathrm{r} = \frac{\text{actual surface area}}{\text{planar area}} \quad \text{(Eq. 1.3)}$$

In the Cassie model, the droplet suspends on the surface and it does not penetrate into cavities (Figure 1.17c). Air pockets are assumed to be trapped in asperities. In this state, the apparent CA (θ_c) is the results of contributions of varied phases:

$$\cos\theta_C = f_{SL}\cos\theta_s + f_{LV}\cos\theta_v \quad \text{(Eq. 1.4)}$$

Where f_{SL} and f_{LV} are the surface fractions of solid-liquid interface and liquid-vapor interface respectively. If only one type of protrusion is present, $f_{\mathrm{SL}} + f_{\mathrm{LV}} = 1$. Water droplet has a CA of 180°, the equation becomes:

$$\cos\theta_C = f_{SL}(1 + \cos\theta_w) - 1 \quad \text{(Eq. 1.5)}$$

In the Cassie-Baxter model, θ_c of an either inherent hydrophilic or hydrophobic material increases with roughness and can therefore become $\theta_c >$ 150° for any material. Consequently, the Cassie model suggests that roughness enhances the hydrophobic character of an either inherent hydrophilic or hydrophobic surface.

Surfaces wetted in Cassie state are usually slippery than Wenzel state which are sticky, thus small CAH. Wenzel and Cassie define the two limits of wetting behaviors, and surfaces may also show intermediate state Wenzel-Cassie sate. In this situation, apparent CA is affected by both solid-surface fraction f_{SL} and roughness factor r as:

$$\cos\theta_C = f_{SL}(r\cos\theta_Y + 1) - 1 \qquad \text{(Eq. 1.6)}$$

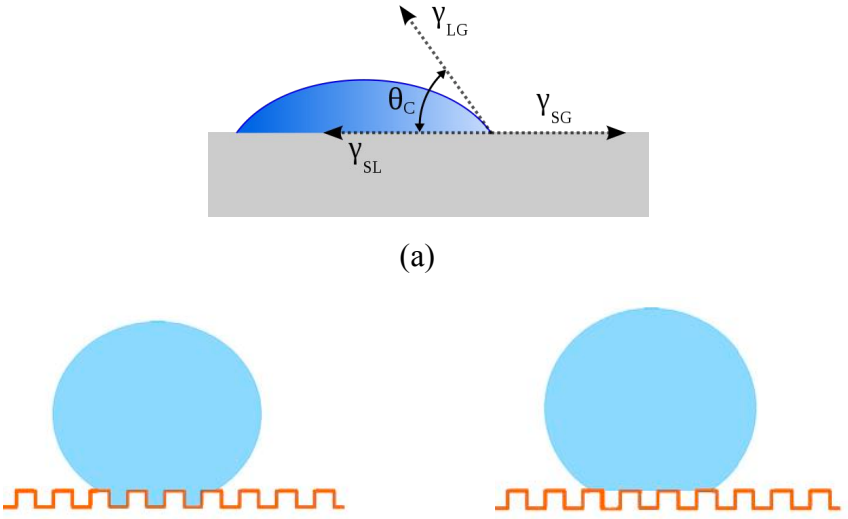

Figure 1.17 Typical wetting behaviour of a droplet on rough solid surface. (a) Young's mode. (b) Wenzel' mode. (c) Cassie's Mode.

In reality, solid-liquid contact model does not persist forever. A transition from Cassie to Wenzel state is observed under conditions of droplet press, impact or vibration [60-63]. Droplets pinned on rose petals are in the Cassie impregnating wetting state in which water penetrated into cavities. The transition or coexistence of these two models was visualized by large-scale

molecular dynamic simulation method by Zeng *et al* [64].

- **Dynamic wetting properties**

In real cases, CA is not enough to characterize the wetting properties of solid-liquid interface. CAH and SA are therefore introduced. When a droplet is inflated, the CA will increase but the contact area will not change until θ_{adv} reaches a critical value and then it begins to advance. θ_{adv} is referred as the advancing angle. Similarly, if a droplet is deflated, there is also a critical value called receding angle θ_{rec} until the droplet begins to recede. By definition, the difference between θ_{adv} and θ_{rec} is termed CAH. Surfaces with low hysteresis allow drops to slide over them easily regardless of the equilibrium CA. The quantitative relationship between the CAH and SA is governed by Eq. 1.7 [65]:

$$mg \sin \alpha = \gamma_{LV}\, w(\theta_{adv} - \theta_{rec}) = CAH\, \gamma_{LV}\, w \qquad \text{(Eq. 1.7)}$$

where g is the gravity force, α is the tilt angle (or SA) and m, w represents the mass and width of the drop, respectively. Essentially, gravity force and capillary force are equal in this equation. It is concluded that the Cassie model will result in a smaller SA than the Wenzel model because of its smaller area fraction. As the CAH is a measure of energy dissipation during droplet movement, the solid surface energy (σ_s) can also be estimated exploiting CAH [66]:

$$\sigma_S = \frac{\sigma_{LV}(1+\cos\theta_{adv})^2}{2+\cos\theta_{adv}+\cos\theta_{rec}} \qquad \text{(Eq. 1.8)}$$

where σ_{LV} is the water surface tension (72.8 mN/m). For superhydrophobic surfaces, the surface energy is significantly smaller than 72.8 mN/m.

1.2.2.3 Fabrication materials

It has been found out and generally acknowledged that the surface roughness at nanometer or sub-micrometer scales combined with the low surface energy material bring superhydrophobic properties.

The raw materials are indispensable in preparing surperhydrophic coatings, since they are decisive in forming nano-micro roughness and/or low surface tension coating. To prepare ultra-repellent surfaces artificially, many kinds of materials and mainly three categories i.e. organic, inorganic and organic-inorganic hybrid materials have been used and reported.

- **Inorganic materials**
- **Silicon based**

In spite of the numerous chemicals used, silanes and silicones play very important roles in the preparation of ultra liquid repellent materials. Approximately 25% of the literature about superhydrophobic and superoleophobic materials is based on silanes and silicones [67]. Silanes and silicones are frequently for constructing appropriate surface topography, decreasing the surface energy, and as binders to link building blocks together or to bind materials of low surface energy to substrates. Silanes with hydrolyzable groups, e.g. Si–Cl, Si–NH–Si, Si–OCH_3 and Si–OCH_2CH_3, could react with water to form silanols, which then couple to hydroxyl groups at the surface of substrates. The alkyl groups of silanes could decrease the surface tension or could be used as active sites for further modification, and

the remaining silanols may further self-condense to form a silicone layer with unique micro-/nanostructures. Thus, there is much scope for tailoring the properties of the coatings by changing the reactive groups of silanes, the alkyl groups and reaction conditions [68].

Silica nanoparticles. To construct super-antiwetting surfaces, silica nanoparticles (NPs) are frequently used to create micro/nanostructures followed by modification with low surface tension materials. Silica NPs are usually obtained by hydrolytic condensation of tetraethyl orthosilicate (TEOS) via Stöber method. Silica-based superhydrophobic surfaces can be fabricated by layer-by-layer (LbL) self-assembly or using core–shell structured silica NPs. Superhydrophobic films were prepared via LbL self-assembly of negatively charged silica NPs and positively charged ionic liquids [67]. The change in the layer numbers, concentration of ammonia and the type of silica precursor could control the wettability.

Polydimethylsiloxane (PDMS). PDMS is an elastomeric material that has been widely employed in soft lithography to prepare super-repellent surfaces. Ultra repellent surfaces can be obtained (1) by surface roughening followed by modification with materials of low surface energy, and (2) directly by surface roughening owing to its hydrophobic property [67]. Rough PDMS surfaces can be formed by soft lithography, plasma etching, H_2O_2 etching or their combination.

PDMS can be used for replicating the surface texture of master moulds such

as plant leaves, patterned silicon wafer, sandpapers, etc. The rough PDMS surfaces can be used as negative replicas for fabricating superhydrophobic and superoleophobic surfaces [67].

Besides, chemical vapor deposition (CVD) of PDMS can make rough surface superhydrophobic. CVD of PDMS is carried out in air at high temperature. During the CVD process, the thermal degradation of PDMS through the heterolytic cleavage of the Si–O bonds leads to a mixture of volatile, low molecular weight products that could react with the hydroxyl groups and form a conformal layer on the surface of the substrates [69, 70]. It was found that not only PDMS but also other silicones could be used as the precursor for the super- hydrophobic coating [71].

Silanes and silicones. Chlorosilanes, alkoxysilanes, other silanes and PDMS can be used to decrease the surface energy via CVD or solvent deposition in the preparation of superhydrophobic and superoleophobic surfaces. Aminosilanes, propylsilanes, vinylsilanes and other silanes with functional groups, assembly of NPs modified with different silanes, and silicones can be used as binders between the substrates and coatings. Silanes and silicones play two or three roles in forming superhydrophobicity and superoelophobicity simultaneously. On one hand, the reactive groups of hydrolyzed silanes and silicones can cross-link with each other to form certain roughness at multiple scales. On the other hand, the alkyl groups of silanes could decrease the surface tension or could be used as active sites for further

modification, and the remaining silanols could be used for further condensation of silanes, silicones or other reagents. For the simultaneous construction of micro-/nanostructures and decrease of surface energy, one can use a single silane or silicone via a one-step process, mixture of silanes and silicones via a one-step process or multi-step process [67]. Silanes and silicones may also be used as binders and for decreasing the surface energy simultaneously. Likewise, mixtures of silanes can be used for constructing nanometric roughness, as binders and decreasing the surface energy simultaneously. The frequently used mixtures are TEOS/perfluorosilanes, TEOS/alkylsilanes with aminopropylsilanes as the binder and TEOS/alkylsilanes with other silanes as the binder [67].

- **Carbon based**

Since the discovery of some innovative carbon materials e.g. carbon nanotube (CNT), carbon nanofiber (CNF), graphene and fullerene-C, carbon-based materials have been exploited in many fields which include superhydrophobic coating. Carbon itself is a good warranty of mechanical, chemical stability and robustness. However, the design of nano-roughness is very challenging when carbon-based materials are used. For example, it is difficult to achieve structural hierarchy of two-dimensional graphene for superhydrophobicity. Jang et al. solved this problem by presenting a simple route toward a superhydrophobic graphene surface via thermal reduction method [72]. The excellent properties of transparent superhydrophobic graphene can potentially be exploited for versatile applications. Comparing with graphene,

using CNT to fabricate superhydrophobic nanocoating would be easier. Men et al. prepared a superhydrophobic nanocoating by spraying multiwall CNTs onto substrates followed by surface fluorination [73]. Water CA of this coating reached 163°.

- **Metal and metallic oxides**

In general, metallic superhydrophobic nanocoating is obtained by electrochemical processes. It is not abnormal that metals need superhydrophiobic protecting coatings, but it is very difficult to use metal itself as coating. There are few examples in literature [74, 75]. Compared to metallic superhydrophobic nanocoatings, there are a larger number and more kinds of metallic oxide examples in this field. Methods such as low temperature plasma, CVD, solution immersion etc. were utilized [76, 77].

- **Organic materials**

Attributing to their flexibility, diverse molecular design, processability, low cost, availability etc. polymers are widely used in constructing superhydrophobic coatings. Ultra repellent surfaces can be obtained staring from simple polystyrene (PS), polyethylene (PE), polypropylene (PP) [78-80]. For example, Yuan et al. obtained a lotus-leaf-like superhydrophobic low density polyethylene (LDPE) with CA ~156° and low SA ~1° [79]. The multifarious synthetic methods are another advantage of polymer materials e.g. copolymerization, atoms transfer radical polymerization (ATRP), and graft polymerization [81]. Among all polymers, fluorinated polymers are the

most popular materials due to their low surface energy. Yuan *et al*. synthesized a kind of fluorinated acrylic random copolymer to fabricate superhydrophobic nanocoating on Al substrate [82]. The as-prepared superhydrophobic coating is not only resistant to low temperature and durable under water, but also delays water to freeze at low temperature.

Natural polymers, e.g. chitosan which incorporate environmentally and biologically friendly materials, are also promising raw materials in fabricating superhydrophobic coatings. Ivanova et al. designed a superhydrophobic anti-bacterial textile by simply using chitosan-based nanoparticles for biomedical applications [83].

- **Inorganic-organic hybrid materials**

Inorganic–organic superhydrophobic coatings are prepared by using inorganic nanomaterials to create dual-hierarchical roughness on organic polymer coatings. These hybrid surfaces possess the advantages of both organic and inorganic materials simultaneously. Silicon-based, carbon-based, metallic oxides and other inorganic materials can be used to form inorganic–organic hybrid superhydrophobic coatings with polymers. ZnO/poly- styrene nanocomposite coating was fabricated by Zheng et al via a straightforward, inexpensive method [84]. Chakradhar and coworkers prepared polyvinylidene fluoride (PVDF)– multiwalled carbon nanotube (MWCNT) nanocomposite coating [81]. When the CNT content increased, a transformation from hydrophobic to superhydrophobic state was achieved. A

green method means an economical, nontoxic and eco- friendly method, which was explored for a PEG–SiO_2 nano- composite coating with superhydrophobic and transparent property by Shen et al [85].

1.2.2.4 Fabrication methods

The techniques can be divided to top-down and bottom-up approaches [50]. Top-down approaches include lithography, template-based techniques, and plasma treatments of surface. Bottom-up approaches involve mainly self-assembly and self-organization, and examples are chemical deposition, layer-by-layer (LBL) deposition, and colloidal assemblies. There are also methods based on the combination of both top-down and bottom-up techniques such as casting of polymer solution, phase separation, and electrospinning. Yet, some researchers distinguish these methods based on their chemical and physical origins [48]. These approaches have both advantages and drawbacks from different points of view. The most frequently employed methods are as follows.

- **Sol-gel process**

Sol-gel method has been exploited to fabricate super repellent surfaces on various substrates e.g. metals, silicon wafer, glass textile, wood, stone etc. During the process, the precursor (chemical solution or sol) is converted into a glassy material through a series of hydrolysis and polycondensation reactions. The surface roughness can be controlled by varying the conditions

and reaction mixtures while the surface properties can also be controlled by the functional groups of resulting gel and the preparation process. This method has been using since the early stage of research on this topic, and now it is a very practical method in preparing superhydrophobic surfaces.

Recently, Lin *et al.* reported a simple sol-gel dip coating method to prepare transparent superhydrophobic nanocoating by using 3-aminopropyltriethoxylsilane and cetyltrimethoxysilane as aggregating agent and modifying agent [86]. As-prepared coating show good moisture resistant, and besides, the wettability of coating could switch from superhydrophobic (>160°) to superhydrophilic (0°) when the temperature was higher than 500 °C. Superhydrophobic antireflective or transparent surfaces were prepared by sol–gel technique [87, 88]. Some researchers have prepared superhydrophobic coatings for the protection of stone materials though sol-gel process, and more detailed discussion will be in the following section. One drawback of this method is the relatively long gelation time of sols, and a few days or weeks are often required.

- **Lithography**

Lithographic methods have been frequently used to create superhydrophobic surfaces. The structure and morphology can be easily controlled through this method. Surfaces patterned with circular pillars, squared pillars, star-shaped pots, indented square pots, with different diameters, height, and spacing have been prepared [89-92]. The possibility to design and to compare features

allows to investigate the relationship between the structure and the wetting state of the surface [93]. Using colloidal lithography (a soft lithography technique), superhydrophobic surfaces can be created from hydrophilic materials. Superhydrophobic and superoleophobic surfaces with a triple-scale structure were produced on PMMA [poly-(methyl methacrylate)] using PS microparticles [94]. This method is not applicable in the field of coating for stone conservation since it requires substrate modification process.

- **Layer-by-layer (LBL)**

LBL technique, widely used in designing superhydrophobic surfaces, is a method by which thin films, particularly of oppositely charged layers, are deposited. In general, the LBL assembly can be represented as sequential adsorption of positive or negative charged species by alternatively dipping into the solutions. The excess or remaining solution after each adsorption step is rinsed with solvent leading to a thin layer of charged species on the surface ready for next adsorption step [50]. LBL can also be utilized for nanoparticles assembly [95-100]. Hierarchically-organized composite surfaces were obtained by LBL assembly using silica NPs with different size and functionality [95]. The wettability of surface was lowered by hydrophobization of the last layer. The hydrophobicity of the surface is determined by the number of layers of silica NPs and surface topology. Sun et al. assembled silica nanoparticles on a honeycombs-patterned PDMS substrate [97]. Superhydrophobic surfaces with both high and low adhesion were obtained with different bilayers of assembly (with thermal cross-linking

and surface fluorination by CVD), indicating that different levels of nano- to micro-structural hierarchy can be realized using this method. It should be pointed out that this method can be used to fabricate superhydrophobic surfaces on non-planar surfaces.

- **Solution immersion process**

It is simple to render substrates superhydrophobicity via one-step immersion in a solution that contains low surface tension agents. One drawback of this approach is time-consuming, and the control of nanoscale roughness is also difficult. Many researchers are trying to tackle these problems. Yan et al. recently reported the use of pristine multiwall carbon nanotubes (MWNTs) and polybenzoxazine in a solution immersion process to construct nanocomposite coating on ramie fabric [101]. The ramie fabric was first immersed into MWNTs/benzoxazine monomer mixture suspension, and then washed with deionized water and ethanol, dried under vacuum and finally heated at 130°C. The water CA of immersed fabric for 20 cycles reached 152°. Superhydrophobic surfaces were also made on metal substrates through this one-step method [102].

- **Spray**

Spray is the simplest process and practical method for nanocoatings. Zhou et al. reported the fabrication of superhydrophobic surface on various substrates by simply spraying an emulsion of $[CH_3(CH_2)_{10}COO]_2Cu$ in a hydro-alcoholic solvent with N_2 gas and the died at room temperature [103]. As-

prepared surface reached water CA of 160° and a sliding angle of 5°. Recently, a large number of literature related to spray process has been published [82, 105], yet more in-depth research is needed to improve the adhesion between coating and substrate and the control of surface morphology or nanoscale roughness.

- **Other techniques**

There are many other methods and techniques such as hydrothermal method, etching, CVD, template, electrospinning, electroless galvanic deposition, anodization, composite method etc. employed in preparing super repellent surfaces on a wide range of substrates in recent years. Similar to the above mentioned methods, they have both advantages and disadvantages. Some methods are only applicable on certain kinds of substrates, and some methods require complex and expensive facilities. Harsh fabrication conditions and tedious procedures do impede their wide application and commercialization. Such problems shall be well addressed before introducing into industrial world and daily life. It is not acceptable for those methods in which substrate processing is necessary, e.g. lithography, chemical etching etc. to be used in creating protective, ultra repellent coating for stone artworks where the physical and chemical integrity shall never be impaired. Besides, methods that cannot be applied in situ are also inappropriate.

1.2.2.5 Application in stone conservation

Bioinspired ultra water/oil repellent surfaces with self-cleaning property ("lotus effect") are the most ideal materials for protecting building stones, and the reasons are twofold: 1) liquid water adhesion, penetration and vapor condensation are inhibited on such surfaces, water-driven damaging effects are therefore prohibited; 2) undesirable surface dispositions e.g. atmospheric pollutants, dust, bird poop etc., can be removed exploiting the self-cleaning properties in presence of liquid water. Equipped with such surfaces, the physical and chemical integrity together with the aesthetic properties of building stones can be well maintained.

In literature, some superhydrophobic surfaces with "lotus effect" behavior have been proposed for building stones which include stone artefacts. Mosquera *et al.* reported the fabrication of superhydrophobic coating on sandstone via sol-gel process [106]. The starting sol was prepared as following: 1) preparation of 1.57 M aqueous solution of n-octylamine; 2) mixing of TES40 (a hydroxyl terminated polydimethylsiloxane), silica colloidal particles and aqueous solution of n-octylamine under ultrasonic stirring; 3) adding PDMS dropwise to mixture while maintaining stirring for 10 mins. The prepared sol was then applied on sandstone surface by brushing. As-prepared surface shows a water CA of 149±2° and CAH of 7±1°. The amount of water absorbed by stone after coating was dramatically reduced, and water did not penetrate into stone after immersion for 48 h. The coating also preserves the aesthetic feature of substrate. However, in my opinion, the

amount of product applied which affects the performance of coating is not very clear in the paper. With very high amount of coating material, superhydrophobicity can be achieved, yet simultaneously, the open pore network could also be damaged which results in severe reduction of vapor diffusivity. Generally, 10 g/m^2 of coating material is suggested for the protection of such kind of sandstone. The vapor diffusivity of stone after coating was not evaluated. A drastic reduced vapor diffusivity could facilitates water condensation below the coating layer, which consequently could induce a series of physical decay effects such as free-thaw cycles, differential stress, salt recrystallization etc.

In 2008, Karapanagiotis *et al.* reported fabrication superhydrophobic surfaces starting from a polymer-NPs suspension that composed of silica NPs, PMMA or polyalkylsiloxane (Rhodorsil 224) [107]. Coating was done by simply spraying the suspension on various substrates i.e. silicon, glass, silk, aluminium, wood, marble, and concrete. The effect of silica NPs was assessed by varying the concentration (i.e. 0.1, 0.3, 0.5, 1.0, 1.5 and 2.0%). As-prepare surface showed water CA ranges from 154°- 164° together with CAH ranging from 3°-5°. Similar to previous publication, the exact amounts of coating materials were not clear. Additionally, for the coating on marble and concrete the vapor diffusivity variation shall be evaluated before applying on stone artworks.

In 2016, Karapanagiotis *et al.* prepared a water soluble emulsion enriched with silica NPs (7 nm) to spry on marble and sandstone surface to fabricate superamphiphobic, self-cleaning coating [108]. As-prepared surface shows water and oil CA>150° with tilting angle <7°. They also demonstrated when the concentration of silica NPs is higher than 2% (w/w), a continuous structure collapses is observed on surface, and large grooves are formed. These grooves do not have influence on static CA, but they are responsible for the transition from Cassie-Baxter state to Wenzel state of liquids with low surface tension e.g. oil, ethylene, glycol drops. Subsequent monitoring of water evaporation showed the drops follows the constant CA model which is agreement with superhydrophobic surface with low adhesion property. This sol-gel process is very simple, and the application method (spray) is also easy to handle. Surfaces with not only superamphiphobic but also self-cleaning property were obtained. As above publications, the authors did not evaluate the vapor diffusivity change after coating application. Besides, to manifest the versatility of their approach on building stones, application on stones with high porosity e.g. Lecce stone, tuff is ought to be done.

Cappelletti *et al.* reported a sol-gel method to produce superhydrophobic surface on various stones [109]. The sol was prepared by adding non-ionic surfactant (Lutensol ON70) to obtained TiO_2 NPs. The sol was stirred for 30 mins at room temperature and then mixed with siloxane polymeric agent (Alpha SI30) in varied percentages (resin/TiO_2 sol 7:3, 5:5, 3:7). The application was done by spraying. Superhydrophobicity was only observed

on marble surface with water CA>150°. However, the CAH was not measured to indicate the adhesive or slippery property of this coating.

There are some other publications regarding the preparation of superhydrophobic coatings for stone maintenance [110-113]. However, similar to above mentioned ones, they have some drawbacks in common, e.g. unclear coating amount, unknown vapor diffusivity after coating, not versatile towards stones with both low and high porosity etc. In all the literature, NPs of either SiO_2 or TiO_2 are employed to create dual-scale hierarchy microstructures. Future research could be focusing on reducing or eliminating the use of NPs, reducing coating amounts and in-depth characterisation of physicochemical property variation of stone materials after coating etc. Besides, developing superhydrophobic coatings for stones with high porosity e.g. Lecce stone, tuff, shall not be ignored. Moreover, superhydrophobic, self-cleaning coatings that incorporate anti-biofouling properties are also favorable for protecting building materials. Yet, there is no such research in literature.

Chapter II

Aim of the thesis

The survival of our mankind's stone heritage is confronted with severe, diverse degradation events that derive from physical, chemical and biological origins. Nowadays, to mitigate or/and halt the decay phenomena, synthetic polymers are widely used owing to their good hydrophobicity, chemical compatibility, stability and in some cases, the ability to act also as consolidation agents [19, 30]. Yet, they also show several drawbacks in long-term use. Acrylic polymers have poor photo-oxidative stability due to structural reasons, while silicon based resins are reactive with some specific stones and may become insoluble after in-situ polymerization [19-23]. Weighing the pros and cons of these commercial protective agents, new products that incorporate high hydrophobicity, compatibility, stability and reversibility are urgently demanded. During the research for my Master's thesis, a partially fluorinated oligoadipamide which contains pendant perfluoropolyether (PFPE) segments (FAD) has been synthesized and tested. FAD was proved to be a good water repellent for low porous stones, but it is not very effective for the protection of stones of high porosity [40]. In general, the aim of my PhD research is the synthesis, characterization, performance, stability and durability testing of new compounds as protective agents for both low and high porous stone materials. Specifically, the first aim is the

synthesis, characterization and performance testing of novel oligoamides containing PFPE blocks that are homologous to FAD. The similarities and differences of these compounds, in terms of physiochemical properties, performance as water repellents etc. will be investigated and understood. Secondly, innovative, bioinspired ultra repellent coatings will also be developed for building materials including stone artefacts. Meanwhile, by varying the synthetic routes, reagents, conditions etc. superamphiphobic coatings with self-cleaning and anti-biofouling properties will also be achieved. Last but not least, the stability and durability of newly synthesized products will be evaluated as well.

2.1 Partially fluorinated oligoamides

Previously obtained FAD demonstrates very high protective efficacy for low porous stone e.g. marble without compromising the physical characteristics of substrate such as vapor diffusivity, chromatic features. Additionally, FAD has good solubility in common organic solvents e.g. alcoholic and hydro-alcoholic solvents, which not only enables simple treatment by brushing or spray, but also makes treatment reversible. However, FAD is not very effective for the protection of stones of high porosity e.g. Lecce stone. Referring to literature, the partially fluorinated oligosuccinamide (FSC2) previously synthesized by Pappacchini A. demonstrated the opposite properties, being more effective on Lecce stone (PE%>90%) than on marble [114]. These performance variations may originate from the specific

molecular structures of FAD and FSC2; for instance, the length of the hydrogenated chain (oligosuccinamide, oligoadipamide) may influence the formation and the intensity of intra- and inter-molecular hydrogen bonding which in turn affects the distribution or deposition of products on porous substrates. More studies and additional experiments (including durability test) shall be done for better understanding, and different analogous products will be synthesized and tested.

Therefore, to better understand structure-property relationship, partially fluorinated suberamide with pendant PFPE blocks will be synthesized firstly via two-step poly-condensation reactions as the syntheses for FAD and FSC2. The same type of PFPE derivative will be used. By adjusting the conditions in the first step e.g. molar ratio between two reagents (i.e. ethylenediamine and diethyl suberate), reaction temperature, solvent amount, reaction time etc. oligosuberamides with differed number average molecular weights will be obtained. After in-depth characterization by spectroscopic techniques (FT-IR and ^{1}H, ^{13}C, ^{19}F-NMR spectroscopy), the protective performance of synthesized products is going to be evaluated by application on stones with both low and high porosity i.e. marble, sandstone and Lecce stone. The wetting properties and morphology of as-prepared surfaces will be characterized as well by CA, CAH measurements, SEM-EDX analysis etc. The characteristics of oligomers distribution and deposition on surface will be investigated and studied in comparison with previous products FAD and FSC2. In addition, the variations of physical properties of stone materials

after coating will also be assessed as well. Moreover, the performance durability will be evaluated by water immersion test for short and long time. The best product/s for stone protection will be proposed.

2.2 Bioinspired ultra repellent coatings

As explained in "Introduction", bioinspired superhydrophobic surfaces equipped with self-cleaning property is the most ideal protective coating for outdoor build heritage, owing to the fact that such surfaces not only inhibit liquid water adhesion, penetration and vapor condensation, but they can also clean the undesired surface depositions e.g. atmospheric pollutants, dust, bird poop etc. spontaneously in presence of liquid water.

New synthesis aiming to achieve superhydrophobicity and self-cleaning property will be carried out. One-step amidation reaction between one coupling agent of silane i.e. 3-aminopropyltrimethoxylsilane and an acyl fluoride functionalised PFPE will be exploited to obtain a silane with a perfluorinated chain. The product will be further characterized by FT-IR and ^{1}H-NMR spectroscopy. To verify its performance and versatility on building materials as protective coating, coating material will be applied on various substrates of both low and high porosity, e.g. commercial red brick, commercial plain ceramic, sandstone, Lecce stone etc. Concerning the wetting properties, static water and oil CA, CAH will be measured on as-prepared surfaces. Besides, to further demonstrate its high repellence towards

complex water dispersion and emulsion systems, CA of coffee, milk, tea drops will also be measured. The water inhibition efficiency of various coated stones will be tested for short and long time (from 30 mins to 24 h). Besides, the physical properties change of stones i.e. vapor diffusivity and chromatic features will also be estimated after coating. Furthermore, the stability of as-prepared coating to various chemical agents (pH 3-14) is going to be verified. The durability of superhydrophopbicity will be estimated by water immersion test up to 48 h.

Aiming to obtain superhydrophobic, self-cleaning coating which also incorporates anti-biofouling property, new synthesis based on fluorinated silane and TiO_2 NPs will be conducted. Commercial hydrophilic TiO_2 nanoparticles will be introduced into alcoholic dispersion of previous fluorinated silane with varied concentrations. Once characterized by spectroscopic techniques (FT-IR and ^{1}H-NMR spectroscopy), coating will be prepared on different stones i.e. marble, sandstone and Lecce stone. Similarly, the wetting properties and morphology of as-prepared surface will be analysed by CA, TEM and SEM-EDX analysis. Its performance as water repellent for stones will be assessed according to standard methods, in terms of water inhibition efficacy, vapor diffusivity and surface color. More importantly, the photo-catalytic activity will be evaluated on the basis of methylene blue ISO test method.

Comparative studies on these two types of compounds which are superhydrophobic, self-cleaning or superhydrophobic, self-cleaning and anti-

biofouling will be done in order to propose the most appropriate product for specific conservation purposes under certain environmental conditions.

2.3 Stability and durability of products

In order to be applied on stone materials and build heritage in environmental conditions, the stability of newly synthesized products and the durability of their performance is ought to be evaluated, by means of accelerated ageing tests and/or field exposure test. Although the main results of stability study will not be reported in the thesis due to the relatively short time of this three-year PhD career, the accelerated ageing test of products by exploiting a climatic chamber equipped with a UV lamp is undergoing. The stability and performance durability of the products obtained will be reported whenever possible.

Chapter III

Partially fluorinated oligomers

3.1 Successfully synthesized and tested products

A partially fluorinated oligoadipamide bearing PFPE blocks—FAD was successfully synthesized and partially studied during my research for my master's thesis. The two-step poly-condensation reactions are represented by Scheme 3.1 and Scheme 3.2. After several tentative syntheses by means of varying the reaction conditions e.g. reaction temperature, molar ratio between reagents, solvent type and amount etc., the relatively pure oliogoadipamide (ADC2) was obtained with such conditions i.e. molar ratio between diethyl adipate and ethylenediamine as 1:5, solvent free and higher reaction temperature (95-100 °C). Employing FT-IR spectroscopy, the first step condensation was considered finished when the characteristic C=O stretching (~1733 cm^{-1}) of diethyl adipate disappeared completely (Figure 3.1). The purified oligoamide is soluble in alcoholic solvents, and its number average molecular weight (M_n) was determined to be 296 g/mol by exploiting its ^{1}H-NMR spectrum. The detailed method to estimate the M_n was reported in our paper [40].

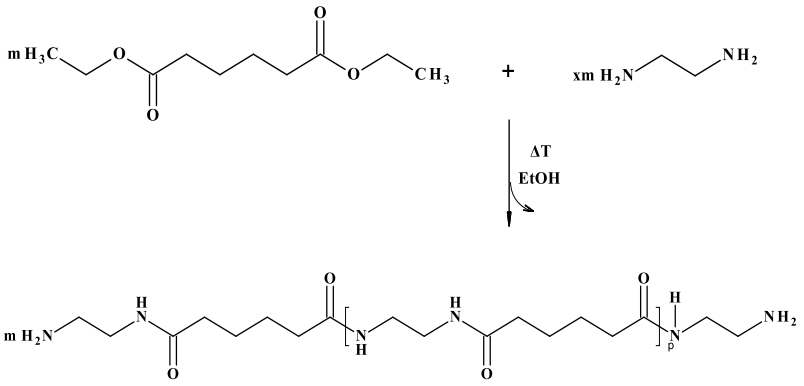

where x=5

Scheme 3.1 Synthesis of non-fluorinated oligoadipamide.

In the second step, based on the M_n of ADC2 found by ^{1}H-NMR, the molar ratio ADC2: PFPE (1:2) was adopted. Similar to the first-step synthesis, reaction kinetics was monitored using FT-IR spectroscopy. The conversion of ADC2 into FAD was considered completed when the peak height of C=O stretching of PFPE ester in the FT-IR spectrum (1792 cm^{-1}) tended to zero, while the peak height ratio between C=O stretching of fluorinated amide (1705 cm^{-1}) and C=O stretching of not fluorinated amide (1641 cm^{-1}) remained constant. The final product FAD shows good solubility in alcoholic and hydro-alcoholic solvents, which makes it easy to apply and possible to remove.

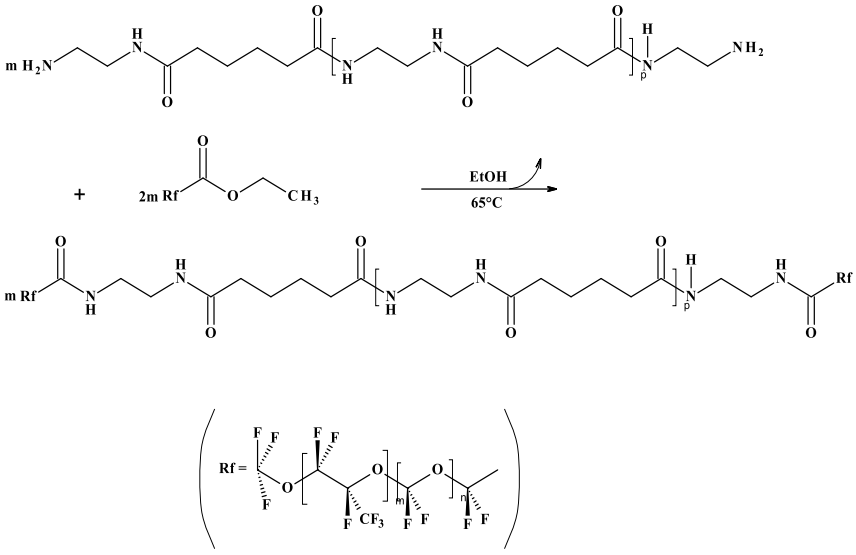

Scheme 3.2 Synthesis of partially fluorinated oligoadipamide.

Regarding its performance as water repellent for stone materials, as finalized in this thesis and reported in the paper [40], FAD is generally more effective for the protection of low porous stone (Table 3.1). Compared with a commercial fluoroelastomer (N215), FAD showed comparable WIE values when tested on Lecce stone for both short (30 min) and long times (1 h, 2 h). However, their WIE (Water Inhibition Efficiency) values are not very high, being all below 80%. It is noticed, when applied on marble, FAD demonstrated much higher WIE values than N215 in all testing times. Specifically, its WIE values are 94%, 92%, 90% and 90% after 1 h, 2 h 3 h, and 4 h absorption test respectively. On the other hand, N215 is not a good protective agent for marble, with WIE all below 60%.

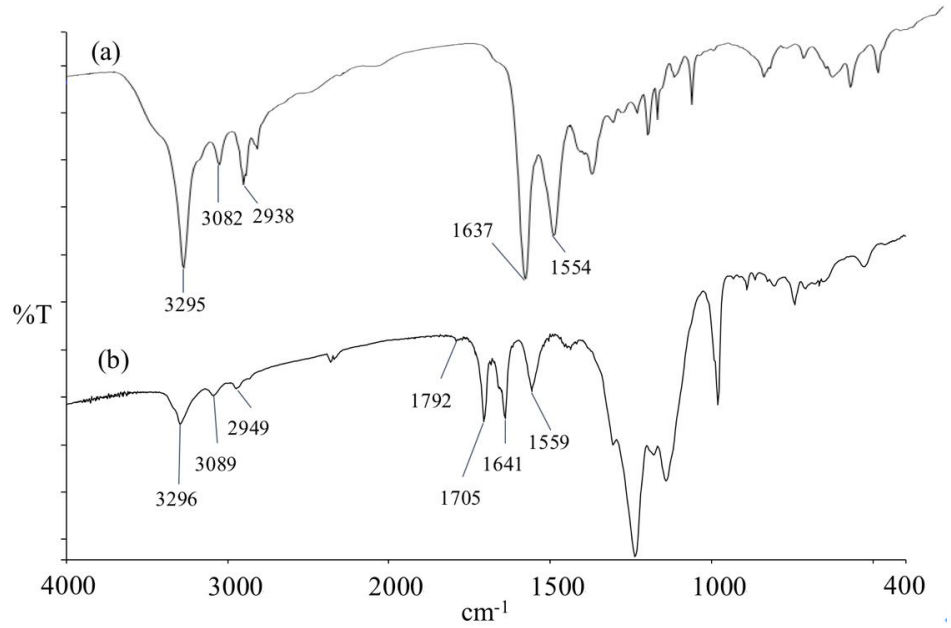

Figure 3.1 FT-IR spectrum of ADC2 (a) and FAD (b) on KBr windows.

Table 3.1 Water inhibition efficacy (WIE%) of FAD, N215 coated stone samples at different time of water absorption.

Treatment	Stone	WIE%* at				
		30 min	60 min	120 min	180 min	240 min
N215	Lecce stone	75	66	48	-	-
	marble	-	56	46	39	30
FAD	Lecce stone	79	67	44	-	-
	marble	-	94	92	90	90

*=WIE% was calculated as the mean value of two absorption tests

The hydrophobicity of FAD coating was also proved by water CA

measurements, and the morphology of neat and coated stone was also investigated by SEM-EDX analysis. In addition, based on the standard tests conducted, FAD was found to well preserve the original vapor diffusivity and chromatic features of stone substrates. All these results indicate the potential use of FAD as a protective coating for low porous stone materials, including stone artworks.

Yet, another homologous compound, a partially fluorinated oligosuccinamide (FSC) reported by Pappacchini A. seems to have the contrary characteristics as FAD [114]. FSC is good at protecting porous stones like Lecce stone, while it is not able to inhibit water absorption of marble. Therefore, in order to better characterize and understand the structure-property relationship of oligomers, the oligomer-stone substrate interaction mechanism, etc., more synthesis of homologous compounds and more in-depth studies are ought to be carried out.

3.2 New syntheses and new products

3.2.1 Materials

- **Reagents and solvents**

Ethylenediamine: Fluka product, purity > 99.5%

Diethyl succinate: Sigma-Aldrich product, purity 99%

Diethyl adipate: Sigma-Aldrich product, purity 99%

Suberic acid: Sigma-Aldrich product, purity 98%

Absolute Ethanol: J. T. Baker product

Anhydrous sodium bicarbonate: Carlo Erba product

Galden acid: monocarboxylic acid of perfluoropolyether with Mn≈880 (determined by titration), product kindly provided by Ausimont S.p.A.

Tetrahydrofuran: Sigma-Aldrich product, purity>99.9%

2-Propanol: EMSURE product

Diethyl ether, anhydrous: J.T. Baker product

Sulfuric acid: J. T. Baker product, purity 95-97%

Double-distilled water: produced in laboratory prior to use

Acetone: J.T. Baker product

Deuterated water 99.9% atom D, Sigma-Aldrich product

Methanol 99.9% deuterated atoms D, Sigma-Aldrich product

- **Stone materials**

Lecce stone

Lecce stone, a fine bio-calcarenite, is widely used in southern Italy as constituent material of large-scale architecture since ancient times. It has a rough, beige surface, characterized by homogeneous and fine grains (grain size distribution between 100 and 200 μm) between which microfossils are commonly seen. The water porosity is around 35-47%, with pore size ranging from 0.01 to 2 μm [115-117]. Lecce stone samples were selected and tested based on three sequences of water absorption tests conducted under the guidance of standard method [118]. Specimens that demonstrated constant water absorptivity were chosen. Samples were previously cut into 5·2·0.2 cm^3

slices (Figure 3.2) and 5·5·2 cm^3 slabs (Figure 3.3).

Carrara marble

Carrara marble, quarried from north Tuscany in Italy, has been extensively employed for construction since ancient times. Its main mineralogical constituent is calcite ($CaCO_3$) associated with small percentages of accessory minerals which influence color and veining. The water porosity is about 2%, with pore size distributing from 0.0001- 1 μm [119]. Marble samples are also in dimension 5*5*2 cm^3 (Figure 3.3).

Figure 3.2 Lecce stone slices.

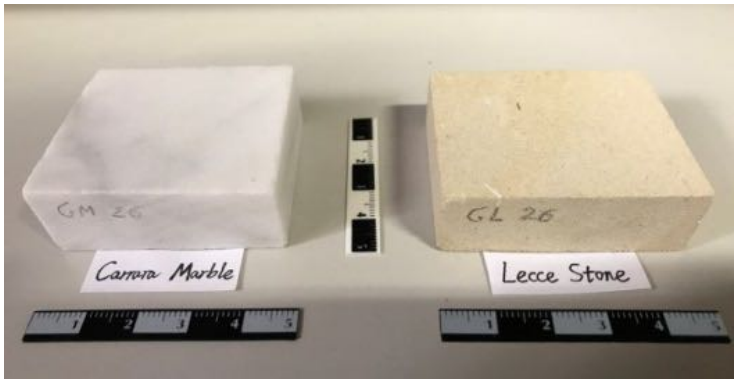

Figure 3.3 Lecce stone and Carrara marble slabs.

3.2.2 Instruments and methods

- **FT-IR spectroscopy**

The infrared spectra in Fourier Transform Infrared Spectroscopy (FT-IR) were recorded by the FT-IR Spectrometer Perkin Elmer Spectrum 1000 and processed by the software Spectrum v.3.0202.

Two types of analytical models were used: KBr (potassium bromide) windows and diamond cell (Specac England) based models. Spectra were recorded from 4000 cm^{-1} to 400 cm^{-1}, with a resolution of 2 cm^{-1} and 16 scans, when KBr windows were used. A little amount of sample (~0.01mg) was deposed homogeneously between two windows and analyzed in transmission mode. For rigid samples, diamond anvil cell was used. Spectra (in transmission mode) were recorded from 4000 cm^{-1} to 400 cm^{-1}, with a resolution of 2cm^{-1} and 64 scans.

- **NMR spectroscopy**

^{1}H-NMR

^{1}H-NMR analysis was performed with a Varian Mercury VXR400 spectrometer operating at a frequency of 399.921 MHz. Spectra are reported in chemical shift (ppm) relative to tetramethylsilane (TMS) at 0 ppm. The processing of the spectra was performed using Mestre-C 4.3.2.0.

^{13}C-NMR

The ^{13}C-NMR spectra were recorded Varian Mercury VXR400 spectrometer

operating at a frequency of 100.571 MHz. All spectra are reported in ppm using TMS as external standard (0 ppm). Spectra processing was done by using Mestre-C 4.3.2.0.

^{19}F-NMR

^{19}F-NMR spectra were recorded with a Bruker Avance III spectrometer operating at a frequency of 376.5 MHz. $CFCl_3$ is referred to as external standard (0 ppm) for all spectra. The processing of spectra was done by using software Mestre-C 4.3.2.0.

- **Solubility test**

The solubility percentage (%) of non-fluorinated oligoamides and final partially fluorinated oligoamides was estimated by dissolving 10 mg of product in 1 g of solvent (i.e. at solution concentration of 1% w/w solute/solvent) at room temperature (20-25 °C) and hot conditions (about boiling point of the solvent).

- **CA and CAH measurement**

CA of neat and coated Lecce stone and Carrara marble samples were measured using a Ramè-Hart Model 190 CA Goniometer. Static CA of 5 µl sessile droplets of liquid on stone surfaces was measured. Deionized water and extra virgin olive oil were employed as liquids for CA measurements. The contact angle reported is the average of five discrete drops per sample at different locations. For CAH measurement, a KRÜSS DSA 30 CA system was employed. Advancing or receding CA was measured by increasing or

decreasing the volume of the water droplet deposited on the surface with a small syringe and was recorded when the contact line began to advance or retract. Droplets of 6 µl with an increase of 2 µl for the advancing CA measurements were used. The CAH was defined as the difference between advancing and receding CA.

- **Surface morphology**

The surface morphology and elemental mapping analysis of virgin and coated samples was done by employing an environment scanning electron microscopy (ESEM Quanta – 200 FEI) equipped with an energy - dispersive x-ray spectrometer (X-EDS). Images in secondary (LFD) and backscattered electrons (BSE) were acquired, and elemental composition was obtained working at pressure of 1.00 and 0.50 Torr with a voltage of 25 KeV. Elemental mapping, both on surface and in depth (stratigraphy), was also done at 25 KeV with an amplification time of 10 µs. 11 frames of scan were performed. Mapping on slice treated with 18.3 g/m^2 of FSB was done by using a Zeiss EVO MA 15 SEM equipped with an RSD detector and Oxford INCA 250 X-EDS operated at 20 KeV, pressure of 1 Torr and current of 2.4 µA. The stratigraphic elemental mapping analysis was conducted on the internal cross section surface of slices obtained by breaking the slice gently by hand.

- **Surface adhesive property**

The adhesion force (AF) of superhydrophobic surfaces was estimated by simple calculation based on the maximum volume of water droplet (released

from a micro syringe) that can pin at interface. AF was calculated as AF(N) = mass·g, where mass is the weight of water droplet, g = 9.8 m/s^2 is the standard acceleration in free fall.

- **Water evaporation test**

The water evaporation process on superhydrophobic surfaces was studied by taking micrographs during evaporation of a 1 µl droplet over time. Photos were taken by a Digital C-Mount Camera TP3100 mounted on an optical microscope (Nikon SMZ745T) at different intervals until complete evaporation. The CA and contact diameter were recorded and studied.

- **Water immersion test**

The stability and durability of superhydrophobic surfaces with high AF were evaluated by immersing them thoroughly in deionized water for 2, 8 and 24 hours. The CA and AF were measured after each test, after drying the samples in air.

- **Water inhibition test**

The water capillary absorption of stone samples (Figure 3.4), before and after protective treatment, were performed under the guidance of Norm UNI-EN 15801-2010 "Conservation of Cultural Heritage – Test methods – Determination of water absorption by capillarity" [118]. The results were processed and reported as water inhibition efficiency (WIE) as described by Camaiti et al. [114]

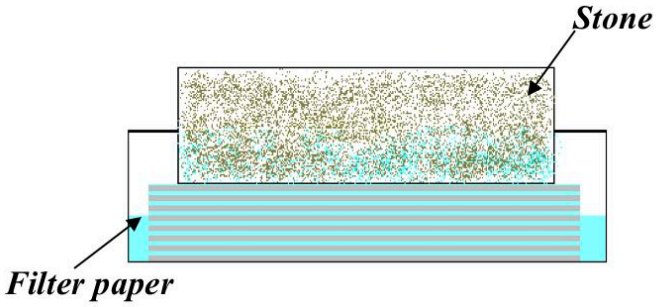

Figure 3.4 Schematic description of set-up of water capillary absorption test.

- **Vapor diffusivity test**

The measurements of residual vapor permeability of polymeric film were carried out on the basis of Norm UNI-EN 15803-2010, "Conservation of Cultural Heritage – Test methods – Determination of the permeability of water vapor" [120]. Results were processed and presented as residual diffusivity RD (%).

Besides, the effective diffusion coefficient (D_{eff}) of coated stone samples was assessed, by plotting the weight of "Cup" versus time and exploiting Fick's law of diffusion (Figure 3.5). On the basis of Fick's Law, the molar flux of gas J (moles/area/time), in the steady-state diffusion through a polymeric film is defined as:

$$J = D\frac{(c_1 - c_0)}{L} \qquad \text{(Eq. 3.1)}$$

where D is the diffusivity of gas in the polymer, c_1 and c_o ($c_1 > c_o$) are the concentration of gas at the two ends of the polymeric film with a thickness of L. In the system of "Cup", where normal pressure and temperature are used,

a similar situation is observed: the gas is represented by vapor, c_1 and c_o are the concentration (or partial pressure) of vapor (calculated at 30°C) inside and outside the cup, respectively. L is the thickness of the rock slab [121]. In these conditions, the gas diffusion is controlled by molecular diffusion within the gas-filled pores rather than by collisions with pores, and the diffusive flux of vapor through the porous medium was expressed as:

$$J = D_{eff} \frac{(c_1 - c_0)}{L} \qquad \text{(Eq. 3.2)}$$

where D_{eff} is the effective diffusion coefficient, and it was related to the molecular diffusion coefficient of vapor D, the porosity ε and tortuosity τ of the porous material,

$$D_{eff} = \frac{\varepsilon}{\tau} D \quad (\tau > 1) \qquad \text{(Eq. 3.3)}$$

Figure 3.5 Set-up of Cup method.

- **Colorimetric measurement**

The colorimetric analysis on stone surfaces was performed before and after

products application in order to perceive possible chromatic changes induced by protective coatings. For each sample, specific spots were selected by using a mask prior to analysis. All measurements were conducted by exploiting a portable reflection colorimeter X-Rite SP60 according to Norm UNI-EN 15886-2010 “Conservation of Cultural Heritage – Test methods – Measurement of the color of the surface” [122] (Figure 3.6). Results were elaborated and reported in CIE-L*a*b* standard color system, and the color alteration (ΔE*) was calculated.

Figure 3.6 X-Rite SP60 colorimeter.

3.2.3 Partially fluorinated oligosuberamide

3.2.3.1 Synthesis of diethyl suberate

The reaction apparatus consists of a round bottom flask, equipped with a three way adapter, a thermometer and a bent vacuum-distilling. After setting up, an Erlenmeyer flask was connected to the end of the bent vacuum-distilling adapter for distillate collection. Besides, a drying tube, containing anhydrous

$CaCl_2$, was mounted on the bent vacuum-distilling adapter in order to maintain an anhydrous environment.

3.131 g (17.99 mmol) of suberic acid (white solid) and 15ml (11.8350 g, 256.89 mmol) of ethyl alcohol were introduced into the round bottom flask successively. With a moderate stirring, the mixture was heated up to 80 °C for 8 hours in an oil bath. Then, the temperature was increased to 110 °C for 1 hour to distill water/ethanol azeotrope, promoting the reaction towards ester formation. After distillation, an additional 10ml of ethyl alcohol was added as compensation. Temperature fluctuation cycles as such (80°C -110 °C) were performed 2 times. At 20 hours, 10 drops of sulfuric acid (>98%) was introduced as catalyst. Temperature cycles were performed continuously till the end of reaction. The excess of ethyl alcohol was evaporated under vacuum by using a vacuum pump.

The kinetics of esterification was monitored at regular intervals by FT-IR spectroscopy. Esterification was considered finished when the suberic acid was completely reacted. By testing the mixture with $NaHCO_3$ in presence of ethanol, if in the FT-IR spectrum the corresponding salt of suberic acid (around 1560 cm^{-1}) was absent, the reaction was considered completed. After 48 h, sodium salt of suberic acid was not detectable after salification test, meaning ending of esterification. Finally, 3.98 g of colorless, transparent liquid (diethyl suberate) was obtained after evaporation of ethyl alcohol.

IR (KBr): 2980, 2936, 2861 cm^{-1} (ν_{C-H}) 1734 cm^{-1} ($\nu_{C=O}$), 1373 cm^{-1} (δ_{C-H}).
FT-IR spectrum (on KBr windows, Figure I): in Appendix.

3.2.3.2 Synthesis of non-fluorinated oligosuberamide (SubC2)

- **First synthesis—SubC2 (1:2)** (molar ratio diethyl suberate/ ethylenediamine= 1/2)

In a two-necked 100 ml flask, equipped with a reflux condenser and a dropping funnel, ethylenediamine (0.83 ml, 12.44 mmol) was introduced in nitrogen atmosphere and room temperature. Under vigorous magnetic stirring, diethyl suberate (1.43 g, 6.27 mmol) and then 2-propanol (3.00 ml) were added dropwise through the dropping funnel. The temperature was first kept at room temperature for 8 h, and then it was raised up to 60 °C and kept for 38 h. After evaporation of solvent, the solid obtained was washed with 10 ml of diethyl ether for 4 times and then dried under vacuum. The white solid (1.154 g, yield 56%) was characterized by FT-IR and ^{1}H- NMR spectroscopy. The number-average molecular weight, estimated by ^{1}H-NMR spectroscopy, was 326 g/mol.

During the reaction, the kinetics was monitored by FT-IR spectroscopy at regular intervals (every 4 h) till reaction completion. Time, color and properties were accurately documented when precipitation first occurred. First yellowish precipitation occurred after 8 h.

IR (KBr): 3301 and 3076 cm^{-1} (ν_{N-H}), 2938 and 2862 cm^{-1} (ν_{C-H}), 1639 cm^{-1} ($\nu_{C=O}$), 1556 cm^{-1} (δ_{N-H}), 1469 cm^{-1} (ν_{C-N}).

^{1}H-NMR (D_2O, 399.921 MHz) δ: (D_2O, 399.921 MHz) δ: 3.36 (s, 4H, -NH-C$\underline{H}_2$-C$\underline{H}_2$-NH-), 3.34 (t, J_{H-H} = 6.2 Hz, 2H, H_2N-CH_2-C$\underline{H}_2$-), 2.87 (t, J_{H-H} = 6.2 Hz, 2H, H_2N-C$\underline{H}_2$-), 2.27 (t, J_{H-H} = 6.2 Hz, 4H, -CO-C$\underline{H}_2$-$(CH_2)_2$-$(CH_2)_2$-C$\underline{H}_2$-), 1.59 (s, 4H, -CO-CH_2-C$\underline{H}_2$-$(CH_2)_2$-C$\underline{H}_2$-CH_2-CO), 1.32 (s, 4H, -CO-$(CH_2)_2$-C$\underline{H}_2$-C$\underline{H}_2$-$(CH_2)_2$-CO).

FT-IR spectrum (on KBr windows, Figure II): Appendix.

^{1}H-NMR spectrum (D_2O, 399.921 MHz, Figure III): Appendix.

- **Second synthesis—SubC2 (1:3)** (molar ratio diethyl suberate/ ethylenediamine= 1/3)

The same reaction apparatus was set up. 1.741 ml (26.08 mmol) of ethylenediamine was first introduced into a two-necked 100 ml flask in nitrogen atmosphere. Then, under vigorous stirring, 2 g (8.69 mmol) of diethyl suberate and 2 ml of 2-propanol were added dropwise from dropping funnel. The temperature was kept at room temperature for 48 h and then increased to 80-85 °C and kept for 12 h. After solvent evaporation, the solid obtained was washed with 10 ml of diethyl ether for 4 times and then dried under vacuum. The white solid (1.85 g, yield 72%) was characterized by FT-IR and ^{1}H-, ^{13}C-NMR spectroscopy. The number-average molecular weight, estimated by ^{1}H-NMR spectroscopy, was 296 g/mol.

During the reaction, the kinetics was monitored by FT-IR spectroscopy at regular intervals till reaction completion. Time, color and properties were accurately documented when precipitation first occurred. First yellowish precipitation occurred after 24 h at room temperature.

IR (KBr): 3300 and 3076 cm^{-1} (ν_{N-H}), 2935 and 2861 cm^{-1} (ν_{C-H}), 1634 cm^{-1} ($\nu_{C=O}$), 1550 cm^{-1} (δ_{N-H}), 1448 cm^{-1} (ν_{C-N}).

^{1}H-NMR (D_2O, 399.921 MHz) δ: 3.27 (s, 4H, -NH-C$\underline{H}_2$-C$\underline{H}_2$-NH-), 3.19 (t, J_{H-H} = 6.2 Hz, 2H, H_2N-CH_2-C$\underline{H}_2$-), 2.69 (t, J_{H-H} = 6.2 Hz, 2H, H_2N-C$\underline{H}_2$-), 2.17 (t, J_{H-H} = 6.2 Hz, 4H, -CO-C$\underline{H}_2$-$(CH_2)_2$-$(CH_2)_2$-C$\underline{H}_2$-), 1.51 (s, 4H, -CO-CH_2-C$\underline{H}_2$-$(CH_2)_2$-C$\underline{H}_2$-CH_2-CO), 1.23 (s, 4H, -CO-$(CH_2)_2$-C$\underline{H}_2$-C$\underline{H}_2$-$(CH_2)_2$-CO).

^{13}C-NMR (D_2O, 100.571 MHz) δ: 177.40 (s, $\underline{C}$=O), 40.78 (s, H_2N-CH_2-$\underline{C}H_2$-), 39.52 (s, H_2N-$\underline{C}H_2$-CH_2-), 35.55 (s, -CO-NH-$\underline{C}H_2$-$\underline{C}H_2$-NH-CO-), 27.67 (s, -CO-$\underline{C}H_2$-$\underline{C}H_2$ -), 24.97 (s, -CO-$(CH_2)_2$-$\underline{C}H_2$-$\underline{C}H_2$-).

FT-IR spectrum (on KBr windows): Figure 3.8.

^{1}H-NMR spectrum (D_2O, 399.921 MHz): Figure 3.7.

13C-NMR spectrum (D_2O, 100.571 MHz, Figure IV): Appendix.

- **Third synthesis—SubC2 (1:5)** (molar ratio diethyl suberate/ ethylenediamine= 1/5)

Employing the same reaction set-up, in nitrogen atmosphere, 2.9 ml (44.78

mmol) of ethylenediamine was first added in two a two-necked round bottom 100 ml flask which was equipped with reflux condenser and a dropping funnel. 2 g (9.70 mmol) of diethyl suberate and 2 ml of 2- propanol were introduced dropwise into flask subsequently through the dropping funnel. The temperature remained at room temperature for 67 h. After solvent evaporation, the solid obtained was washed with 10 ml of diethyl ether for 5 times and then dried under vacuum. The white solid (1.87 g, yield 68%) was characterized by FT-IR and ^{1}H-, ^{13}C-NMR spectroscopy. The number-average molecular weight, estimated by ^{1}H-NMR spectroscopy, was 286 g/mol.

During the reaction, the kinetics was monitored by FT-IR spectroscopy at regular intervals till reaction completion. Time, color and properties were accurately documented when precipitation first occurred. First yellowish precipitation occurred after 27 h at room temperature.

IR (KBr): 3301 and 3078 cm^{-1} (ν_{N-H}), 2935 and 2859 cm^{-1} (ν_{C-H}), 1636 cm^{-1} ($\nu_{C=O}$), 1551 cm^{-1} (δ_{N-H}), 1466 cm^{-1} (ν_{C-N}).

^{1}H-NMR (D_2O, 399.921 MHz) δ: 3.24 (s, 4H, -NH-C<u>H</u>$_2$-C<u>H</u>$_2$-NH-), 3.19 (t, J_{H-H} = 6.2 Hz, 2H, H_2N-CH$_2$-C<u>H</u>$_2$-), 2.69 (t, J_{H-H} = 6.2 Hz, 2H, H_2N-C<u>H</u>$_2$-), 2.18 (t, J_{H-H} = 6.2 Hz, 4H, -CO-C<u>H</u>$_2$-(CH$_2$)$_2$-(CH$_2$)$_2$-C<u>H</u>$_2$-), 1.51 (s, 4H, -CO-CH$_2$-C<u>H</u>$_2$-(CH$_2$)$_2$-C<u>H</u>$_2$-CH$_2$-CO), 1.23 (s, 4H, -CO-(CH$_2$)$_2$-C<u>H</u>$_2$-C<u>H</u>$_2$-(CH$_2$)$_2$-CO).

^{13}C-NMR (D_2O, 100.571 MHz) δ: 177.40 (s, C=O), 40.84 (s, H_2N-CH_2-CH_2-), 39.55 (s, H_2N-CH_2-CH_2-), 35.57 (s, -CO-NH-CH_2-CH_2-NH-CO-), 27.69 (s, -CO-CH_2-CH_2 -), 24.99 (s, -CO-$(CH_2)_2$-CH_2-CH_2-).

FT-IR spectrum (on KBr windows, Figure V): Appendix.

^{1}H-NMR spectrum (D_2O, 399.921 MHz, Figure VI): Appendix.

^{13}C-NMR (D_2O, 100.571 MHz, Figure VII): Appendix.

3.2.3.3 Synthesis of ethyl ester of Galden acid

The same apparatus for diethyl suberate synthesis was used. A round bottom flask was equipped with a three way adapter, a thermometer and a bent vacuum-distilling. An Erlenmeyer flask was connected to the end of the bent vacuum-distilling adapter for distillate collection. Besides, a drying tube in which there was anhydrous $CaCl_2$, was mounted on the bent vacuum-distilling adapter in order to maintain an anhydrous environment.

10.00 g (11.40 mmol) of Galden Acid and 30 ml (0.53 mol) of anhydrous EtOH were added to the flask. The temperature was maintained at about 50-60 °C for 20 h. The kinetics of reaction was monitored regularly by FT-IR spectroscopy. After 20 h, the temperature was raised to about 80-85 ° C to distill the H_2O-EtOH azeotrope. Then the temperature was reduced to 50-60 °C and another 20 ml of anhydrous ethanol was added. At the end of the reaction, the H_2O: EtOH azeotrope was removed by the same procedure

above, and 9.15 g (yield 90%) of colorless liquid was obtained.

IR (KBr): 2995 cm^{-1} (ν_{C-H}), 1792 cm^{-1} ($\nu_{RfC=O}$), 1400-900 cm^{-1} (ν_{C-F}).
FT-IR spectrum (on KBr windows, Figure VIII): Appendix.

3.2.3.4 Synthesis of partially fluorinated oligosuberamide (FSB)

After characterization by ^{1}H-NMR spectroscopy, SubC2 (1:2) was found to be impure due to the presence of unreacted ethylenediamine residues. Consequently, only SubC2(1:3) and SubC2 (1:5) were used for the second step reaction.

Synthesis of partially fluorinated oligosuberamide with SubC2 (1:3)
In a two-necked 100 ml flask, 2-propanol (15 ml) was added to SubC2 (1:3) (0.167g, 0.56 mmol) under nitrogen atmosphere and vigorous magnetic stirring. When SubC2 (1:3) was almost completely dissolved, ethyl ester of Galden acid (1.027 g, 1.13 mmol) was introduced dropwise. The mixture was stirred for 20 h at room temperature before heating up to 65-70 °C for 40 hours. The slightly yellowish waxy product (0.890 g, yield 77%) was recovered after solvent evaporation under reduced pressure, and then it was purified with trichlorotrifluoroethane (A113) for 3 times. The product was further characterized by FT-IR, ^{1}H- and ^{19}F-NMR spectroscopy.

IR (KBr): 3300 and 3085 cm^{-1} (ν_{N-H}), 2937 and 2858 cm^{-1} (ν_{C-H}), 1706 cm^{-1}

($\nu_{Rf\text{-}C=O}$), 1642 cm^{-1} ($\nu_{C=O}$), 1559 cm^{-1} ($\delta_{N\text{-}H}$), 1400-900 cm^{-1} ($\nu_{C\text{-}F}$).

^{1}H-NMR (CD_3OD:D_2O, 95:5 w/w): δ: 3.42 (t, $J_{H\text{-}H}$ = 6.0 Hz, 4H, R_f-CO-NH-CH_2-C$\underline{H}_2$-), 3.30 (m, 4H, R_f-CO-NH-C$\underline{H}_2$-CH_2-), 3.02 (t, $J_{H\text{-}H}$ = 6.1 Hz, 4H, –CO-NH-C$\underline{H}_2$-C$\underline{H}_2$-NH-CO–), 2.22 (t, $J_{H\text{-}H}$ = 7.6 Hz, 4H, -CO-C$\underline{H}_2$-$(CH_2)_2$-$(CH_2)_2$-C$\underline{H}_2$-), 2.17 (t, $J_{H\text{-}H}$ = 7.3 Hz, 4H, -CO-CH_2-C$\underline{H}_2$-$(CH_2)_2$-C$\underline{H}_2$-CH_2-CO), 2.16 (t, $J_{H\text{-}H}$ = 7.3 Hz, 4H, -CO-$(CH_2)_2$-C$\underline{H}_2$-C$\underline{H}_2$--$(CH_2)_2$-CO).

^{19}F-NMR (CD_3OD, 376.5 MHz) δ: -56.8 (C$\underline{F}_3$-O-), -77.1 [s, 3F, –O-C$\underline{F}_2$-CO-NH-R], -81.2 (–O-C$\underline{F}_2$-CF(C$\underline{F}_3$)-O–), from -85.8 to -87.5 (C$\underline{F}_3$-$\underline{CF}$OR(OCF_3), C$\underline{F}_3$-C$\underline{F}_2$O–), -146.2 (-O-CF_2-C$\underline{F}$(CF_3)-O-).

FT-IR spectrum (on KBr windows): Figure 3.8.

^{1}H-NMR spectrum (CD_3OD:D_2O, 95:5 w/w, 399.921 MHz, Figure IX): Appendix.

^{19}F-NMR (CD_3OD, 376.5 MHz, Figure X): Appendix.

Synthesis of partially fluorinated oligosuberamide with SubC2 (1:5)

In a two-necked 100 ml flask, 2-propanol (5 ml) was added to SubC2 (1:5) (0.152g, 0.53 mmol) under nitrogen atmosphere and vigorous magnetic stirring. When SubC2 (1:3) was almost completely dissolved, ethyl ester of Galden acid (0.934 g, 1.06 mmol) was introduced dropwise. The mixture was stirred and then heated to 55-60 °C for 56 h. The slightly yellowish waxy product (0.826 g, yield 79%) was recovered after solvent evaporation under reduced pressure, and then it was purified with A113 for 5 times. The product

was further characterized by FT-IR spectroscopy.

IR (KBr): 3301 and 3085 cm^{-1} (ν_{N-H}), 2938 and 2861 cm^{-1} (ν_{C-H}), 1704 cm^{-1} ($\nu_{Rf-C=O}$), 1645 cm^{-1} ($\nu_{C=O}$), 1557 cm^{-1} (δ_{N-H}), 1400-900 cm^{-1} (ν_{C-F}).

FT-IR spectrum (on KBr windows, Figure XI): Appendix.

3.2.4 Partially fluorinated oligosuccinamide

3.2.4.1 Synthesis of non-fluorinated oligosuccinamide (SucC2)

In a two-necked 100 ml flask, equipped with a magnetic stirring bar, a bubble condenser and a dropping funnel, ethylenediamine (1.381 g, 22.9 mmol) was introduced under nitrogen atmosphere. At room temperature and under vigorous stirring, diethyl succinate (2.004 g, 11.5 mmol) in 2 ml of THF was then added dropwise through the funnel. The flask was placed in an oil bath for reaction at 90-95 °C for 7 hours. FT-IR analysis was performed at regular intervals of approximately 2 hours to monitor the kinetics of reaction. The precipitate obtained was decanted and washed with diethyl ether (20 ml each time for three times), and finally dried by using a rotary evaporator. 1.944 g (yield 98%) of white solid was obtained. The product was further characterized by FT-IR spectroscopy, ^{1}H-NMR spectroscopy, and the number-average molecular weight (330 g/mol) was estimated by ^{1}H-NMR spectroscopy as well.

IR (KBr): 3295 and 3084 cm^{-1} (ν_{N-H}), 2973 and 2938 cm^{-1} (ν_{C-H}), 1636 cm^{-1} ($\nu_{C=O}$), 1561 cm^{-1} (δ_{N-H}).

^{1}H-NMR (D_2O, 399.921 MHz): δ 3.31 ppm (s, 4H, -CO-NH-C$\underline{H}_2$-C$\underline{H}_2$-NH-CO- of oligoamide with longer chains), 3.27 ppm (t, J_{H-H}=6.16 Hz, 8H, -CO-NH-C$\underline{H}_2$-CH_2-NH_2), 2.75 ppm (t, J_{H-H}=6.16 Hz, 8H, -CO-NH-CH_2-C$\underline{H}_2$-NH_2), 2.56 ppm (s, 4H, -CO-C$\underline{H}_2$-C$\underline{H}_2$-CO- of oligoamide with shorter chains), 2.54 ppm (s, 8H, -CO-C$\underline{H}_2$-C$\underline{H}_2$-CO- of oligoamide with longer chains).

FT-IR spectrum (on KBr windows): Figure 3.8.

^{1}H-NMR spectrum (D_2O, 399.921 MHz, Figure XII): Appendix.

3.2.4.2 Synthesis of partially fluorinated oligosuccinamide (FSC)

The same reaction apparatus was adopted. In a two-necked 100 ml flask, equipped with a magnetic stirring bar, a bubble condenser and a dropping funnel, oligosuccinamide (0.678 g, 2.0 mmol) was introduced in nitrogen atmosphere. Thereafter, at room temperature and under stirring, ethyl ester of Galden acid (2.495 g, 3.7 mmol) in 15 ml of ethanol was added slowly into the flask. After 3 hours, additional 0.161 g (0.2 mmol) of fluorinated ester was added at room temperature and under stirring. Then, after 11.5 h, other 0.166 g (0.2 mmol) of fluorinated ester was added at the same conditions after 11.5 hours. Finally, another 0.508 g (0.6 mmol) of fluorinated ester was added

after 16.5 hours from the beginning of the reaction. In total, 3.330 g (3.7 mmol) of fluorinated ester, corresponding to approximately 10% less than the stoichiometric amount, was introduced. After the last addition of fluorinated ester, the temperature was raised up to 75-80° C and maintained at this temperature for 25 hours. The reaction kinetics was monitored by FT-IR spectroscopy at intervals of 3 and 8 hours. The precipitate obtained was decanted and washed with A113 and 2-propanol successively and dried by a rotary evaporator. 2.629 g (yield 67%) of waxy white solid was recovered. The final product was further characterized by FT-IR spectroscopy, ^{1}H-NMR and ^{19}F-NMR spectroscopy.

IR (KBr): 3295 and 3084 cm^{-1} (ν_{N-H}), 2936 and 2890 cm^{-1} (ν_{C-H}), 1703 cm^{-1} ($\nu_{Rf-C=O}$), 1636 cm^{-1} ($\nu_{C=O}$), 1556 cm^{-1} (δ_{N-H}), 1400-900 cm^{-1} (ν_{C-F}).

^{1}H-NMR (CD_3OD:D_2O 95:5, 199.985 MHz): δ 3.45 ppm (m, 4H, –C$\underline{H}_2$-CH_2-NH-CO-R_f), 3.38 ppm (m, 4H, -C$\underline{H}_2$-NH-CO-R_f), 3.03 ppm (m, 4H, -CO-NH--C$\underline{H}_2$-C$\underline{H}_2$-NH-CO-), 2.47 ppm (m, 8H, -CO-C$\underline{H}_2$-C$\underline{H}_2$-CO-).

^{19}F-NMR (CD_3OD:D_2O 95:5, 188.114 MHz): -57.0 ppm (C$\underline{F}_3$-O–), -76.8 -77.3 ppm (–O-C$\underline{F}_2$-CO-NH-R), -81.4 (–O-C$\underline{F}_2$-CF(C$\underline{F}_3$)-O–), from -85.9 to -87.6 ppm (C$\underline{F}_3$-C$\underline{F}$OR(OCF_3), C$\underline{F}_3$-C$\underline{F}_2$O–), -146.0 ppm (–O-CF_2-C$\underline{F}$(CF_3)-O–).

FT-IR spectrum (on KBr windows): Figure 3.8.

^{1}H-NMR spectrum (CD_3OD:D_2O 95:5, 199.985 MHz, Figure XIII): Appendix.

^{19}F-NMR (CD_3OD, 188.114 MHz, Figure XIV): Appendix.

3.3 Stone sample selection

Prior to product application and subsequent tests, Lecce stone and Carrara marble samples were selected based on three sequences of water capillary absorption tests conducted following the standard method [118]. In our case, water capillary absorption is depicted by the uniaxial penetration of water into a 5x5 cm^2 surface for 2 cm-distance, indicated as numerical value of wet weight changes.

The dry weight of sample was measured before absorption tests (oven at 60°C was used to facilitate drying for wet samples). Samples of the same kind of stone were put on stacks of absorbent paper in a plastic box with cover, with water reaching half height (1cm) of the absorbent paper (Figure 3.4). The marked faces of samples were settled on the wet paper, enabling absorption by capillarity. Wet weight of samples was measured at intervals of 30 mins, 60 mins, 120 mins, 180 mins after settling on paper for Lecce stone, and more measurement at 240 mins and 24 h for marble samples. In total, there were 25 pieces of Lecce stone samples and 25 pieces of marble samples, and for each type of stones 3 series of absorption tests were performed.

After the 3rd absorption test, the collected data were processed. Average water absorption amount within a certain time range (30 mins; 60 mins, etc.) and its standard deviation were calculated for each sample. Moreover, the value *"(max-min)/max*100"* (referred to water absorption amount) for each sample at each time interval were obtained, which were regarded as the most significant value for sample selection. Based on all the data acquired, samples that demonstrate "constant" water absorptivity were selected for the following experiment. Taking Lecce stone specimens as an example (Table 3.2), it is not difficult to figure out that specimen GL1, GL3, GL4 etc. meet the criteria.

Table 3.2Water capillary absorption of Lecce stone samples (after 1 h).

Sample #	Water absorption after 1 h (g)			Average (g)	σ	*(Max-min) /max *100**
	1st test	2nd test	3rd test			
GL1	9.516	9.719	9.574	9.603	0.085	2.089
GL2	10.049	9.233	9.188	9.490	0.396	8.568
GL3	9.516	9.398	9.252	9.389	0.108	2.774
GL4	10.049	9.986	9.959	9.998	0.038	0.896
GL5	9.869	9.744	9.625	9.746	0.100	2.472
GL6	9.957	9.89	9.715	9.854	0.102	2.430
GL7	9.837	9.721	9.664	9.741	0.072	1.759
GL8	9.373	9.2	8.438	9.004	0.406	9.975
GL9	9.996	9.876	9.565	9.812	0.182	4.312
GL10	9.618	9.459	8.866	9.314	0.324	7.819

* For Lecce stone, *"(max-min)/max*100"* < 5 indicates a "constant"

absorption property. For marble, the value is considered as 10.

Moreover, among all the specimens that absorb water constantly (*max-min)/max*100"* < 10), samples that absorb high amount of water, samples that absorb medium amount and samples absorb low amount of water are selected within each type of stone in a certain testing time range e.g. 3 h for marble.

Finally, nine Lecce stone samples and nine marble samples were selected for product application and performance tests, together with three samples serving as references for each lithotype.

3.4 Coating preparation

- **On slices**

Aiming at investigating the relationship between product amounts and hydrophobicity, various quantities, i.e. 5.8 g/m^2, 11.1 g/m^2, 18.3 g/m^2 and 22.9 g/m^2 of FSC, FSB and FAD (0.5% w/w 2-propanol solutions) were applied on one larger face (5*2 cm^2) of the Lecce stone slices by using a pipette with the method "wet on wet". FAD is the product of previous study [40]. A pipette is used when small areas must be coated with well defined amount of product. The treatment can be equated to a brush coating. "Wet on wet" is a technique mostly used in stone consolidation, in which additional treatment was applied to previously executed wet surface.

- **On slabs**

To test their performance as hydrophobic coating, the products were also applied on Lecce stone and marble slabs. 1% (w/w) 2-propanol mixtures of FSC, FSB and FAD were prepared. A graduated pipette (0.5 ml) was used for deposing solutions on one larger face of the rocks with the same method "wet on wet". Treatment was stopped before saturation (about 15 g/m^2), considering the best CA results observed on slices. The exact amount applied was calculated as the weight difference between dry weight before treatment and after treatment. After treatment and before subsequent tests, all treated samples (three slabs and one slice per product), together with the references, were left under laboratory conditions for solvent evaporation (typically one week) and then put in desiccator until a constant weight was reached. Table 3.3 summarizes the actual amount of coating materials applied on slabs.

Table 3.3 Amount of coating materials applied on Lecce stone and marble slabs.

Coating material	Lecce stone		Marble	
	Theoretical g (g/m^2)	Actual g (g/m^2)	Theoretical g (g/m^2)	Actual g (g/m^2)
FSB		0.041±0.003 (16)		0.008±0.000 (3.2)
FAD	0.037 (15)	0.037±0.006 (15)	0.0125 (5)	0.01±0.001 (4)
FSC		0.033±0.005 (13)		0.013±0.001 (5.2)

3.5 Results and discussion

3.5.1 Synthesis and characterization of non-fluorinated oligoamides

The synthesis was realized via condensation reactions (Scheme 3.3). Ethyl esters of dicarboxylic acids reacted with ethylenediamine (in excess) to form oligoamides with terminal amine groups which is necessary for successive reactions. As explained before [40], instead of acids, esters were used to avoid salts formation which require higher temperature for amide formation.

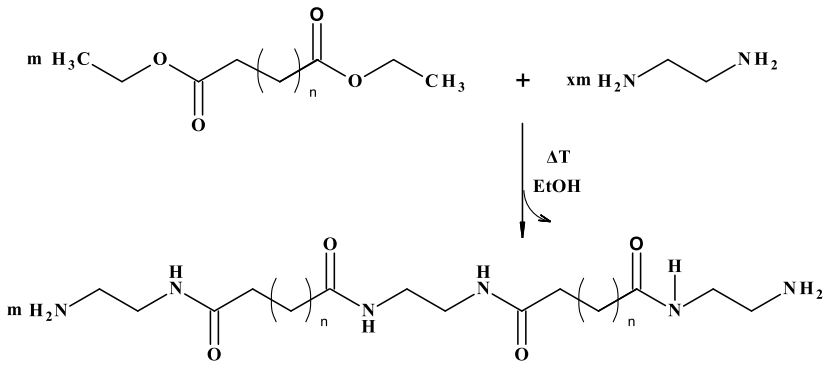

Where n= 1 and x=2 for SucC2; where n= 5 and x=2, 3, 5 for SubC2

Scheme 3.3 Synthesis of non-fluorinated oligoamides.

To synthesize oligosuberamide, three syntheses with varied amounts of ethylenediamine (i.e. ester/ethylenediamine: 1/2, 1/3, 1/5) and reaction conditions were conducted (Table 3.4). The second synthesis, SubC2 (ester/ethylenediamine= 1/3), completed with a high yield (72%) within the shortest reaction time (12 h). Besides, exploiting ^{1}H-NMR analysis (Figure

3.7), SubC2 (1:3) was also proved to be the purest product (least interfering signals attributing to reagents residuals) among these three. Thereby, SubC2 (1:3) was selected for the subsequent FSB synthesis.

In comparison with previously reported oligoadipamide (ADC2) synthesis, in all the oligoamides syntheses, an excess of ethylenediamine was used to obtain oligomers with terminal amine groups. However, the most appropriate molar ratios between esters and ethylenediamine were different, being 1:3, 1:2 and 1:5 for oligosuberamide (SubC2), oligosuccinamide (SucC2) and oligoadipamide (ADC2) and, respectively (Table 3.5). Reaction time also differed. In fact, SucC2 was obtained within the shortest time (7 h) whereas 22 h were used for synthesizing ADC2. With the shortest reaction time, SucC2 also had the highest yield among all. This is probably due to the varied solubility of oligoamides in the solvent used in the synthesis, and to the possibility to form intra/inter-molecular hydrogen bonding between NH of amidic groups and C=O of carbonyl or of not reacted carboxylic groups. Constituted of four carbon atoms, which is the shortest chain among these three esters, diethyl succinate is less flexible than adipate and suberate, and more likely to form intra-molecular hydrogen bonding, giving rise to a high yield within short time. For all reactions, FT-IR spectroscopy was used to monitor the kinetics periodically (Figure 3.8 and Figure 3.9), and special attention was paid to the characteristic absorption bands, e.g. carbonyl groups of ester and amide. These oligoamides are homologous, with slightly differed band positions of functional groups (Table 3.6). The peak position of amide I

(C=O stretching) varied for about 4-5 cm^{-1} from one to another. Specifically, amide I had its absorption band at the highest wavenumber in ADC2 (1637 cm^{-1}) and the lowest wavenumber in SucC2 (1631 cm^{-1}). Additionally, the peak of amide II (C-N stretching) in ADC2 (1441 cm^{-1}) was at a lower wavenumber than it is in SucC2 and/or SubC2 (1448 cm^{-1}).

The number-average molecular weight ($\overline{M_n}$) of oligoamides was estimated (Table 3.5), exploiting the method previously reported [40]. All the oligoamides had low molecular weight (~ 300 g/mol), providing sufficient solubility for subsequent reactions. In specific, with similar average molecular weight, the newly synthesized SubC2 showed the best solubility percentage at 1% (w/w) solute/solvent in all tested solvents among all (Table 3.7). Whereas, SucC2 is the least soluble one and ADC2 is intermediate.

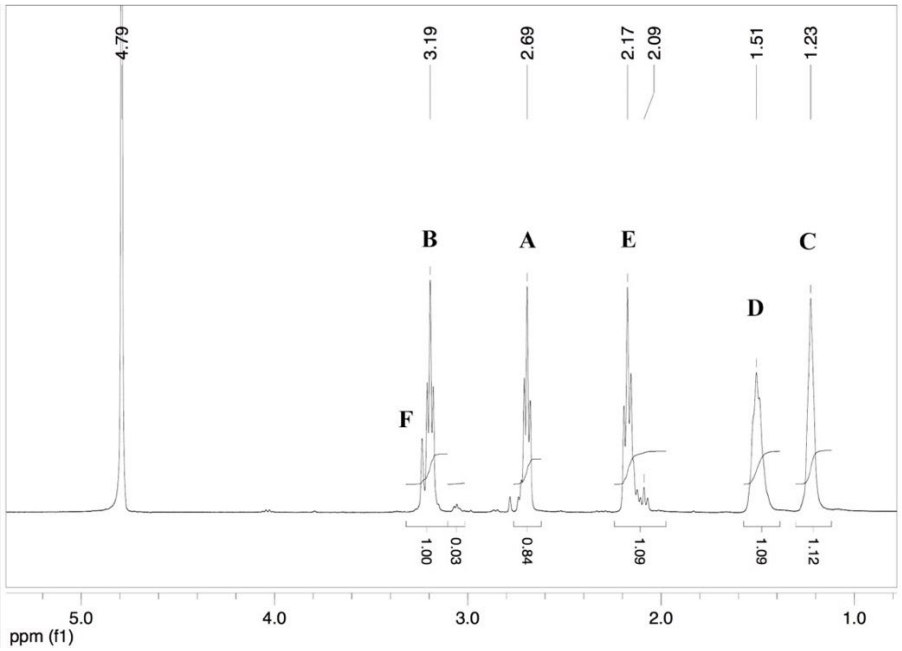

Figure 3.7 ^{1}H-NMR spectrum of SubC2 (1:3)

H_2N-CH_2-CH_2-NH-CO-CH_2-CH_2(CH_2)$_2$$CH_2$-$CH_2$-CO-[HN-$CH_2$-$CH_2$-NH-CO-$CH_2$-$CH_2$-($CH$)$_2$$CH_2$-$CH_2$-CO]$_p$-NH-$CH_2$-$CH_2$-$NH_2$

where p is the polymerization degree

Scheme 3.4 Chemical structure of SubC2.

When p=0:

H_2N-CH_2-CH_2-NH-CO-CH_2-CH_2(CH_2)$_2$$CH_2$-$CH_2$-CO-NH-$CH_2$-$CH_2$-$NH_2$

A B E D C D E B A

When p=1:

H_2N-CH_2-CH_2-NH-CO-CH_2-CH_2(CH_2)$_2$$CH_2$-$CH_2$-CO-NH-($CH_2$)$_2$-NH-CO

A B E D C C E F

-CH_2-CH_2(CH_2)$_2$$CH_2$-$CH_2$-CO-NH-$CH_2$-$CH_2$-$NH_2$

E C C D E B A

When p=2…

Table 3.4 Reaction conditions of SubC2 syntheses.

R#	Ethylene-diamine g (mmol)	Diethyl suberate g (mmol)	Solvent (ml)	T. (°C)	Time (h)	Yield (%)	M_n (^{1}H-NMR)
SubC2 (1:2)	0.750 (12.43)	1.430 (6.22)	3[b]	60-65	36	57	326
SubC2 (1:5)	2.610 (43.48)	2.000 (8.70)	2[b]	20-25	67	75	286
SubC2 (1:3)	1.565 (26.08)	2.000 (8.69)	2[b]	80-85	12	72	296

[a]: THF; [b]: 2-propanol

Table 3.5 Reaction conditions of non-fluorinated oligoamides syntheses.

Product	Ethylene-diamine (g) [mmol]	Ethyl succinate (g) [mmol]	Ethyl adipate (g) [mmol]	Ethyl suberate (g) [mmol]	Solvent (ml)	T (°C)	Time (h)	Yield (%)	$\overline{M_n}$ (^{1}H-NMR)
SucC2	1.381 [22.93]	2.000 [11.48]			2[a]	90-95	7	98	330
ADC2 [40]	1.280 [24.74]		1.000 [4.94]		0	95-100	22	61	296
SubC2	1.565 [26.08]			2.000 [8.69]	2[b]	80-85	12	72	296

[a] = THF; [b] = 2-propanol

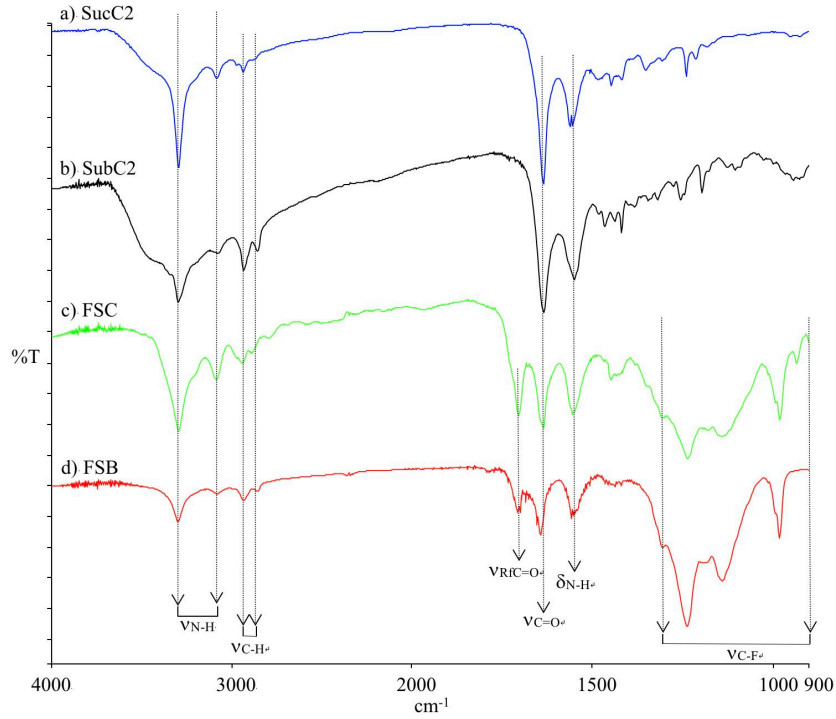

Figure 3.8 FT-IR spectra of a) SucC2, b) SubC2, c) FSC and d) FSB (on KBr windows).

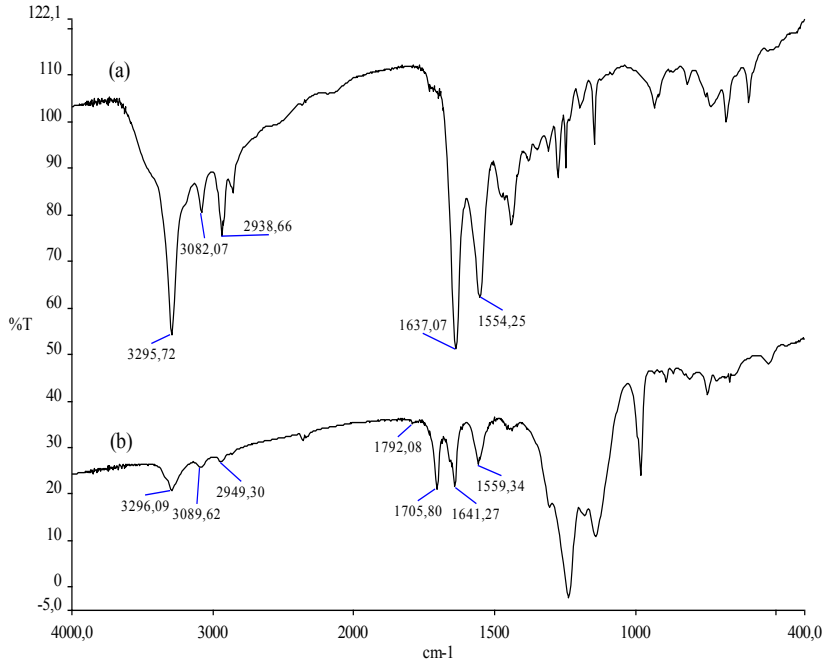

Figure 3.9 FT-IR spectrum of ADC2 (a) and FAD (b) on KBr windows [40].

Table 3.6 Assignments of the main FT-IR absorption peaks of oligoamides.

Product	Absorption (cm^{-1})					
	ν_{N-H}	ν_{C-H}	$\nu_{C=O}$	δ_{N-H}	ν_{C-N}	ν_{C-F}
SubC2	3300(s)	2935(s)	1634(s)	1550(s)	1448(s)	/
	3076(m)	2861(m)				
FSB	3300(s)	2937(s)	1706(s)	1559(s)	1450(s)	1400-900(s)
	3085(m)	2858(m)	1642(s)			
ADC2	3295(s)	2938(s)	1637(s)	1554(s)	1441(s)	/
	3082(m)	2857(m)				
FAD	3296(s)	2949(s)	1705(s)	1559(s)	1440(s)	1400-900(s)
	3089(m)		1641(s)			
SucC2	3295(s)	2940(s)	1631(s)	1561(s)	1448 (s)	/
	3084(m)	2938(m)				
FSC	3295(s)	2936(s)	1703(s)	1556 (s)	1448 (s)	1400-900(s)
	3084(m)	2890(m)	1636(s)			

s=strong; m= medium

Table 3.7 Solubility percentage of oligoamides determined at the solution concentration of 1% (w/w) solute/solvent.

$\overline{M_n}$ (g/mol)	SubC2 296		ADC2 296		SucC2 330	
Solvent	Cold	Hot	Cold	Hot	Cold	Hot
H_2O	100	100	100	100	100	nd

Ether	0	nd	0	nd	0	nd
THF	20	60	0	nd	0	15
Ethanol	80	nd	20	nd	0	nd
2-propanol	80	100	15	80	0	20
2-propanol/ H_2O (70:30)	100	nd	50	nd	0	70
2-propanol/ H_2O (90:10)	90	nd	20	n.d.	0	40

nd = not determined.

3.5.2 Synthesis and characterization of partially fluorinated oligoamides

In the second step, reaction conditions were similar for all syntheses (Scheme 3.5), and the molar ratio between oligoamides and ester of PFPE was the same i.e. 1:2 (Table 3.8). A higher yield (90%) was achieved in synthesizing FAD. During the reaction, attention was drawn on the peak features of amide I in FT-IR spectra, as a strong peak attributing to the amidic groups connected with PFPE segments appeared. Besides, the disappearance of C=O stretching of PFPE ester (1792 cm^{-1}) was also monitored. For all products, the absorption band positions of amide I of the amidic group that connects PFPE

chains are very similar, being around 1705 cm^{-1} (Table 3.6). The peak positions of amide II are relatively constant. Yet, the absorption band position of amide I of the amidic group of internal oligoamide backbones has changed. In specific, all the peak positions of amide I have shifted towards higher wavenumbers, i.e. shifted from 1634 to 1642 cm^{-1}, from 1631 to 1636 cm^{-1} and from 1637 to 1641 cm^{-1} for amide I in FSB, FSC and FAD, respectively. These results indicate the chemical properties of oligoamide backbones have been modified, due to the presence of PFPE segments, resulting in bond energy enhancing of amidic groups.

Although FSB, FAD and FSC are homologous compounds with similar molecular weight (~2000 g/mol), they show distinct solubility behaviors (Table 3.9) in some organic solvents. The new product FSB has very good solubility in alcoholic and hydro-alcoholic solvents at room temperature, while FSC is soluble only at hot condition and remains partially soluble when the solution was cooled down to room temperature. FAD has intermediate solubility. The solubility variations, which may induce different properties or performance in surface treatment, are closely related to the length of alkyl chains derived from dicarboxylic acids.

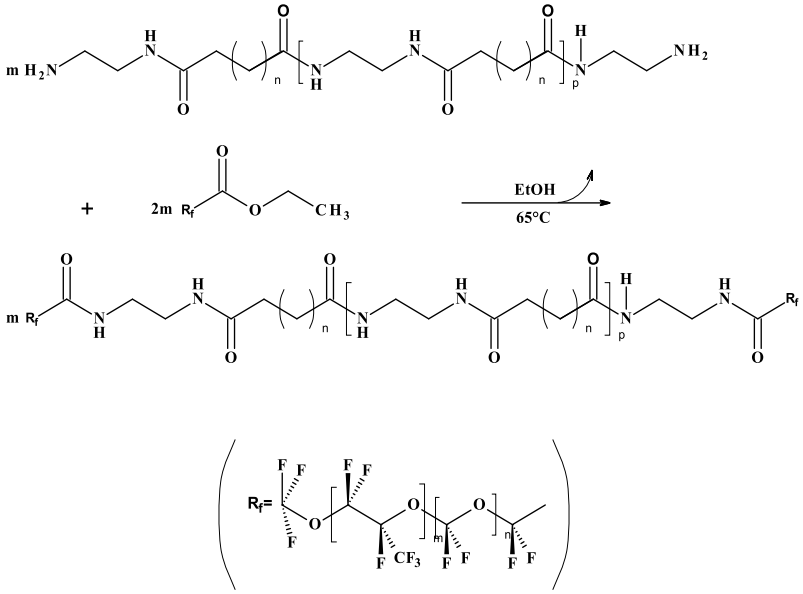

Where n= 1, 5 for FSC and FSB respectively; p is the degree of polymerization.

Scheme 3.5 Synthesis of partially fluorinated oligoamides.

Table 3.8 Reaction conditions of FSC, FAD and FSB syntheses.

Product	Reagents g (mmol)				Solvent (ml)	T. (°C)	Time (hours)	Yield (%)
	SucC2	ADC2	SubC2	Et-PFPE				
FSC	0.68 (2.00)			3.33 (3.70)	15[a]	Room T[b]; 75-80[c]	41.5	67
FAD		0.15 (0.51)		0.89 (1.02)	15[d]	65-70	40	90
FSB			0.17 (0.56)	0.99 (1.13)	15[d]	65-70	40	77

[a] = ethanol; [b] = at room T for 16.5 h; [c] = 75-80 °C for 25 h; [d] = 2-prapanol.

Table 3.9 Average molecular weight ($\overline{M_n}$) and solubility of FSC, FSB and FAD on several solvents. The solubility percentage of final products determined at solution concentration of 1% (w/w) solute/solvent.

	FSB		FAD		FSC	
$\overline{M_n}$ (g/mol) (by ^{1}H-NMR)	2056		2096		2090	
Solvent	Cold	Hot	Cold	Hot	Cold	Hot
Ether	0	nd	0	nd	0	0
THF	30	60	nd	nd	0	60
Ethanol	100	nd	90	100	30	100
2-propanol	100	100	80	100	50	100
2-propanol/ H2O (70:30)	70	100	50	90	50	100
2-propanol/	90	nd	nd	nd	50	nd

H2O (90:10)						
A113	80	nd	0	nd	0	nd
A113/ 2-propanol (90/10)	90	nd	nd	nd	0	nd
A113/ 2-propanol (10/90)	100	nd	nd	nd	0	

Cold = 20-25°C; Hot = 60-65°C; nd = not determined.

3.5.3 Wetting property and morphology of coatings

Although the surface tension of the oligoamides bearing short PFPE pendant groups (FSC, FAD and FSB) is not known, it is not expected to be very different from that of PFPEs with branched structure (16-18 mN/m) [123]. Considering that the surface tension of water (73 mN/m [124]) and olive oil (32 mN/m [125]) is much higher than that of PFPEs, and the surface has a natural roughness, necessary condition to make super oil/water repellent surfaces [60, 126, 127], the wetting properties of the coated stone substrate are assumed to be evidently modified. Moreover, as the amount of fluorinated oligoamides applied on the stone reflects the degree of coverage of the stone surface, a decreasing of the actual surface tension of the coated rock and an increase in water and oil CAs with an increase of product applied are expected [128].

Plots of water and oil CAs versus product amounts are shown in Figure 3.10. In general, peak values exist for all coatings, before reaching the apexes both water and oil CAs increase as the increasing of product quantity applied. Yet, once the peak value is reached, CA tends to stabilize. The static oil and water CA on neat substrate is 0° and 35°, respectively. When 11.1 g/m^2 of FSC was applied (coating "FSC-11"), a near superamphiphobic surface was generated, on which the static water and oil CA is 154.1±2.4° and 142.1±1.7°, respectively. By quadrupling the original water CA, FSC-11 has modified the wetting property of the neat substrate dramatically. On the surface treated

with the same amount of FSB (coating “FSB-11”) and FAD (coating “FAD-11”), though the same rising of water and oil CA is observed, superhydrophobic surfaces were not created. Another near superamphiphobic surface was realized by applying 18.3 g/m^2 of FSB (coating “FSB-18”), with the water and oil CA of 153.2±2.9° and 140.1±2.1°, respectively. However, when the amount of product applied was further increased, higher water and oil CAs were not observed for all coating materials. For FSC and FSB coatings made by 22.9 g/m^2 of product (coating “FSC-22” and “FSB-22”), both their water and oil CAs reduced slightly, being 152.6°, 136.5° for FSC-22 and 152.2°, 132.3° for FSB-22, respectively. Contrarily, the water and oil CAs on surface coated with 22.9 g/m^2 of FAD (coating “FAD-22”) were enhanced to around 130°. The varied hydrophobic effects observed on the same substrate coated with the same amount of homologous partially fluorinated oligomers may be explained by the different distribution of coating materials on porous surface and partial coverage of the stone surface, which could create micro differences on surface morphology (formation or not of additional roughness). Besides, when high amounts of product are applied, an accumulation of coating on surface and near the pore throats can induce a hierarchical structure, and the segregated hydrophobic perfluorinated chains may be superimposed by oligoamides molecules bearing extended polar chains (Figure 3.11). This disorganized conformation may justify the reducing of water and oil CAs.

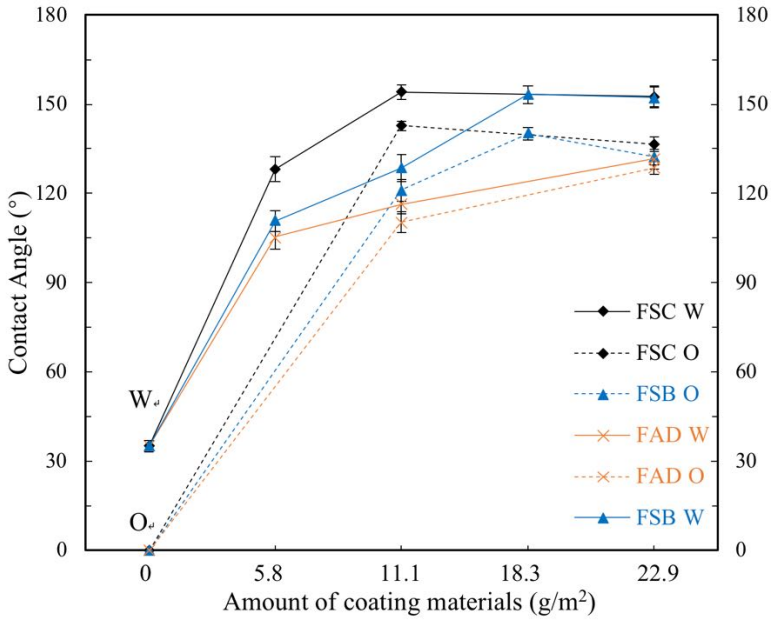

Figure 3.10 Water (W) and oil (O) Contact angles (CAs) of various coatings.

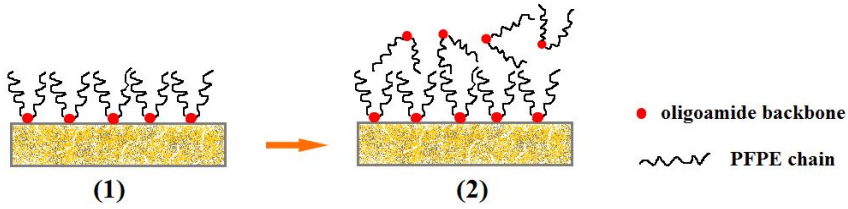

Figure 3.11 Schematic descriptions of surface orientation of coating materials on porous substrate when the product amount is ideal (1) and oversaturated (2).

In order to verify these assumptions, SEM micrographs of neat and coated stone slices were taken and elemental mapping analysis on both treated and stratigraphic surfaces was also conducted. As shown in Figure 3.12 a, the virgin rock (LS-NT) is very rough and porous. EDS analysis of the surface (rectangular area in Figure 3.12 a) and fluorine element mapping confirmed that no fluorine is present (Figure 3.13). Once 11.1 g/m^2 of FSC were applied,

substrate with different surface morphology was observed (Figure 3.12 b-1 and Figure 3.12 b-2). Some amorphous, wrenched lamellar-like materials, which partially cover surface and fill in pores are clearly seen on coating FSC-11 (Fig. 3b). The presence of FSC was proved by EDS analysis (Figure 3.13). Previous studies have demonstrated that properly controlled surface chemistry and surface microstructure are two indispensable factors for creating ultra-repellent surfaces [59, 127]. In our case, the originally porous surface has been covered by very thin (and probably non-continuous) film as well as by agglomerates and clusters of FSC in dimension varying from nanometer to as large as 120 μm (Figure 3.12 b). The agglomerates and clusters, indeed, create dual or multi-hierarchically rough microstructures. Additionally, when a thin film is present, the original surface tension is drastically reduced by the PFPE segments of FSC exploiting fluorine surface segregation phenomenon [129-131]. Hence, FSC-11 renders Lecce stone nearly superamphiphobic. The distribution behavior of FSC on substrate was examined by fluorine mapping analysis (Figure 3.12). A large amount of fluorine atoms distributes homogeneously on surface, while in depth the fluorine content is much less; fluorine atoms also distribute uniformly and some atoms have arrived to the bottom. Nonetheless, on coatings made with the same amount of FSB and FAD, different morphologies are seen. Unlike on FSC-11, on FSB-11 and FAD-11, though fluorine atoms with low weight percentages were detected (Figure 3.13), no evident coating materials are observed at the same magnification (Fig. 3c and Fig. 3d). In these cases, the oligoamides form a very thin film, which is not visible by SEM analysis. The

results of fluorine element mapping are in agreement with the morphologies, i.e. less concentrated fluorine atoms are present on the surface of FSB-11 and FAD-11 (Figure 3.12 c and Figure 3.12 d). However, it seems more FSB and FAD than FSC reside in depth, since fluorine atoms are more concentrated in stratigraphy (Figure 3.12 c and Figure 3.12 d). Specifically, FAD and mainly FSB tend to gather at the right side of image, which is the direction of treatment and gravity. These distribution and penetration variations can be due to their solubility differences (Table 3.9). In alcoholic solvents the solubility is FSB>FAD>>FSC. Indeed, FSC easily forms suspension during treatment when the concentration becomes slightly higher than 0.5% as a consequence of solvent evaporation. Therefore, once introduced as solution, FSB and FAD are more likely to penetrate inside substrate rather than remaining on surface. Hydrophobic surfaces are successfully produced, but the water and oil CAs on FSB-11 and FAD-11 are not as high as on FSC-11 because of lower fluorine content on the surface (partial coverage of the stone surface with a non-continuous coating layer). Moreover, since the original surface texture and microstructure of Lecce stone is microscopically intact, FSB-11 and FAD-11 render the rock surface hydrophobic by mainly fluorine segregation phenomenon. When the amount of FSB and FAD are increased, the fluorine content on surface is also enhanced. In the SEM micrograph of coating FSB-18, some clumps of product spread over the surface and also insert into pores and interstice (Figure 3.12 e), which is similar to FSC-11, and a similar superhydrophobic effect is achieved. In stratigraphy, FSB penetrated thoroughly, and it is more concentrated in the untreated face (right

side) (Figure 3.12 e). Surface morphologies of FSC-11 and FSB-18 well substantiate the widely acknowledged criteria for achieving superhyophobicity. On coated surface with 22.9 g/m^2 (FSC-22 and FSB-22), similar morphologies as FSC-11 (or FSB-18) were observed, but more product deposing on surface was observed (Figure 3.13). This morphology justifies a random distribution of hydrophobic and hydrophilic functional groups of oligoamides, like the illustration in Figure 3.11(2). With such disorganized surface orientation, higher water and oil CAs are not expected, and accordingly not found.

In addition to near superamphiphocity, these coatings also exhibit very high AF. On coatings FSC-11, FSB-18, FSC-22 and FSB-22, water droplet pins tightly and does not slide down even when the substrate was tilted vertically or turned upside down (Figure 3.14). Meanwhile, the high CA hysteresis (>100°) and low receding angles (≤50°) observed also implies surfaces with high stickiness (Figure 3.15). Previous researchers have found, on surfaces where high water adhesion is observed, the three phase contact lines at the liquid/solid interface pin steadily on the surfaces [56, 132]. In order to verify, the dynamic water CA behaviors and the wetting states of droplet on the coatings were investigated by evaporating experiments with a small water droplet. In Figure 3.16, the optical micrographs of a droplet on a FSB coated surface (FSB-22) during varied evaporation time are reported as an example. It is evident that CA decreased rapidly from 151° to around 100° after 12 minutes, and then to less than 10° after 18 minutes. Yet, the three phase

contact line (or the contact diameter) kept relatively constant, being 1320 μm (start of evaporation), 1409 μm (over 12 mins), 1500 μm (over 15 mins) and 1545 μm (over 18 mins) until complete evaporation, thus obeying the so-called "Constant Contact Diameter" mode [132]. Contrary to the superhydrophobic self-cleaning surfaces on which the three phase contact lines are easy to change due to low CA hysteresis, the contact lines pin and the contact area does not shrink on surfaces with high water adhesion [56]. Providing the dual-hierarchically rough surface, air pockets trapped inside are impregnable by water, but they prevent the wetting of coating materials and the substrate, displaying the Cassie impregnating wetting state [54, 60] (Figure 3.17). For all coatings, the AF increases as the amount of coating material is added. The maximum AF was found for coating FSC-22 and was about 165 μN. This value is higher than the ones reported in recent literature [53, 56]. The different AF are in accordance with their varied CA hysteresis, since FSC-22 and FSB-22 which show higher AF also have much higher CA hysteresis than FSC-11 and FSB-18. Yet, surfaces that exhibit similar AF also have comparable CA hysteresis, e.g. FSC-11 and FSC-18, FSC-22 and FSB-22. To further understand the origin and changes of AF, the physicochemical structure of both coating materials and substrate are ought to be considered. With pore size ranging from 0.01 to 2 μm and water porosity about 40 %, strong capillary force can be generated on Lecce stone surface. Once a relatively high amount of product is introduced, the coatings can not only be distributed in a mono-molecular layer, but also creates an additional microscopic roughness. Coating enters and covers the pore walls and micro-

fissures, which results in partially filling of small pores and in diameter reduction of relatively larger pores. This specific micro-porosity enables strong capillary force as the virgin substrate, which is comparable with the gravity force of water droplets. Similar results have also been found by other researches [133, 134], where the micro-orifices and the wall roughness on surface produces a miniscule capillary force which is sufficient to balance the weight of certain droplets. On the other hand, the fact that the highest AFs were found on coatings FSC-22 and FSB-22, where the CAs were slightly reduced compared with FSC-11 and FSB-18 respectively, shall not be neglected (Figure 3.18). An over saturation (i.e. 22.9 g/m^2 of products) of oligoamides actually disrupted the ordered, well segregated hydrophobic PFPE chains which expose outwards at the air-solid interface, thus impairing hydrophobic effect (Figure 3.11). Yet, this conformation change enhanced the AF due to the exposure of the polar oligoamides backbones. Each amidic group can form at most four hydrogen bonds with water molecules, among which carbonyl oxygen forms the strongest hydrogen bond with water [135]. Since the superhydrophobic surfaces are in the Cassie impregnating wetting state, water can wet the air pockets trapped inside micro-structures. With an overloading of coating (disorganized structures), the polar amidic groups are more reachable for water molecules, producing stronger hydrogen bonds and facilitating AF. Therefore, the decreasing of CA and the increasing of AF are not contradictory, rather, they are in great harmony. Likewise, the hydrogen bonds formed between hydrophilic nitro groups on the PTES (1*H*,1*H*,2*H*,2*H*-perfluorooctyltriethoxysilane)-NC (nitrocellulose) modified TiO_2 spongelike

film and water also provides good adhesion force [136].

In essence, considering the solubility of the fluorinated oligoamides (mainly FSC and FSB), it is possible to tune the near superamphiphobicity by simple deposition of controlled amounts of coating as dilute solution in solvents with a relatively low vapor pressure. Indeed, FSC (the less soluble product) is prone to spread out on the external surface giving superhydrophobicity and near superoleophobicity with small amount of product. On the contrary, FSB (the most soluble product) enters the pores of the rock and forms a dual-hierarchical rough surface with a larger amount of coating than FSC. In case that the AF parameter is more relevant than superamphiphobicity, an oversaturated surface improves its value.

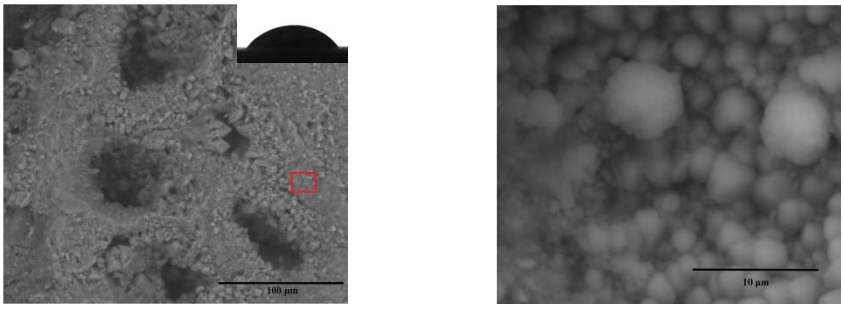

(a) LS-NT

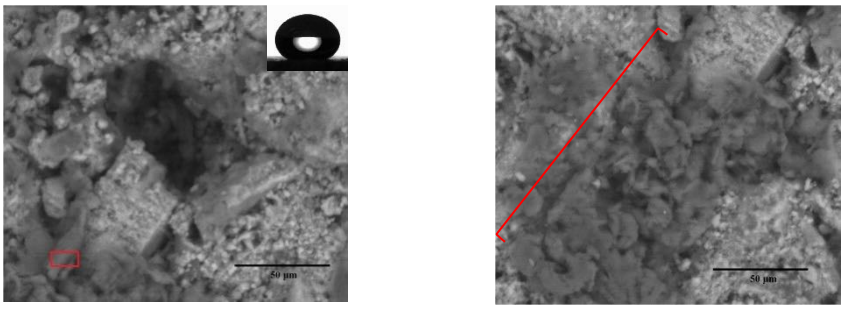

(b-1) (b-2)

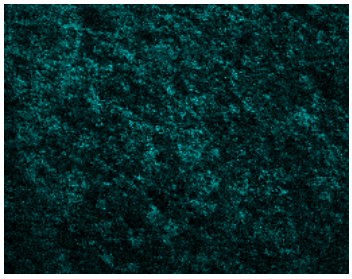

(b-3) Surface F mapping

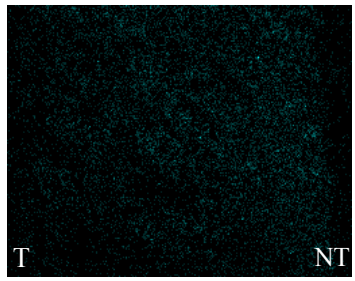

(b-4) Stratigraphic F mapping

(b) FSC-11

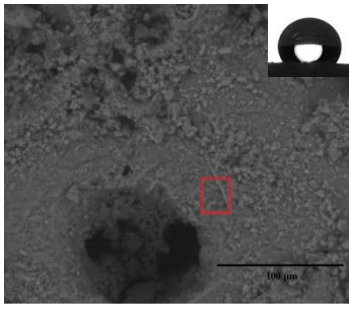

(c-1)

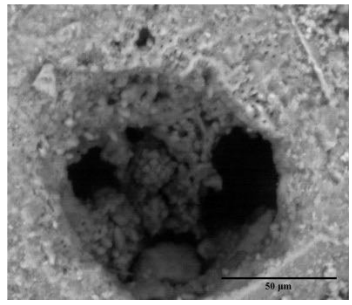

(c-2)

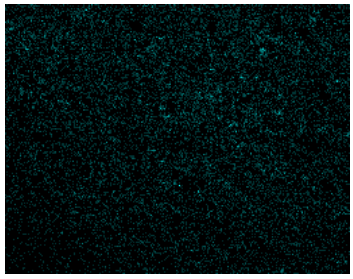

(c-3) Surface F mapping

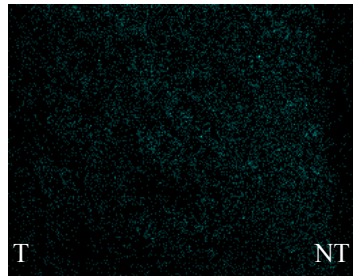

(c-4) Stratigraphic F mapping

(c) FSB-11

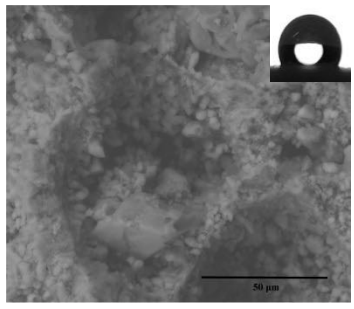

(d-1)

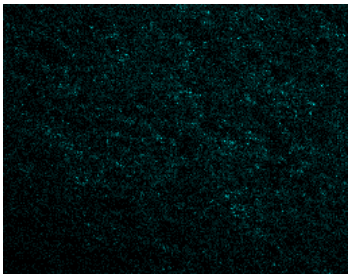

(d-2) Surface F mapping

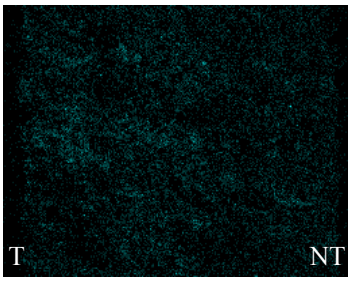

(d-3) Stratigraphic F mapping

(d) FAD-11

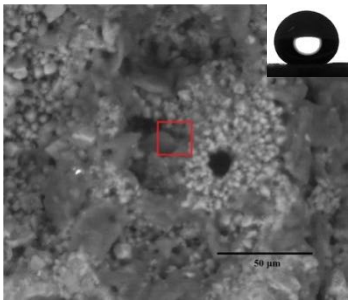

(e-1)

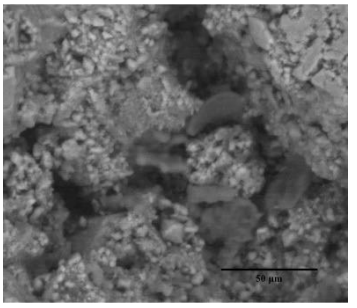

(e-2)

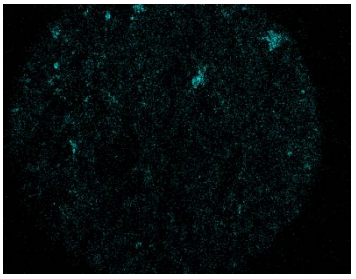

(e-3) Surface F mapping

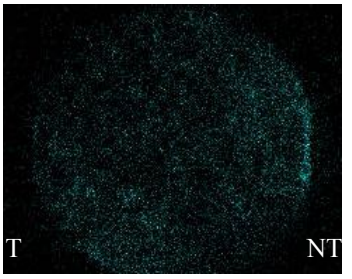

(e-4) Stratigraphic F mapping

(e) FSB-18

Figure 3.12 SEM micrographs and fluorine maps of not treated (LS-NT) (a), and treated stone substrate with FSC-11 (b), FSB-11 (c), FAD-11 (d) and FSB-18 (e). The insets are images of water CA on corresponding surface. T= treated face and NT = untreated face.

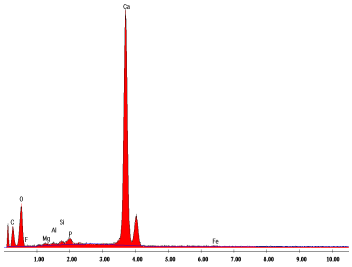

(a-1) Surface EDS spectrum of LS-NT

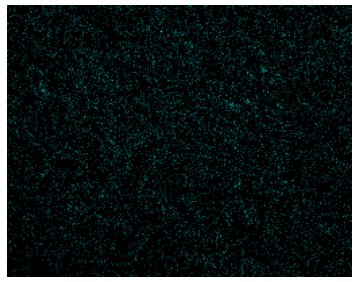

(a-2) Surface mapping of LS-NT

(a) LS-NT

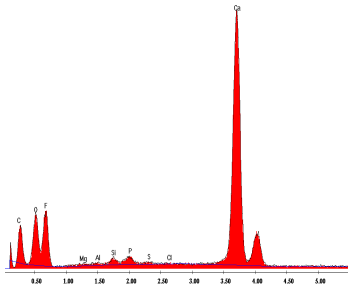

(b-1) Surface EDS spectrum

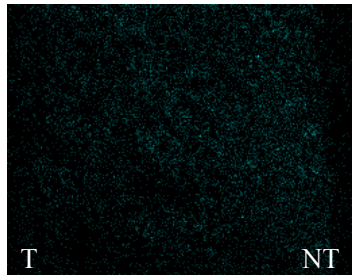

(b-2) Stratigraphic F mapping

(b) FSC-11

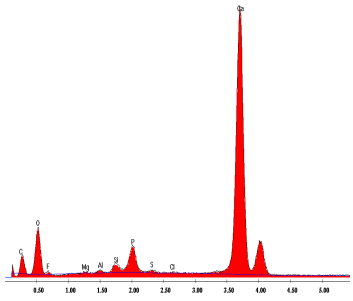

(c) Surface EDS spectrum

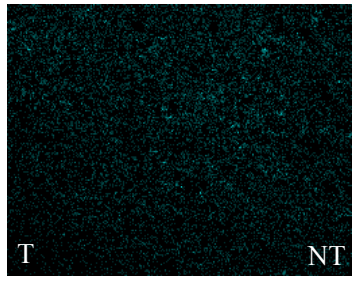

(c-2) Stratigraphic F mapping

(c) FSB-11

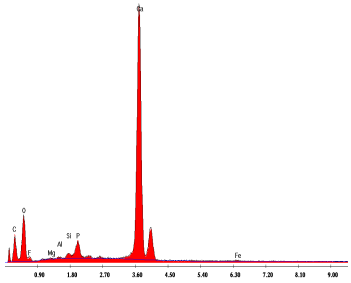

(d) Surface EDS

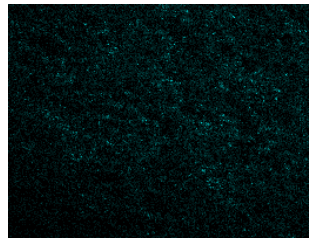

(d-2) Surface F mapping

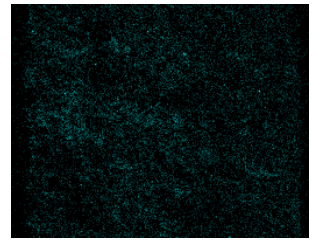

(d-3) Stratigraphic F mapping

(d) FAD-11

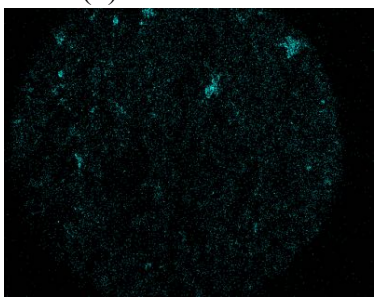

(e) FSB-18 surface F mapping

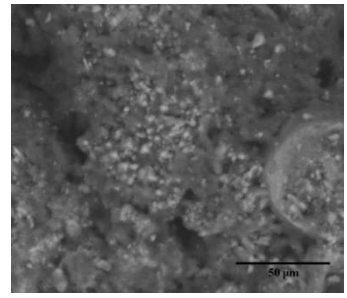

(f) SEM micrograph of coating FSB-22

Figure 3.13 SEM micrographs and fluorine maps of several coatings. The denotation “T” means the treated face and “NT” means the untreated face.

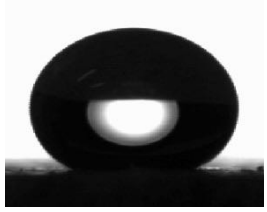

(a)

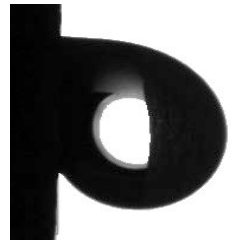

(b)

(c)

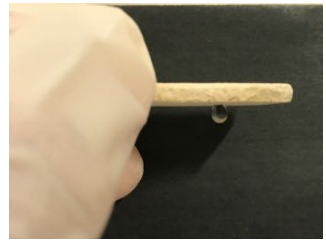

(d)

Figure 3.14 Static contact angle of water droplets on FSC-11 with tilt angle of 0° (a), 90° (b) and 180° (c). 17 µl of water droplet pinned on FSC-22 (d).

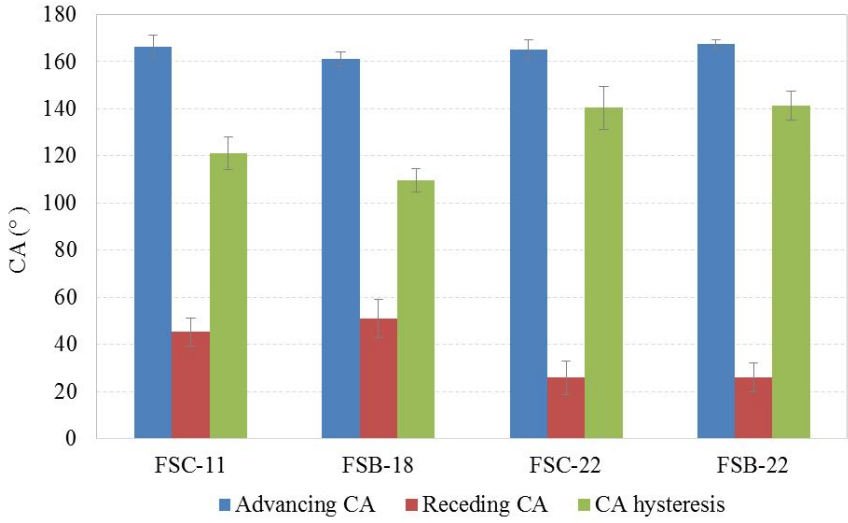

Figure 3.15 Advancing CA, receding CA and CA hysteresis of FSC and FSB coatings made with different amounts.

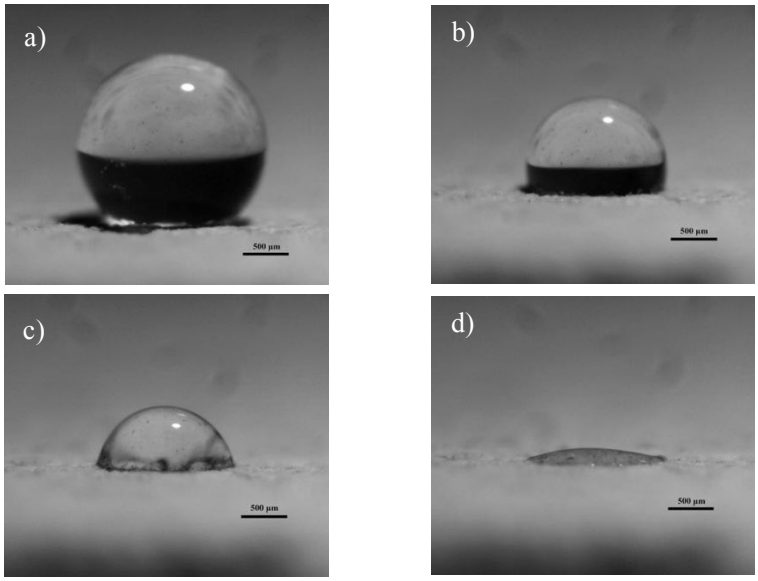

Figure 3.16 Optical micrographs of dynamic water droplet

evaporation on FSB-22 coated surface after 0 min (a), 12 mins (b), 15 mins (c) and 18 mins (d).

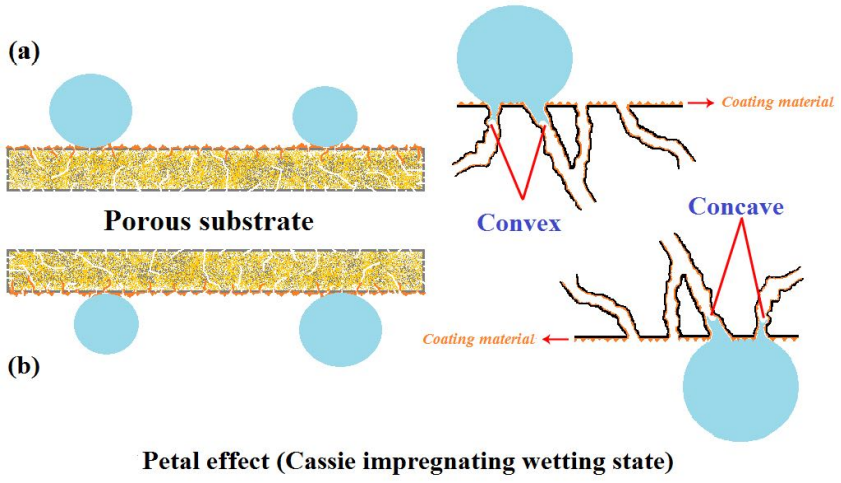

Figure 3.17 Schematic illustrations of water droplets in contact with the as-prepared adhesive superhydrophobic surfaces at tilting angle of 0° (a) and 180° (b).

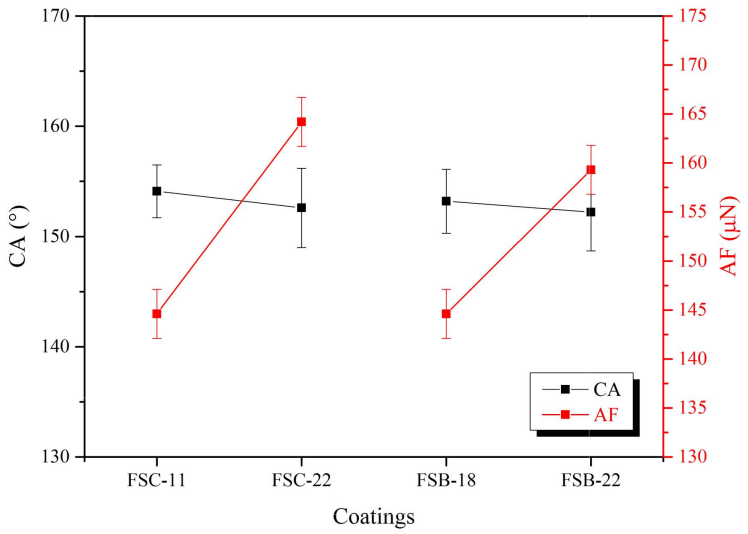

Figure 3.18 Contact angle (CA) and adhesion force (AF) of FSC and FSB coatings made with different amounts.

The stability and durability of these sticky surfaces was also evaluated by means of water immersion test; the CA and AF variations are shown in Figure 3.19 and Figure 3.20, respectively. Though the CA of all these four surfaces decreased slightly after immersion, the average CA values are always above 150°, maintaining superhydrophobicity. Further, the AF of all surfaces is relatively durable, and no evident performance decay was seen. Results indicate the hydrophobic and adhesive properties of these surfaces are stable and durable.

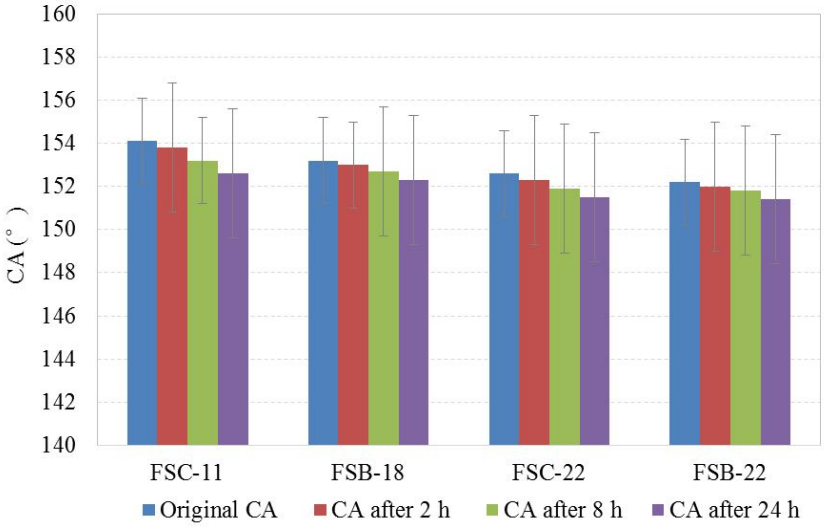

Figure 3.19 CA variations of sticky ultra-repellent coatings after 2 h, 8 h and 24 h water immersion test.

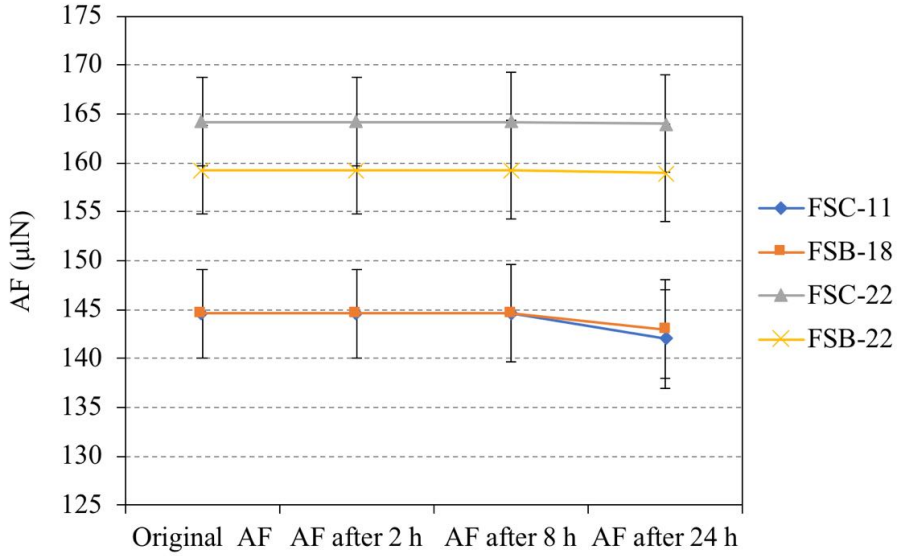

Figure 3.20 AF variations of sticky ultra-repellent coatings after 2 h, 8 h and 24 h water immersion test.

3.5.4 Water inhibition efficiency, vapor diffusivity and other performance

3.5.4.1 On Lecce stone

To evaluate the physical property changes of substrates after coating by standard tests, products were also applied on slabs. Founded on CA results, the amount of materials was kept being around 15 g/m^2 to provide the best hydrophobicity. With such quantities applied, FSC and FSB have manifested good hydrophobicity (WIE ≥84%) in two-hour test (Table 3.10). In particular, FSC has higher WIE values than FSB although its amount applied was slightly lower (13 g/m^2 versus 16 g/m^2). Yet, FAD is not very effective as

water repellent for Lecce stone, and its WIE values decreased rapidly to 50% within two hours. These WIE values are in good accordance with the water CA (Fig 3. 10). As demonstrate by SEM-EDS and fluorine mapping analyses, the best WIE values obtained with FSC coatings owing to its propensity to concentrate at the external surface of slab (i.e. lower penetration depth than FSB and FAD), creating an efficient barrier to liquid water. On the contrary, the better hydrophobic effect of FSB coated surface than the FAD one is not yet well understood, but it might be related to the potential formation of intermolecular hydrogen bonding in the oligoamides solutions with certain length of alkyl chain in the starting dicarboxylic acid; this property can influence the fluorine segregation during the coating process.

Table 3.10 Water inhibition efficiency (WIE), residual vapor diffusivity (RD) and chromatic changes (ΔE*) of Lecce stone samples coated with fluorinated oligoamides.

	Product quantity		WIE (%) at			RD	ΔE*
	Theoretical g (g/m^2)	Actual g (g/m^2)	30 min	60 min	120 min	(%)	
FSB		0.041±0.003 (16)	92	88	84	96±3.4	3.0
FAD	0.037 (15)	0.037±0.006 (15)	80	69	50	99±2.1	1.5
FSC		0.033±0.005 (13)	95	93	90	97±3.8	2.8

To investigate the vapor diffusivity through neat and coated Lecce stone surface, the standard “Cup” method was exploited. Following this method,

the molar flux of water vapor pass through the sample is expressed as the time rate of liquid loss in the system:

$$< J >= D\frac{(c_1 - c_0)}{L} = \frac{moles_{H_2O}}{Area \cdot time} = -\frac{1}{A \cdot M_{H_2O}}\frac{dW_{H_2O}}{dt} \qquad \text{(Eq. 3.4)}$$

where W_{H2O} is the mass of water loss, and M_{H2O} is the molecular weight of water. An example of calculation is given below, along with plots of W_{H2O} versus time for neat and all coated stones (Figure 3.21-3.24). Using Eq. 3.4, the average D_{eff} values found for FSC, FSB and FAD coated Lecce stone are reported in Table 3.11.

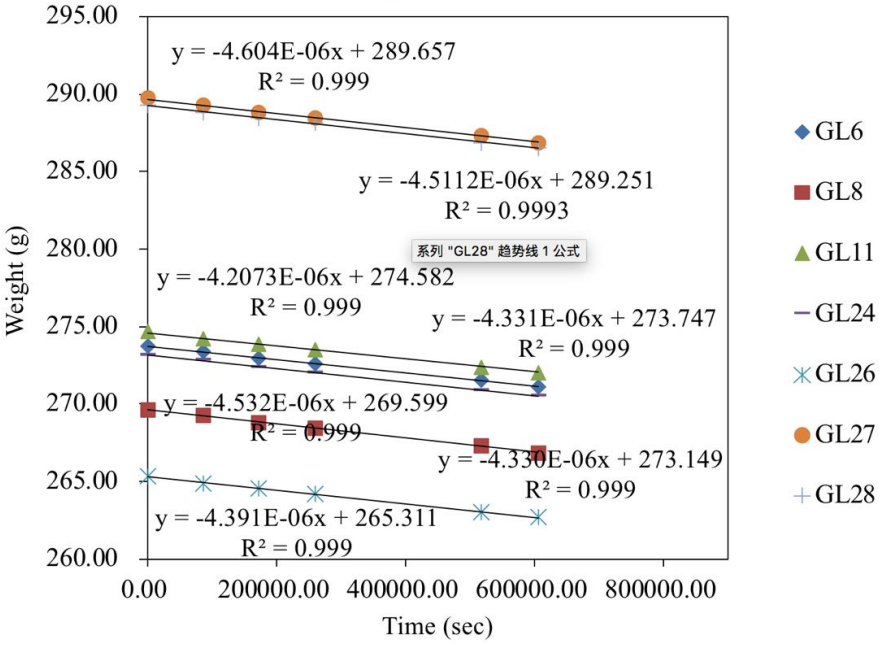

Figure 3.21 Plot of weight loss of neat Lecce stone.

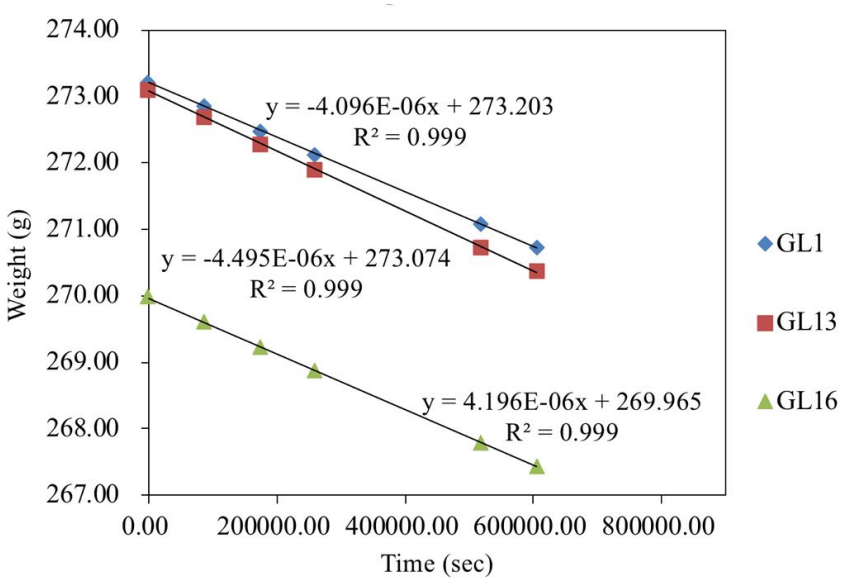

Figure 3.22 Plot of weight loss of FSC coated Lecce stone.

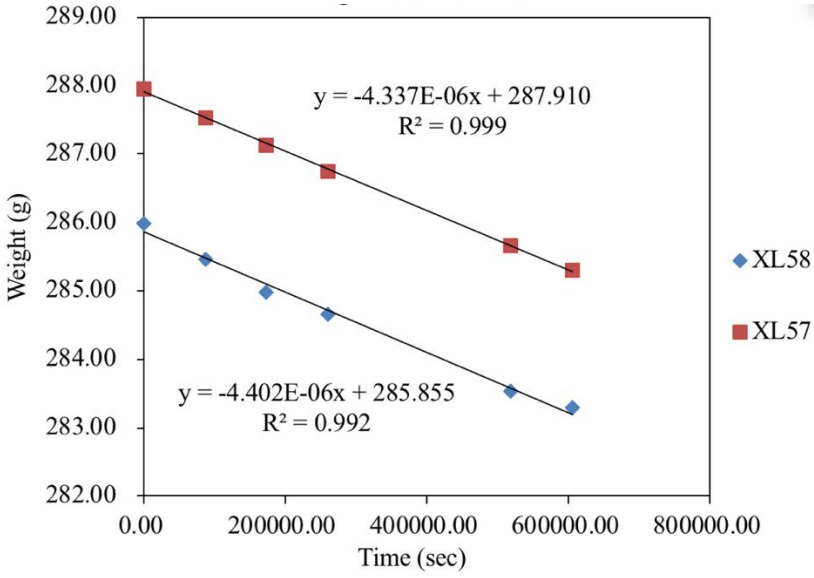

Figure 3.23 Plot of weight loss of FAD coated Lecce stone.

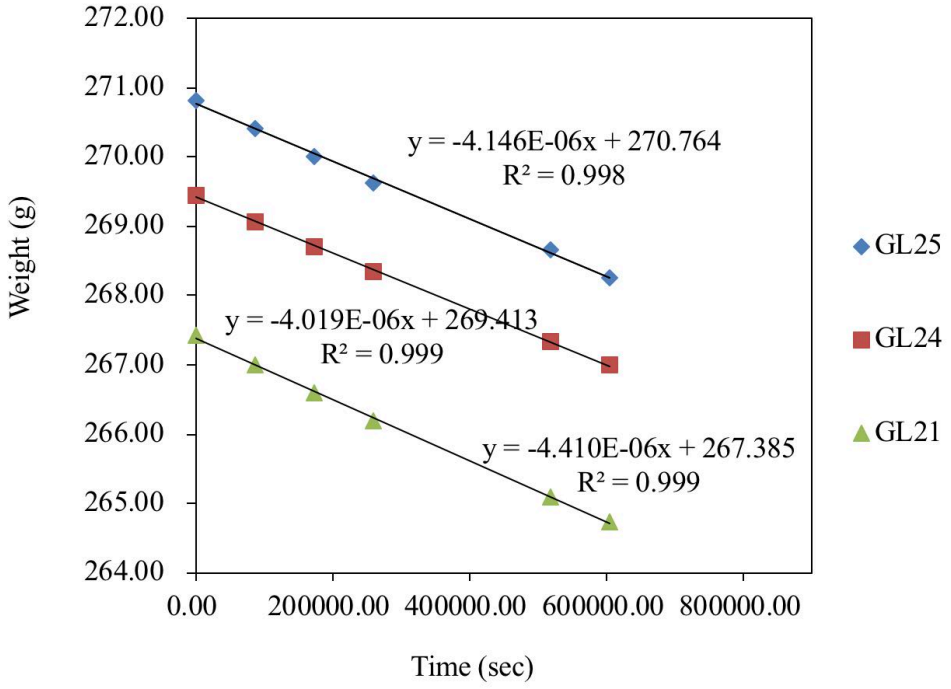

Figure 3.24 Plot of weight loss of FSB coated Lecce stone.

An example of calculating D_{eff} of neat Lecce stone is as following. Correlating Eq. 3.4 and Eq. 3.5, D_{eff} can be obtained as Eq. 3.6.

$$-\frac{1}{A \cdot M_{H_2O}} \frac{dW_{H_2O}}{dt} = D_{eff}\left[\frac{c_1 - c_0}{L}\right] = \frac{D_{eff}}{RT}\left[\frac{p_1 - p_0}{L}\right] \qquad \text{(Eq. 3.5)}$$

where W_{H2O} is the slope of the linear curves in Figure 3.21 to Figure 3.24.

$$D_{eff} = \text{slope}(RTL)/M_{H2O}*A*(p_1-p_0) \qquad \text{(Eq. 3.6)}$$

Knowing:
A = 15.9 cm^2
L= 1.8 cm;
R = PV/nT = 0,08205 l*atm/(moli*K) = 0,08205*1000*29,9*25,4/(moli*°K) = 6,23137*10^4 cm3*mmHg/(moli*°K);
M_{H2O}= 18.016;
T = 30 ºC = 272.039K;
p_0 = 1.68475mmHg;

p_1= 31.84338 mmHg;

The D_{eff} of neat Lecce stone =
$4.512*10^{-6}(6.23137*10^4 * 272.039* 1.8) / 18.016* 15.9*(31.84338-1.68475)$ (cm^2/sec)= $1.59*10^{-2}$ (cm^2/sec)

An estimation of D_{eff} can also be computed based on Eq. 3.3, when ε and τ are properly calculated as follows. Since D_{eff} of neat Lecce stone is experimentally known and the diffusion coefficient of vapor in air is also known (D=$2.02 *10^{-1}$ cm^2/sec) from the literature [137], assuming 35% as the average porosity of Lecce stone, the tortuosity of this rock is calculated using Eq. 3.3 (τ= 4.50). The calculated τ is much larger than the value reported in a recent paper (τ=2.32) where relaxation times of NMR were used to calculate the τ providing the time dependence of the self-diffusion coefficient (D) approaches an asymptotic value [138]. There are some reasons accounting for this difference. Based on literature, it is of great difficulty to calculate (or measure) the τ of porous media, whereas the methods to measure D are relatively easier. Tortuosity is usually deduced from the diffusion coefficient [139], but sometimes the tortuosity has been interpreted in conflicting ways [140]. Besides, although the type of our rock is the same as the one used in the explained article [138], the physical properties, e.g. porosity and tortuosity of the stone samples quarried from varied quarries can be different.

Furthermore, the porosity change after coating could be estimated as well. Taking 0.2 cm as the medium penetration depth and 1 g/ml as the lowest density of products, the maximum volume reduction caused by coating

materials are 0.033, 0.041 and 0.037 ml for FSC, FSB and FAD, respectively.

Table 3.11 Residual vapor diffusivity (RD), effective diffusivity (D_{eff}) and estimated porosity (ε) reduction of stone samples after coating.

Coating	RD (%)	Experimental D_{eff} @RH%=5% (cm^2/sec)	τ	Estimated ε reduction (%)	Estimated D_{eff}^* (cm^2/sec)
Neat	/	$1.57 \cdot 10^2$ ±0.05	4.50 (2.32) [138]	/	/
FSB	96	$1.48 \cdot 10^{-2}$ ± 0.06		2.34	$1.47 \cdot 10^{-2}$
FAD	99	$1.54 \cdot 10^{-2}$ ± 0.01		2.11	$1.48 \cdot 10^{-2}$
FSC	97	$1.51 \cdot 10^{-2}$ ± 0.06		1.89	$1.49 \cdot 10^{-2}$

* = D_{eff} was calculated based on porosity reduction; Neat = not treated stone.

Presuming 35% as the mean original porosity of substrate, less than 3% of pore space was filled after coating (Table 3.11). Based on the estimated porosity change and calculated tortuosity, the corresponding estimated D_{eff} is reported in Table 3.11. Generally, for each coating, the estimated D_{eff} value is slightly reduced, and it is in good agreement with the value measured by the "Cup" method. Among the experimental $D_{eff,}$ a greater tendency to decrease is observed for the FSB treatment; it cannot be explained only with the porosity reduction, since it is the most penetrating product. As presented in a previous paper [114], the vapor diffusion process is compromised by the presence of non-wettable pore walls which restrains the vapor condensation that assists the diffusion process. Therefore, the slightly lower D_{eff} and

residual diffusivity are in accordance with the explanation. In any case, however, pore blockage does not occur in all the coating systems.

Last but not least, all the coating materials did not induce any perceivable chromatic changes ($\Delta E \leqq 3$) on surface (Table 3.10), permitting large area application in practice where color features matter.

3.5.4.2 On marble

Figure 3.25 is the plot of water CA of FSB coating on two substrates. Similar to coatings on Lecce stone, CA on marble also rises with the increase of product amount applied until it reaches the peak value. The highest CA (128±3.1°) was seen on treatment with 4.3 g/m^2 of FSB. Then, with 10 g/m^2 of FSB applied, over saturation was reached, resulting in rapid CA decrease (115°). Unfortunately, superhydrophobicity was not achieved on marble.

The surface morphology of neat and treated marble surfaces was observed by SEM analysis. In fact, unlike coated Lecce stone surfaces, there is not an evident modification on marble surface after coating, indicating no dual-hierarchy rough structure was created. As it is widely accepted, surface roughness at multiple scales (sub-micrometer to nanometer) is dispensable in achieving superhydrophobicity.

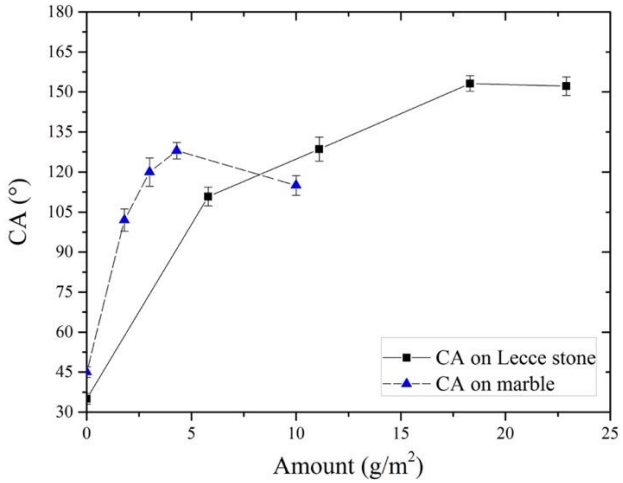

Figure 3.25 Plot of water CA on FSB coating on Lecce stone and marble surfaces.

As shown in Table 3.12, compared with FSB and FAD, FSC is not effective in inhibiting water adsorption and penetration on marble in all testing times even though its amount applied is the highest among all (5.2 g/m^2). The highest WIE observed on FSC coated surface is only 30% after 1 h test, which is in agreement with previously found results [141]. Yet, FSB and FAD have comparable, high WIE in all testing times. In specific, in the first three testing times, FSB and FAD show the same WIE, being, 94%, 92% and 90% for absorption test after 1 h, 2 h and 3 h respectively. After 4 h, though the WIE of FSB (88%) is slightly lower than that of FAD (90%), FSB prevents water penetration effectively.

On the other hand, the physical property changes i.e. residual diffusivity and chromatic change of marble after surface coating are shown in Table 3.13. These coatings do not reduce the original vapor diffusivity dramatically,

since all RD values are ≥ 90%. With the lowest amount applied (3.2 g/m^2), FSB coated marble has the least vapor diffusivity reduction (~8%). Last but not least, these coatings also preserved the original aesthetic features of marble, with all ΔE* values lower than the detection limit of naked human eyes (ΔE*=3).

Table 3.12 WIE (%) of coatings on marble

Product	Quantity		WIE (%) at			
	Theoretic-al (g/m^2)	Actual (g/m^2)	60 mins	120 mins	180 mins	240 mins
FSB	5	3.2	94	92	90	88
FAD		4.0	94	92	90	90
FSC		5.2	30	15	7	0

Table 3.13 RD (%) and ΔE* variations of coatings

Product	Quantity		RD (%)	ΔE*
	Theoretical (g/m^2)	Actual (g/m^2)		
FSB	5	3.2	92	2.1
FAD		4.0	90	1.5
FSC		5.2	91	1.6

3.6 Conclusion

In this chapter, a previously reported oligoadipamide incorporating pendant

PFPE blocks, FAD was briefly reviewed. The special characteristics of FAD i.e. very effective for low porous stone protection while not effective for protecting high porous stone, lead to subsequent experiments and comprehensive studies.

New partially fluorinated oligosuberamide with varied molecular weights (or varied molecular weight distributions), which is homologous to FAD, has been successfully synthesized via the same route as FAD synthesis. Having similar number average molecular weight to FAD (~2000 g/mol), FSB shows even better solubility than FAD, and it is very soluble in alcoholic and hydro-alcoholic solvents. Surface treatment with FSB solution can be simply done by brushing or spray. Besides, aiming at investigating and studying these homologous compounds (i.e. oligoamides bearing PFPE segments) systematically, the partially fluorinated oligosuccinamide (FSC) has also been synthesized following the method descripted in literature.

Applied firstly on Lecce stone surfaces, the wetting properties of these three coatings i.e. FAD, FSB and FSC were characterized. By accurately adjusting the amounts of coating materials applied, several near superamphiphobic surfaces were created by simply deposing coating solution on Lecce stone surfaces. These surfaces exhibit very high water and oil CA (water CA>150°, oil CA>140°). The highest water and oil CA are observed on surface coated with 11.1 g/m^2 of FSC and/or 18.3 g/m^2 of FSB, being 154.1±2.4°, 142.1±1.7° and 153.2±2.9°, 140.1±2.1° respectively. Meanwhile, SEM-EDX

morphological analysis revealed the dual-hierarchy rough structures on Lecce stone surfaces after coating. In addition to superamphiphobicity, these surfaces show very high adhesion force to water droplets. The maximum AF assessed, about 165 μN, was found on the stone surface coated with 22.9 g/m^2 of fluorinated oligosuberamide (FSB-22) and oligosuccinamide (FSC-22). Results showed the strong AF arises from the combination of capillary force due to the natural and newly created micro-pores and orifices at multiple dimension scales in the substrate, and the hydrogen bonds formed between amidic groups and water molecules. The superhydrophobic and adhesive properties of these surfaces are proved to be stable according to short and long time water immersion test. Such characteristics offer potential application in some important fields, e.g. liquid transport without loss or contamination in microsample analysis, sticky tape, dew collection, etc. Complementary to those sticky ultra-repellent surfaces generally obtained on smooth, flat substrates, these coating materials and methods may shed light on functional applications on porous and rough substrates.

Moreover, when applied as water repellent on Lecce stone slabs, FSB and FSC manifested very high WIE in both short (0.5 h) and long testing times (2 h). FSC showed WIE value as high as 90 % after 2 h of absorption test, while it was 84% for FSB. In accordance to already reported results, FAD, which had a WIE value of 50 % after 2 h, is not efficient as FSB and FSC. It is notified as well, these three coatings also preserved the physical properties of substrate, since the vapor diffusivity reduction is lower than 3% and surface

color change is unperceivable. FSB and FSC are good water repellents for highly porous building stones.

On the other hand, once applied on marble, good protective performance was seen on FAD and FSB coatings. With very low WIE values found, FSC was unable to block water adsorption and penetration on marble. FSB coated (amount: 4.3 g/m^2) marble surface showed high water CA (128±3.1°), although superhydrophobicity was not achieved. FSB and FAD protected marble effectively for long time, and their WIE values after 4 h absorption are 88% and 90% respectively. Additionally, these three coatings did not compromise the original vapor diffusivity and color features of marble, indicating good candidates for marble protection, particularly FSB and FAD.

The good performance demonstrated by these coatings in terms of efficiency and durability of water inhibition, vapor diffusivity and color features make them eligible products as protective agents for outdoor stone artifacts (e.g. historic buildings, statues). In particular, FSB was proved to be the best coating material because it provides comparably high hydrophobic effect as FSC on Lecce stone and as FAD on marble. These partially fluorinated oligoamides show good solubility in solvents with medium polarity and medium/low vapor pressure, such as alcohols and hydro-alcoholic solvents, allows the optimal coating conditions, and specifically, FSB has the best solubility among all.

Chapter IV

Fluorinated siloxane

4.1 Introduction

Aiming to mimicking the unique antiwetting phenomena in nature, e.g. water rolling off on lotus leaves [42], dew, rain nonwettable and dust-free cicada wings [43], dirt-free gecko feet [44], water pinning on rose petals [45], etc. artificial super anti-wetting surfaces have been extensively studied over the last two decades. In particular, on superhydrophobic surfaces with CA >150° and CAH < 10° have been drawn great attention, owing to their great value in both theoretical research and functional application in self-cleaning, anti-biofouling, anti-icing, oil/water separation fields [52].Many methods, i.e. physical and chemical methods have been proposed by researchers, which include layer-by-layer assembly, electrochemical etching, templating method, lithography, sol-gel process etc. [48-50]. Yet, in order to scale up both fabrication and application, problems such as expensive raw materials and equipment, tedious processes and harsh conditions are ought to be well tackled. It shall be noticed, aiming to create surfaces with multi-level roughness at nano- or submicro-meter scales, surface processing is indispensable in some methods, e.g. electrochemical method, lithography, plasma method, thus making them inapplicable under certain circumstances, e.g. in situ surface treatment on modern and historic architectures, where the

integrity of substrates should never be impaired. Moreover, nanomaterials are widely employed in the majority of these approaches to create dual-hierarchically rough surfaces and/or low surface tension coatings. Although the use of nanoparticles is significant, a comprehensive understanding of their stability in long term use, their potential toxicity towards mankind and environment is urgently demanded [142]. To our best knowledge, in literature, there is few approach depicting ultra repellent surfaces preparation without adopting surface processing or nanomaterials.

As has been explained above, bioinspired ultra water/oil repellent surfaces with self-cleaning property ("lotus effect") are the most ideal materials for protecting building stones. Equipped with such surfaces, the physical and chemical integrity together with the aesthetic properties of building stones can be well maintained. In literature, some superhydrophobic surfaces with "lotus effect" behavior have been proposed for building stones [106, 108, 109], however, relatively high amounts of nanomaterials were incorporated, and high amounts of coating materials are required for satisfactory effects which lead to visible aesthetic change and/or vapor diffusivity loss of stone materials. Besides, no material was tested and suggested for highly porous stones, e.g. Lecce stone.

Herein, in this chapter, a facile approach to fabricate superamphiphobic, self-cleaning coatings on two substrates (i.e. Lecce stone and Pietra Serena) which have varied porosity and roughness will be presented. On as-prepared

surfaces, both water and oil CA are higher than 150°, whereas the water CAH are lower than 10°. The coating material (Si-PFPE) was synthesized via one-step amidation. In this one-step strategy, neither surface processing nor nanomaterials was integrated. Nanoscaled roughness and low surface tension coating are achieved simultaneously by simple brushing/deposing coating dispersion with very low concentration (1%) and low amounts (≤15 g/m^2). Additionally, no expensive materials, equipment or harsh conditions were required during surface preparation. This coating is an excellent water repellent for building stones with both low and high porosity, since it manifests very high WIE without compromising the original vapor diffusivity and aesthetic properties of substrates. It is also noted that superhydrophpobic feature of our coating is stable towards chemical agents and long time water immersion, thereby permitting outdoor application in rainy areas and areas where acid rain presents.

4.2 Experimental

4.2.1 Materials

(3-Aminopropyl)trimethoxysilane (APTMS, 97%) and 2-propanol (>99.5%) were purchased from Sigma-Aldrich (Germany). Acyl fluoride-end functionalized perfluoroether (AF-PFPE, 97%) was obtained from Wuhan HongRuiKang Reagent Co. Ltd (China). The chemical formula of AF-PFPE is shown as following:

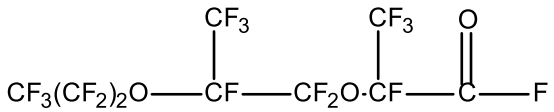

Scheme 4.1 Chemical structure of AF-PFPE.

Acetic acid (100%) and potassium hydroxide pellets were products of Merck (Germany). All chemicals were used as received without further purification. Distilled water was prepared in lab prior to use. Marble powder was obtained by crushing a piece of Carrara marble in lab.

Two types of natural building stones, i.e. Pietra Serena and Lecce stone, were employed. Pietra Serena, a light grey sandstone that mainly constituted by sandy fraction, clay matrix and a small amount of calcite. Owing to its workability and relative compactness, Pietra Serena was frequently used during the Renaissance for ornamental purposes (e.g. as capitals, columns) and also as road paving, household furnishing nowadays in Florentine areas. Varied from quarry to quarry, Pietra Serena has a water accessible porosity around 3-6%, with pores size ranging from 0.004-0.3 μm [143]. Whereas Lecce stone, a fine bio-calcarenite, has much higher porosity and larger pores (water accessible porosity about 35-47%, pore size ranging from 0.01 to 2 μm) [115]. Lecce stone has a beige and rough surface, on which microfossils are usually seen. Pietra Serena and Lecce stone samples were previously cut as slabs in dimension 5·5·1 and 5·5·2 cm^3 respectively. Samples were tested and selected based on three sequences of standard water capillary absorption tests [118], and only samples that demonstrated constant water absorptivity were selected for subsequent surface treatment and tests.

4.2.2 Synthesis and characterization of fluorinated silane (Si-PFPE)

In a two-necked 50 ml flask equipped with a reflux condenser connected to a $CaCO_3$ (marble powder) trap for HF blockage, (3-Aminopropyl)trimethoxysilane (0.88 ml, 5.05 mmol) was introduced in nitrogen atmosphere and at room temperature. Under vigorous magnetic stirring, AF-PFPE (1.47 ml, 5.02 mmol) was added dropwise. At room temperature, reaction lasted for 8 h until completion, and then white, viscose semi-liquid (2.63 g, yield 80%) product was collected.

The product was characterized by FT-IR and ^{1}H-NMR spectroscopy. FT-IR spectra were recorded employing a Perkin Elmer (Spectrum 1000) spectrometer in the mid-IR range (4000 cm^{-1} to 400 cm^{-1}) in transmission mode with 16 scans and 2 cm^{-1} spectral resolution. KBr windows were used as sample holder. ^{1}H-NMR spectra were obtained with a Varian Mercury VXR400 operated at 399.921 MHz, using CD_3OD as solvent. ^{1}H-NMR chemical shifts are reported in ppm relative to tetramethylsilane (TMS) at 0 ppm.

4.2.3 Application on stone slabs

To coat stone samples, 1% (w/w) 2-propanol dispersion of Si-PFPE was prepared at room temperature and under vigorous magnetic stirring. Though

simply brushing the surface with dispersion is applicable, a graduated pipette (0.5 ml) was used for deposing the coating material on one larger face of samples with the method “wet on wet” aiming to precisely control the amount of coating material. The ideal amounts of coating material were determined on the basis of the results reported in our previous paper [40, 41], being 15 g/m^2 and 10 g/m^2 for Lecce stone and Pietra Serena respectively. Treated specimens (3 samples for each lithotype) and references (2 samples for each lithotype) were left at lab conditions for 7 days and then were put in a desiccator until they reached constant weights. The actual amounts of coating materials applied were calculated as the weight difference between the dry weight of samples before and after coating.

Table 4.1 Amounts of coating materials on substrates.

Stone substrate	Coating amount	
	Theoretical g (g/m^2)	Actual g (g/m^2)
Pietra Serena	0.025 (10)	0.013±0.004 (5)
Lecce stone	0.038 (15)	0.033±0.002 (13)

4.2.4 Wetting properties, morphology and other measurements

The surface morphology of pristine and coated stone substrates was

characterized at MEMA (University of Florence) using a Zeiss EVO MA 15 SEM equipped with an RSD detector and Oxford INCA 250 X-EDS. All samples were firstly gold sputtered, and images in secondary (SE) and backscattered electrons (BSE) were acquired, and chemical analysis and elemental mapping were done operating the instrument at 15 KeV, pressure of 1 Torr and current of 2.4 μA.

Static contact angle (CA) and contact angle hysteresis (CAH) of coatings were measured exploiting a Drop Shape Analyzer DSA30 system (KRÜSS GmbH). Static CA of 5 μl sessile droplets of water and extra virgin olive oil on coated stone surfaces was measured. The static CA reported was the average of five discrete drops per sample at varied locations. Advancing and receding CA was measured by increasing and reducing the volume of water droplet deposited on coated surfaces with a small syringe, and they were recorded when the contact line started to advance or retract. Droplets of 5 μl with an addition of 2 μl were used for measuring advancing CA. The difference between advancing CA and receding CA was defined as CAH. In addition, the repellence of coatings towards complex water dispersion and emulsion systems (i.e. coffee, black tea and milk) was also assesses by CA measurements.

The evaluation of self-cleaning capability of coating was conducted by dirt-removal tests. Coated stone substrates previously stained with a mixture of black deposition (a combination of soot, dust that was collected from building

surface in Florence, Figure 4.1) and common sandy soil were placed obliquely on the rim of petri dishes, with a slope angle about 10°. Water drops were released from a pipette onto the stained surface to assess the self-cleaning behaviour. Pictures were recorded using a digital camera (Canon 550D).

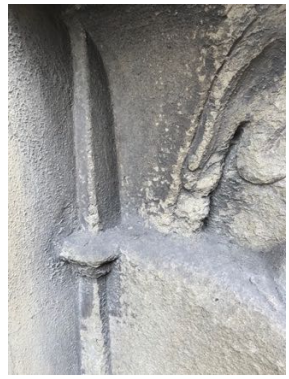

Figure 4.1 Black deposition on stone surface.

The capillary water absorption tests of stone samples, before and after surface coating, were carried out by following the standard method [118]. The results were processed and expressed as water inhibition efficiency (WIE) as reported previously [114]. The vapor diffusivity variations of samples after treatment were evaluated according to standard "Cup" method [120], and the results were reported as residual diffusivity percentage (RD, %). Moreover, the surface chromatic changes of substrates induced by coating were also examined by colorimetric analysis [122]. Exploiting a portable X-Rite SP60 spectrophotometer in specular component excluded mode, measurements on the specific located spots on surfaces (prior and after coating) were done. The color alteration (ΔE^*) was calculated by processing the obtained results in

CIE-L*a*b* standard color system, expressed as:

$$\Delta E = \sqrt{\Delta L^{*2} + \Delta a^{*2} + \Delta b^{*2}} \quad \text{(Eq 4.1)}$$

The chemical stability of coating was estimated by measuring the CA of corrosive liquids, (i.e. 0.01M and 0.1M acetic acid, distilled water, 1M and 2M KOH) and the stability of CA over time (30 min) was also assessed. The durability of coating was evaluated by immersing the coated samples thoroughly in deionized water for 2, 8, 24, and 48 h. Water CA was measured after drying the samples.

Additional tests aiming to verify the versatility of potential substrates apart from natural stones, commercial bricks, ceramics were also coated with Si-PFPE. Wetting property change after coating was investigated by CA measurements as well.

4.3 Results and discussion

4.3.1 Synthesis and characterization of Si-PFPE

The synthesis of Si-PFPE has been accomplished via one-step amidation (Scheme 4.2). At room temperature, amidation completed in 8 h. Figure 4.2 shows the FT-IR spectra of AF-PFPE, APTMS and Si-PFPE. After amide formation, the diagnostic carbonyl group (~1769 cm^{-1}) of acyl fluoride (COF) of AF-PFPE disappeared, whereas a strong peak at about 1701 cm^{-1}

(attributing to amide I of amidic group) presented. The characteristic peaks of amide II ($\nu_{C\text{-}N}$) also appeared (~1445 cm^{-1}) in spectrum of product as well. The main featured absorption peaks have been assigned and summarised in Table 4.2. Peaks attributed to Si-O-Si stretching vibration are usually reported in a wide region from about 950 to 1150 cm^{-1}[144]. In the spectrum of APTMS, the peaks of Si-O stretching which present at 1030 cm^{-1} and 1127 cm^{-1} have then shifted to 1071 cm^{-1} and 1132 cm^{-1} respectively in the spectrum of Si-PFPE. Besides the factor that APTMS is connected to a highly fluorinated segment (PFPE), the main reason accounts for the shifting of Si-O stretching vibration is the cross-linking of silanes which forms oligo-siloxane or poly-siloxane (Si-O-Si bond formation).

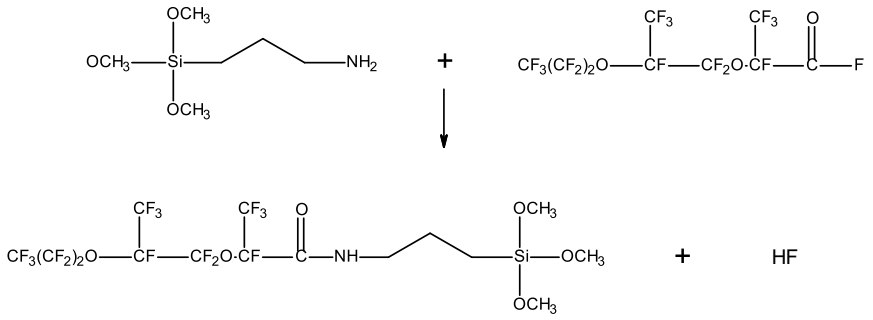

Scheme 4.2 One-step amidation of Si-PFPE synthesis

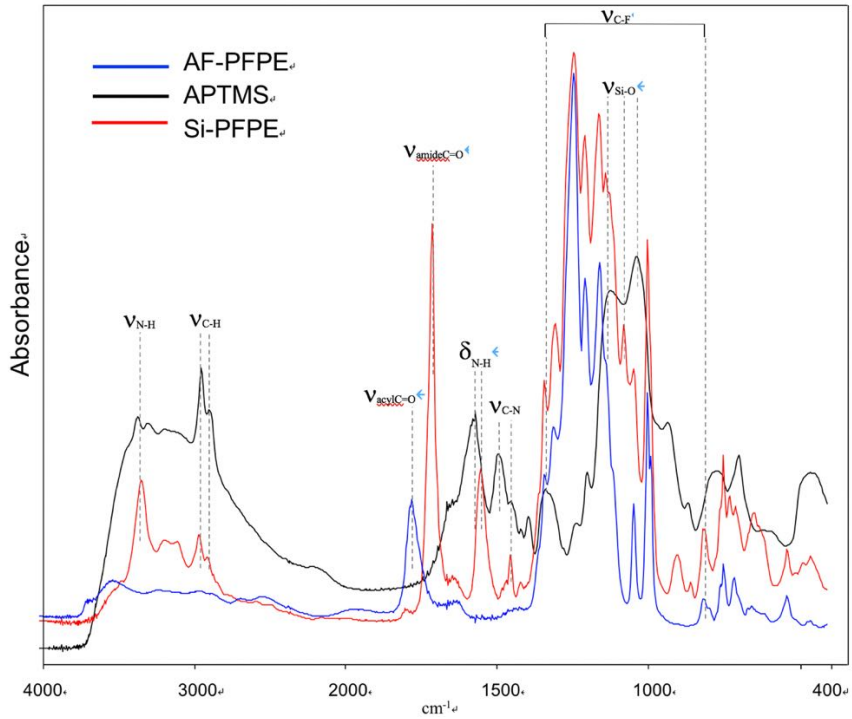

Figure 4.2 FT-IR spectra of reagents and product

Table 4.2 Assignments of the main FT-IR absorption peaks.

Material	Absorption (cm^{-1})						
	ν_{N-H}	ν_{C-H}	$\nu_{C=O}$	δ_{N-H}	ν_{C-N}	ν_{C-F}	ν_{Si-O}
APTMS	3349(s); 3280(w)	2930(s); 2875(m)	/	1560(s)	1483(s)	/	1127(s); 1030(s)
AF-PFPE	/	/	1769(s)	/	/	1400-900(s)	/
Si-PFPE	3325(s)	2945(s); 2893(m)	1701(s)	1545(s)	1445(s)	1400-900(s)	1132(m); 1071(s)

s=strong; m= medium; w= weak.

Figure 4.3 is the ^{1}H-NMR spectrum of Si-PFPE, while Table 4.3 reports the corresponding signal assignments. Since Si-PFPE is partially soluble in methanol, the ^{1}H-NMR spectrum obtained is actually the spectrum of the more soluble fraction which is less cross-linked, i.e. $(Si\text{-}O)_n$-CONH-PFPE. Compared with the spectrum of original APTMS, the chemical shifts of protons of the propyl group have all shifted slightly towards low field due to the deshielding effects of fluorine atoms of PFPE after amidation. The weak singlet at 4.03 ppm attributing to protons of Si-OC**H**$_3$ indicates that the soluble part is not completely gelled, but the majority of product has self-condensed.

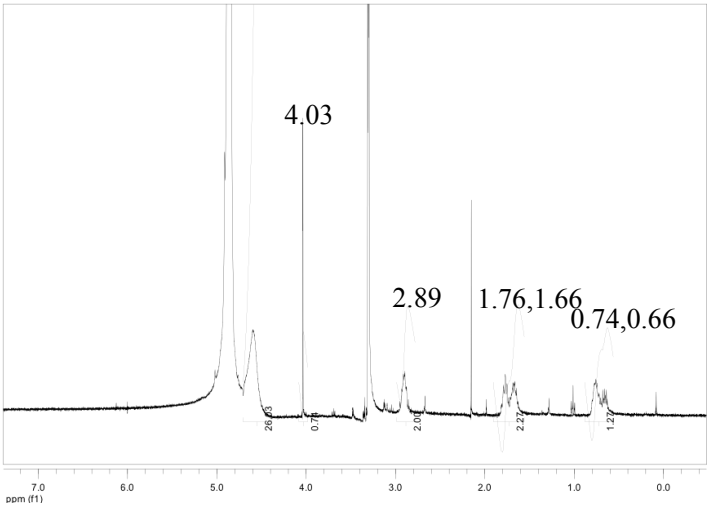

Figure 4.3 ^{1}H-NMR of the soluble fraction of Si-PFPE

Table 4.3 Assignments of ^{1}H-NMR signals of APTMS and Si-PFPE.

Si-OC**H**$_3$	Si-C**H**$_2$-	Si-CH_2C**H**$_2$-	Si-CH_2CH_2C**H**$_2$-NH_2	Si-CH_2CH_2C**H**$_2$-NH-CO-

					PFPE
APTMS		0.54	1.60	2.78	/
Si-PFPE	4.03	0.74, 0.66	1.76, 1.66	/	2.89

4.3.2 Morphology and wetting properties

Exploiting SEM-EDS, nanometrically morphological study was carried out on virgin and coated stone substrates. As shown in Figure 4.4a and 4.4c, with pore diameters mainly ranging from 500 nm to 2 μm, the neat Lecce stone is very rough and porous. These structural features render its high water uptake ability and very low water CA (inset in Figure 4.4c). After surface treatment, the coating material which is nanoscaled, amorphous and needle-like (~500 nm in width) has modified the morphology of Lecce stone evidently (Figure 4.4d), since a multi-level roughness in the nanometre to sub-micrometer scale has been created superficially. The presence of Si-PFPE coating has been confirmed by chemical analysis conducted at the positons indicated by the red dots in Figure 4.4d. The combination of multi-hierarchical roughness and low surface tension of Si-PFPE coating gives rise to superhydrophobicity (photo of water CA inserted in Figure 4.4d). It is worth noting the original pores are not blocked (no continuous film formed on surface), and the open-pore network is intact. As revealed by the carbon, silicon and fluorine mapping analysis (Figure 4.4e and 4.4f) done at the position of Figure 4.4d, with an appropriate amount applied, coating penetrated inside relatively large

(diameter >1 μm) and small pores and distributed alongside the pore walls rather than filling the pores (white bars in Figure 4.4d, 4.4e, 4.4f and 4.4g indicate the locations of pores).

Compared with Lecce stone, Pietra Serena is more compact (much less porous), and it also has smaller pores (Figure 4.5c). Besides, its surface seems smoother too. After coating, the originally surface is covered with nanoscaled, amorphous material (1 μm in width) that have varied morphologies (e.g. needle-like or lamellar-like) and dimensions (from ~500 nm to ~6 μm) (Figure 4.5b, 4.5d). Though coating material was detected at positions 1 and 2 indicated by red dots in Figure 4.5d, no fluorine atom was found at position 3. This is highly probably due to the low amount of Si-PFPE introduced (5 g/m^2) which results in not uniform and heterogeneous distribution phenomena. Silicon and fluorine mapping also proved the very low amount of coating material (Figure 4.5e, 4.5f) applied. Yet, this low amount of Si-PFPE is able to endow Pietra Serena with superhydrophobicity (photo of water CA inserted in Figure 4.5d)

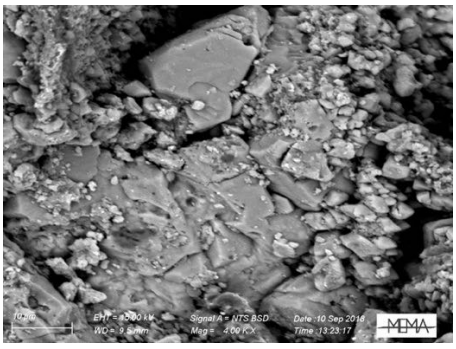

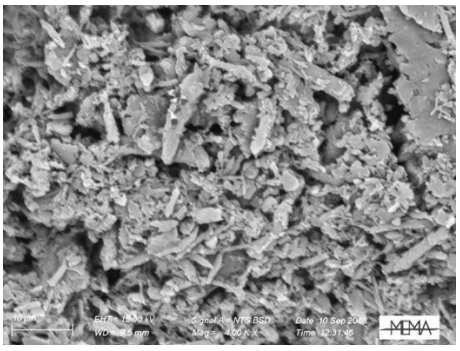

(a) LS-NT (10 μm)

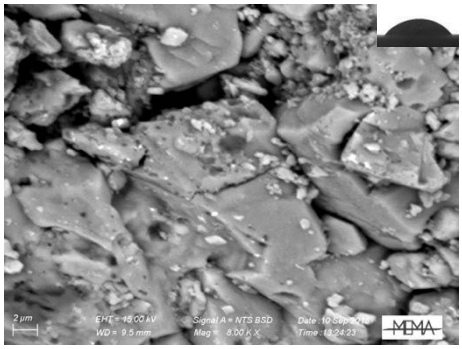

(b) LS-T (10 μm)

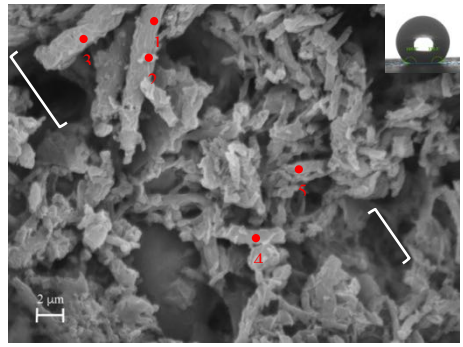

(c) LS-NT (2 μm)

(d) LS-T (2 μm)

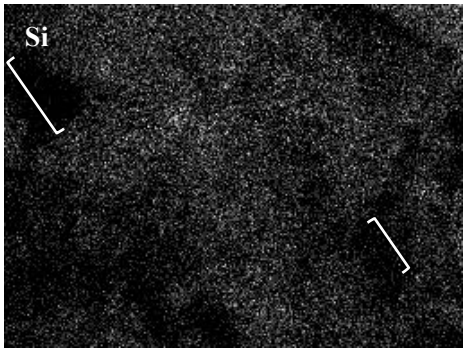

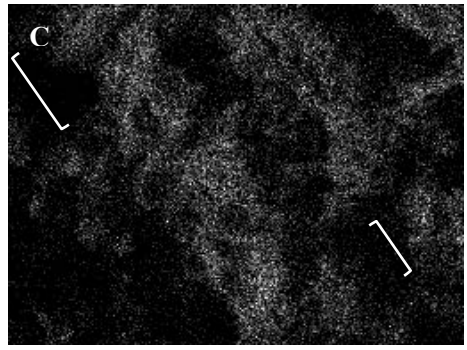

(e) Si mapping

(f) C mapping

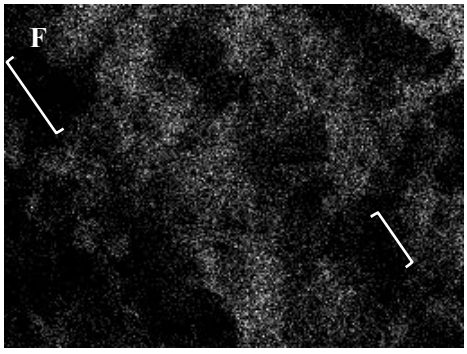

(g) F mapping

Figure 4.4 SEM micrographs of virgin (a; c) and coated (b; e) Lecce stone (the insets are photos of water CA on corresponding surface), and the

mappings of silicon (e), carbon (f) and fluorine (g). LS = Lecce stone, NT = not coated, T = coated.

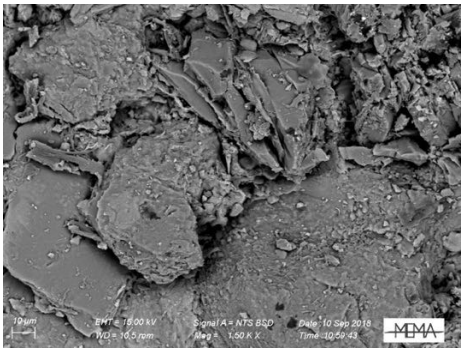

(a) PS-NT

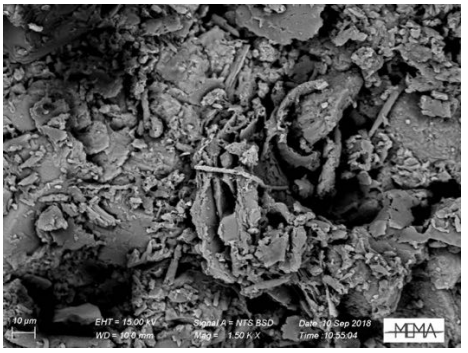

(b) PS-T

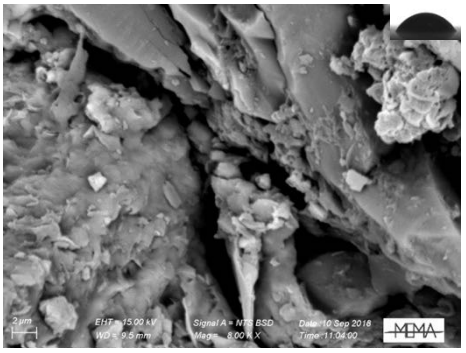

(c) PS-NT

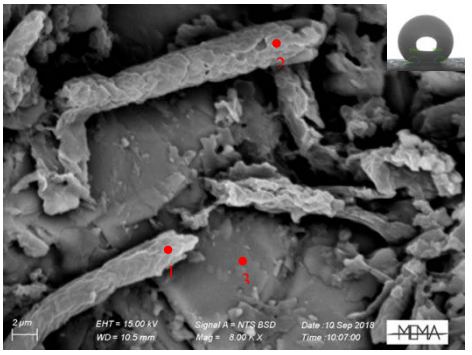

(d) PS-T

(e) Si mapping

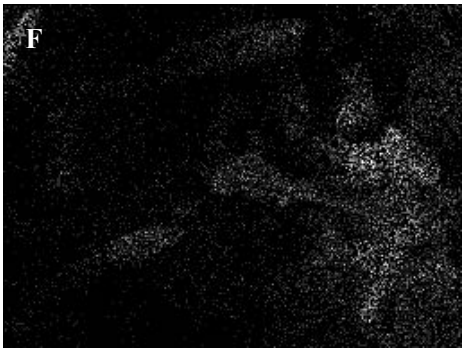

(f) F mapping

Figure 4.5 SEM micrographs of virgin (a, c) and coated (b, d) Pietra Serena (the insets are photos of water CA on corresponding surface), and the mappings of silicon (e) and fluorine (f). PS = Pietra Serena, NT = not coated, T = coated.

Figure 4.6 illustrates the CA variations of virgin and coated substrates. In general, the original wetting property of substrates has been remarkably modified from hydrophilic to superhydrophobic by the coating, as evidenced by CA increasing from 35.2° and 56° to 158.5° and 162.8° for Lecce stone and Pietra Serena, respectively. Besides, with water and oil CA >150°, the coating manifests superamphiphobicity (Figure 4.7). In specific, coating on Pietra Serena shows slightly higher amphiphobicity than on Lecce stone (water CA 162.8° versus 158.5°; oil CA 154.2° versus 152.7°), though its amount applied was lower (Table 4.1). Similarly, coating on Pietra Serena is also more slippery, since its CAH are 4.5° and 8.5° on Pietra Serena and Lecce stone respectively. Moreover, the coating also shows ultra repellence to complex water dispersion and emulsion systems (Figure 4.8). In contact with coffee, black tea and milk drops, the CA are all higher than 150°, and these high CA are also stable over long time (30 min). The self-cleaning property derived from high CA and low CAH is verified by dirt-removal test in Figure 4.9 and Figure 4.10. Once water drops were released and contacted with coated substrate, they picked up dirt, dust and rolled off immediately. Gradually, previously stained surface was cleaned, and the original aesthetic features were recovered.

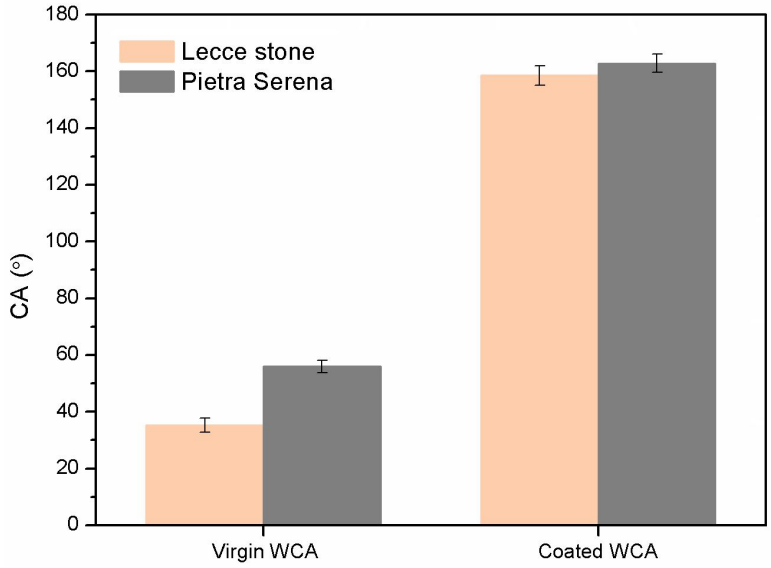

Figure 4.6 Plot of water CA of virgin and coated Lecce stone and Pietra Serena.

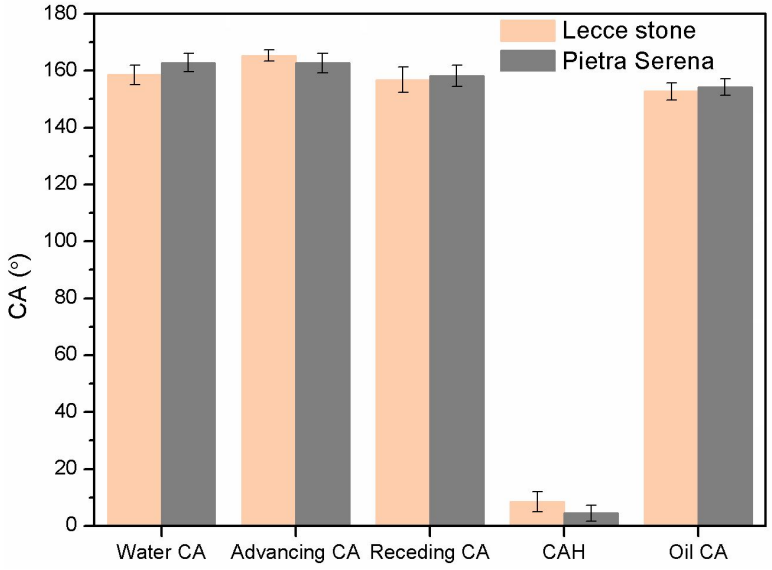

Figure 4.7 Plot of water, oil CA and CAH of coating on Lecce stone and Pietra Serena.

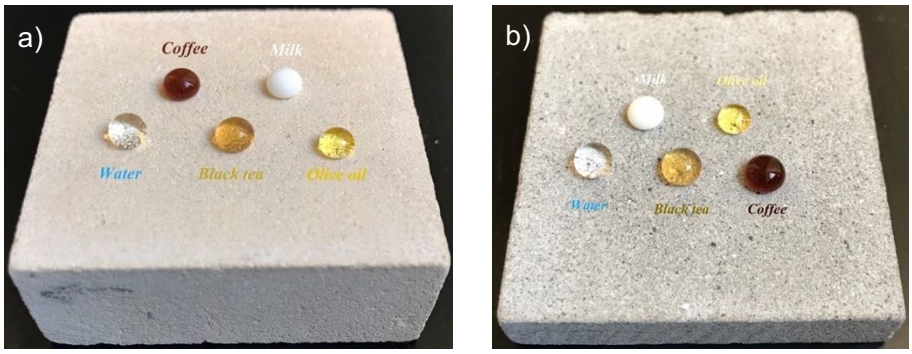

Figure 4.8 Digital photos of water, black tea, olive oil, coffee and milk drops in contact with coated Lecce stone (a) and Pietra Serena (b) samplers. All drops are quasi spherical and this spherical shape is stable over time.

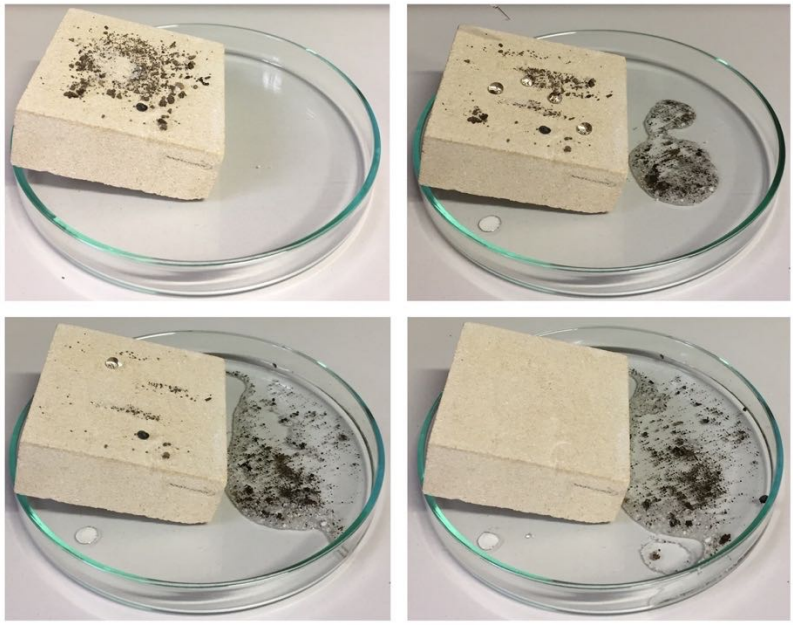

Figure 4.9 Digital photos of self-cleaning property of as-prepared surface on Lecce stone substrate. The contaminants are a mixture of black deposition (a combination of soot, dust that was collected from building surface in Florence, Figure 4.1) and common sandy soil.]

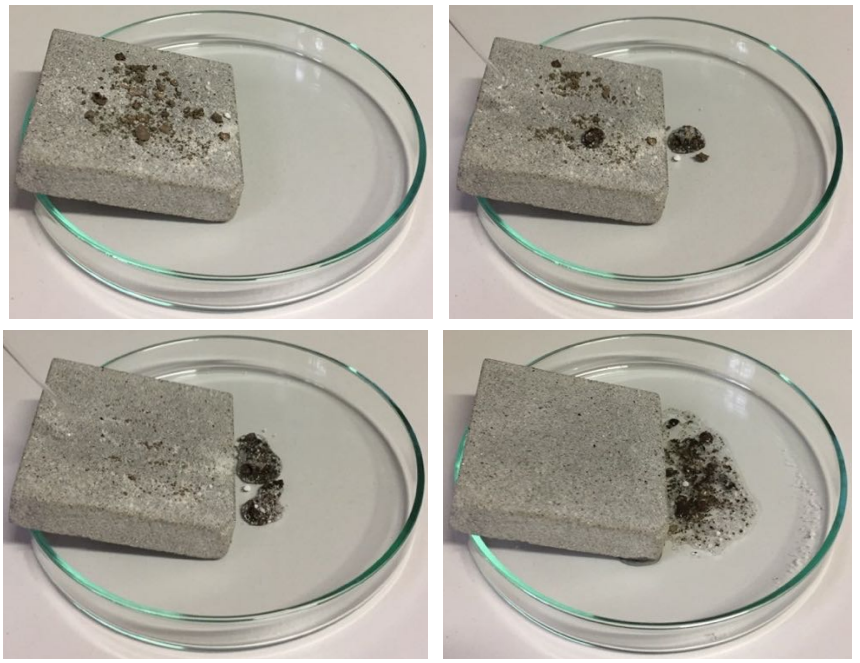

Figure 4.10 Digital photos of self-cleaning property of as-prepared surface on Pietra Serena substrate. The contaminants are a mixture of soot, dust and sandy soil.

4.3.3 Performance as water repellent for building stones

To assess the performance as water repellent for building stones, the WIE of as-prepared coating against water absorption by capillarity was evaluated initially. The virgin Lecce stone absorbs water very fast in the first 30 minutes i.e. 7 g of water absorbed, and then another 3 g of water was absorbed after 24 h (Figure 4.11). In total, about 10 g of water was absorbed by the 5*5 cm^2 face of Lecce stone sample. To protect Lecce stone, high inhibition efficacy in the first 30 minutes is very significant. Whereas, Pietra Serena absorbs

much less water than Lecce stone (1.8 g in 24 h, Figure 4.12). In the first hour, more than 0.8 g of water was absorbed, and then in each hour the amount absorbed were relatively similar, i.e. around 0.3 g of water absorbed in the second and third hour. It is conspicuous, after treatment, the amounts of water absorbed were dramatically reduced for both two stones (Figure 4.11 and 4.12). In particular, only 0.08 g, 0.14 g, and 0.20 g of water was absorbed by treated Lecce stone after 30 min, 1h and 2h respectively, and the corresponding WIE values are 98%, 98% and 98%. It is notified as well, as-prepared coating inhibits water absorption efficiently even after 24 h, and as little as 0.93 g of water was absorbed (WIE=91%). On the other hand, with WIE values being 91%, 90% and 90% at 1 h, 2 h and 3 h testing times, coating also manifested very high water repellence on Pietra Serena, despite of the very low amount of coating material introduced. After 24 h, about 0.54 g of water penetrated inside coated Pietra Serena, giving rise to a WIE value of 71%. This lower WIE than that of Lecce stone can be attributed to the low amount of coating which was not able to distribute and cover homogeneously all over the surface which is visualized by SEM analysis in Figure 6. Some micro "defects" that coated with few coating material may not be able to block water penetration for 24 h. However, to improve the WIE for long testing times e.g. 24 h, 36 h, a higher amount of coating material is suggested i.e. 10 g/m^2, which is also the generally recognised amount for Pietra Serena protection. We only applied 5 g/m^2 of coating on Pietra Serena (Table 4.1), because this low amount is sufficient for achieving superamphiphobic and self-cleaning properties.

Concerning the physical properties of stone substrates after surface treatment, coating well preserved the original vapor diffusivity. The RD values are 90%±2 and 94%±4 for Lecce stone and Pietra Serena respectively (Figure 4.13), meaning less than 10% of the pore networks were blocked or damaged after coating. These results are in good agreements with the morphological study conducted above, i.e. the original pore structures are not impaired by coating. Besides, the original chromatic features of substrates are also maintained, since the overall color change (ΔE*=1.0 and 2.1 for Lecce stone and Pietra Serena respectively) is below the detection limit of naked human eyes (ΔE*=3) (Figure 4.14).

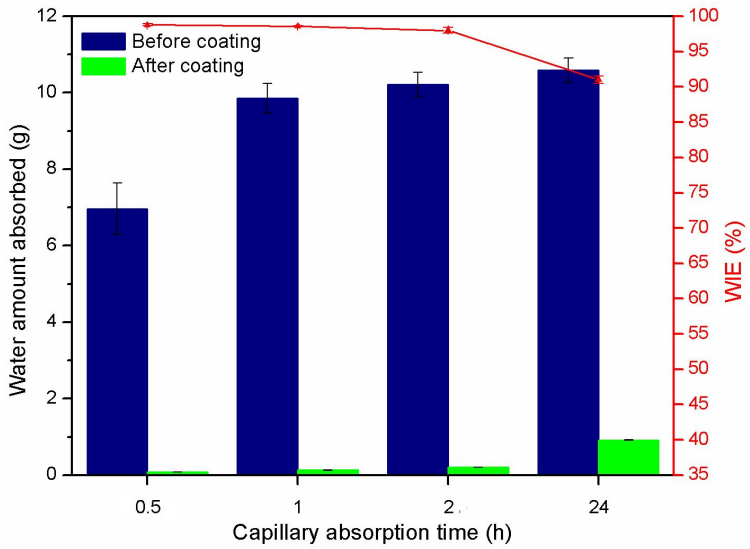

Figure 4.11 Amounts of water absorbed by capillarity by Lecce stone after 0.5 h, 1 h, 2 h and 24 h before and after coating, and the WIE accordingly.

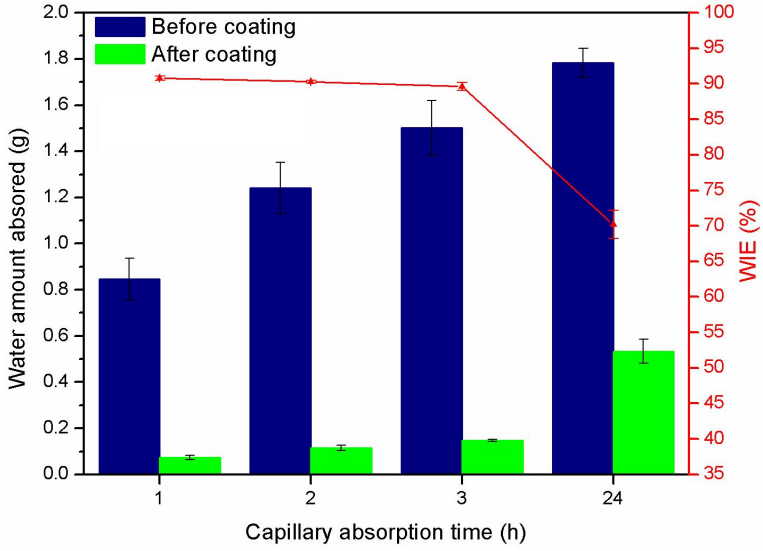

Figure 4.12 Amounts of water absorbed by capillarity by Pietra Serena after 0.5 h, 1 h, 2 h and 24 h before and after coating, and the WIE accordingly.

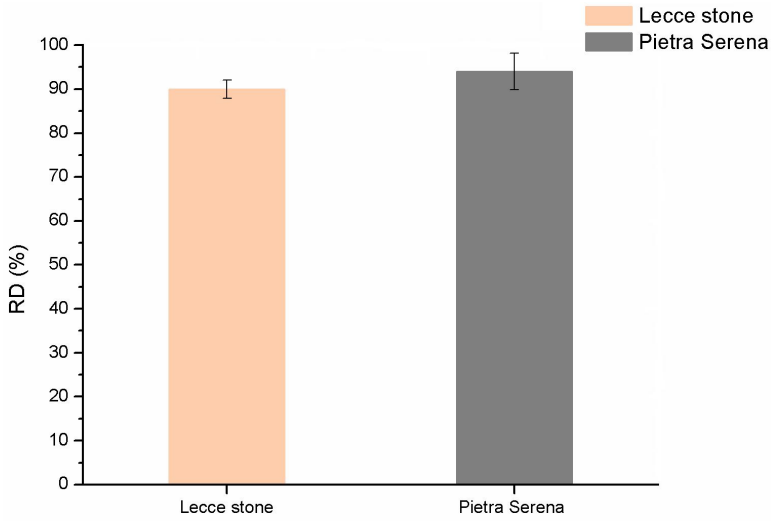

Figure 4.13 Residual vapor diffusivity (RD) of Lecce stone and Pietra Serena after coating.

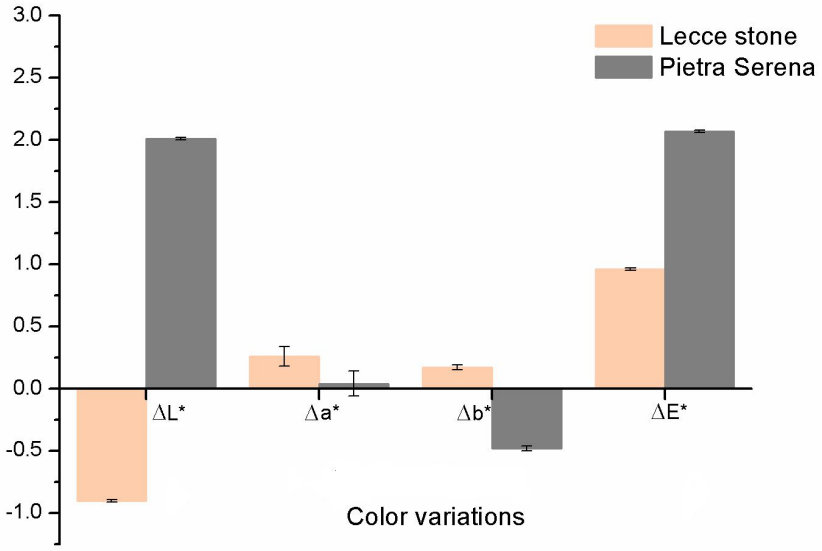

Figure 4.14 Chromatic changes on Lecce stone and Pietra Serena after coating. L* indicates brightness and ranges from 0 (black) to 100 (white); a* and b* are the color axes and range from -60 to +60. On the a* axis, positive values indicate red, whereas the negative ones indicate green. On the b* axis, yellow is positive while blue is negative.

4.3.4 Chemical stability and durability

In order to be applied on building materials in outdoor environment, the chemical stability and durability of coating were investigated. CA of several corrosive chemical agents with varied molarities and pH e.g. 0.01M and 0.1M acetic acid, 1M and 2M KOH, on coated stone substrates were measured. Results revealed, the superhydrophobicity of as-prepared coating is stable in the pH range 2.9-14, since CA are all higher than 150° and are stable over long time (30 min) (Figure 4.15). Stability over pH 2.9-14 allows the

application in presence of acid rain which usually has a pH value around 4.0-5.6 [145]. In addition, water immersion test was employed to evaluate the durability. As shown in Figure 4.16 and Figure 4.17, water CA on both two kinds of substrates decreased slightly after 24 h immersion and then tended to stabilize. After 48 h immersion, as-prepared surfaces are still superhydrophobic, and CA are about 153° and 157° for Lecce stone and Pietra Serena respectively. Therefore, our coating is capable to act as superhydrophpobic, self-cleaning surface also in regions where it rains frequently and where acid rain deposition occurs.

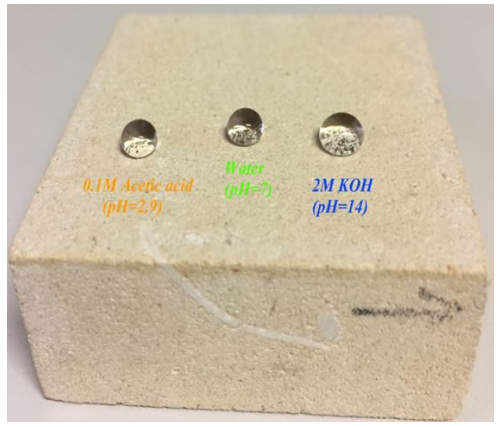

Figure 4.15 Digital photo of 0.1 M acetic acid, deionized water and 2M KOH drops in contact with coated Lecce stone sample. All drops are quasi spherical and this spherical shape is stable over time.

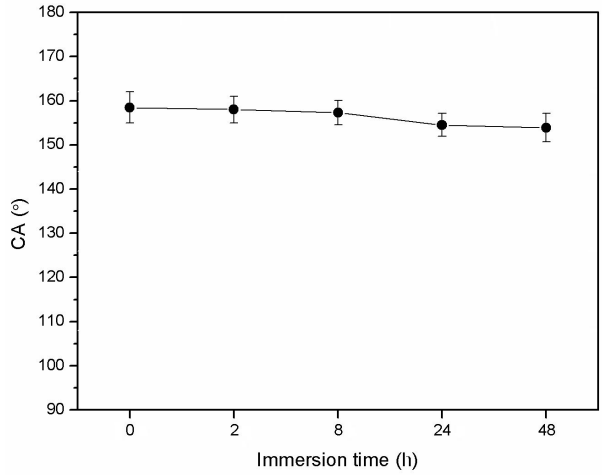

Figure 4.16 Water CA variations of coated Lecce stone before and water immersion for 2 h, 8 h, 24 h and 48 h.

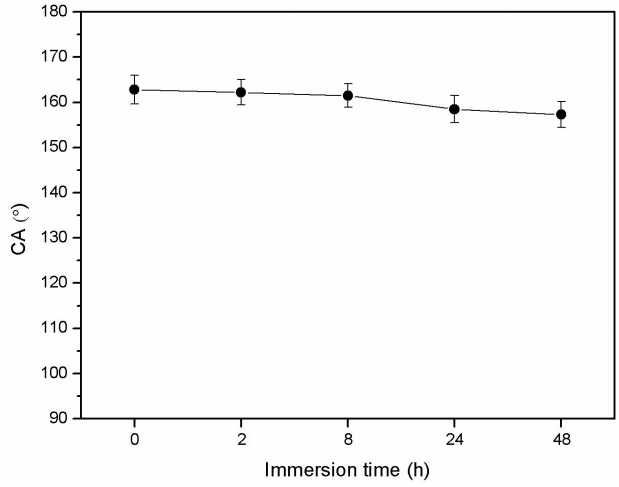

Figure 4.17 Water CA variations of coated Pietra Serena before and water immersion for 2 h, 8 h, 24 h and 48 h.

The coating material is versatile in application in terms of potential substrates, since it works efficiently on almost all kinds of building materials apart from natural stone, e.g. bricks, ceramics. In Figure 4.18, the water and oil drops are

quasi aspheric on the coated brick sample, and the corresponding CA are > 150° for both water and oil. Figure 4.19 shows the coated brick sample is non-wettable even by running tape water.

Figure 4.18 Digital photo of water, black tea, olive oil, coffee and milk drops in contact with coated red brick. All drops are quasi spherical and this spherical shape is stable over time.

Figure 4.19 Digital image of coated red brick under running tap water. The surface maintained completely dry and water rolled off.

4.3.5 Comparative study with oligoamides grafted with PFPE segments

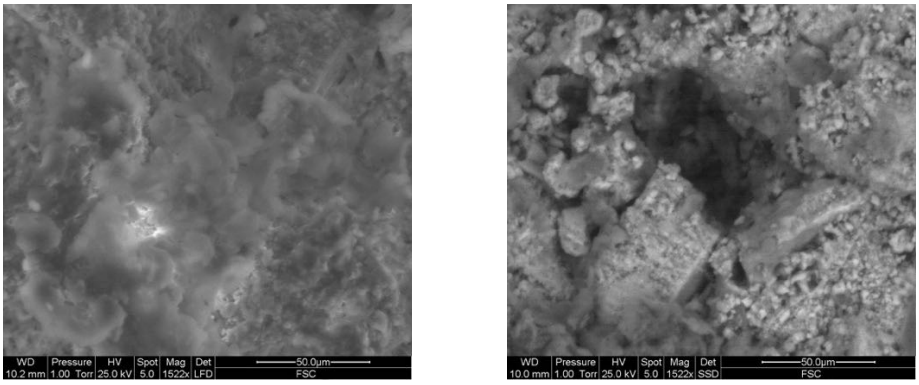

(a) (b)

Figure 4.20 SEM micrographs of Lecce stone coated with oligosuccinamide grafted with PFPE segments (FSC)

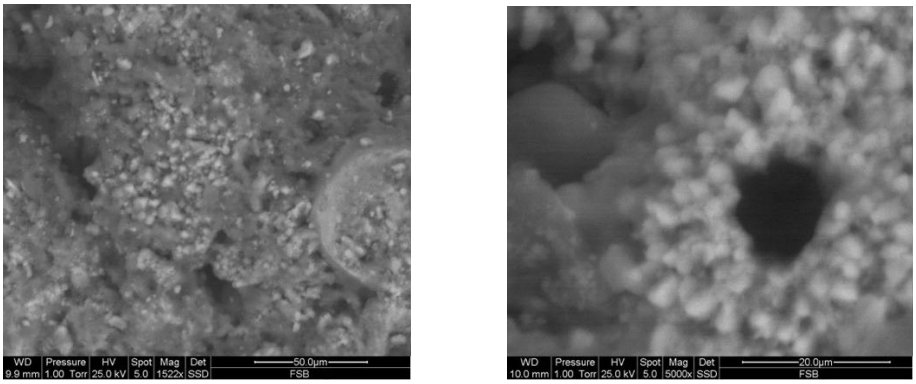

(a) (b)

Figure 4.21 SEM micrographs of Lecce stone coated with oligosuberamide grafted with PFPE segments (FSB)

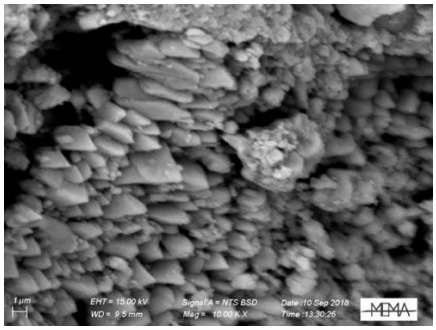

(a) LS-NT

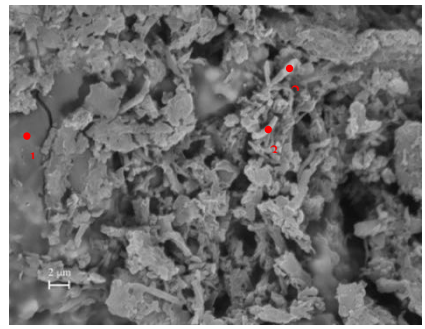

(b) LS-T

(c) Si

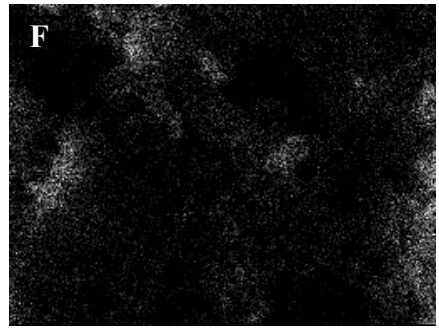

(d) F

Figure 4.22 SEM micrographs of virgin (a) and coated (b) Lecce stone, and the corresponding silicon and fluorine mappings done at the same position of (b). The red dots in (b) indicate the positions where chemical analysis was done. LS = Lecce stone, NT = not coated, T = coated.

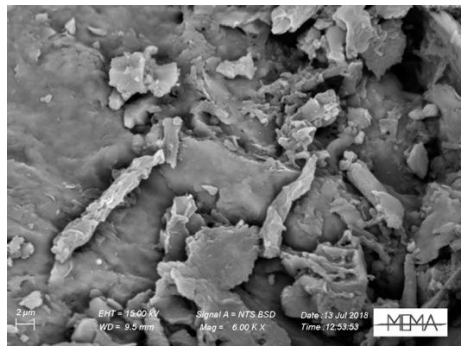

Figure 4.23 SEM micrographs of coated Pietra Serena.

In comparison with the surface morphology of Lecce stone coated with oligoamides grafted with PFPE segments (Figure 4.20, 4.21), Si-PFPE which incorporates another type of PFPE group manifests varied morphology. Though applied as 2-propanol solutions due to their good solubility, FSB and FSC tend to form agglomerates or clusters that are preferred to concentrate around relatively large pores (Figure 4.20b and Figure 4.21b). Some large slice-like substances (~20 μm) have also penetrated inside pores while less product was seen on areas distant from pores. Unlike FSC/FSB, Si-PFPE distributes more uniformly all over the surface, and no preferred areas for product distribution was observed. Silicon and fluorine atoms were detected at all positions evidenced by red dots in Figure 4.22b, and the corresponding mappings of these elements are shown in Figure 4.22e and 4.22f. Areas around pores and areas distant from pores were covered with product of similar amount (or thickness). Moreover, the twisted lamellar-like of Si-PFPE (width≤ 2μm, Figure 4.22b) have much smaller dimensions than clusters of FSC/FSB (~20 μm), thus creating a multiple roughness at nanometer to sub-micrometer scales. Similar morphology was also seen on coated Pietra Serena (Figure 4.23). One possible reason for the much more homogeneous arrangement of Si-PFPE is its lower molecule weight (657 g/mol) than that of FSC/FSB (~2000 g/mol). The short chain PFPE (498 g/mol) of Si-PFPE, which are less flexible than the long chain PFPE (880 g/mol) of FSC/FSB, are not inclined to entangle with each other to form agglomerates that have larger dimensions and not uniform distribution. These specific morphology differences lead to the their differed wetting behaviors, in terms of water and

oil CA. Owing to the multi-level, nanometric roughness of Si-PFPE, it demonstrates higher water and oil CA (158.5°; 152.7°) than that of FSC and FSB. Furthermore, compared with the PFPE blocks in FSC/FSB, the low molecular weight PFPE of Si-PFPE is more "mobile" which can induce more apparent surface fluorine segregation phenomenon. Hence, more liquid repellent—superamphiphobicity and less adhesive—self-cleaning surfaces were generated by Si-PFPE. Contrary to FSC/FSB coated surfaces which have high adhesion to water droplets (CAH>90°), Si-PFPE coated surfaces are very slippery (CAH<10°). As I have explained in previous chapter, the high adhesion force is attributed to the combination of capillary force generated by the multi-level rough and porous structures and the hydrogen bonding between polar amidic groups and water molecules. In the case of Si-PFPE coated surfaces, on one hand, since there is only one amidic group in each molecule (6-8 amidic groups in each FSC/FSB molecule), the effect of hydrogen bonding with water molecules is dramatically reduced. On the other hand, the capillary force is not evident because of the uniform distribution of coating material.

In accordance with its higher water CA than FSC/FSB, coating Si-PFPE also shows higher WIE (i.e. 98%, 98%, 98% versus 95%, 93%, 90% of FSC) on the same Lecce stone substrate at 30 min, 1 h and 2 h testing times. Besides, Si-PFPE well inhibits water even after 24 h test (WIE 91%), surpassing all previously reported products.

4.4 Conclusion

In summary, needless of employing nanomaterials or surface modification process, a facile strategy to fabricate superamphiphobic surface with self-cleaning property was proposed. The coating material, Si-PFPE, was obtained effortlessly via one-step amidation at room temperature. Surface treatment can be easily done by brushing surface with alcoholic dispersion of Si-PFPE. Confirmed by SEM, the as-prepared surface is nanometrically rough at multiple levels, and it demonstrates ultra-high water and oil repellence on two widely used natural stone substrates. The high water CA and low CAH bestow as-prepared surface with self-cleaning property. Yet, as-prepared surface also shows superhydrophpbicity to complex water dispersion and emulsion systems. Practically, when applied and tested as water repellent, as-prepared surface exhibits high WIE in addition to good maintenance of the physical properties of substrates, i.e. vapor diffusivity and chromatic features. Last but not least, as-prepared coating is stable in acidic and alkali environments (pH 2.9-14), and its superhydrophobicity is also durable towards long time water immersion (up to 48h). All results indicate as-prepared coating show great technological promise in preserving building materials, including natural stones, bricks, concretes, ceramics etc., of modern and historic constructions. More importantly, the coating can work effectively also in polluted urban environment where acid rain presents and in regions where it rains frequently. Furthermore, since no harsh conditions or sophisticated equipment was used during fabrication, this method is easy to scale up.

Chapter V

Hybrid nanocomposite based on nano-TiO_2 and fluorinated siloxane

5.1 Introduction

Ever since the discovery of photogeneration of a superamphiphilic TiO_2 surface under UV radiation which showed self-cleaning and antifogging characteristics reported by Fujishima et al. in 1997 [146], a new era in designing TiO_2-based, biomimetic super-wetting/-antiwetting surfaces has begun. In the past decade, thanks to its ready availability, economical convenience, chemical and thermal stability and low toxicity, TiO_2-based nanomaterials were widely adopted for developing bio-inspired surfaces with special wettability and varied adhesion properties [147, 148].

In the field of build heritage preservation, two strategies for preparing TiO_2-based products can be generalized. In the first method, hydrophilic nano-TiO_2 dispersions in different solvents e.g. water, alcohol, ethylene glycol etc. is prepared and then applied on the surface of building stones directly, giving rise to hydrophilic or superhydrophilic, self-cleaning properties [149, 150]. Whereas, the second approach is to introduce nano-TiO_2 into oligomeric, polymeric or inorganic matrix to achieve functionalised nanocomposites.

Aiming to convey hydrophobic, superhydrophopbic and/or consolidating properties, alkyl silane and alkyl aryl polysiloxane, fluorinated or partially fluorinated polymers, or acrylic copolymers are typically employed as matrices [151-153].

As aforementioned, in order to prevent or mitigate building surfaces from degradation induced by water-related factors and from soiling due to atmospheric pollution, super-repellent surfaces with low adhesion property (or self-cleaning property) is preferred as protective coatings for building materials. Although numerous self-cleaning, superhydrophobic surfaces have already been developed and proposed for the preservation of architectural heritage [106, 108, 109, 112, 113], to my best knowledge, no TiO_2-based material that incorporates superhydrophobicity, self-cleaning and photocatalytic property was tested and suggested for protecting building stones. Some researchers tried to introduce metal nanoparticles (e.g. Au, Ag, CuO nanoparticles) to prepare photoactive nanocomposites with (or without) TiO_2 nanoparticles [154, 155]. Though they manifest high biocidal effect, their high cost and strong color effect should be well addressed before practical application. There do exist, in literature, a number of TiO_2-based hybrid nanocomposites that are slippery, super-repellent and photo-active, yet they are initially designed and tested for industrial use [156-160]. Moreover, during their preparation, usually harsh conditions and/or substrate processing are necessary which do not meet the prerequisites for application in the field of heritage conservation (i.e. the physical, chemical integrity of artworks shall

never be impaired). On the other hand, few of those nano-TiO_2 containing materials recommended for stone protection is superhydrophobic, and the majority are hydrophilic or even superhydrophilic [150]. By understanding the degradation mechanisms of stone materials, it is without doubt that superhydrophobicity is imperative for their long-term safeguard.

Herein, in this chapter, I report a simple strategy to prepare a nano-TiO_2 bearing hybrid nanocomposite that exhibits superhydrophobicity, self-cleaning and photo-catalytic behaviours on compact building stones e.g. Carrara marble. The nanocomposite was effortlessly obtained by mixing activated nano-TiO_2 into a fluorinated siloxane (Si-PFPE) dispersion (in 2-propanol) under sonicating and moderate heating. Coating was fabricated by brushing or deposing dispersion with a graduated pipette. On coated stone surfaces (Lecce stone, sandstone, marble), the static water CA is higher than 150° while the CAH is below 10°, satisfying the criteria of being superhydrophobic and self-cleaning. Subsequent tests also illustrate, though the amount of coating material introduced was very low (8.5 g/m^2 of 1% w/w 2-propanol suspension), nanocomposite coating inhibits capillary absorption efficiently in addition to good maintenance of the original physical properties of substrates, i.e. vapor diffusivity and chromatic features. Compared with several chemically similar nanocomposite formulations that composed of a commercial fluoroelastomer and TiO_2 nanoparticles, our new nanocomposite shows overall better performance in preventing capillary water penetration on stones with both high and low porosities. More importantly, the photo-

catalytic activity of nanocomposite and formulations is evidenced by the positive results of discoloration test of methylene blue dye under UV exposure. Our innovative nanocomposite is also more photo-catalytically active than other formulations, particularly when applied on low porous marble.

5.2 Experimental

5.2.1 Materials

(3-Aminopropyl)trimethoxysilane (APTMS, 97%), 2-propanol (>99.5%), titanium oxide, anatase (99.7%, <25 nm) were purchased from Sigma-Aldrich (Germany). Acyl fluoride-end functionalized perfluoropolyether (AF-PFPE, 97%) was obtained from Wuhan HongRuiKang Reagent Co., Ltd (China). Nitric acid (65%) and ethyl acetate (99.8%) are products of Merck (Germany). Fluroelastomer N215 (poly hexa-fluoropropene-co-vinylidene fluoride, Mw≈ 125,000) was kindly supplied by Solvay Solexis-Milan. Distilled water was prepared in lab prior to use.

Three types of stone materials with distinct chemical and physical properties i.e. Lecce stone, Carrara marble and sandstone (Pietra Serena) were used as coating substrates. Lecce stone is a kind of beige, fine bio-calcarenite with high porosity (water accessible porosity about 35-47%, pore size ranging from 0.01 to 2 μm). Owing to its high workability, golden and warm color,

Lecce stone was broadly employed for Baroque architectures during the 17th and 18th century in southern Italy. While Carrara marble, quarried from north Tuscany and used since ancient Roman times, is very compact (water accessible porosity about 2%, pore size <1 μm). Predominantly constituted of calcite, there is also a small amount of accessary minerals that affect color (grey to blue color) and veining. The sandstone is mainly constituted by sandy fraction, clay matrix and a small amount of calcite, with porosity around 3-6% and pores size ranging from 0.004-0.3 μm. It was frequently used during the Renaissance period. Lecce stone and Carrara marble samples were all cut as slabs in dimension 5·5·2 cm^3, while sandstone samples are slices with dimension 5·5·1 cm^3. To select samples for coating fabrication and successive tests, three sequences of water capillary absorption tests were carried out on all samples. Only samples that demonstrated constant water absorptivity were selected. For each type of coating material, there are three samples of each kind of stone and another two served as references.

5.2.2 Preparation of hybrid nanocomposites

- **Si-PFPE-TiO_2 nanocomposite**

The synthesis of fluorinated siloxane (Si-PFPE) was carried out by following the method reported in Chapter IV. The product obtained just after synthesis was dispersed in 2-propanol (1% w/w) at disposal. In advance to formulation preparation, TiO_2 nanoparticles was activated by HNO_3 (2M) according to the method described in literature [161], and product was collected as solid. Under vigorous magnetic stirring, nanocomposite was obtained by

introducing activated TiO_2 nanoparticles into 1% (w/w) 2-propanol dispersion of Si-PFPE. The mixture was stirred and heated at 40 °C for 6-8 h. Stirring was not stopped until no evident phase separation was observed. To prepare the nanocomposite, two different molar ratios between Si-PFPE and TiO_2 i.e. Si-PFPE/ TiO_2=1/1, 2/3 were adopted. 1.00 g (1.5 mmol) of Si-PFPE and 0.12 g (1.5 mmol) of TiO_2 were used for synthesis with molar ratio Si-PFPE/TiO_2=1/1, while 1.00 g (1.5 mmol) of Si-PFPE and 0.18 g (2.25 mmol) of TiO_2 were used for synthesis with molar ration Si-PFPE/TiO_2=2/3. After introducing TiO_2 nanoparticles and during stirring, heating, FT-IR spectroscopy was exploited to monitor the reaction kinetics. In the collected FT-IR spectra, the absorption positions of Ti-O-Si bond (around 920-926 cm^{-1} and 925-960 cm^{-1}) were payed special attention. Once reaction was completed, and solvent was removed at reduced pressure, 1.15g and 1.26 g of white solid was recovered for the synthesis with molar ratio 1/1 and 2/3 respectively. The products were further characterized by FT-IR spectroscopy.

- **N215-TiO_2 mixtures**

For the purpose to compare the performance of the new nanocomposite with other compounds containing highly fluorinated chains, another formulation was prepared by incorporating a commercial fluoroelastomer (N215) and TiO_2 nanoparticles. 1% (w/w) water dispersion of nano-TiO_2 and 2.5% (w/w) ethyl acetate solution of N215 were firstly prepared at room temperature. These dispersion and solution were used as they are and/or mixed to form blend for coating fabrication. The blend was obtained by adding TiO_2

dispersion into N215 solution under vigorous stirring. The mixture was sonicated for 30 min and then left under magnetic stirring for another 1 h until no apparent phase separation was seen.

5.2.3 Coating fabrication

For coating preparation, nanocomposite synthesized with molar ratio Si-PFPE/TiO_2=1/1 was used as coating material (because of its better organised, no phase separated structure and revealed by FT-IR and TEM analyses) and then subjected to subsequent tests. 1% (w/w) 2-propanol suspension of Si-PFPE-TiO_2 nanocomposite and 1% (w/w) 2-propanol suspension of N215-TiO_2 blend were prepared at room temperature at disposal. Apart from applying N215 and TiO_2 as blend ("N215-TiO_2 blend"), their pure solution or dispersion were also coated on substrates independently. Intended to investigate whether the spatial distribution of TiO_2 can influence the photocatalytic ability of final coating, the orders of coating N215 and TiO_2 solution (or dispersion) were adjusted. There are two coating strategies, i.e. 1) coat stone with N215 firstly and on which TiO_2 was added as the uppermost layer ("N215+TiO_2"); 2) coat TiO_2 layer at first and then N215 layer as the outmost layer ("TiO_2+N215"). Moreover, in the second approach, additional stone samples were primarily saturated thoroughly with distilled water (6 ml) followed by coatings of TiO_2 and then N215 successively ("H_2O+TiO_2+N215"). The idea was to determine the influence of water presence on the penetration of TiO_2 inside the pores of stones and consequently the photocatalytic property efficiency of TiO_2.

In order to accurately control the amounts of coating materials, surface treatment was realised by using graduated pipettes (0.2 ml) with the classical method “wet on wet”. All treated stone samples were placed in lab for 3 days for solvent evaporation, and then they were put in a desiccator until constant weights were reached. The actual amounts of coating materials introduced were obtained by the weight difference between dry weights of virgin stones and treated stones (Table 5.1). It shall be noticed that, the amount of product to apply was determined based on the minimum amount of Si-PFPE-TiO_2 to obtain superhydrophobicity and self-cleaning characteristics Afterwards, aiming to compare the performance of different formulations quantitatively, the amounts of N215-TiO_2 blend, successive and independent N215 and TiO_2 coatings were determined based on the actual amount of nanocomposite applied. The amount of N215 to be applied was calculated from the actual amount of fluorinated fraction (Si-PFPE) of nanocomposite, while the amount of nano-TiO_2 was known by the amount of TiO_2 of nanocomposite accordingly. In Table 5.1, the amounts of different coatings on various stone substrates are reported.

Table 5.1 Amounts of coating materials on several substrates.

Stone substrate	/	Coating materials				
		Si-PFPE-TiO_2 nanocomposite	N215-TiO_2 Blend	1) N215→ TiO_2	2.1) TiO_2→ N215	2.2) H_2O+ TiO_2→ N215
	Theoretical g (g/m^2)	Actual g (g/m^2)				
Carrara marble	0.025 (10)	0.021±0.002 (8.5)	0.015 ±0.002 (6.0)	0.015 ±0.001 (6.0)	0.015 ±0.003 (6.0)	/
Lecce stone	0.050 (20)	0.032±0.004 (12.8)	0.037 (14.8)	0.048 (19.2)	0.031 (12.4)	0.041 (16.4)
Sandstone	0.025 (10)	0.0125±0.002 (5.0)	/	/	/	/

5.2.4 Wetting property and morphology characterization

The wetting properties of neat and coated stones were characterized by water CA and CAH measurement using a Drop Shape Analyzer DSA30 system (KRÜSS GmbH). The static CA of 5 μl sessile droplets of water was measured and reported as the average value of five measurements done at different locations on sample surfaces. CAH is estimated as the difference between advancing and receding CA, Specifically, advancing CA and receding CA were measured by increasing and reducing the volume of water droplet deposited on surfaces with a small syringe, and they were recorded when the contact line started to advance or retract. Droplets of 5 μl with an addition of 2 μl were used for measuring advancing CA. Besides, the repellence of coatings towards complex water dispersion and emulsion systems (i.e. coffee, black tea and milk) was also assessed by CA measurements.

The self-cleaning capability of coatings was assessed by dirt-removal tests. Coated stone substrates previously stained with a mixture of black deposition (Figure 4.1) and common sandy soil were placed obliquely on the rim of petri dishes, with a slope angle about 10°. Water drops were released from a pipette onto the stained surface to evaluate the self-cleaning behaviour. Pictures were recorded using a digital camera (Canon 550D).

Transmission electron microscopy (TEM) analysis, by employing a TEM CM

12 Philips equipped with CRYO-GATAN UHRST 3500e microanalysis technology, was conducted to characterize the morphology, structure as well as chemical composition of nanocomposite.

5.2.5 Standard tests for water repellents

The capillary water absorption tests of stone samples, both before and after surface coating, were carried out based on the standard method [118]. Results were processed and expressed as water inhibition efficiency (WIE) as aforementioned [114]. The vapor diffusivity variations of stones after treatment were evaluated according to standard "Cup" method [120], and results were reported as residual diffusivity percentage (RD, %). Additionally, the surface chromatic changes of substrates induced by coating were also examined by colorimetric analysis [122]. A portable X-Rite SP60 spectrophotometer operated in specular component excluded mode was exploited, and measurements on the specifically located spots on surfaces (the same positions before and after coating) were done. The color alteration (ΔE^*) was calculated by interpreting obtained results in CIE-L*a*b* standard color system as described in previous chapter.

5.2.6 Photocatalytic property assessment

The photocatalytic activity of coatings was evaluated by discoloration test of methylene blue (MB) under UV exposure. Since the nanocomposite coating

is superhydrophobic, MB was dissolved in ethyl alcohol rather than water, aimed to facilitate the distribution of MB on coated surface. The concentration of ethyl alcohol dispersion of MB is $1.37 \cdot 10^{-3}$% (w/w). To stain substrates, a pipette was used to depose dye dispersion on surface uniformly, and staining was stopped until obvious color difference was observed. After dye application, samples were left overnight in dark laboratory environment. Stained samples were first subjected to color measurement by spectrophotometer then sprayed with distilled water all over the surface and irradiated with a Spectroline Lamp (model ENF-260C/FE) with an emission wavelength at 365 nm (tube of 6 W) in UV-A range for 5 h (Figure 5.1). During the 5 h, color variations were analyzed by spectrophotometer (X-Rite SP60) at every hour. The photo-degradation of MB was estimated by overall color change ($D_{\Delta E^*}$) (Eq. 5.1), and meanwhile by discoloration of blue color (D_{b^*}) (Eq. 5.2) calculated after each hour.

$$D_{\Delta E^*} = \frac{|\Delta E_t^* - \Delta E_0^*|}{\Delta E_0^*} * 100 \qquad \text{(Eq. 5.1)}$$

$$D_{b^*} = \frac{|b_t^* - b_{MB}^*|}{|b_{MB}^* - b_0^*|} * 100 \qquad \text{(Eq. 5.2)}$$

In Eq. 5.1, ΔE_0^* is the average color change induced by MB application, while ΔE_t^* is the mean value of color variation measured after t (t= 1, 2, 3, 4, 5) hours of radiation under UV in comparison with the chromatic feature of surface before MB stain. b_0^*, in Eq. 5.2 is the average value of color coordinate b^* measured before MB stain, whereas b_{MB}^* means the mean value of after MB application and drying. b_t^* indicates the mean value of b^* after t hours of UV exposure.

Figure 5.1 MB stained and then water sprayed samples ready for UV radiation.

5.3 Results and discussion

5.3.1 Synthesis and characterization of nanocomposite

Under vigorous magnetic stirring, the preparation of nanocomposite was carried out by simply introducing activated TiO_2 nanoparticles into 2-propanol dispersion of Si-PFPE. In order to have superficial Ti-OH groups, the activation of TiO_2 nanoparticles is necessary. By slightly heating the mixture to 40 °C for 4-6 hours, nanocomposite formulation was obtained when no phase separation was seen. The synthetic procedures are schematically represented in Figure 5.2. As shown in Figure 5.2b, the compositions and structures of final nanocomposite could vary, due to unknown degree of polymerization of siloxanes and varied number of Ti-O-

Si bonding formed with one single TiO_2 nanoparticle.

Figure 5.3 shows the FT-IR spectra of Si-PFPE and Si-PFPE-TiO_2 nanocomposite, and the corresponding peak assignments are reported in Table 5.2. Generally, after the interaction with TiO_2, the positions of absorption bands of the characteristic amidic groups (i.e. ν_{N-H}, δ_{N-H}, $\nu_{C=O}$ and ν_{C-N}) and siloxane groups (ν_{Si-O}, δ_{Si-O}) remain relatively constant (Table 5.2). Besides, the broad absorption area of ν_{C-F} between 1400-900 cm^{-1} is also clearly perceivable.

The absorption position of Ti-O-Si bond, nonetheless, seems to be ambiguous and complicated, mainly due to its relatively weak intensity and the superimposition of Si-O-Si stretching vibrations (~1200-800 cm^{-1}). Since the paper published by Zeitler et al in 1957 [144], bands locate between 926 and 919 cm^{-1} are usually ascribed to stretching vibrations of Ti-O-Si linkages. Yet, other researchers have found later, owing to the varied number of Ti-O-Si bonds, varied physical phase of analyte (as solid, in dispersion etc.), chemical environment of Ti-O-Si bonds, and specific specie of surface Ti complex (e.g. bipodal, tripodal etc.), bands appear in the 960-925 cm^{-1} range can also be assigned to Ti-O-Si bonds [162-165]. In our case, the peak that locates at around 936 cm^{-1} (medium intensity) in the IR spectra of nanocomposite is ought to be attributed to the chemical bonding between siloxane and surface hydroxylized TiO_2. Similarly, the Ti-O-Si bonds of TiO_2-oligoamide obtained by reaction between the same coupling agent as for our nanocomposite (i.e.

APTMS) and TiO_2 nanoparticles were reported to have the IR absorption peaks at 933 or 945 cm^{-1}[161], which are in agreement with our assignment.

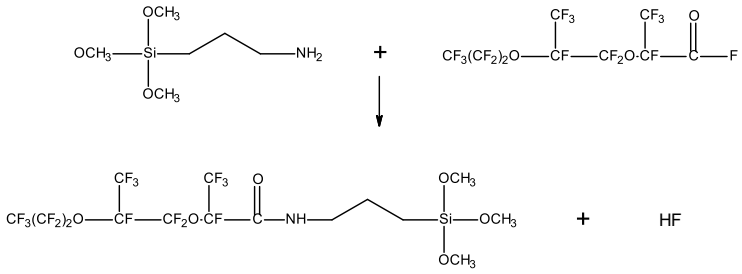

(a) Step one

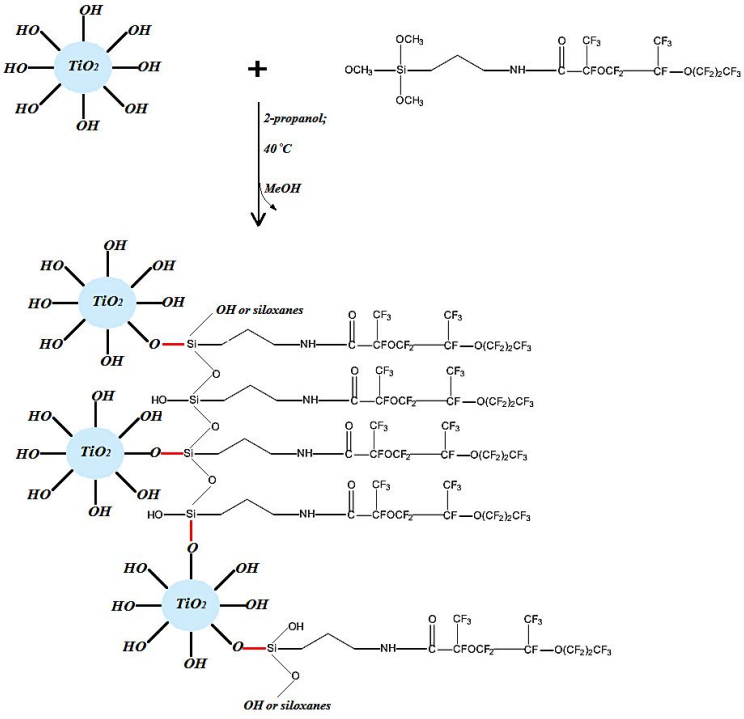

(b) Step two

Figure 5.2 Schematic representation of nanocomposite synthesis

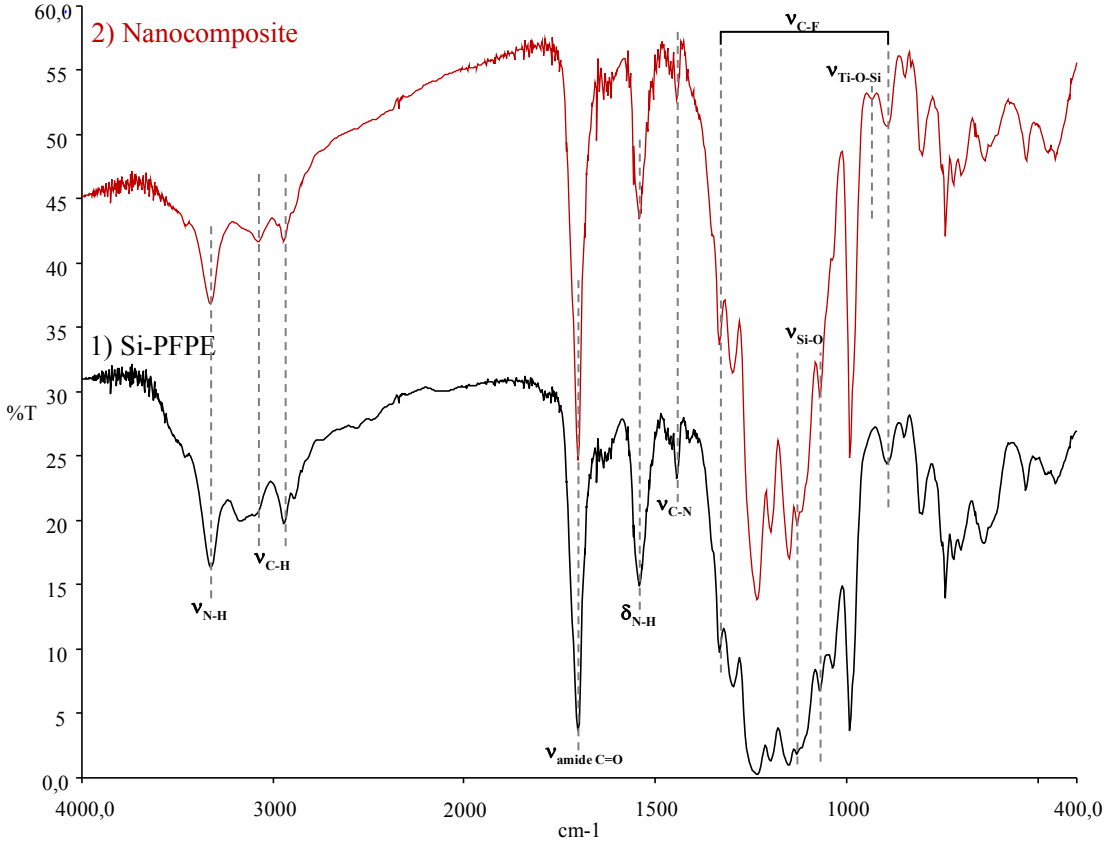

Figure 5.3 FT-IR spectra of 1) Si-PFPE and 2) nanocomposite (Si-PFPE/TiO_2 ratio 1/1) collected on KBr windows.

Table 5.2 Assignments of main FT-IR absorption peaks of Si-PFPE and nanocomposite.

Material	Absorption (cm^{-1})								
	ν_{N-H}	ν_{C-H}	$\nu_{C=O}$	δ_{N-H}	ν_{C-N}	ν_{C-F}	ν_{Si-O}	δ_{Si-O}	$\nu_{Ti-O-Si}$
Si-PFPE	3325(s)	3090(w); 2945(s)	1701(s)	1545(s)	1445(s)	1400-900(s)	1132(m); 1071(s)	458(s)	/
Nanocomposite (ratio 1/1)	3329 (s)	3081(s); 2945(s)	1703(s)	1545(s)	1445(s)	1400-900(s)	1131(s); 1072 (s)	457(s)	936(m)

As shown in Figure 5.4a, it is clearly shown titania particles (size around 30 nm) are well embedded in dense siloxane matrixes which have size ranging from 10 to 200 nm. The spectrum in Figure 5.4c is the elemental composition of the central spot of Figure 5.4b., With the molar ratio Si-PFPE/TiO_2=1:1, TiO_2 nanoparticles are well dispersed in Si-PFPE matrix (Figure 5.4d). The titania nanoparticles do not aggregate, and their average lateral size is about 30 nm. With higher magnification applied (Figure 5.4e), surrounding the outer surface of partially cross-linked siloxanes (~1.5 μm in dimension) and between two aggregated siloxane moieties, there is a thin layer of uniformly distributed TiO_2 nanoparticles, indicating effective chemical interaction (Si-O-Ti linkages formation). The morphology of nanocomposite obtained with molar ratio 2/3 is depicted in Figure 5.5a. With a higher amount of TiO_2 employed in synthesis, TiO_2 nanoparticles tend to aggregate occasionally, forming aggregation with dimension larger than 200 nm. Results of chemical analysis are also in agreement with their relative amounts (Figure 5.5b), since Ti is much more abundant than Si in the area of Figure 5.5a.

The Structure and morphology revealed by TEM analysis confirms the uniform and effective interaction between the two phases i.e. titania nanoparticles and Si-PFPE, since there is no apparent phase separation (especially in nanocomposite with ratio 1/1).

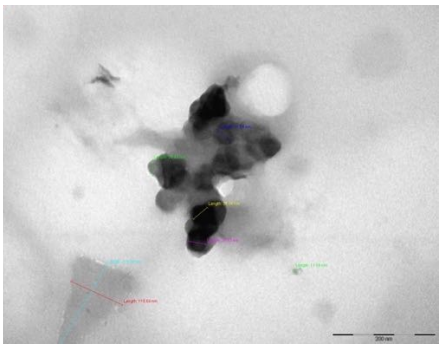

(a)

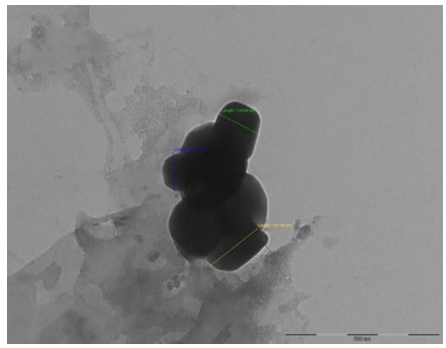

(b)

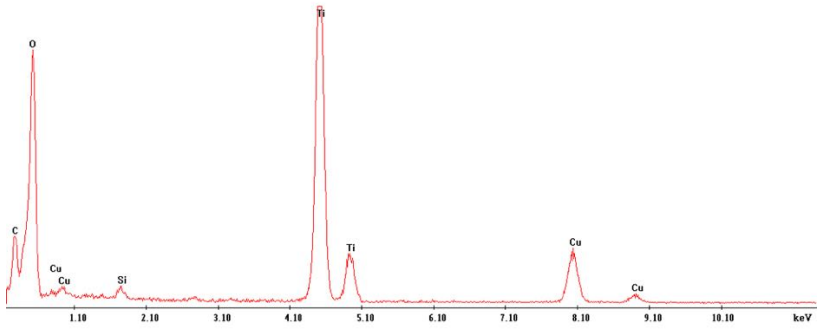

(c)

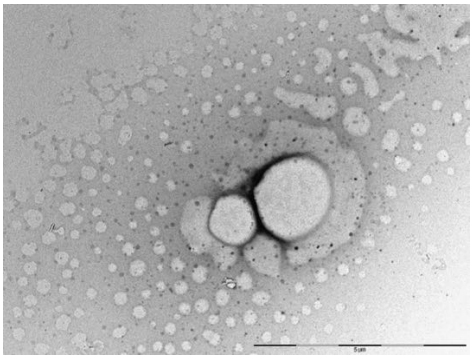

(d)

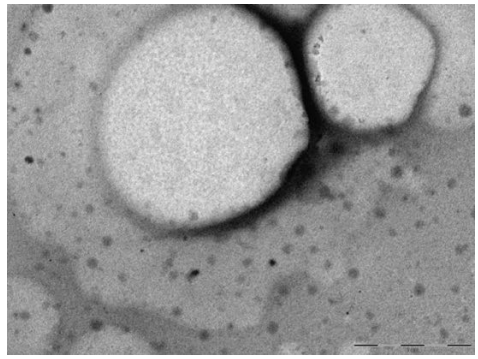

(e)

Figure 5.4 TEM images of Si-PFPE-TiO_2 nanocomposite (ratio 1/1) (a, b, d, e), and corresponding EDS spectrum of the central spot of image b (e).

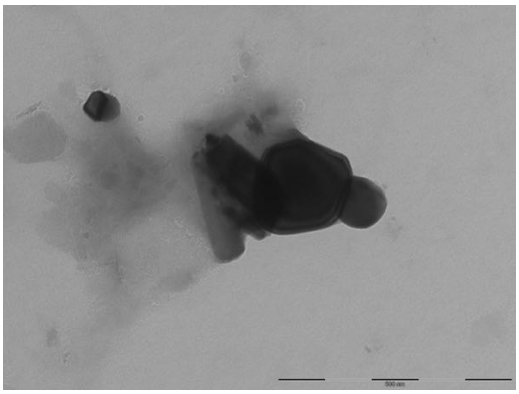

(a)

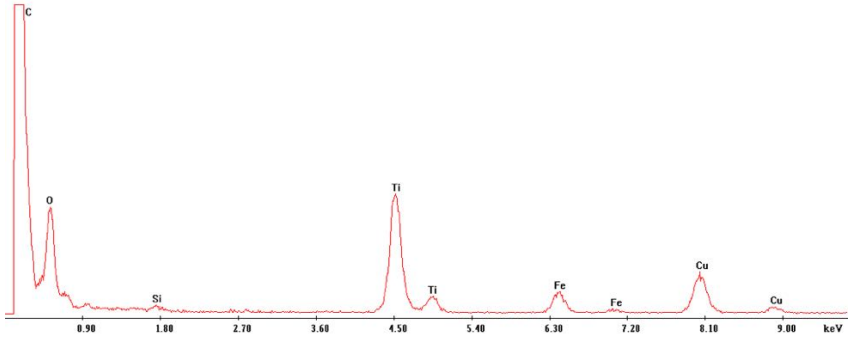

(b)

Figure 5.5 TEM images of Si-PFPE-TiO_2 nanocomposite (ratio 2/3) (a), and corresponding EDS spectrum of its central area (b).

5.3.2 Wetting properties and morphologies

- **Si-PFPE-TiO_2 nanocomposite (ratio 1/1)**

Figure 5.6 is the plot of water CA and CAH measured on coated stone substrates. It is apparent, superhydrophobicity was achieved on all types of substrates after treating with Si-PFPE-TiO_2. After treatment, the average

water CA have enormously increased from about 40° to higher than 150° (CA of virgin Lecce stone and marble were reported in Ref. n.40). Meanwhile, the CAH are also below 10°, fulfilling the requirements for defining a superhydrophobic coating with self-cleaning property. It shall be mentioned, superhydrophobicity was generated with relatively low amount of nanocomposite applied, i.e. 8.5 g/m^2, 12.8 g/m^2 and 5 g/m^{2}for marble, Lecce stone and sandstone respectively. The nanocomposite coating, specifically, shows the highest water CA and lowest CAH on marble and sandstone, being 157.6°, 8.3° and 157°, 7° respectively. Noticing that, the CAH and its standard deviation found on coated Lecce stone are relatively large (10±6.8°), the superficial coating is not very uniform which may be due to the low amount of dispersion which could not wet the surface uniformly and hence the heterogeneous distribution of product. As stated in previous chapters, the superhydrophobicity observed on nanocomposite coating is attributed to the synergistic effects of surface roughness at multiple scales (nano- to sub-micrometre roughness generated by TiO_2 nanoparticles) and low surface tension material (i.e. Si-PFPE).

Though the addition of TiO_2 nanoparticles into Si-PFPE, the water CA on Lecce stone and sandstone (i.e. 158.5° and 162.8° respectively, reported in Chapter IV) does not worsen due to the hydrophilic effect of titania, but TiO_2 nanoparticles are supposed to confer other important properties to the product e.g. photocatalytic, anti-biofouling properties which will be discussed in the following sections.

Furthermore, the ultra-repellency of nanocomposite coating is also verified by CA test using a series of complex water dispersion and emulsion systems such as black tea, coke, coffee and milk as liquid sources. In Figure 5.7 and 5.8, all the liquid drops are quasi spherical, indicating CA>150° or superhydrophobicity.

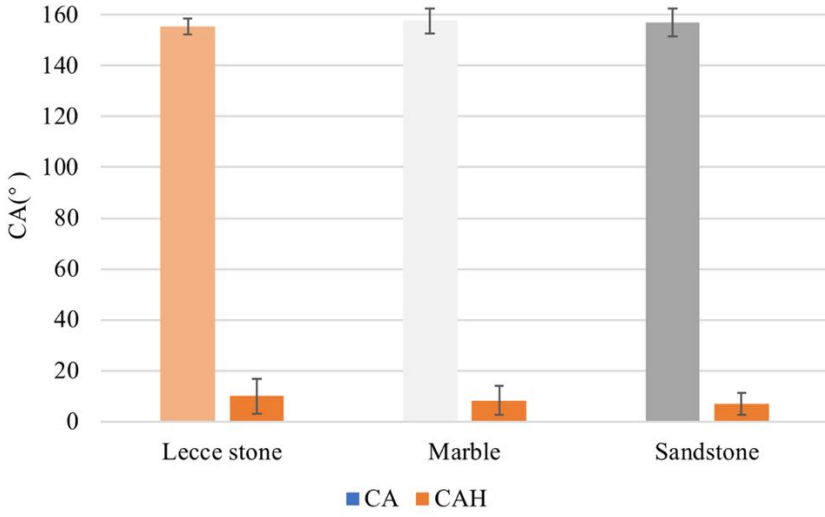

Figure 5.6 Water CA and CAH of coated Lecce stone, marble and sandstone samples coated with nanocomposite (ratio 1/1).

Figure 5.7 Digital image of water drops are coated marble surface coated with nanocomposite (ratio 1/1).

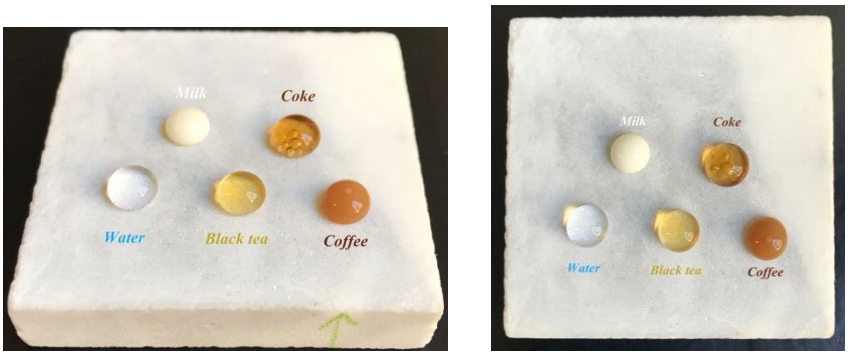

Figure 5.8 Water repellence of marble surfaces coated with nanocomposite (ratio 1/1) towards complex water emulsion and dispersion systems.

The self-cleaning behaviour of nanocomposite coating can be easily evidenced by dirt-removal test as shown in Figure 5.9. A nanocomposite coated marble surface was stained with dust. When water drops were in contact with stained surface at a proper sliding angle (≈10°), they tended to collect dirt, dust and meanwhile slid downside spontaneously. After releasing a certain amount of water, all dust and dirt were cleaned so that the stained surface regained its aesthetic characteristics.

- **N215-TiO_2 mixtures**

Unfortunately, superdrophobicity was not accomplished on stone substrates coated with any type of N215-TiO_2 mixtures (Figure 5.10). After treatment, the wetting property of both two substrates have been modified, being from hydrophilic to hydrophobic except on marble coated with "N215+TiO_2" (CA increased but still hydrophilic). Regarding Lecce stone, the highest water CA (134.2°, 126.1°) were observed on the coating "TiO_2+N215". The lowest

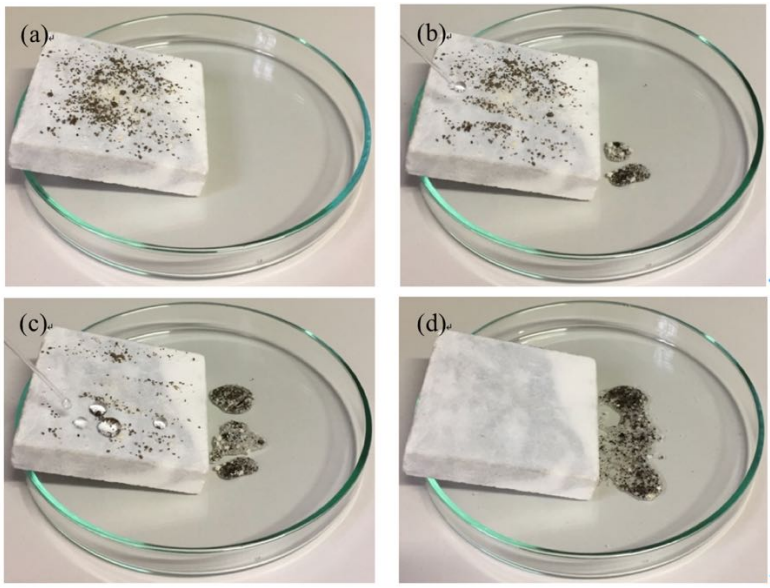

Figure 5.9 Dirt-removal test conducted on coated marble samples.

water CA (96.3°) measured is on the coatings which has a superficial layer of TiO_2, whereas the blend coating has an intermediate water CA (110.8°). Compared with pure N215 coating on Lecce stone (113°, Ref. n.40), hydrophobicity is improved when a layer of TiO_2 is added below N215, while it is impaired if an additional layer of TiO_2 is added above N215. These results are in accordance with what we have expected. Owing to the fact that TiO_2 is intrinsically hydrophilic, it effectively compromises the hydrophobicity of N215 effectively if TiO_2 is the outmost layer. On the contrary, if TiO_2 is applied firstly as the ground layer and N215 as the upper layer, the entire hydrophobicity of coating is enhanced due to the micro-roughness or multi-hierarchical roughness created by TiO_2 nanoparticles.

On coated marble samples, the “positive” and “negative” effects of TiO_2

nanoparticles are also well shown. Water CA is 89° on marble surface coated with pure N215 [40]. Due to the presence of TiO_2 nanoparticles as the uppermost layer, water CA decreased to about 82.6° on coating "N215+TiO_2". However, taking advantage of the multi-scaled surface roughness created by TiO_2 nanoparticles, water CA increased significantly to around 122.3° on coating "TiO_2+N215". On the surface treated with "N215-TiO_2 blend", water CA is similar to pure N215 coating, being 91.5°. This could be due to the heterogeneous nature of the blend in which the two phases were not effectively integrated.

5.3.3 Photocatalytic activity

- **Nanocomposite (ratio 1/1)**

The photocatalytic activity of the novel nanocomposite, blend and mixtures were assessed by evaluating their degradation efficacy of MB dye deposed on coated surfaces. The degradation efficiency expressed by the overall color change ($D_{\Delta E^*}$) is very intuitive (Figure 5.11). Despite of the same nanocomposite applied, it is well visible the photo-induced catalytic activity varied greatly on different substrates. After 5 h of UV exposure, about 90% of MB was discolorated on marble, yet the final degradation efficacy found on Lecce stone and sandstone was very low (~ 10%). The MB stain on marble decayed gradually with the increasing of time of UV radiation, starting from around 40% after 1 h to 90% after 5 h. However, there are not generalized trends of color change on treated Lecce stone and sandstone samples, and the

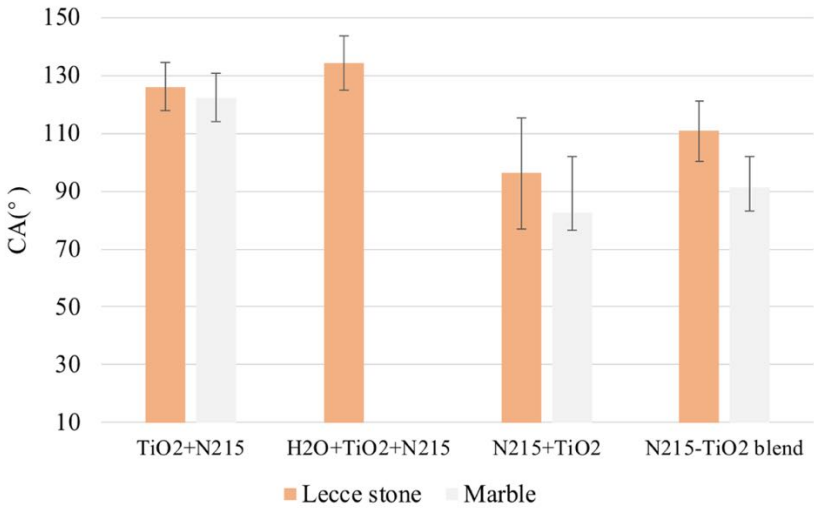

Figure 5.10 Water CA of Lecce stone and marble treated with different coatings.

$D_{\Delta E^*}$ fluctuated. After the first hour, no obvious color change was observed on Lecce stone and sandstone, since their $D_{\Delta E^*}$ values were below 10%. The peak $D_{\Delta E^*}$ values for both Lecce stone and sandstone appeared after 3 h, being 21% and 30% respectively. Their $D_{\Delta E^*}$ decreased afterwards and arrived at low values after 5 h (13 % and 5 % for Lecce stone and sandstone).

Likewise, the stain degradation efficacy represented by $D_{\Delta b^*}$ showed similar trend as $D_{\Delta E^*}$ on marble (Figure 5.12). Starting from lower than 40% after 1 h UV exposure, $D_{\Delta b^*}$ value experienced a progressive increase until 89% after 5 h. While for Lecce stone and sandstone their $D_{\Delta b^*}$ fluctuated in these 5 h and ended with very low values. Their $D_{\Delta b^*}$ values were almost all lower than 10%, except the values found after 3 h of radiation, being around 15%. It can be concluded that, the photocatalytic property is active on marble surface

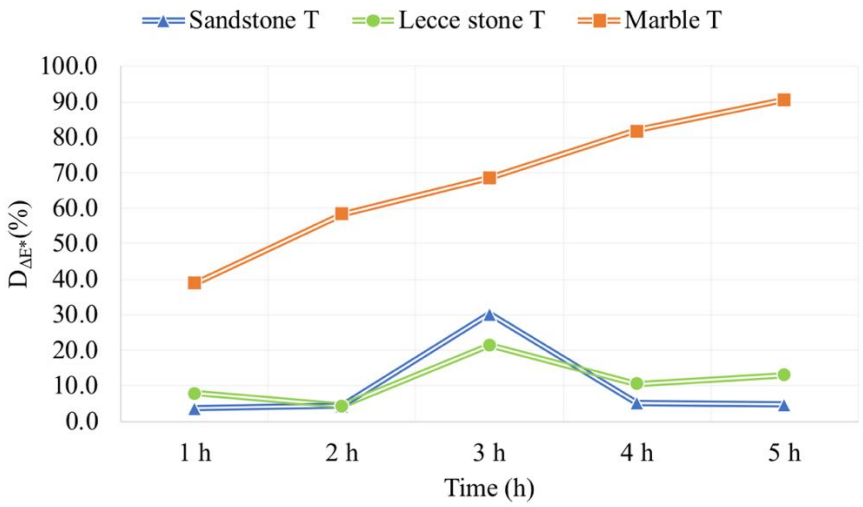

Figure 5.11 Degradation efficiency of MB over time (D) expressed as proportion of reduction of ΔE* values ($D_{\Delta E*}$) on surfaces coated with nanocomposite (ratio 1/1).

while it is not effective on Lecce stone and sandstone. Figure 5.13 reports the digital images of MB stained marble sample after 0 h 2 h and 5 h of UV radiation. After 5 h of UV radiation, MB dye decayed significantly, and the original texture and chromatic features of marble were recovered.

The possible reason for the varied photocatalytic activity observed on marble, Lecce stone and sandstone could be principally attributed to the distinct physical characteristics of these stones and the resulted spatial distribution of TiO_2. With very low porosity and small pore size, Carrara marble is a very compact stone, and its surface is smoother than the other two types of stones. Once applied as suspension, the nanocomposite particles (probably

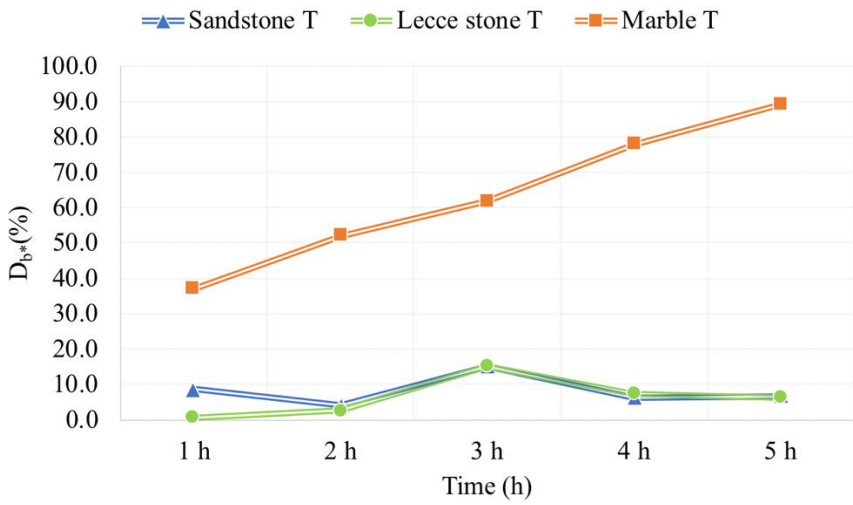

Figure 5.12 Degradation efficacy of MB over time (D) expressed as percentage of reduction of b* values (D_{b^*}) on surfaces coated with (ratio 1/1).

are not able to penetrate inside pores (< 1μm), and the majority remained on the surface. Conversely, Lecce stone and sandstone have higher porosity and larger pores which are favourable for the penetration of nanocomposites during surface treatment, thereby reducing the amount of TiO_2 nanoparticles on surface. The varied amounts and distribution of TiO_2 present on the surface are the predominant reasons for the photocatalytic activity variation. Moreover, due to the specific physical characteristics of Lecce stone and sandstone, MB penetrated inside the bulk sample rather than remaining on the surface (such as on marble) once its solution was deposed. The photo-catalytic ability of nanocomposite was greatly compromised when the UV radiation could not reach the MB dye which was at a certain depth beneath the sample surface. Additionally, the presence of water on the surface is of

relevant importance for the photo-catalytic reaction: marble remained wet for longer time than Lecce stone and sandstone.

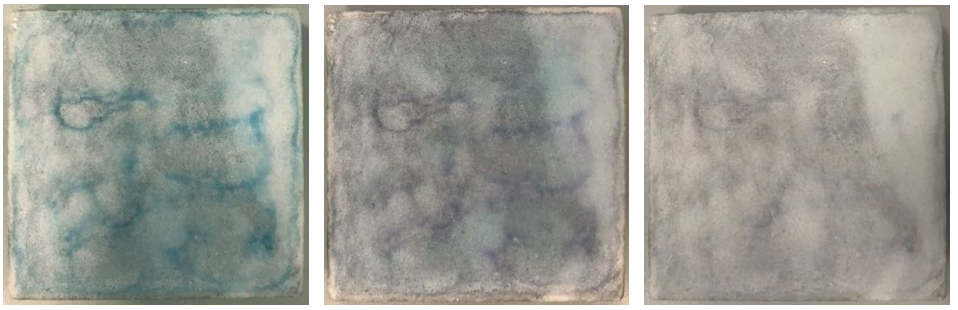

(a) (b). (c)

Figure 5.13 Digital images of MB stained marble sample which was previously coated with nanocomposite after 0 h (a), 2 h (b) and 5 h (c) of UV radiation.

- **N215-TiO_2 mixtures**

Figure 5.14 and 5.15 show the degradation efficacy of N215-TiO_2 mixtures found on marble samples. Considering $D_{\Delta E^*}$ firstly, these mixtures worked effectively as photo-catalysts, yet their efficacy differed. All coatings experienced a general increasing of degradation efficacy along with radiation time. Among all, coating "N215+TiO_2" showed the highest $D_{\Delta E^*}$ among all mixtures, with $D_{\Delta E^*}$=57% after 5-hour UV radiation. The $D_{\Delta E^*}$ of "N215+TiO_2" started with less than 20% after the first hour, and it increased progressively in the following 4 hours. The $D_{\Delta E^*}$ of coating "TiO_2+N215" was the second highest, being around 30% after 5 h. The least effective one was the coating "N215-TiO_2 blend" which showed the final $D_{\Delta E^*}$ about 20%. When the discoloration efficacy was represented by D_{b^*}, higher values than their $D_{\Delta E^*}$ counterparts were observed for all coatings at the end of test.

Besides, the evolution profiles of D_{b*} were also similar to that of $D_{\Delta E*}$, and they boosted gradually with time. Likewise, started from about 30% after the first hour, D_{b*} of coating "N215+TiO_2" arrived to around 70% at the end of test, which was also the highest among all. Increased step-by-step, coatings "TiO_2+N215" exhibited also high degradation efficacy ($D_{b*} \approx$ 60%) after the 5 hours. It is notified, though coating "N215-TiO_2 blend" seemed to be not photo-catalytically effective if we consider only $D_{\Delta E*}$, it had a decent D_{b*} value ($D_{b*} >$ 60%) meanwhile. However, simply by visual inspection, it was clear that the marble sample coated with coating "N215-TiO_2 blend" was still bluish after UV radiation, indicating the ineffectiveness of coating. These results are in agreement with our expectation, in which coating "N215+TiO_2" should be the most efficient photo-catalyst among these three coatings, owing to its superficial TiO_2 layer which is in charge of the photo-catalysis.

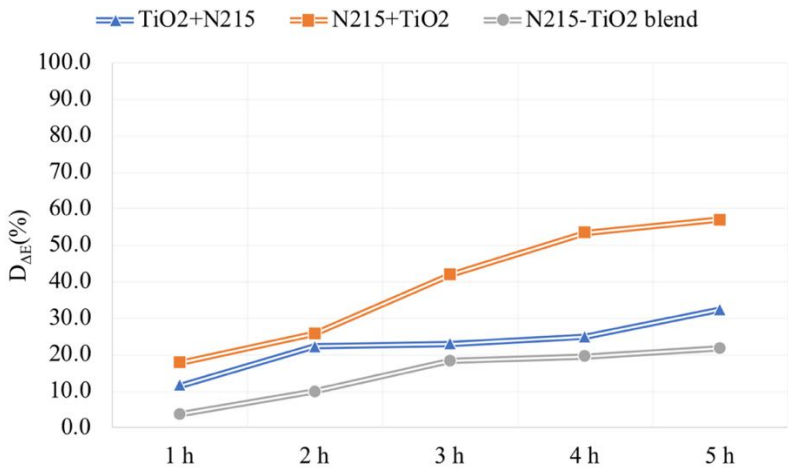

Figure 5.14 Degradation efficiency of MB observed on marble samples, coated with varied N215/TiO_2 systems, over time (D) expressed as proportion of reduction of ΔE* values ($D_{\Delta E^*}$).

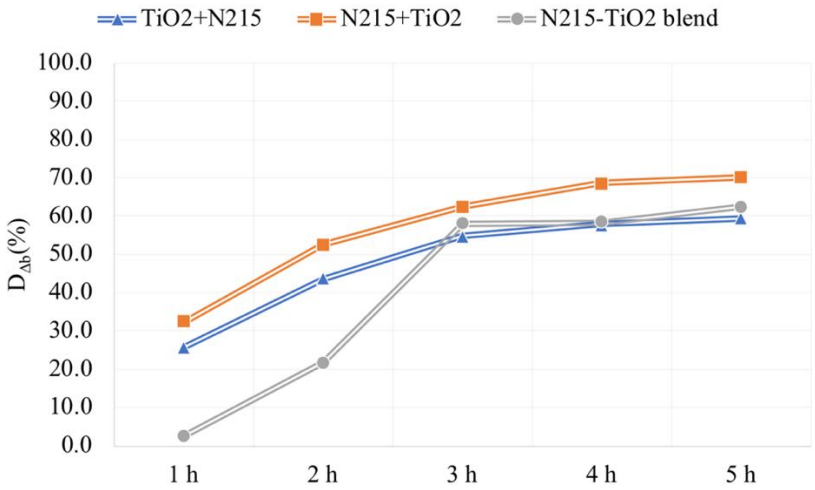

Figure 5.15 Degradation efficiency of MB observed on marble samples, coated with varied N215/TiO_2 systems, over time (D) expressed as proportion of reduction of Δb* values ($D_{\Delta b^*}$).

On the other hand, N215-TiO_2 mixtures are not photo-catalytically active when applied on Lecce stone samples. Discoloration efficacy expressed as both $D_{\Delta E^*}$ and D_{b^*} were very low, being below 10% for all coatings (Figure 5.16 and 5.17). Having explained previously and similar to Lecce stone samples coated with nanocomposite, photo-catalytic discoloration was not working because UV radiation was not able to reach the depth where it was stained by MB. Neglecting the inaccurate color coordinate "L", coating "N215-TiO_2" manifested slightly higher D_{b^*} (D_{b^*}= 9%) than the other

coatings while coating "N215-TiO_2 blend" had the secondly highest (D_{b*}= 6%). These results are also in agreements with the theoretical results above mentioned (i.e. surface TiO_2 layer accounts for photo-catalysis). In Figure 5.18c, the MB stained surface is still bluish after 5 h of UV radiation

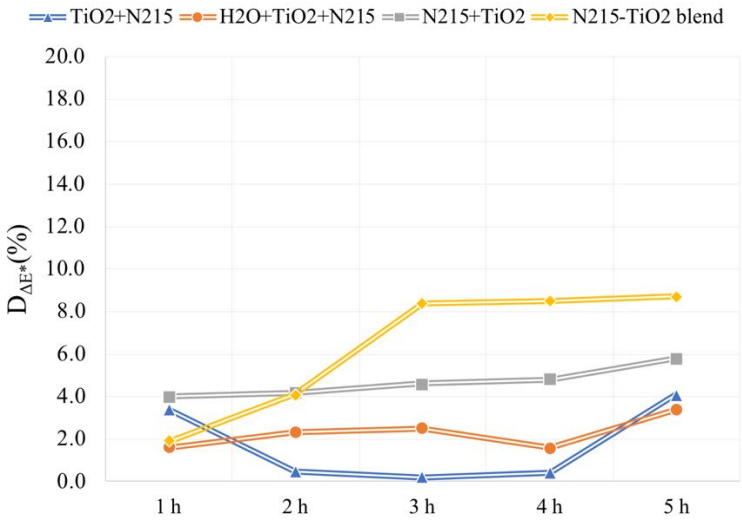

Figure 5.16 Degradation efficiency of MB observed on Lecce stone samples, coated with different N215/TiO_2 systems, over time (D) expressed as percentage of reduction of ΔE* values ($D_{\Delta E*}$).

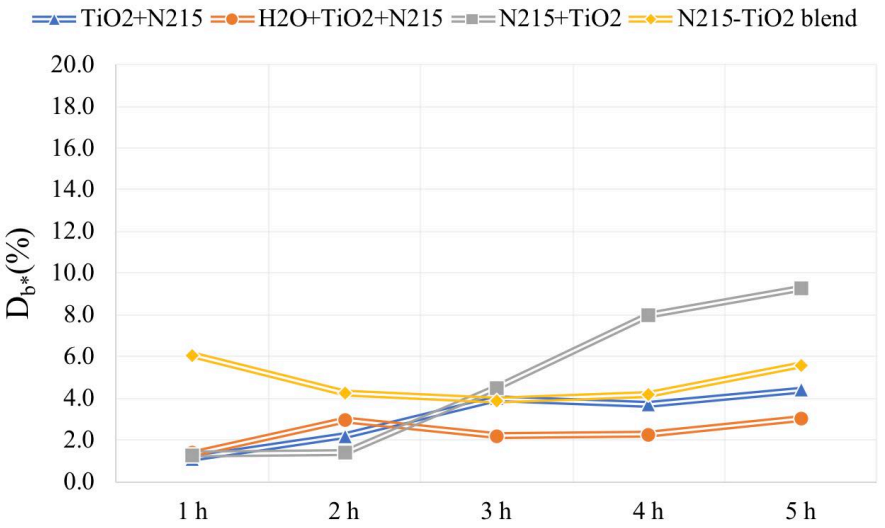

Figure 5.17 Degradation efficiency of MB observed on Lecce stone samples, coated with different N215/TiO_2 systems, over time (D) expressed as percentage of reduction of Δb* values ($D_{\Delta b^*}$).

(a) (b) (c)

Figure 5.18 Digital images of MB stained Lecce stone sample which was previously coated with "TiO_2 +N215" after 0 h (a), 2 h (b) and 5 h (c) of UV radiation.

5.3.4 Performance as water repellents

- **N215-TiO_2 mixtures**

The WIE of N215-TiO_2 systems tested on Lecce stone samples is shown in Figure 5.19 In accordance to their water CA, coatings "TiO_2+N215" and "H_2O+TiO_2+N215", which manifest higher water CA, show also higher WIE values than the other mixtures in 2-hour test. In particular, coating "TiO_2+N215" has the highest WIE values among all, being 79% and 49% after 1 h and 2 h test respectively. Though coating "H_2O+TiO_2+N215" are more hydrophobic than coating "TiO_2+N215", its WIE values are lower, being 65% and 17 % after 1 h and 2 h test respectively. These two coatings show similar WIE values as pure N215 coatings (66% and 48%, Ref. n.40). They can prevent capillary water absorption and penetration mediocrely in the first hour, yet, WIE decreased evidently in the second hour. The other two coatings, "N215+TiO_2" and "N215-TiO_2 blend", are not effective for protecting Lecce stone since their WIE values are all below 30%. It is noticed, these coatings actually show not low water CA i.e. 96.3°, 110.8° for "N215+TiO_2" and "N215-TiO_2 blend" respectively, but the water CA does not guarantee effective water protection ability. The main reason lies on the measuring mechanisms of static water CA and water capillary absorption. The static water CA was measured point by point (5 points each sample) and instantly, while water capillary absorption test was carried out for much longer time e.g. 1 h, 2 h. In fact, a decent protective coating requires uniformly distributed coating material which means no defects shall exist and the entire surface shall be equally hydrophobic. However, high static water CA only

represents the high hydrophobicity of measured points or small area on surface. Once the whole surface is in contact with capillary water, the coating defects are wetted by water, and the overall WIE is not high. In our case, coating "N215+TiO_2" and "N215-TiO_2 blend" are not uniform on stone samples as I already realised during coating fabrication. For coating "N215+TiO_2", applying an additional layer of nano-TiO_2 on hydrophobic N215 coating was difficult, and the distribution of nano-TiO_2 was heterogeneous which can be known from surface whiteness difference. On the other hand, coating "N215-TiO_2 blend" underwent serious phase separation during preparation, which resulted in not uniform coating. These coatings that have micro-defects on surface are not efficient protective coatings.

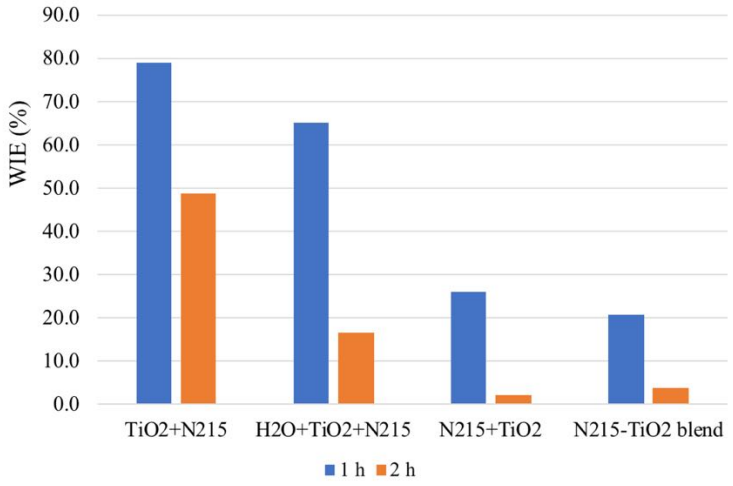

Figure 5.19 WIE of N215-TiO_2 systems found on Lecce stone.

On marble surface, likewise, coating "N215-TiO_2 blend" is not able to inhibit capillary water penetration and it exhibits the lowest WIE values among all,

i.e. 14% and 7% after 1 h and 2 h respectively (Figure 5.20). The main reason is the not uniform coating formed. The other two coatings i.e. "TiO_2+N215" and "N215+TiO_2", have equivalent WIE values in 2-hour test. On the contrary to the relatively lower CA found on "N215+TiO_2", its WIE after the first hour is the highest among three coatings, being 78%. This is another example showing that the static water CA can not represent the overall hydrophobicity of a surface. Coating "N215+TiO_2" have decent hydrophobicity all over the surface, and hence decent water inhibition efficacy upon capillary absorption. After 2 hours of capillary absorption, coating "TiO_2+N215", which is expected to be more hydrophobic show slightly higher WIE value than "N215+TiO_2", being 68% and 64% for "TiO_2+N215" and "N215+TiO_2" respectively. Compared with their WIE found on Lecce stone, coatings "TiO_2+N215" and "N215+TiO_2" are more effective for the protection of marble, since they can prevent water penetration also for longer time (WIE> 60% after 2 h).

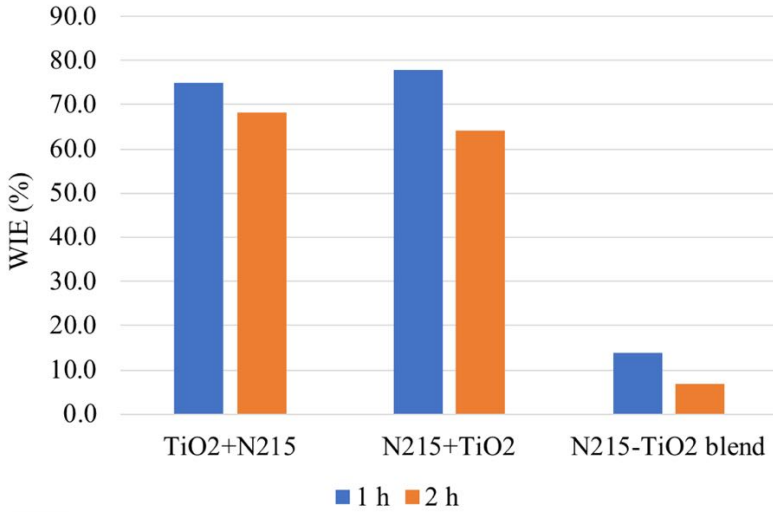

Figure 5.20 WIE of N215-TiO_2 systems found on Marble.

Besides water inhibition efficacy, another important criterion for evaluating water repellents is the residual vapor diffusivity. The RD parameter gives us a rough idea on to what extent the original pores, pore structures of substrates have been modified (or damaged) by the coating material. It is well recognised that, if stone loses its vapor diffusivity after surface treatment, the degradation process initiated by inner water condensation (on hydrophobic film) and other water-related processes could be accelerated. The RD data of Lecce stone and marble samples treated with N215-TiO_2 systems is shown in Figure 5.21. With the lowest RD found on coating "H_2O+TiO_2+N215" (90%), the RD of coated Lecce stone samples are all above 90%, indicating a good maintenance of the original porosity and pore structures after treatment. The amounts of N215-TiO_2 applied on Lecce stone (< 20 g/m^2) did not induce conspicuous pore blockage on high porous Lecce stone. On the other hand, though the amount of N215-TiO_2 applied on marble is the same (6.0 g/m^2), they show varied permeability to water vapor. "TiO_2+N215" has the highest RD (94%) and RD of coating "N215-TiO_2" is intermediate (80%), while coating "N215-TiO_2" has blocked a significant number of pores and the RD is as low as 36%. These properties are closely related to the physical-chemical characteristics of the coating materials, and the detailed discussion will be presented in the following part together the RD results of Si-PFPE-TiO_2 nanocomposite.

Additionally, the surface color changes induced by N215-TiO_2 mixtures were also estimated (Figure 5.22 and 5.23). It is clear, coating "N215-TiO_2 blend"

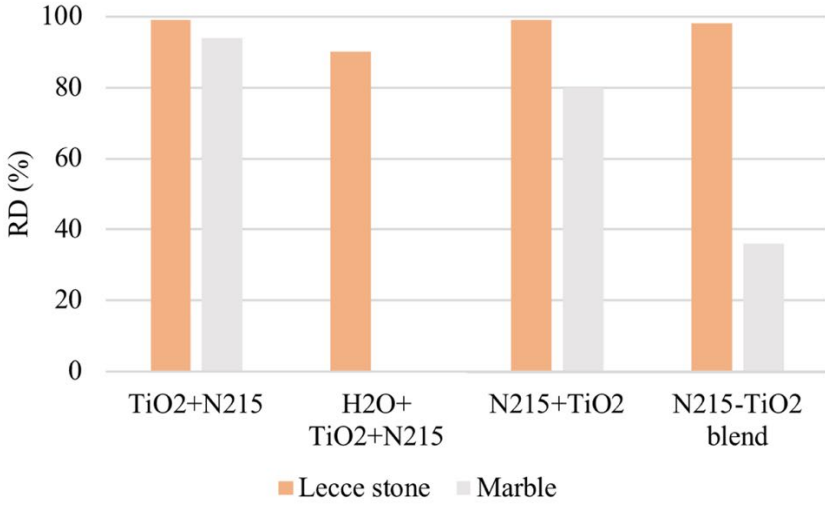

Figure 5.21 Residual vapor diffusivity of stone samples coated with TiO_2 and N215 systems

has modified the original chromatic features of Lecce stone, since the overall color change (ΔE=4) is beyond the detection limit of naked human eyes (ΔE=3). With ΔL*=3, Lecce stone became whitish after coating with "N215-TiO_2 blend". This whitening effect could also be attributed to the obvious phase separation between N215 polymer and TiO_2 nanoparticles. Unlike the heterogeneous mixture, "N215-TiO_2 blend", other coating mixtures well maintained the color effects of Lecce stone, since their ΔE values are smaller than 3. Owing to the intrinsic whitish features of marble, N215-TiO_2 mixtures did not change its surface color effects. Similar to its behaviour on Lecce stone surface, the most evident color change found was also caused by coating "N215-TiO_2 blend". Fortunately, this slight color change is hardly discernible (ΔL*=2, ΔE=3).

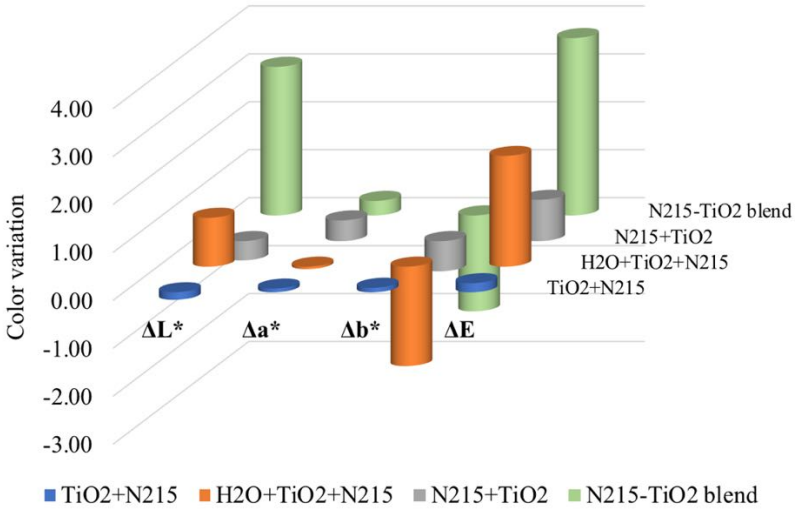

Figure 5.22 Color variation of Lecce stone samples treated with N215-TiO_2 systems.

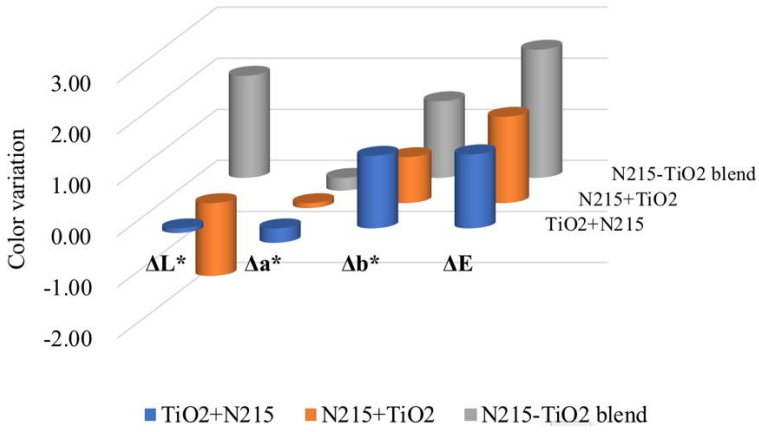

Figure 5.23 Color variation of marble samples coated with N215-TiO_2 systems.

- **Si-PFPE-TiO_2 nanocomposite**

In general, in comparison with N215-TiO_2 mixtures, Si-PFPE-TiO_2

nanocomposite demonstrates overall better water inhibition efficacy on all three types of substrates (Figure 5.24). In specific, the best performance of nanocomposite was found on marble, with all WIE values ≥88% for 4-hour test. In the first and second hour of capillary absorption test, nanocomposite coating shows very high protective efficacy on marble and the corresponding WIE are all above 90% (i.e. 91%; 91%). Good water prevention efficiency was also observed on sandstone, and the measured WIE values are 85%, 82% and 81% after 1 h, 2 h and 3 h of test respectively. In the 2-hour test conducted on Lecce stone samples, the WIE values are 77% and 57% after 1 h and 2 h of test respectively. Though these values are not very high, they are comparable with the "best" N215-TiO_2 mixture (coating "TiO_2+N215"; WIE: 79%, 49%).

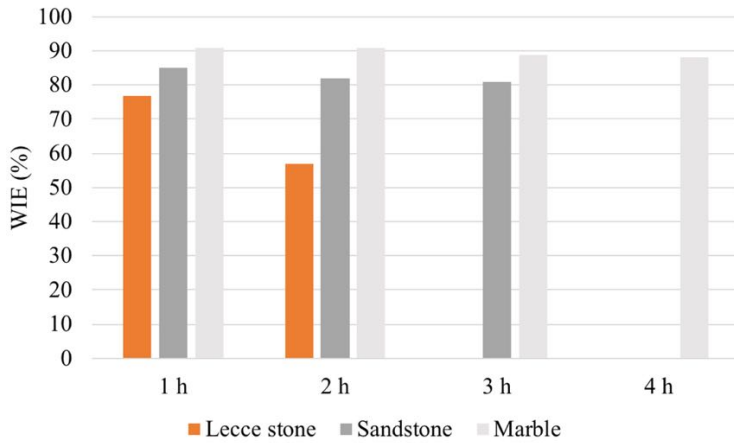

Figure 5.24 WIE of nanocomposite on various substrates.

However, it is notified that, since the overall color change (ΔE*) is higher than the detection limit of naked human eyes, perceivable color changes have

been induced on Lecce stone and sandstone by nanocomposite coating. On coated Lecce stone samples, the original chromatic feature has been modified apparently (ΔE=12). The surface is whitish and blueish, as evidenced by the obvious increasing of L value (ΔL*=7) and decreasing of b value (Δb*=-9) (Figure 5.25). Similarly, sandstone samples have also lost its original color features after coating (ΔE=8.6), and they become whitish and blueish too (ΔL*=8 and Δb*=-4) (Figure 5.26). Whereas, on coated marble surfaces, the original color characteristics are well preserved, since the overall color change is less than 3 (ΔE=3) (Figure 5.27). A slightly whitening effect (ΔL*=3) does not cause visible color change. As a matter of fact, since TiO_2 nanoparticles which have a strong white color are incorporated in the nanocomposite, the as-fabricated coating will be undoubtedly whitish to some extent. Regarding the application with such nanocomposite, it is of vital importance to adjust properly the concertation, amount of coating material, as well as a good selection of stone substrates (white to light grey stones are preferred).

Last but not least, the vapor diffusivity reduction induced by nanocomposite coating was also evaluated. As shown in Figure 5.28, after surface coating, the vapor diffusivity of both Lecce stone and marble are 98%, meaning their original pore structures are not damaged by nanocomposite. Although the amount of nanocomposite applied (8.5 g/m^2) is higher than the N215-TiO_2 systems (6.0 g/m^2), nanocomposite coating is more permeable to water vapor

than “TiO_2+N215”, “N215+TiO_2” and “TiO_2-N215 blend” coatings (Figure 5.21). It should be mentioned, unlike “N215+TiO_2” and “TiO_2-N215 blend” coatings, “TiO_2+N215” coating preserved the vapor diffusivity well (RD=94%, Figure 5.21). The main reason accounting for the higher RD values of Si-PFPE-TiO_2 nanocomposite than TiO_2-N215 mixtures is ought to ascribed to the fact that, the nanocomposite is more chemically homogenous (evidenced by TEM analysis) than the two different layers of coatings or blend (phase separation exists), which leads to uniform distribution all over marble surfaces. Additionally, the higher RD of “TiO_2+N215” than “N215+TiO_2” and “TiO_2-N215 blend” coatings is owing to the fact that, when marble surface was coated with a hydrophobic layer (i.e. N215 coating) firstly, the subsequent TiO_2 coating (in “N215+TiO_2” and “TiO_2-N215 blend” coatings) could not penetrate inside the bulk and remained mostly on surface, thus blocking the pores accessible.

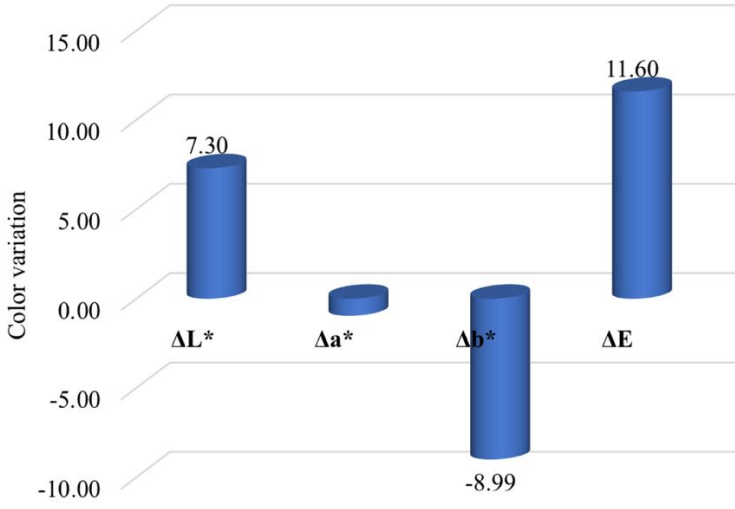

Figure 5.25 Color variation on Lecce stone samples induced by nanocomposite coating.

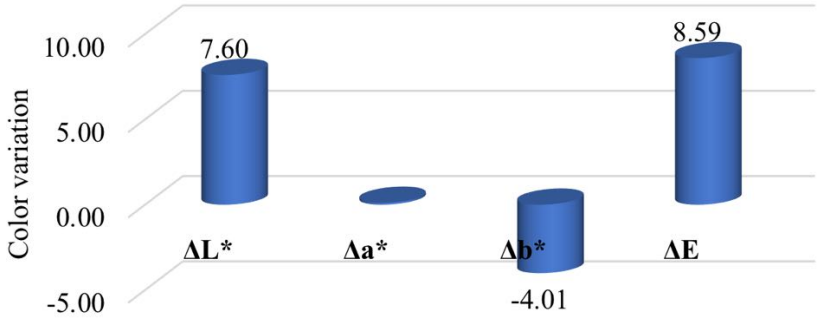

Figure 5.26 Color variation on sandstone samples induced by nanocomposite coating.

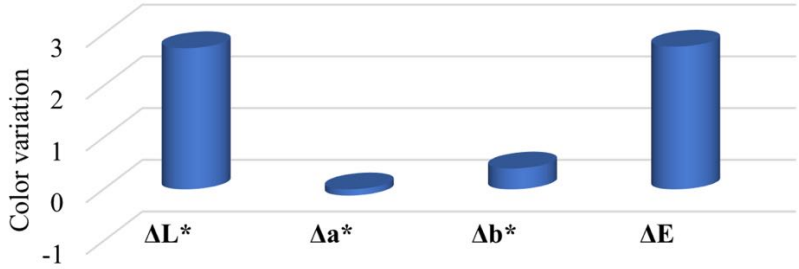

Figure 5.27 Color variation on marble samples induced by nanocomposite coating.

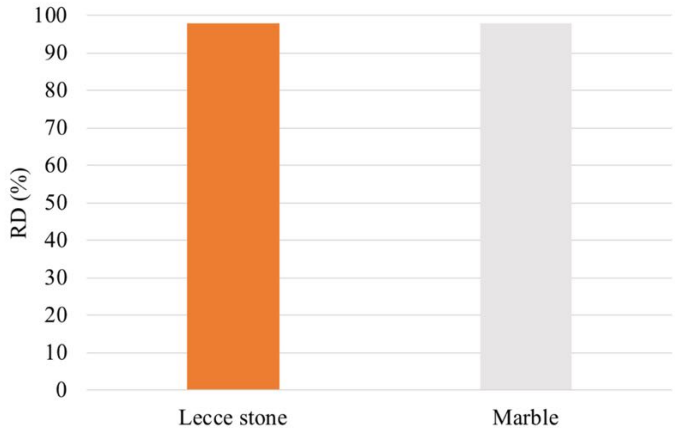

Figure 5.28 Residual vapor diffusivity of samples coated with nanocomposite coating.

5.4 Conclusion

A hybrid nanocomposite based on fluorinated siloxane and TiO_2 nanoparticles was prepared under sonicating and moderate heating for short time. The effective chemical bonding between siloxane and titania nanoparticles (Si-O-Ti linkages), as well as its morphology and structure are confirmed by FT-IR and TEM analyses. The absence of phase separation in nanocomposite with ratio 1/1 is approved by TEM analysis. Simply brushing or deposing (using a pipette) its alcoholic suspension, superhydrophobic, self-cleaning surfaces (water CA>150° and CAH<10°) are easily created on building stones with both high and low porosities i.e. Lecce stone, sandstone and marble. The self-cleaning property is further verified by dirt-removal test. Furthermore, nanocomposite coating also demonstrates super-repellent to complex water dispersion and emulsion systems.

In order to better evaluate the performance of nanocomposite as water repellent and as photo-catalyst, three other coatings composed of a commercial fluoroelastomer and the same the type of TiO_2 nanoparticles (i.e. coatings "N215+TiO_2", "TiO_2+N215"and "N215-TiO_2 blend") were also applied and tested on the same stone materials. The amount of the fluorinated

fraction (i.e. Si-PFPE; N215) and the amount of TiO_2 nanoparticles of nanocomposite and N215-TiO_2 mixtures were intentionally kept identical. Regarding the performance as water repellent for low porous stone (i.e. marble), nanocomposite shows overall better WIE than N215-TiO_2 mixtures (WIE=88% after 4-h test). The N215-TiO_2 systems are less effective in inhibiting water penetration for marble, with the highest WIE=68% found on "TiO_2+N215" after 2-h test. Additionally, nanocomposite coating also preserves the original residual diffusivity and surface color features of marble samples. Concerning its the performance on high porous Lecce stone, nanocomposite also exhibits higher water inhibition efficacy (WIE=57% after 2-h test) than the best coating of N215-TiO_2 mixture i.e. "TiO_2+N215". Nanocomposite does not cause pore blockage of Lecce stone, but Lecce stone samples are a little bit whitish after coating due to the presence of TiO_2 nanoparticles. It is noticed as well, on the basis of the hydrophobicity (water CA) and water inhibition capability observed on the three types of N215-TiO_2 mixture coatings, the following conclusions can be drawn. Compared with pure N215 coating, the hydrophobicity of mixed coatings is enhanced when a layer of TiO_2 is added below N215, while it is compromised if an additional layer of TiO_2 is added above N215. WIE measured by means of capillary absorption test is a more accurate and objective parameter than water CA test, when it comes to the evaluation of water repellence.

Moreover, as regards to photo-catalytic activity, on Lecce stone, neither nanocomposite nor N215-TiO_2 systems show decent activity owing to the fact

that MB dye penetrated and resided beneath the surface where UV radiation could not reach. Whereas, on marble, in comparison with N215-TiO_2 mixtures which manifest limited activity (the highest D_{b*}=70% after 5-h test for coating "N215+TiO_2"), the nanocomposite has much better performance ($D_{\Delta E*}$=90% and D_{b*}=89% after 5-h test). Another finding regarding N215-TiO_2 mixed coatings is, photo-catalytic activity is governed by the superficial TiO_2 layer. As a matter of fact, the surface TiO_2 layer is a double-edged sword for N215-TiO_2 mixed coatings, since on one hand it accounts for the photo-catalytic activity while it blemishes the hydrophobicity on the other hand.

To my best knowledge, it is the first time that a photo-catalyst, which also have superhydrophobicity and self-cleaning capability is ever proposed for the safeguard of building stones. Equipped with such promising properties, the hybrid nanocomposite is a good candidate as water repellence, anti-biofouling and anti-pollution coating agent for stone materials, in particular stones with white to grey colors.

Chapter VI

Conclusions

Since the general aim of the thesis is synthesis, characterization and performance testing of new partially fluorinated compounds, three categories of products, i.e. partially fluorinated oligoamides, fluorinated siloxane and hybrid nanocomposite, which show promising properties and satisfying performance have been presented. Some of these coating materials are potential artificial bioinspired super-antiwetting agents for wide applications which include protective coating for stone artworks. In specific, the coatings fabricated with partially fluorinated oligoamides, predominantly partially fluorinated oligosuccinamide and oligosuberamide, exhibit superhydrophobicity (water CA>150°) and near superoleophobicity (oil CA>140°) together with high adhesive property to water droplets. These properties resemble the "Petal effect" in nature. Yet, surface prepared with fluorinated siloxane is very slippery while being superamphiphobic (water, oil CA>150°, water CAH<10°), mimicking the so called "Lotus effect". Moreover, the hybrid nanocomposite coating is also photo-catalytically active in addition to being superhydrophobic and self-cleaning. As a whole, the original aim of the PhD research has been accomplished.

On the basis of the results stated and discussed in previous chapters, the following conclusions regarding: 1) the synthetic procedure and effectiveness

in obtaining products; 2) properties and performance of newly acquired products as water repellents for building stones and/or as photo-catalysts; 3) potential applications in build heritage conservation and other fields, can be drawn.

- **Partially fluorinated oligoamides**

By adjusting the molar ratios between diethyl suberate and ethylenediamine (i.e. diethyl suberate/ethylenediamine ratio= 1/2, 1/3, 1/5), oligosuberamides with varied number average molecular weights were synthesized. With relatively low number average molecular weights (~300 g/mol), oligosuberamides have good solubility in alcoholic and hydro-alcoholic solvents at room temperature. Among all these three oligosuberamides, SubC2 (1:3) which was synthesized with the shortest reaction time (12 h) and the highest yield (72%), was also found to be the purest by ^{1}H-NMR spectroscopy. Compared with previous SucC2 and ADC2 syntheses, the synthesis of SubC2 (1:3) took longer time than SucC2 (1:2) (7 h) while shorter time than ADC2 (1:5) (> 40 h), and the main reasons are: 1) the different molar amounts of ethylenediamine added (larger the amount, longer the reaction time); 2) the varied solubility of oligoamides in the solvent used for synthesis; 3) differed lengths of the chain of diethyl succinate/adipate/suberate (e.g. varied possibility to form intra/inter-molecular hydrogen bonding between NH of amidic groups and C=O of carbonyl or of not reacted carboxylic groups). SubC2 shows better solubility percentage at 1% (w/w) solute/solvent in common organic solvents than

SucC2 and ADC2. In the second step, adopting fixed molar ratio (SubC2/ester of PFPE=1/2), FSB (1:3) and FSB (1:5) were obtained with high yields. After uniting with perfluorinated chains, the bond energy of the amidic groups (amide I) of oligsuberamides has enhanced, as evidenced by shifting of the absorption band towards higher wavenumber in FT-IR spectra. Though FSB has similar molecular weight (~2000 g/mol) as FSC and FAD, owing to the relatively longer alkyl chains (i.e. oligosuberamides) which are more capable to balance the insoluble nature of PFPEs, FSB exhibits better solubility than the other two homologous compounds in common solvents at room temperature.

Regarding the properties of these coatings, superhydrophobic and near superoleophobic surfaces have been prepared on Lecce stone by coatings FSB-18, FSB-22, FSC-11 and FSC-22. The highest water and oil CA are observed on surface coated with FSC-11 and FSB-18, being 154.1±2.4°, 142.1±1.7° and 153.2±2.9°, 140.1±2.1° respectively. SEM-EDX analysis revealed the surface multiple roughness at sub-micrometer scales created by agglomerates of coating materials is indispensable in achieving superamphiphobicity. In addition to near superamphiphobicity, these surfaces also show very high adhesion force to water droplets. The maximum AF estimated, about 165 μN, was found on surface coated with FSB-22 and FSC-22. The strong AF is ought to be attributed to the combination of capillary force (due to the natural and newly created micro-pores and orifices at multiple dimension scales) and the hydrogen bonding formed between amidic

groups and water molecules. On the other hand, superhydrophobicity was not generated on marble, and the highest water CA is 128±3.1° on surface treated with 4.3 g/m^2 of FSB.

Once applied and tested as water repellents on Lecce stone slabs, FSB and FSC manifest very high WIE in both short (0.5 h) and long testing times (2 h). FSC shows WIE value as high as 90% after 2 h of absorption test, while it is 84% for FSB. FAD, tested in previous studies, is not effective for protecting high porous stones like Lecce stone (WIE=50% after 2 h). Besides, these three coatings preserve the physical properties of Lecce stone, since the residual vapor diffusivity is higher than 97% of the original value and the surface color is not changed ($\Delta E^*<3$). For low porous marble, FSB and FAD are able to protect marble effectively for long time, and their WIE values after 4 h absorption are as high as 88% and 90% respectively. FSC, however is not a decent protective agent for marble. Additionally, these coatings do not compromise the original vapor diffusivity and color features of marble.

FSC is a good water repellent for highly porous building stones, and contrarily FAD is a good candidate for low porous stone protection like marble. FSB, among these three, exhibits good performance on both high and low porous stones, indicating its capability and versatility as water repellent for building stones and stone artworks. Moreover, with proper applied amounts of FSB and FSC, they are also good coating materials for fabricating stick, near superamphiphobic surfaces which have functional applications in

fields such as liquid transport without loss or contamination, microsample analysis, sticky tape, dew collection, etc.

- **Fluorinated siloxane**

The partially fluorinated siloxane was synthesized through one-step reaction between an acyl-functionalised perfluoroether and (3-Aminopropyl)trimethoxysilane at room temperature in 8 h. Due to the two factors: 1) APTMS is connected to a short highly fluorinated segment (PFPE); 2) partial cross-linking of silanes which forms oligo-siloxane or poly-siloxane (Si-O-Si formation); the absorption bands of ν_{Si-O} of Si-PFPE have shifted to higher wavenumbers in comparison to ν_{Si-O} of APTMS. The fluorinated siloxane is partially soluble in alcoholic solvents. Found by ^{1}H-NMR analysis, the chemical shifts of protons of propyl group of Si-PFPE have also shifted slightly towards low field thanks to the presence of PFPE block.

Superamphiphobic surfaces were easily generated on a series of common building stones which include Lecce stone, sandstone (Pietra Serena), commercial red brick, commercial ceramic, by simply brushing surfaces with relatively low amounts of alcoholic dispersion of Si-PFPE. Besides, Si-PFPE coating is also super-repellent towards complex water dispersion and emulsion systems. Furthermore, these superamphiphobic surfaces manifest “Lotus effect”, possessing self-cleaning property. As-prepared coating is stable in acidic and alkali environments (pH 2.9-14), and its superhydrophobicity is also durable towards long time water immersion.

When applied and evaluated as water repellent on Lecce stone and Pietra Serena slabs, as-prepared coating demonstrates very high WIE even after 24 h-test while preserving the original physical properties of substrates, in terms of vapor diffusivity and surface chromatic features.

Since no harsh conditions nor sophisticated equipment or procedure is required, this fluorinated siloxane offers a facile and cost-effective strategy for fabricating bioinspired super-antiwetting surfaces that show "Lotus effect". Potential practical applications are in both industry and daily life, e.g. self-cleaning, anti-icing, oil/water separation, anti-fogging etc. Moreover, it is also a very good water repellent for wide varieties of building materials, including natural stones, bricks, ceramics, concretes etc. of modern and historic architecture. It is worth mentioning, Si-PFPE works efficiently also in polluted areas where acid rain presents.

- **Hybrid nanocomposite based on fluorinated siloxane and TiO_2 nanoparticles**

The hybrid nanocomposite was prepared by simply introducing TiO_2 nanoparticles into alcoholic dispersion of fluorinated siloxane, under magnetic stirring and moderate heating for 6 h. Prior to add into siloxane, the activation of TiO_2 nanoparticles by HNO_3 is vital in nanocomposite preparation. The superficial hydroxyl groups of activated TiO_2 nanoparticles condensed with partially cross-linked silane (oligo-siloxane or poly-siloxane), giving rise to effective chemical bonding (Ti-O-Si linkages with absorption

band at 936 cm^{-1} in FT-IR spectrum) which is evidence by FT-IR and TEM analyses. TEM analysis also showed no phase separation between TiO_2 nanoparticles and Si-PFPE.

Surface treatment on building stone samples can be done by applying its 2-prapanol suspension, because nanocomposite is not completely soluble. On as-prepared surfaces (stone substrates are with low to high porosities, i.e. Lecce stone, sandstone and marble), self-cleaning property ("Lotus effect") was also achieved in addition to superhydrophobicity. Supplementary dirt-removal test well demonstrates its self-cleaning capability. Besides, the nanocomposite is also non-wettable by complex water dispersion and emulsion systems.

Once applied and tested on stone slabs as water repellent, nanocomposite manifests overall better performance in comparison with three types of N215-TiO_2 mixtures, in terms of WIE. On marble, it has WIE as high as 88% even after 4-h test, while the best coating of N215-TiO_2 mixtures (i.e. "TiO_2+N215") only shows WIE of 68% after 2-h test. It also exhibits higher water inhibition efficacy (WIE: 57% versus 48% after 2-h test) than "TiO_2+N215", when tested on high porous Lecce stone samples. Additionally, nanocomposite well preserves the physical properties of marble, i.e. surface color and vapor diffusivity. However, due to the presence of TiO_2, Lecce stone seems whitish after coating. Regarding the hydrophobicity and water inhibition capability of N215-TiO_2 systems, the following findings can be

concluded. Compared with pure N215 coating, the hydrophobicity of mixed coatings or formulations is enhanced when a layer of TiO_2 is added below N215, while it is compromised if an additional layer of TiO_2 is added superficially. To verify the water repellence, WIE measured based on capillary absorption test is a more accurate and objective parameter than water CA test.

More importantly, the new nanocomposite also demonstrates much higher photo-catalytic activity than the N215-TiO_2 formulations, in particular when tested on marble samples. The photo-catalytic activity of nanocomposite expressed by both overall color change (ΔE^*) and "b*" value changes are very high, being 90% and 89% respectively. On the other hand, the highest D_{b^*} found on the most active coating of formulations i.e. "N215+TiO_2" is only 70% after 5-h test. Yet, on high porous Lecce stone substrates, neither nanocomposite nor N215-TiO_2 mixtures shows decent activity. Unlike low porous marble, the relatively high porosity and pore sizes of Lecce stone facilitate the penetration of MB dye in depth where UV radiation could not reach. Conclusions regarding the performance of N215-TiO_2 formulations are: 1) the photo-catalytic activity is governed by the superficial TiO_2 layer; 2) the surface TiO_2 layer is a double-edged sword, because it accounts for the photo-catalytic activity but simultaneously it impairs the overall hydrophobicity.

Overall, the novel nanocomposite exhibits better performance than N215-TiO_2 formulations, in terms of being water repellent and being photo-catalyst.

It could be effectively used as water repellent and anti-biofouling, anti-pollution coating agent on natural and artificial stone materials which have low to high porosities. Yet, the potential stone substrates are preferred to have white to grey colors.

Bibliography

[1] ICOMOS-ISCS: Illustrated glossary on stone deterioration patterns. Glossaire illustré sur les formes d'altération de la pierre, ed. V. Vergès-Belmin, Ateliers 30 Impression, Champigny/Marne, France, 2008 ISBN 978-2-918086-00-0.

[2] Raccomandazione NORMAL 1/88, Alterazioni Macroscopiche del Materiale Lapideo: lessico, CNR-ICR, Roma, 1990.

[3] E. Doehne, C. A. Price, Stone conservation—an overall review of current research, 2nd ed., The Getty Conservation Institute, Los Angeles, 2010 ISBN 978-1606060469.

[4] M. M. Rosa, W. S. George, Advance in understanding damage by salt crystallization, *Accounts of Chemical Research*, 43 (2010) 897-905.

[5] E. Doehne, S. Simon, U. Mueller, D. Carson, A. Ormsbee. Characterization of carved rhyolite tuff: The Hieroglyphic Stairway of Copán, Honduras, *Restoration of Buildings and Monuments,* 11 (2005) 247–254.

[6] I. Jiménez-González, C. Rodríguez-Navarro, G. W. Scherer, Role of clay minerals in the physicomechanical deterioration of sandstone, *Journal of Geophysical Research: Earth surface*, 113 (2008) F02021.

[7] P. Duffus, T. Wangler, G. W. Scherer, Swelling damage mechanism for clay-bearing sandstones, *Proceedings of the 11th International Congress on Deterioration and Conservation of Stone,* 15–20 September 2008, Torun´, Poland, ed. J. W. Lukaszewicz and P. Niemcewicz, pp. 65–72.

[8] B. Holmer, Flaking by insolation drying and salt weathering on the Swedish west coast, *Zeitschrift für Geomorphologie,* 42 (1998) 39–55.

[9] M. T. Laurenzi, S. Simon, Testing methods and criteria for the

selection/evaluation of products for the conservation of porous building materials, *Reviews in Conservation*, 7 (2006) 67–82.

[10] M. Yang, G. W. Scherer, G. S. Wheeler, Compatible consolidants, *Compatible Materials for the Protection of European Cultural Heritage,* eds. G. Biscontin, A. Moropoulou, M. Erdik, J. Delgado Rodrigues, 1998, pp. 201–208. Athens: Technical Chamber of Commerce.

[11] T. Chen, M. R. Yeung, N. Mori, Effect of water saturation on deterioration of welded tuff due to freeze–thaw action, *Cold Regions Science and Technology*, 38 (2004) 127–136.

[12] F. Bayram, Predicting mechanical strength loss of natural stones after freeze-thaw in cold regions, *Cold Regions Science and Technology*, 83 (2012) 98-102.

[13] G. Caneva, M. P. Nugari, O. Salvadori, Plant biology in cultural heritage, The Getty Conservation Institute, Los Angeles, 2009 ISBN: 978-0-89236-939-3.

[14] T. Warscheid, J. Braams, Biodeterioration of stone: a review, *International Biodeterioration & Biodegradation*, 46 (2000) 347-348.

[15] A. De Ríos, J. Wierzchos, L. G. Sancho, C. Ascaso, Acid microenvironments in microbial biofilms of antarctic endolithic microecosystems, *Environmental Microbiology*, 5 (2003) 231-237.

[16] M. Monte, Oxalate film formation on marble specimens caused by fungus, *Journal of Cultural Heritage*, 4 (2003) 255-258.

[17] S. M. Vinas, Contemporary Theory of Conservation, Oxford: Elsevier Butterworth-Heinemann; 2005 ISBN 0-7506-6224-7.

[18] Raccomandazione NORMAL 20/85, Interventi conservativi: progettazione esecuzione, valutazione preventiva, CNR-ICR, Roma, 1985.

[19] A. E. Charola, Water-repellent treatments for building stones: a practical overview, *APT Bulletin*, 26 (1995) 10-17.

[20] M. L. Tabasso, Acrylic Polymers for the Conservation of Stones: Advantages and Drawbacks, *APT Bulletin*, 26 (1995) 17-21.

[21] M. Lazzari, M. Aglietto, V. Castelvetro, O. Chiantore, Photochemical stability of partially fluorinated acrylic protective coatings IV. Copolymers of 2,2,2-trifluoroethyl methacrylate and methyl α-trifluoromethyl acrylate with vinyl ethers, *Polymer Degradation and Stability*, 79 (2003) 345-351.

[22] M. Favaro, R. Mendichi, F. Ossola, S. Simon, P. Tomasin, P. A. Vigato, Evaluation of polymers for conservation treatments of outdoor exposed stone monuments. Part II: Photo-oxidative and salts induced weathering of acrylic-silicone mixtures, *Polymer Degradation and Stability*, 92 (2007) 335-351.

[23] M. J. Melo, S. Bracci, M. Camaiti, O. Chiantore, F. Piacenti, Photodegradation of acrylic resins used in conservation of stone, *Polymer Degradation and Stability*, 66 (1999) 23-30.

[24] F. Cappitelli, C. Sorlini, Microorganisms attack synthetic polymers in items representing our cultural heritage, *Applied and Environmental Microbiology*, 74 (2008) 564–569.

[25] M. Mazzola, P. Frediani, S. Bracci, A. Salvini, New strategy for the synthesis of partially fluorinated acrylic polymers as possible materials for the protection of stone monuments, *European Polymer Journal*, 39 (2003) 1995-2003

[26] N. Yoshida, Y. Abe, H. Shigeta, K. Takami, H. Osaki, T. Watanabe, K. Hashimoto, *Journal of Sol-Gel Science and Technology,* 31 (2004) 195.

[27] V. Fassina, R. Arbizzani, C. Botteghi, U. Matteoli, E. Passaglia, M. Aglietto, Behaviour of 2,2,2-tri uoroethylmethacrylate polymers as stone protective materials. In Conservation of Monuments in the

Mediterranean Basin: Stone Monuments, Methodologies for the Analysis of Weathering and Conservation, *Proceedings of the 3rd International Symposium, Venice,* 22–25 June 1994, pp. 911-923.

[28] P. Frediani, M. Camaiti, B. Sacchi, A. Toti, Fluorinated and perfluorinated polymers as protective and reinforcing agents for stone artefacts, *Proceedings of international conference on High Performance and Special Elastomers*, Geneva, 20th-21st April, 2005, pp. 1-18.

[29] E. Casazza, S. Russo, M. Camaiti, Polimeri acrilici innestati con perfluoropolieteri-Nuovi protettivi per materiali lapidei", *La Chimica e l'Industria*, 84 (2002) 53-56.

[30] G. Amoroso, M. Camaiti, Scienza dei materiali e restauro. La pietra: dalle mani degli artisti e degli artisti a quelle dei chimici macromolecolari, Firenze: Alinea, 1997 ISBN: 88-8125-155-8.

[31] T. Nishino, M. Meguro, K. Nakamae, M. Matsushita, Y. Ueda, The lowest surface free energy based on -CF_3 alignment, *Langmuir*, 15 (1999) 4321-4323.

[32] G. Moggi, V. Guidetti, A. Pasetti, S. Vicini, Sistemi innovativi a base di polimeri fluorurati per la conservazione di materiali lapidei artificiali", *in Atti del Convegno di Studi "Architettura e Materiali del Novecento: conservazione, restauro, manutenzione"* Bressanone 13-16 Luglio 2004, Edizioni Arcadia Ricerche, Marghera-Venezia pp. 1249-1259.

[33] F. Piacenti, F. Ciampelli, A. Pasetti, Protecting Materials Subject to Degradation by Atmospheric and Polluting Agents by Means of Perfluoropolyethers US 4499146A, 1983.

[34] F. Piacenti, M. Camaiti, Synthesis and characterization of fluorinated polyetheric amides, *Journal of Fluorine Chemistry*, 68 (1994) 227–235.

[35] F. Piacenti, A. Pasetti, U. Matteoli, E. Strepparola, Method for Protecting Stone Materials from Atmospheric Agents by Means of Perfluoropolyether Derivatives US 4745009A, 1986.

[36] C. Botteghi, U. Matteoli, S. Paganelli, R. Arbizzani, F. Ciardelli, M. Aglietto, E. Taburoni, V. Fassina, Polyfluoroalkylmethacrylates as materials for the protection of stones, *Science and Technology for Cultural Heritage*, 1 (1992) 111-122.

[37] M. Aglietto, E. Passaglia, E. Taburoni, F. Ciardelli, C. Botteghi, U. Matteoli, S. Paganelli, R. Arbizzani, A class of fluorinated acrylic polymers: protective materials for stone in *Preprints of the 10th Triennial Meeting ICOM, Committee for Conservation in Washington*, James & James Ed., London, UK, 1993, pp. 553.

[38] L. Toniolo, T. Poli, V. Castelvetro, A. Manariti, O. Chiantore, M. Lazzari, Tailoring new fluorinated acrylic copolymers as protective coatings for marble, *Journal of Cultural Heritage*, 3 (2002) 309-316.

[39] F. Ciardelli, M. Aglietto, V. Castelvetro, L. Toniolo, O. Chiantore, Fluorinated polymeric materials for the protection of monumental buildings, *Macromolecular Symposia*, 152 (2000) 211-222.

[40] Y. Cao, A. Salvini, M. Camaiti, Oligoamide grafted with perfluoropolyether blocks:a potential protective coating for stone materials, *Progress in Organic Coatings*, 111 (2017) 164–174.

[41] Y. Cao, A. Salvini, M. Camaiti, Facile design of “sticky” near superamphiphobic surfaces on highly porous substrate, *Materials & Design,* 153 (2018) 139-152.

[42] W. Barthlott, C. Neinhuis, Purity of the sacred lotus, or escape from contamination in biological surfaces, *Planta,* 202 (1997) 1–8.

[43] T. L. Sun, L. Feng, X. F. Gao, L. Jiang, Bioinspired surfaces with special wettability, *Accounts of Chemical Research,* 38 (2005) 644-652.

[44] W. R. Hansen, K. Autumn, Evidence for self-cleaning in gecko setae, *Proceedings of National Academy of Sciences of the U. S. A.,* 102 (2005) 385-389.

[45] L. Feng, Y. A. Zhang, J. M. Xi, Y. Zhu, N. Wang, F. Xia, L. Jiang, Petal effect: a superhydrophobic state with high adhesive force, *Langmuir*, 24 (2008) 4114–4119.

[46] H. Ollivier, Recherches sur la capillarité, *Annales de Chimieet de Physique*, 10 (1907) 229–288.

[47] X. Li, D. Reinhoudt, M. Crego-Calama, What do we need for a superhydrophobic surface? A review on the recent progress in the preparation of superhydrophobic surfaces, *Chemical Society Reviews*, 36 (2007) 1350–1368.

[48] X. Zhang, J. Niu, Y. Jiang, Z. Wang, Superhydrophobicsurfaces: from structural control to functional application, *Journal of Materials Chemistry,* 18 (2008) 621–633.

[49] N. Shirtcliffe, G. McHale, M. Newton, An introduction to superhydrophobicity, *Advances in Colloid and Interface Science*, 161 (2011) 124–138.

[50] E. Celia, T. Darmanin, E. DeGivenchy, S. Amigoni, F. Guittard, Recent advances in designing superhydrophobic surfaces, *Journal of Colloid and Interface Science*, 410 (2013) 1–18.

[51] X. Wu, Q. Fu, D. Kumar, J. W. C. Ho, P. Kanhere, H. Zhou, Z. Chen, Mechanically robust superhydrophobic and superoleophobic coatings derived by sol–gel method, *Materials & Design*, 89 (2006) 1302–1309.

[52] Z. Chu, S. Seeger, Superamphiphobic surfaces, *Chemical Society Reviews,* 43 (2014) 2784–2798.

[53] A. Gao, Y. Zhao, Q. Yang, Y. Fu, L. Xue, Facile preparation of patterned petal-like PLA surfaces with tunable water micro-droplet adhesion properties based on stereo-complex co-crystallization from non-solvent induced phase separation processes, *Journal of Materials Chemistry A*, 4 (2016) 12058–12064.

[54] B. Bhushan, M. Nosonovsky, The rose petal effect and the modes of superhydrophobicity, *Philosophical Transaction of the Royal Society A*, 368 (2010) 4713–4728.

[55] E. Bormashenko, T. Stein, R. Pogreb, D. Aurbach, "Petal effect" on surfaces based on lycopodium: high-stick surfaces demonstrating high apparent contact angles, *Journal of Physical Chemistry C*, 113 (2009) 5568–5572.

[56] T. Zhu, C. Cai, J. Guo, R. Wang, N. Zhao, J. Xu, Ultra-water repellent polypropylene surfaces with tunable water adhesion, *ACS Applied Materials & Interfaces*, 9 (2017) 10224–10232.

[57] M. Chen, W. Hu, X. Liang, C. Zou, F. Li, L. Zhang, F. Chen, H. Yang, A facile all-solution processed surface with high water contact angle and high water adhesive force, *ACS Applied Materials & Interfaces,* 9 (2017) 23246–23254.

[58] X. Hong, X. F. Gao, L. Jiang, Application of superhydrophobic surface with high adhesive force in no lost transport of superparamagnetic microdroplet, *Journal of the American Chemical Society*, 129 (2007) 1478–1479.

[59] A. R. Parker, C. R. Lawrence, Water capture by a desert beetle, *Nature,* 414 (2001) 33–34.

[60] A. Lafuma, D. Quere, Superhydrophobic states, *Nature Materials*, 2 (2003) 457-460.

[61] M. Reyssat, J. M. Yeomans, D. Quere, Impairment of fakir drops, *Europhysics Letter*, 81 (2008) 26006.

[62] D. Bartolo, F. Bouamrirene, E. Verneuil, A. Buguin, P. Silberzan, S. Moulinet, Bouncing or sticky droplets: Impalement transitions on superhydrophobic micropatterned surfaces, *Europhysics Letter*, 74 (2006) 299-305.

[63] Y. C. Jung, B. Bhushan, Dynamic Effects Induced Transition of Droplets on Biomimetic Superhydrophobic Surfaces, *Langmuir*, 25 (2009) 9208.

[64] T. Koishi, K. Yasuoka, S. Fujikawa, T. Ebisuzaki, X. Zeng, Coexistence and transition between Cassie and Wenzel state on pillared hydrophobic surface, *Proceedings of National Academy of Sciences of the U. S. A.*, 106 (2009) 8435.

[65] C. G. L. Furmidge, Studies at phase interfaces. I. The sliding of liquid drops on solid surfaces and a theory for spray retention, *Journal of Colloid Science*, 17 (1962) 309-324.

[66] I. S. Bayer, C. M. Megaridis, J. Zhang, D. Gamota, A. Biswas, Analysis and Surface Energy Estimation of Various Model Polymeric Surfaces Using Contact Angle Hysteresis, *Journal of Adhesion Science and Technology*, 21 (2007) 1439−1467.

[67] L. Li, B. Li, J. Dong J. Zhang, Roles of silanes and silicones in forming superhydrophobic and superoleophobic materials, *Journal of Materials Chemistry A*, 4 (2016) 13677.

[68] J. Zhang, S. Seeger Superoleophobic Coatings with Ultralow Sliding Angles Based on Silicone Nanofilaments, *Angewandte Chemie International Edition,* 50 (2011) 6652 –6656

[69] J. Yuan, X. Liu, O. Akbulut, J. Hu, S. L. Suib, J. Kong, F. Stellacci, Superwetting nanowire memberanes for selective absorption, *Nature Nanotechnology*, 3 (2008) 332–336.

[70] D. J. Babu, S. N. Varanakkottu, A. Eifert, D. de Koning, G. Cherkashinin, S. Hardt, J. J. Schneider, Inscribing wettability gradients onto superhydrophobic carbon nanotube surfaces, *Advanced Materials Interfaces*, 1 (2014) 1300049.

[71] J. Joo, M. Choun, K. Kim, S. Uhm, Y. D. Kim, J. Lee, Controlled water flooding of polymer electrolyte fuel cells applying superhydrophobic gas

diffusion layer, *Current Applied Physics*, 14 (2014) 1374–1379.

[72] Y. Si, Z. Guo, Superhydrophobic nanocoatings: from materials to fabrications and to applications, *Nanoscale*, 7 (2015) 5922-5946.

[73] X. Zhu, Z. Zhang, B. Ge, X. Men, X. Zhou, Fabrication of a superhydrophobic carbon nanotube coating with good reusability and easy repairability, *Colloids and Surfaces A*, 444 (2014) 252.

[74] J. Liang, D. Li, D. Wang, K. Liu, L. Chen, Preparation of stable superhydrophobic film on stainless steel substrate by a combined approach using electrodeposition and fluorinated modification, *Applied Surface Science*, 293 (2014) 265-270.

[75] Z. She, Q. Li, Z. Wang, C. Tan, J. Zhou, L. Li, Preparation of superhydrophobic titanium surfaces via electrochemical etching and fluorosilane modification, *Applied Surface Science*, 263 (2012) 297-301.

[76] X. Bao, J. Cui, H. Sun, W. Liang, Z. Zhu, J. An, B. Yang, P. La, A. Li, Facile preparation of superhydrophobic surfaces based on metal oxide nanoparticles, *Applied Surface Science*, 303 (2014) 473-480.

[77] L. Gao, J. Zhuang, L. Nie, J. Zhang, Y. Zhang, N. Gu, T. Wang, J. Feng, D. Yang, S. Perrett, X. Yan, Intrinsic peroxidase-like activity of ferromagnetic nanoparticles, *Nature Nanotechnology*, 2 (2007) 577-583.

[78] D. Hong, I. Ryu, H. Kwon, J. J. Lee, S. Yim, Preparation of superhydrophobic, long-neck vase-like polymer surface, *Physical Chemistry Chemical Physics*, 15 (2013) 11862-11867.

[79] Z. Yuan, J. Bin, X. Wang, Q. Liu, D. Zhao, H. Chen, H. Jiang, Preparation and anti-icing property of a lotus-leaf-like superhydrophobic low-density polyethylene coating with low sliding angle, *Polymer Engineering & Science*, 52 (2012) 2310-2315.

[80] E. Huovinen, L. Takkunen, T. Korpela, M. Suvanto, T. T. Pakkanen, T. A. Pakkanen, Mechanically robust superhydrophobic polymer surfaces based on protective micropillars, *Langmuir*, 30 (2014) 1435.

[81] R. P. S. Chakradhar, G. Prasad, P. Bera, C. Anandan, Stable superhydrophobic coatings using PVDF-MWCNT nanocomposite, *Applied Surface Science*, 301 (2014) 208-215.

[82] H. Li, Y. Zhao, X. Yuan, Facile preparation of superhydrophobic coating by spraying a fluorinated acrylic random copolymer micelle solution, *Soft Matter*, 9 (2013) 1005-1009.

[83] N. A. Ivonova, A. B. Philipchenko, Superhydrophobic chitosan-based coatings for textile processing, *Applied Surface Science*, 263 (2012) 783-787.

[84] Y. Qing, Y. Zheng, C. Hu, Y. Wang, Y. He, Y. Gong, Q. Mo, Facile approach in fabricating superhydrophobic ZnO/polystyrene nanocomposite coating, *Applied Surface Science*, 285 (2013) 583-587.

[85] Y. Zhang, J. Li, F. Huang, S. Li, Y. Shen, A. Xie, W. Duan, F. Wang, Controlled fabrication of transparent and superhydrophobic coating on a glass matrix via a Green method, *Applied Physics A*, 110 (2013) 397-401.

[86] J. Lin, H. Chen, T. Fei, J. Zhang, Highly transparent superhydrophobic organic–inorganic nanocoating from the aggregation of silica nanoparticles, *Colloids and Surface A: Physicochemical and Engineering Aspects*, 421 (2013) 51-62.

[87] K. C. Camargo, A. F. Michels, F. S. Rodembusch, F. Horowitz, Multi-scale structured, superhydrophobic and wide-angle, antireflective coating in the near-infrared region, *Chemical Communications*, 48 (2012) 4992-4994.

[88] S. Wang, S. Luo, Fabrication of transparent superhydrophobic silica-based film on a glass substrate, *Applied Surface Science*, 258 (2012)

5443-5450.

[89] S. Y. Chou, C. Keimel, J. Gu, Ultrafast and direct imprint of nanostructures in silicon, *Nature*, 417 (2002) 835-837.

[90] D. Oner, T. J. McCarthy, Ultrahydrophobic Surfaces. Effects of topography length scales on wettability, *Langmuir*, 16 (2000) 7777-7782.

[91] R. Furstner, C. Barthlott, C. Neinhuis, P. Walzel, Wetting and self-cleaning properties of artificial superhydrophobic surfaces, *Langmuir*, 21 (2005) 956-961.

[92] A. Pozzato, S. Dal Zilio, G. Fois, D. Vendramin, G. Mistura, M. Belotti, Y. Chen, M. Natali, Superhydrophobic surfaces fabricated by nanoimprint lithography, *Microelectronic Engineering*, 83 (2006) 884-888.

[93] D. M. Spori, T. Drobek, S. Zurcher, N. D. Spencer, Cassie-state wetting investigated by means of a hole-to-pillar density gradient, *Langmuir*, 26 (2010) 9465-9473.

[94] K. Ellinas, A. Tserepi, E. Gogolides, From superamphiphobic to amphiphilic polymeric surfaces with ordered hierarchical roughness fabricated with colloidal lithography and plasma nanotexturing, *Langmuir*, 27 (2011) 3960-3969.

[95] S. Amigoni, E. T. de Givenchy, M. Dufay, F. Guittard, Covalent layer-by-layer assembled superhydrophobic organic−inorganic hybrid films, *Langmuir*, 25 (2009) 11073-11077.

[96] H. Tsai, Y. Lee, Facile method to fabricate raspberry-like particulate films for superhydrophobic surfaces, *Langmuir*, 23 (2007) 12687-12692.

[97] X. Li, X. Du, J. He, Self-cleaning antireflective coatings assembled from peculiar mesoporous silica nanoparticles, *Langmuir*, 26 (2010) 13528-13534.

[98] X. Du, J. He, A Self-Templated Etching Route to Surface-Rough Silica Nanoparticles for Superhydrophobic Coatings, *ACS Applied Materials & Interfaces*, 3 (2011) 1269-1276.

[99] Y. Zhao, Z. Xu, X. Wang, T. Lin, Photoreactive azido-containing silica nanoparticle/polycation multilayers: durable superhydrophobic coating on cotton fabrics, *Langmuir*, 28 (2012) 6328-6336.

[100] T. Wang, T. T. Isimjan, J. Chen, S. Rohani, Transparent nanostructured coatings with UV-shielding and superhydrophobicity properties, *Nanotechnology*, 22 (2011) 265708.

[101] T. Zhang, H. Yan, Z. Fang, Y. E, T. Wu, F. Chen, Superhydrophobic and conductive properties of carbon nanotubes/polybenzoxazine nanocomposites coated ramie fabric prepared by solution-immersion process, *Applied Surface Science*, 309 (2014) 218-224.

[102] J. Xua, J. Xu, Y. Cao, X. Ji, Y. Yan, Fabrication of non-flaking, superhydrophobic surfaces using a one-step solution-immersion process on copper foams, *Applied Surface Science*, 286 (2013) 220-227.

[103] W. Wu, X. Wang, X. Liu, F. Zhou, Spray-Coated Fluorine-Free Superhydrophobic Coatings with Easy Repairability and Applicability, *ACS Applied Materials & Interfaces*, 8 (2009) 1656-1661

[104] Y. Li, S. Chen, M. Wu, J. Sun, All spray processes for the fabrication of robust, self-healing, superhydrophobic coatings, *Advanced Materials*, 26 (2014) 3344-3348.

[105] M. Wolfs, T. Darmanin F. Guittard, Superhydrophobic surfaces from 3,4-propylenedioxythiophene (ProDOT) derivatives, *European Polymer Journal*, 49 (2013) 2267-2274.

[106] D. S. Facio, M. J. Mosquera, Simple strategy for producing superhydrophobic nanocomposite coatings in situ on a building substrate, *ACS Applied Materials &Interfaces*, 5 (2013) 7517−7526.

[107] P. N. Manoudis, I. Karapanagiotis, A. Tsakalof, I. Zuburtikudis, C. Panayiotou, Superhydrophobic composite films produced on various substrates, *Langmuir*, 24 (2008) 11225-11232.

[108] D. Aslanidou, C. Panayiotou, I. Karapanagiotis, Tuning the wetting properties of siloxane-nanoparticle coatings to induce superhydrophobicity and superoleophobicity for stone protection, *Materials & Design*, 108 (2016) 736–744.

[109] G. Cappelletti, P. Fermo, M. Camiloni, Smart hybrid coatings for natural stones conservation, *Progress in Organic Coatings*, 78 (2015) 511–516.

[110] L. de Ferri, P. P. Lottici, A. Lorenzi, A. Montenero, E. Salvioli-Mariani, Study of silica nanoparticles–polysiloxane hydrophobic treatments for stone-based monument protection, *Journal of Cultural Heritage*, 12 (2011) 356-363.

[111] A. Chatzigrigoriou, P. N. Manoudis, I. Karapanagiotis, Fabrication of water repellent coatings using waterborne resins for the protection of the cultural heritage, *Macromolecular Symposium*, 331 (2013) 158–165.

[112] P. N. Manoudis, I. Karapanagiotis, A. Tsakalof, I. Zuburtikudis, B. Kolinkeová, C. Panayiotou, Superhydrophobic films for the protection of outdoor cultural heritage assets, *Applied Physics A*, 97 (2009) 351–360.

[113] P. N. Manoudis, A. Tsakalof, I. Karapanagiotis, I. Zuburtikudis, C. Panayiotou, Fabrication of super-hydrophobic surfaces for enhanced stone protection, *Surface & Coatings Technology*, 203 (2009) 1322–1328.

[114] M. Camaiti, L. Brizi, V. Bortolotti, A. Papacchini, A. Salvini, P. Fantazzini, An environmental friendly fluorinated oligoamide for producing nonwetting coatings with high performance on porous surfaces, *ACS Applied Materials & Interfaces*, 42 (2017) 37279–37288.

[115] S. Bugani, M. Camaiti, L. Morselli, E. V. De Casteele, K. Janssens, Investigation on Porosity changes of Lecce stone due to conservation

treatments by means of x-ray nano-and improved micro-computed tomography: preliminary results, *X-Ray Spectrometry*, 36 (2007) 316-320.

[116] S. Bugani, M. Camaiti, L. Morselli, E. V. De Casteele, K. Janssens, Investigating morphological changes in treated vs. untreated stone building materials by x-ray micro-CT, *Analytical and Bioanalytical Chemistry*, 391 (2008) 1343-1350.

[117] M. Gombia, V. Bortolotti, R. J. S. Brown, M. Camaiti, L. Cavallero, P. Fantazzini, Water vapor absorption in porous media polluted by calcium nitrate studied by time domain nuclear magnetic resonance, *Journal of Physical Chemistry B*. 113 (2009) 10580-10586.

[118] Norm UNI-EN 15801-2010, Conservation of Cultural Heritage–Test methods. Determination of water absorption by capillarity, 2010.

[119] C. G. Borgia, V. Bortolloti, M. Camaiti, F. Cerri, P. Fantazzini, F. Fratini; F. Piacenti, Caratterizazione struttuale di materiali porosi: un nuovo approccio mediante tecniche NMR, Patron Editore, *Proceedings of National Archaeometry Congress*, Bologna-Italy, 29 January-1 February, 2002, pp. 135-150.

[120] Norm UNI-EN 15803-2010, Conservation of Cultural Heritage–Test methods. Determination of water vapor permeability, 2010.

[121] F. Piacenti, R. G. Carbonell, M. Camaiti, F. E. Henon, E. Luppichini, Protective materials for stone–effects on stone permeability and gas transport, *Proceedings of International Colloquium on "Methods of Evaluating Products for the Conservation of Porous Building Materials in Monuments"* Roma-Italy, 19-21 June, 1995, pp. 389-402.

[122] Norm UNI-EN 15886-2010, Conservation of Cultural Heritage–Test methods. Measurement of the color of the surface, 2010.

[123] T. J. Kałdoński, Ł. Gryglewicz M. Stańczyk, T. Kałdoński, Investigations on lubricity and surface properties of selected

perfluoropolyether oils, *Journal of KONES Powertrain and Transport*, 18/1 (2011) 199-212.

[124] N. R. Pallas, Y. Harrison, An automated drop shape apparatus and the surface tension of pure water, *Colloids and Surface*, 43 (1990) 169-194.

[125] S. N. Sahasrabudhe, V. Rodriguez-Martinez, M. O'Meara, B. E. Farkas, Density, viscosity, and surface tension of five vegetable oils at elevated temperatures: Measurement and modeling, *International Journal of Food Properties*, 20 (2017) S1965–S1981.

[126] S. Shibuichi, T. Yamamoto, T. Onda, K. Tsujii, Super water- and oil-repellent surfaces resulting from fractal structure, *Journal of Colloid and Interface Science*, 208 (1998) 287-294.

[127] S. Wang, L. Jiang, Definition of superhydrophobic states, *Advanced Materials*, 19 (2007) 3423-3424.

[128] G. W. Tyndall, P. B. Leezenberg, R. J. Waltman, J. Castenada, Interfacial interactions of perfluoropolyether lubricants with magnetic recording media, *Tribology Letters*, 4 (1998) 103-108.

[129] J. Schineider, C. Erdelen, H. Ringsdorf, J. T. Rabolt, Structural studies of polymers with hydrophilic spacer groups. 2. Infrared spectroscopy of Langmuir-Blodgett multilayers of polymers with fluorocarbon side chains at ambient and elevated temperatures, *Macromolecules*, 22 (1989) 3475-3480.

[130] Y. Katano, H. Tomono, T. Nakajima, Surface property of polymer films with fluroalkyl side chains, *Macromolecules*, 27 (1994) 2342-2344.

[131] S. J. Hardman, N. Muhamad-Sarih, H. J. Riggs, R. L. Thompson, J. Rigby, W. N. A. Bergius, L. R. Hutchings, Electrospinning superhydrophobic fibers using surface segregating end-functionalized polymer additives, *Macromolecules*, 44 (2011) 6461–6470.

[132] S. A. Kulinich, M. Farzaneh, Effect of contact angle hysteresis on water droplet evaporation from super-hydrophobic surfaces, *Applied Surface Science*, 255 (2009) 4056−4060.

[133] Z. Guo, W. Liu, Sticky Superhydrophobic surface, *Applied Physics Letters*, 90 (2007) 223111-223113.

[134] L. Mahadevan, Non-stick water, *Nature*, 411 (2001) 895-896.

[135] A. Johansson, P. Kollman, S. Rothenberg, J. McKelvey, Hydrogen bonding ability of the amide group, *Journal of the American Chemical Society*, 96 (1974) 3794-3800.

[136] Y. Lai, C. Lin, J. Huang, H. Zhuang, L. Sun, T. Nguyen, Markedly controllable adhesion of superhydrophobic spongelike nanostructure TiO_2 films, *Langmuir*, 24 (2008) 3867-3873.

[137] G. Nellis, S. Klein, Heat transfer, Cambridge University Press, UK, 2008 ISBN: 978-1107671379.

[138] V. Di Tullio, N. Proietti, D. Capitani, Unilateral NMR to study water diffusion and absorption in stone-hydrogel systems, *Microporous and Mesoporous Materials*, 269 (2018) 180-185.

[139] L. L. Latour, R. L. Kleinberg, P. P. Mitra, C. H. Sotak, Pore-size distributions and tortuosity in heterogeneous porous media, *Journal of Magnetic Resonance*, 112 (1995) 83-91.

[140] P. B. Lorenz, Tortuosity in porous media, *Nature*, 189 (1961) 386-387.

[141] A. Papacchini, Nuove oligoammidi parzialmente fluorurate per la protezione dei materiali lapidei, Master's Degree thesis in Chemistry - University of Florence, A.A. 2011/2012, 2013.

[142] L. Xu, H. Liang, Y. Yang, S. Yu, Stability and reactivity: positive and negative aspects for nanoparticle processing, *Chemical Reviews*, (118)

2018 3209-3250.

[143] F. Fratini, E. Pecchioni, E. Cantisani, S. Rescic, S. Vettori, Pietra Serena: the stone of the Renaissance, *Journal of Geological Society of London*, 407 (2014) 173-186.

[144] V. A. Zeitler, C. A. Brown, The infrared spectra of some Ti-O-Si, Ti-O-Ti and Si-O-Si compounds, *Journal of Physical Chemistry,* 61 (1957) 1174–1177.

[145] A. S. Lefohn, R. W. Brocksen, Acid rain effects research-a status report, *Journal of Air Pollution Control Association,* 34 (1984) 1005-1013.

[146] R. Wang, K. Hashimoto, A. Fujishima, M. Chikuni, E. Kojima, A. Kitamura, M. Shimohigoshi, T. Watanabe, Light-induced amphiphilic surfaces, *Nature*, 388 (1997) 431-432.

[147] K. Liu, M. Cao, A. Fujishima, L. Jiang, Bio-inspired titanium dioxide materials with special wettability and their applications, *Chemical Reviews*, 114 (2014) 10044-10094.

[148] Y. Lai, J. Huang, Z. Cui, M. Ge, K. Zhang, Z. Chen, L. Chi, Recent advances in TiO_2-based nanostructured surfaces with controllable wettability and adhesion, *Small*, 12 (2016) 2203-2224.

[149] E. Quagliarinia, F. Bondiolib, G. B. Goffredoa, A. Licciullic, P. Munafò, Self-cleaning materials on architectural heritage: compatibility of photo-induced hydrophilicity of TiO_2 coatings on stone surfaces, *Journal of Cultural Heritage*, 14 (2013) 1-7.

[150] P. Munafò, G. B. Goffredo, E. Quagliarini, TiO_2-based nanocoatings for preserving architectural stone surfaces: An overview, *Construction and Building Materials*, 84 (2015) 201-218.

[151] D. Colangiuli, A. Calia, N. Bianco, Novel multifunctional coatings with photocatalytic and hydrophobic properties for the preservation of the stone building heritage, *Construction and Building Materials*, 93 (2015) 189-196.

[152] M. F. La Russa, S. A. Ruffolo, N. Rovella, C. M. Belfiore, A. M. Palermo, M. T. Guzzia, G. M. Crisci, Multifunctional TiO_2 coatings for Cultural Heritage, *Progress in Organic Coatings*, 74 (2012) 186-191.

[153] F. Gherardi, S. Goidanich, V. Dal Santo, L, Toniolo, Layered nano-TiO_2 based treatments for the maintenance of natural stones in historical architecture, *Angewandte Chemie International Edition*, 130 (2018) 7360-7363.

[154] R. Zarzuela, M. Carbú, M. L. A. Gil, J. M. Cantoral, M. J. Mosquera, CuO/SiO_2 nanocomposites: A multifunctional coating for application on building stone, *Materials & Design*, 114 (2017) 364-372.

[155] M. Luna, J. J. Delgado, M. L. A. Gil, M. J. Mosquera, TiO_2-SiO_2 Coatings with a Low Content of AuNPs for Producing Self-Cleaning Building Materials, *Nanomaterials*, 8 (2018) 177.

[156] K. Lai, Y. Tang, J. Gong, D. Gong, L. Chi, C. Lin, Z. Chen, Transparent superhydrophobic/superhydrophilic TiO_2-based coatings for self-cleaning and anti-fogging, *Journal of Materials Chemistry*, 22 (2012) 7420-7426,

[157] Y. Zhao, Y. Liu, Q. Xu, M. Barahman, A. M. Lyons, Catalytic, self-cleaning surface with stable superhydrophobic properties: printed polydimethylsiloxane (PDMS) arrays embedded with TiO_2 nanoparticles, *ACS Applied Materials & Interfaces*, 7 (2015) 2632-2640.

[158] Z. Deng, W. Wang, L. Mao, C. Wang, S. Chen, Versatile superhydrophobic and photocatalytic films generated from TiO_2–SiO_2@PDMS and their applications on fabrics, *Journal of Materials Chemistry A*, 2 (2014) 4178-4184.

[159] T. Kamegawa, Y. Shimizu, H. Yamashita, Superhydrophobic Surfaces with photocatalytic self-cleaning properties by nanocomposite coating of TiO_2 and polytetrafluoroethylene, *Advanced Materials*, 24 (2012) 3697-3700.

[160] X. Ding, S. Zhou, G. Gu, L. Wu, A facile and large-area fabrication method of superhydrophobic self-cleaning fluorinated polysiloxane/TiO_2 nanocomposite coatings with long-term durability, *Journal of Materials Chemistry*, 21 (2011) 6161-6164.

[161] R. Oliva, A. Salvini, G. Di Giulio, L. Capozzoli, M. Fioravanti, C. Giordano, B. Perito, TiO_2-oligoaldaramide nanocomposites as efficient core-shell systems for wood preservation, *Journal of Applied Polymer Science*, 132 (2015) 42047.

[162] F. Milanesi, G. Cappelletti, R. Annunziata, C. L. Bianchi, D. Meroni, S. Ardizzone, Siloxane-TiO_2 hybrid nanocomposites. The structure of the hydrophobic layer, *Journal of Physical Chemistry C*, 114 (2010) 8287–8293

[163] J. M. Fraile, J. I. García, J. A. Mayoral, E. Vispe, Catalytic sites in silica-supported titanium catalysts: silsesquioxane complexes as models, *Journal of Catalysis*, 233 (2005) 90-99.

[164] A. N. Murashkevich, A. S. Lavitskaya, T. I. Barannikova, I. M. Zharskii, Infrared absorption spectra and structure of TiO_2–SiO_2 composites, *Journal of Applied Spectroscopy*, 75 (2008) 73-734.

[165] S. Hu, F. Li, Z Fan, Preparation of SiO_2-coated TiO_2 composite materials with enhanced photocatalytic activity under UV Light, *Bulletin of the Korean Chemical Society*, 33 (2012) 1895-1899.

Appendix

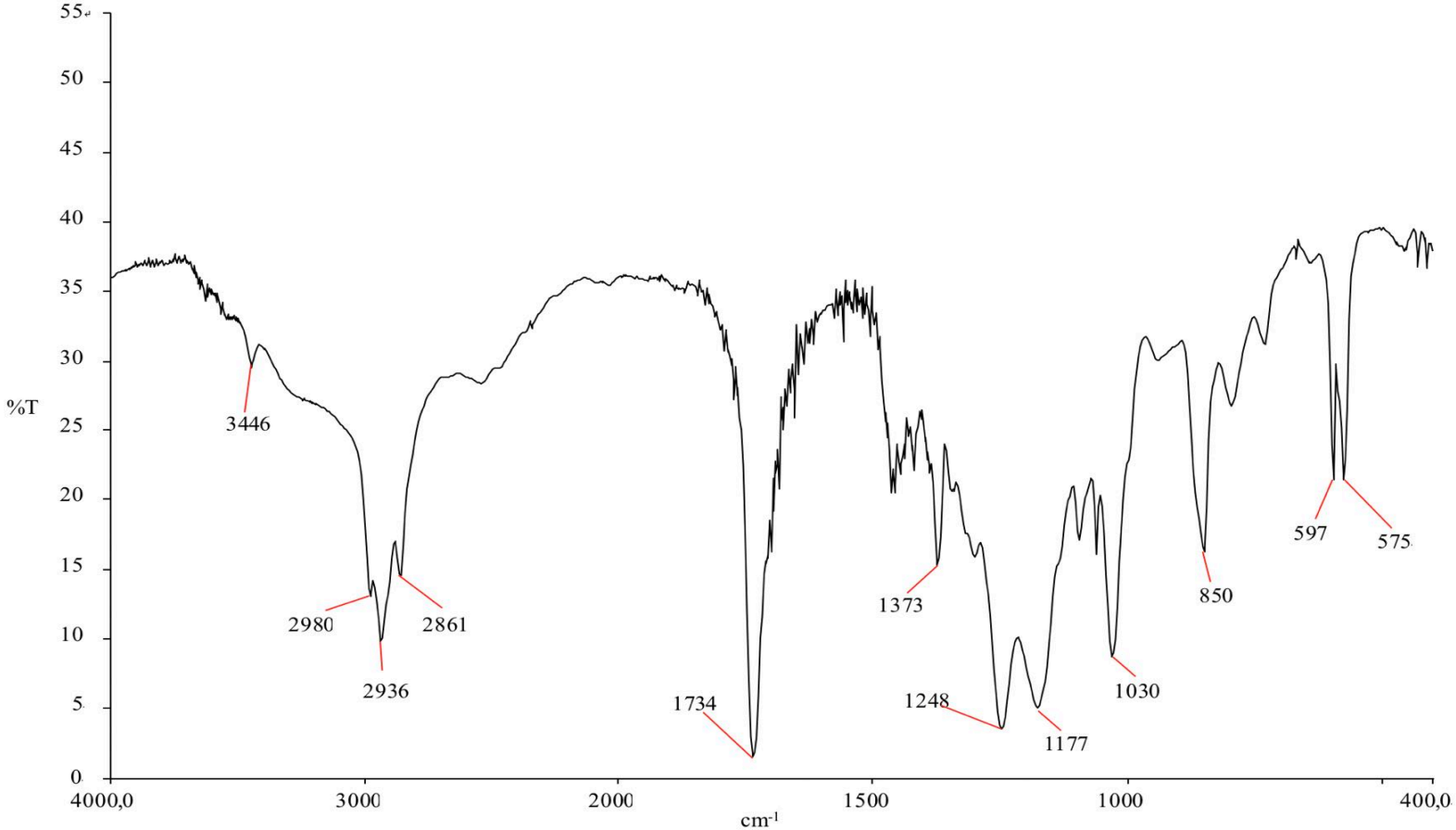

Figure I FT-IR spectrum of diethyl suberate on KBr windows.

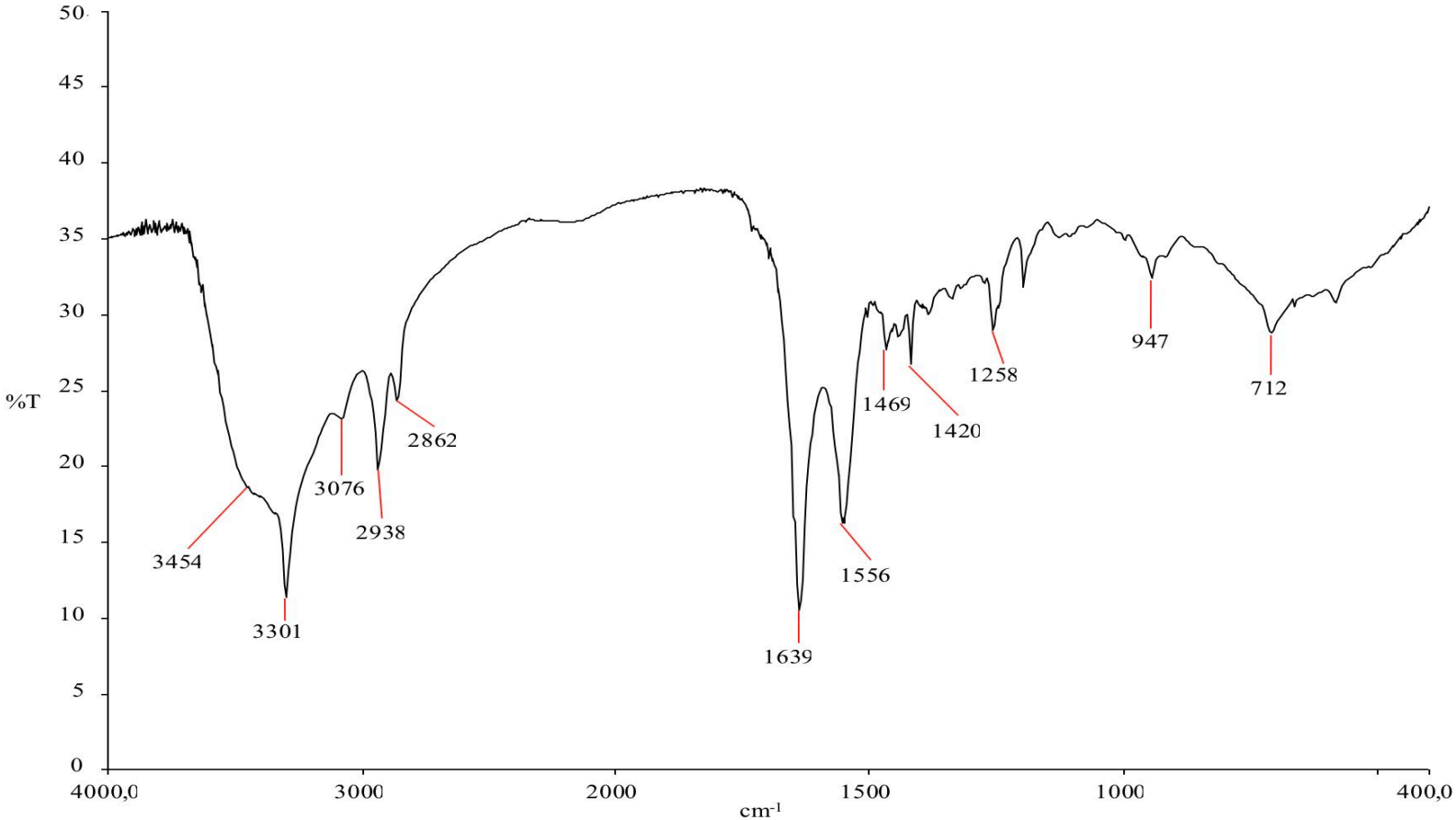

Figure II FT-IR spectrum of synthesis of SubC2 (1:2) on KBr windows.

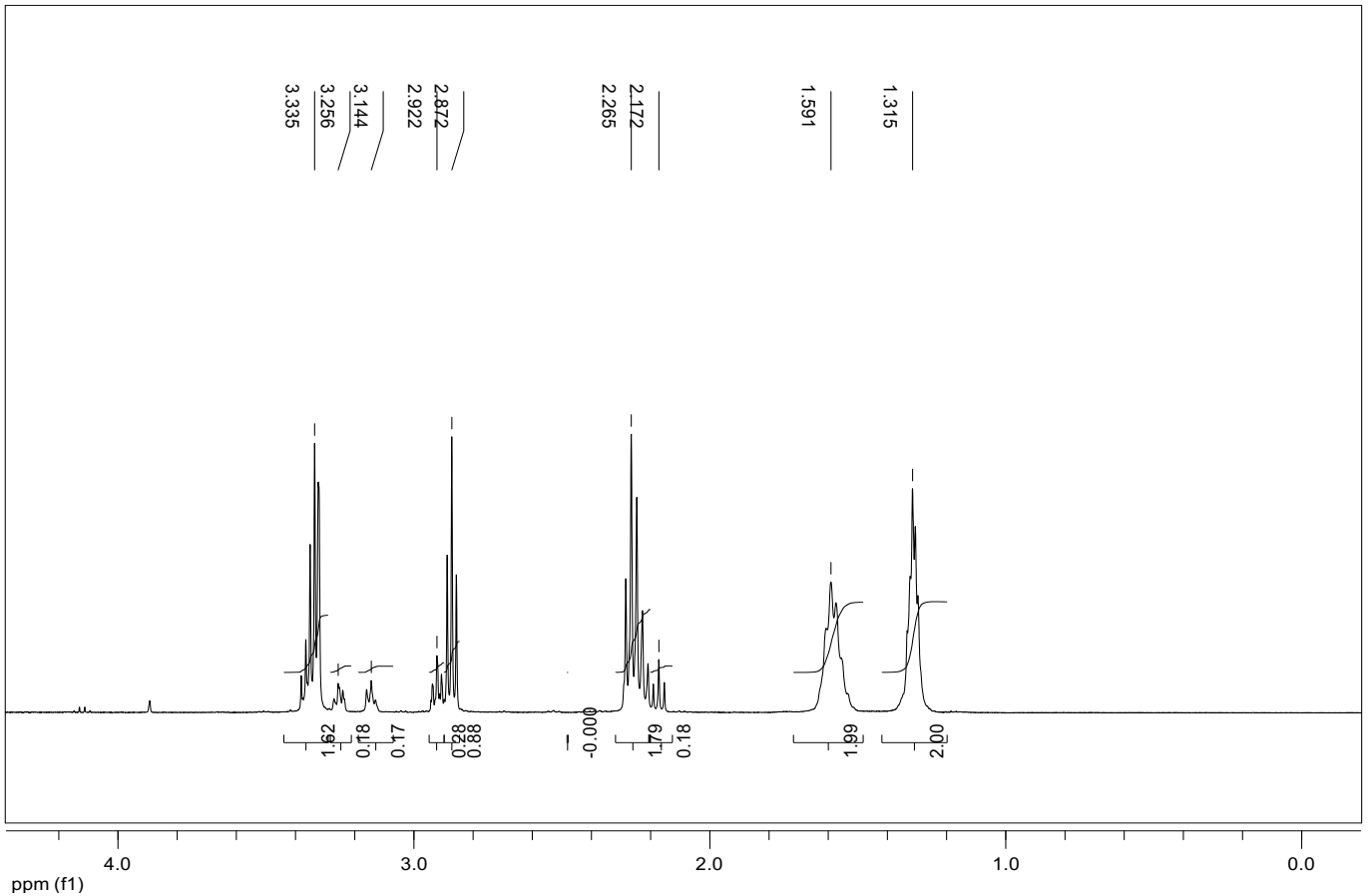

Figure III ^{1}H-NMR spectrum of SubC2 (1:2) in D_2O.

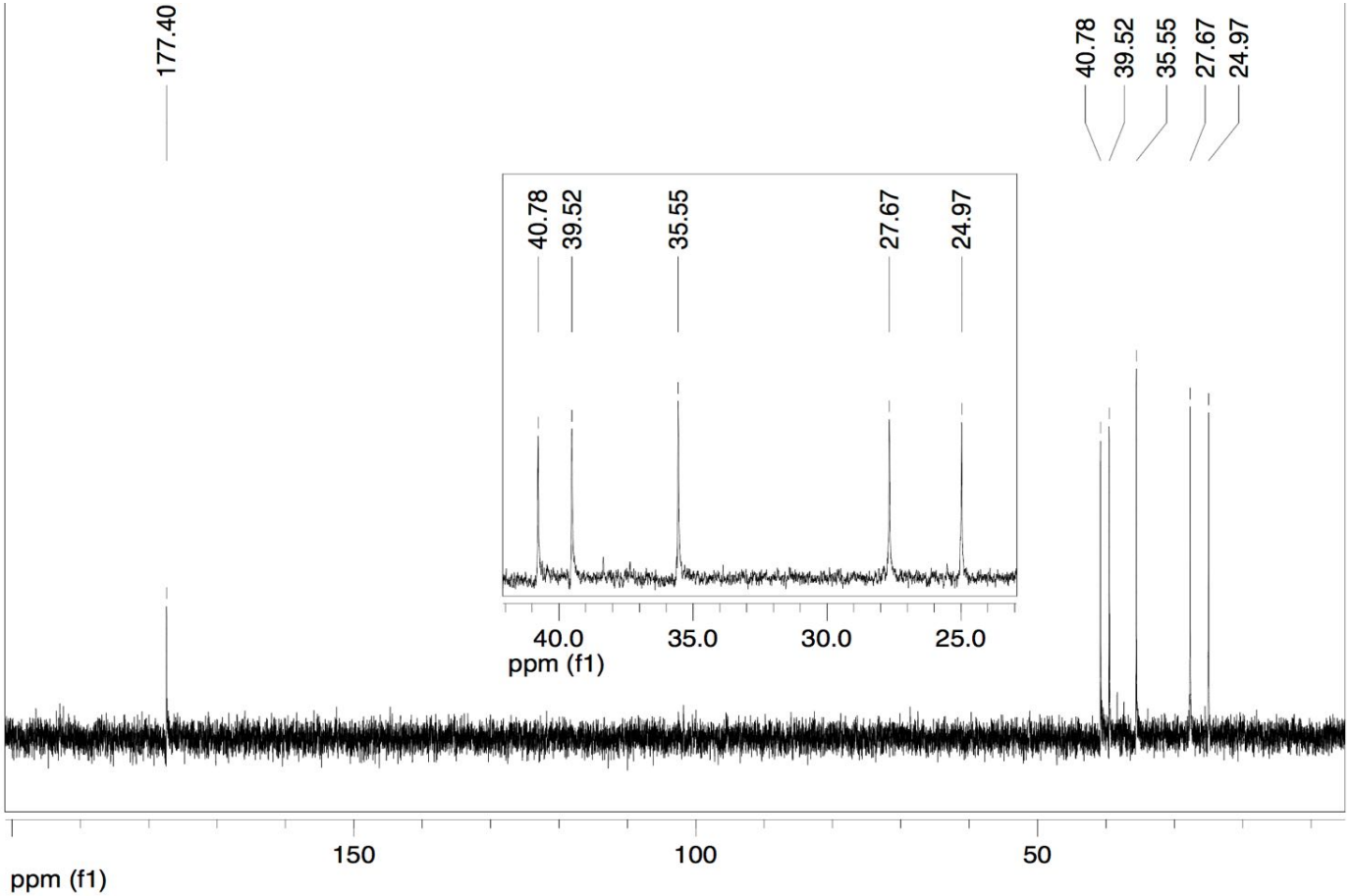

Figure IV ^{13}C-NMR spectrum of SubC2 (1:3) in D_2O.

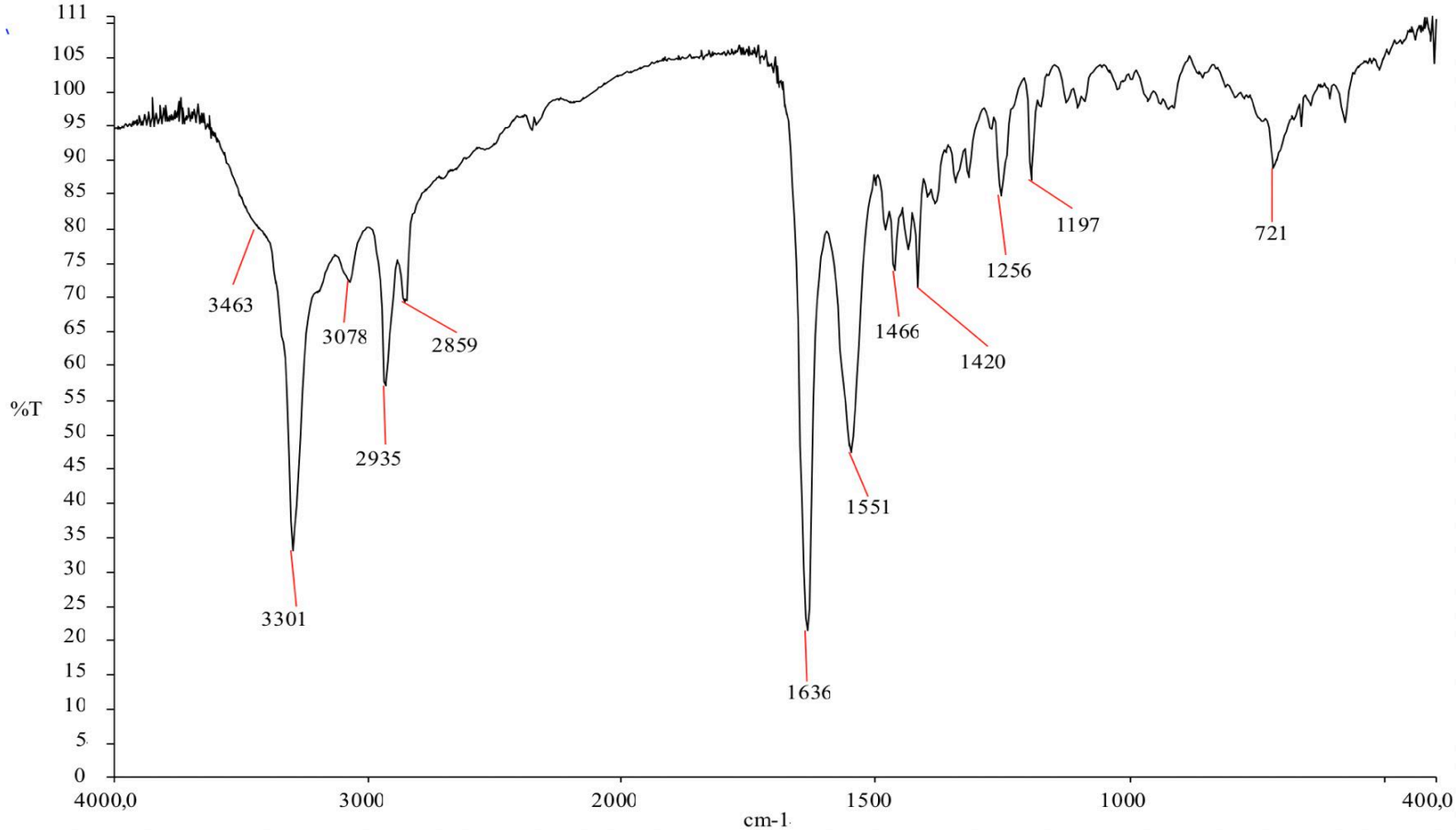

Figure V FT-IR spectrum of synthesis of SubC2 (1:5) on KBr windows.

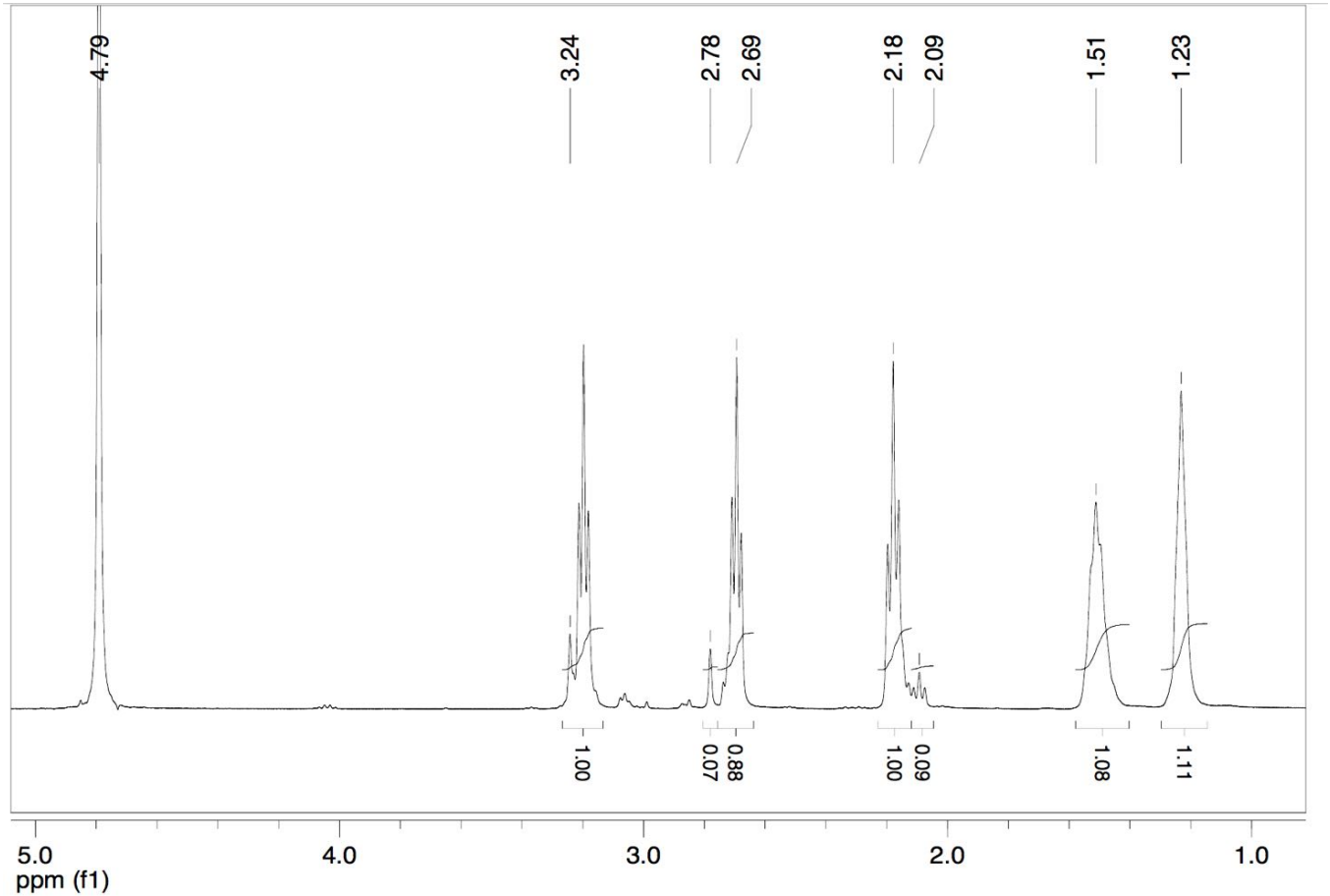

Figure VI ^{1}H-NMR spectrum of SubC2 (1:5) in D_2O.

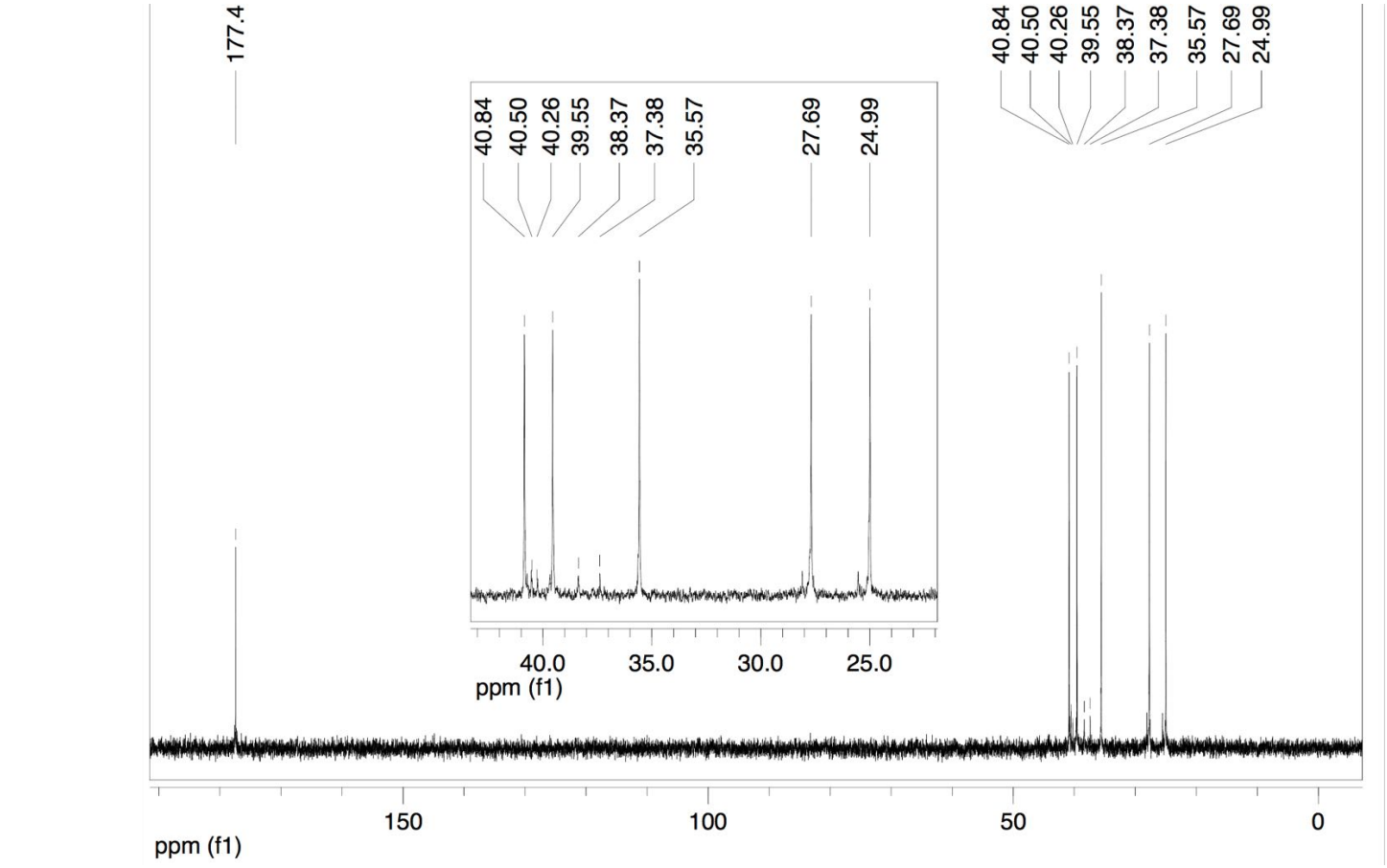

Figure VII ^{13}C-NMR spectrum of SubC2 (1:5) in D_2O.

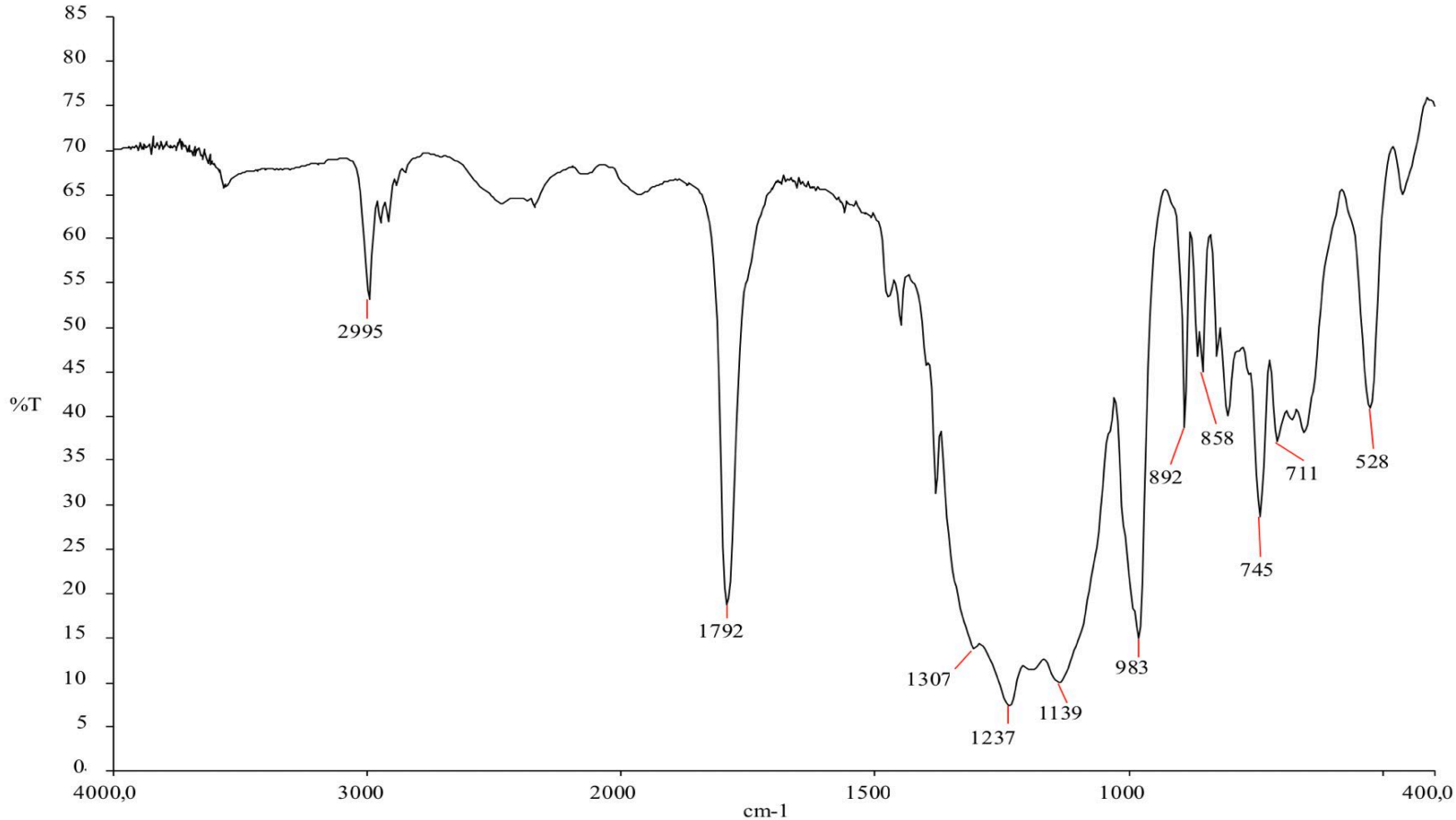

Figure VIII FT-IR spectrum of diethyl ester of Galden acid G800 on KBr windows.

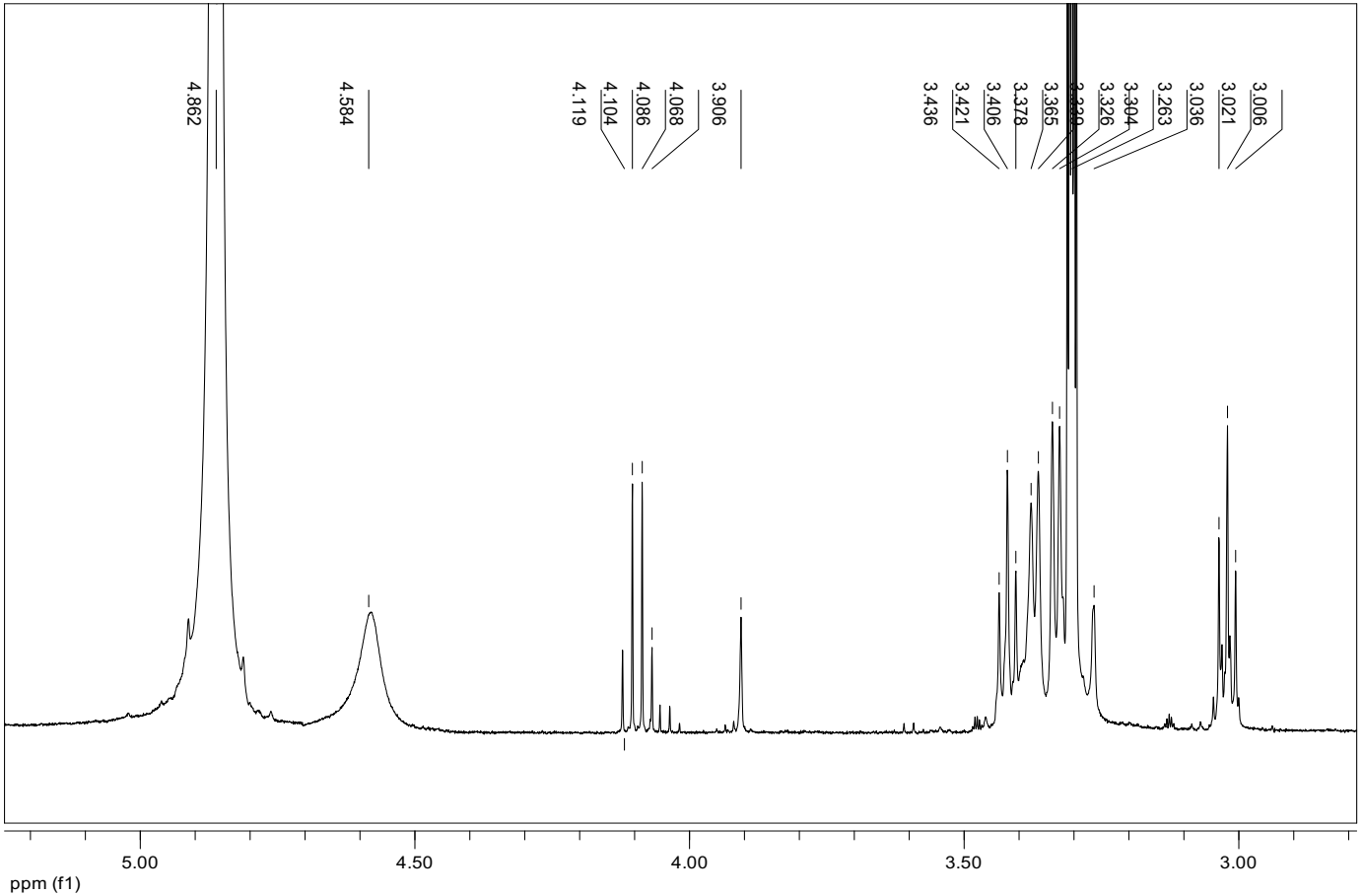

Figure IX ^{1}H-NMR spectrum of FSB (1:3) in CD_3OD:D_2O (95/5 w/w).

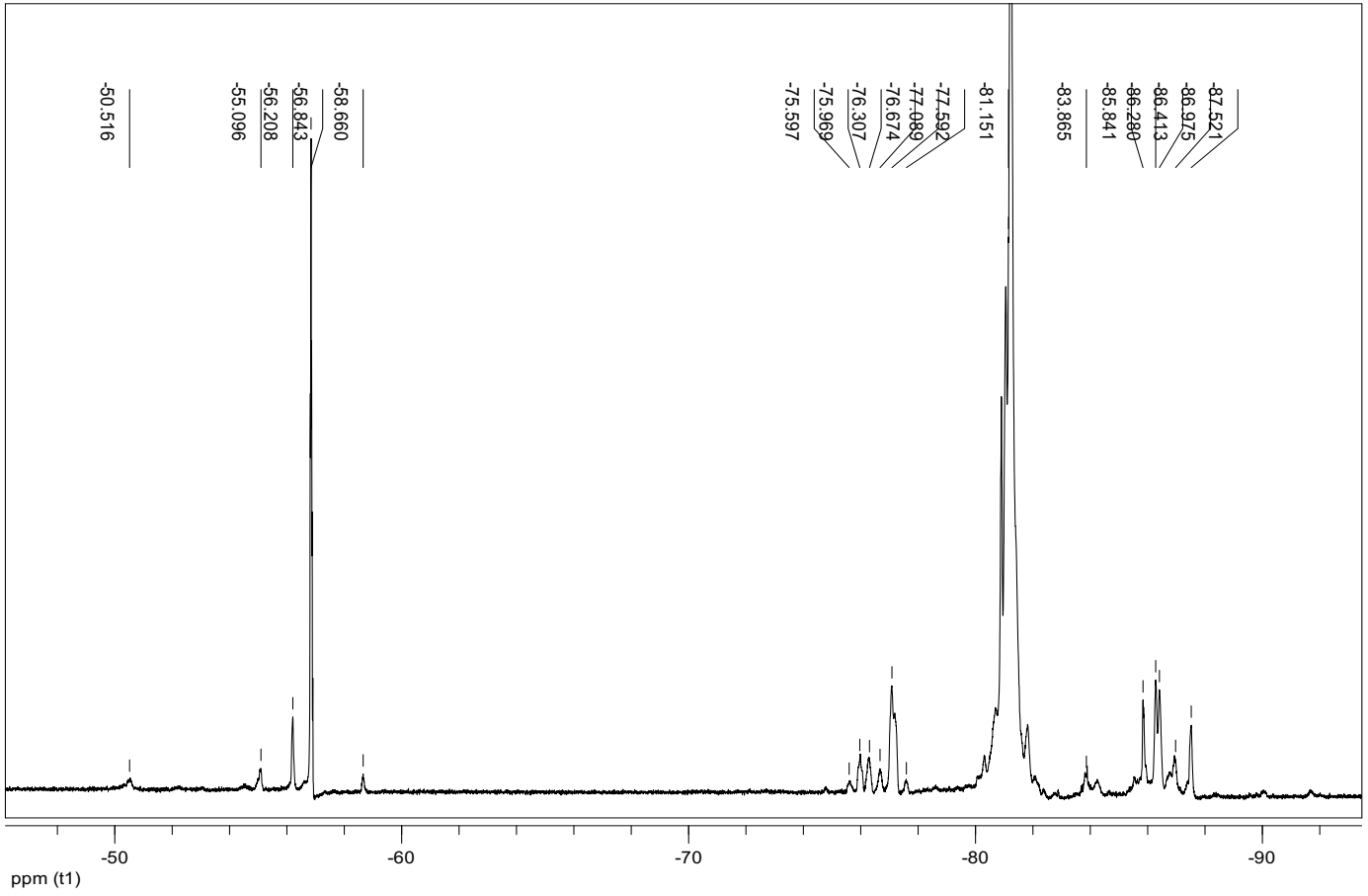

Figure X ^{19}F-NMR spectrum of FSB (1:3) in CD_3OD.

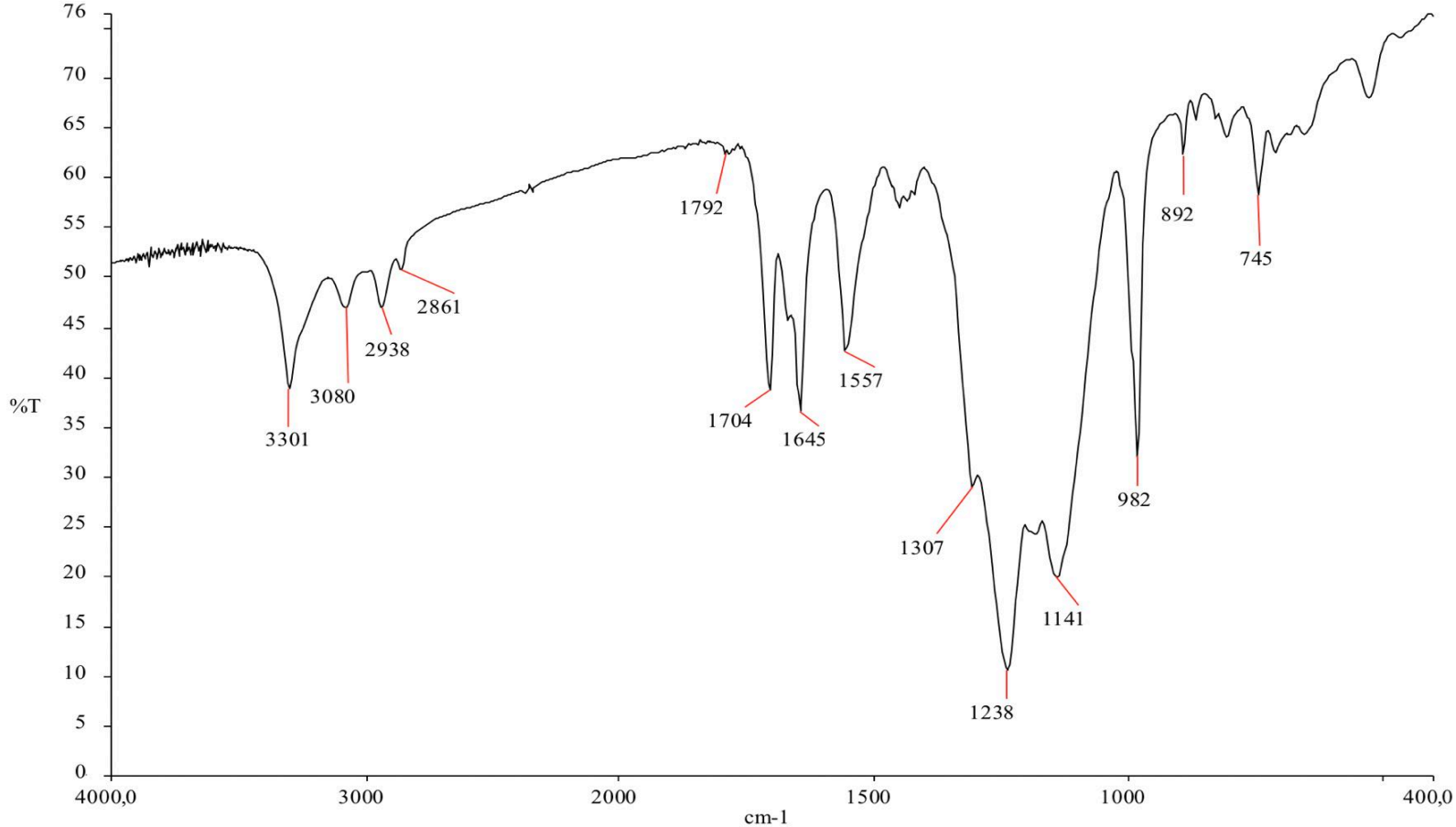

Figure XI FT-IR spectrum of FSB (1:5) in CD_3OD.

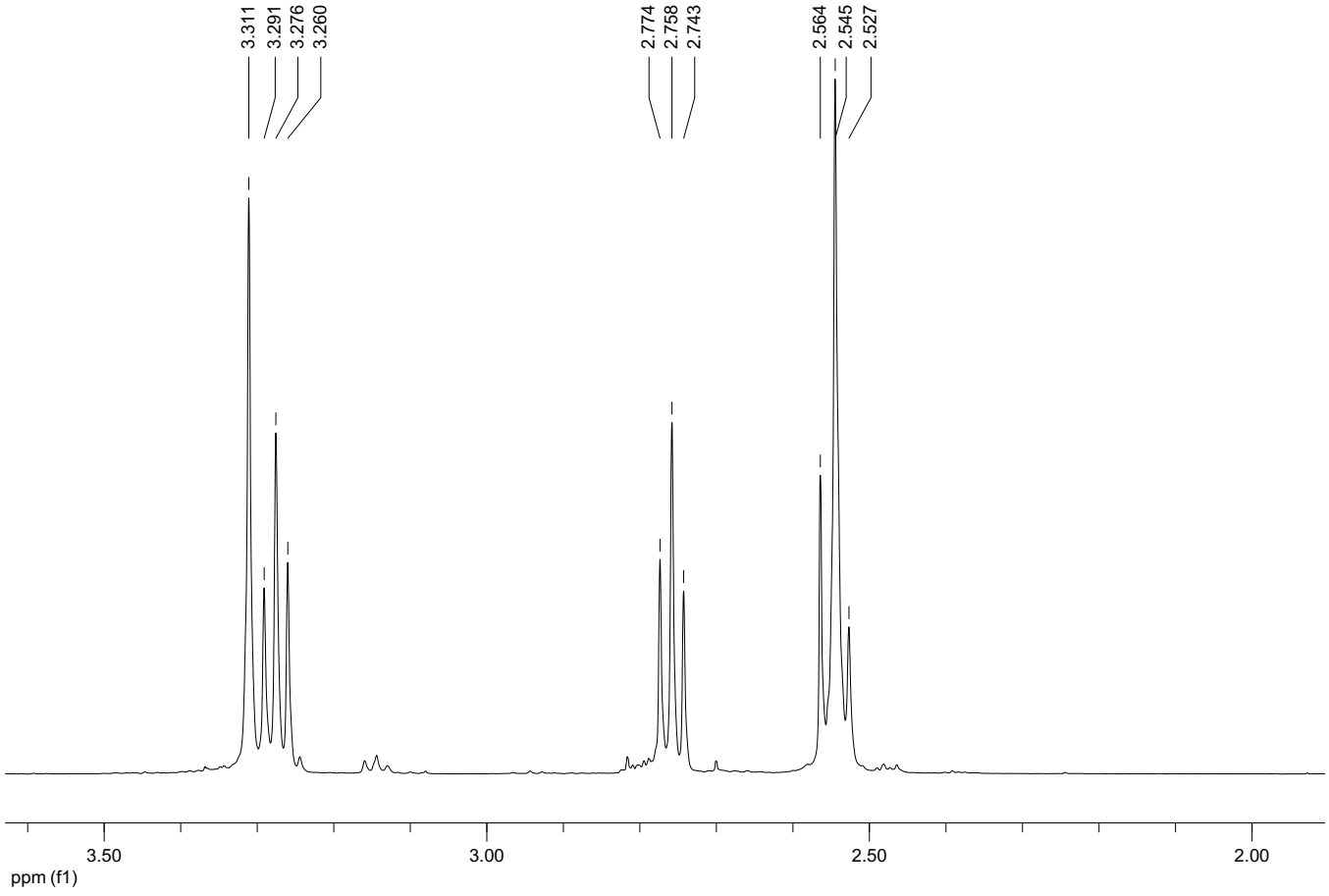

Figure XII ^{1}H-NMR spectrum of SucC2 in D_2O.

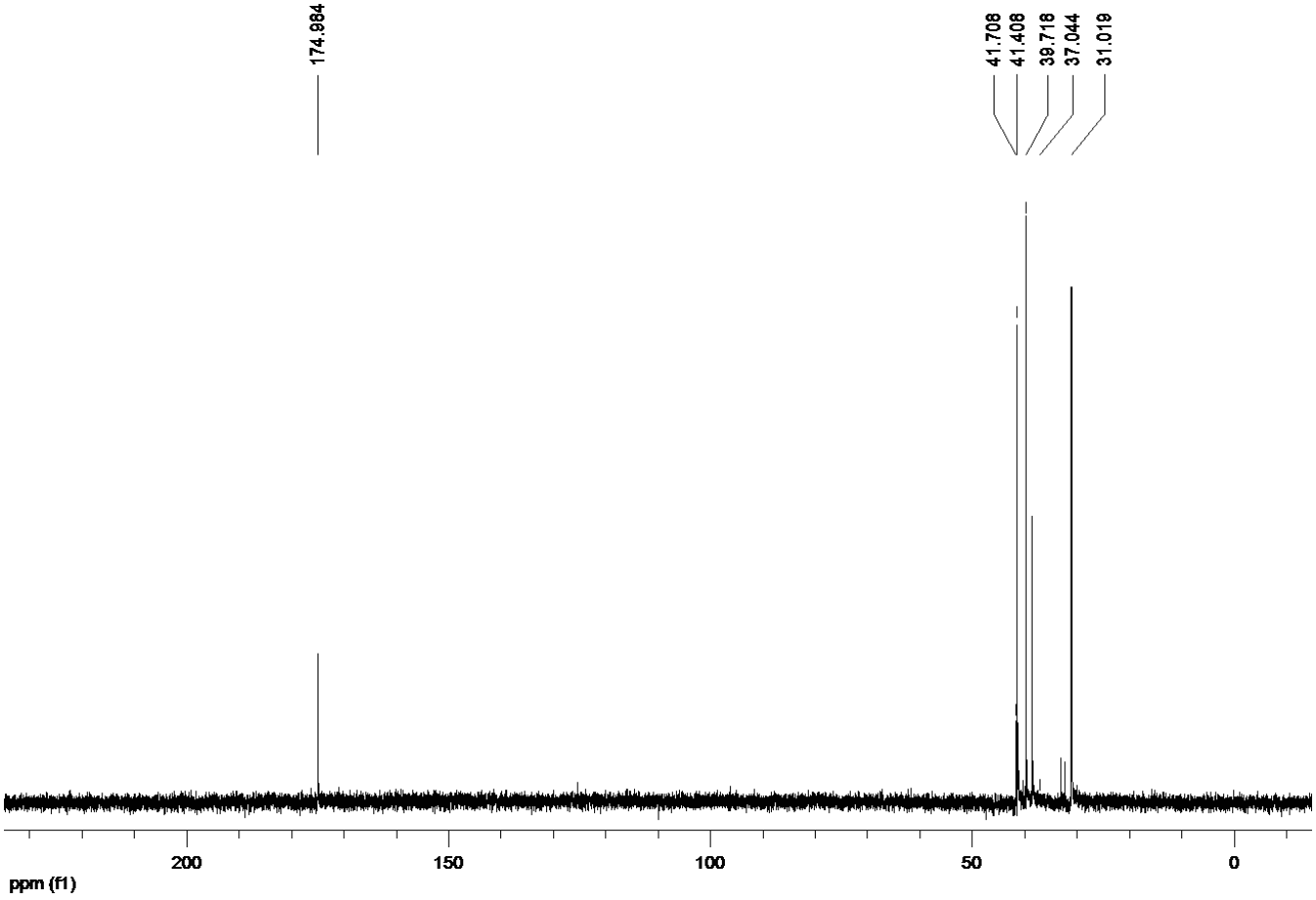

Figure XIII ^{13}C-NMR spectrum of SucC2 in D_2O.

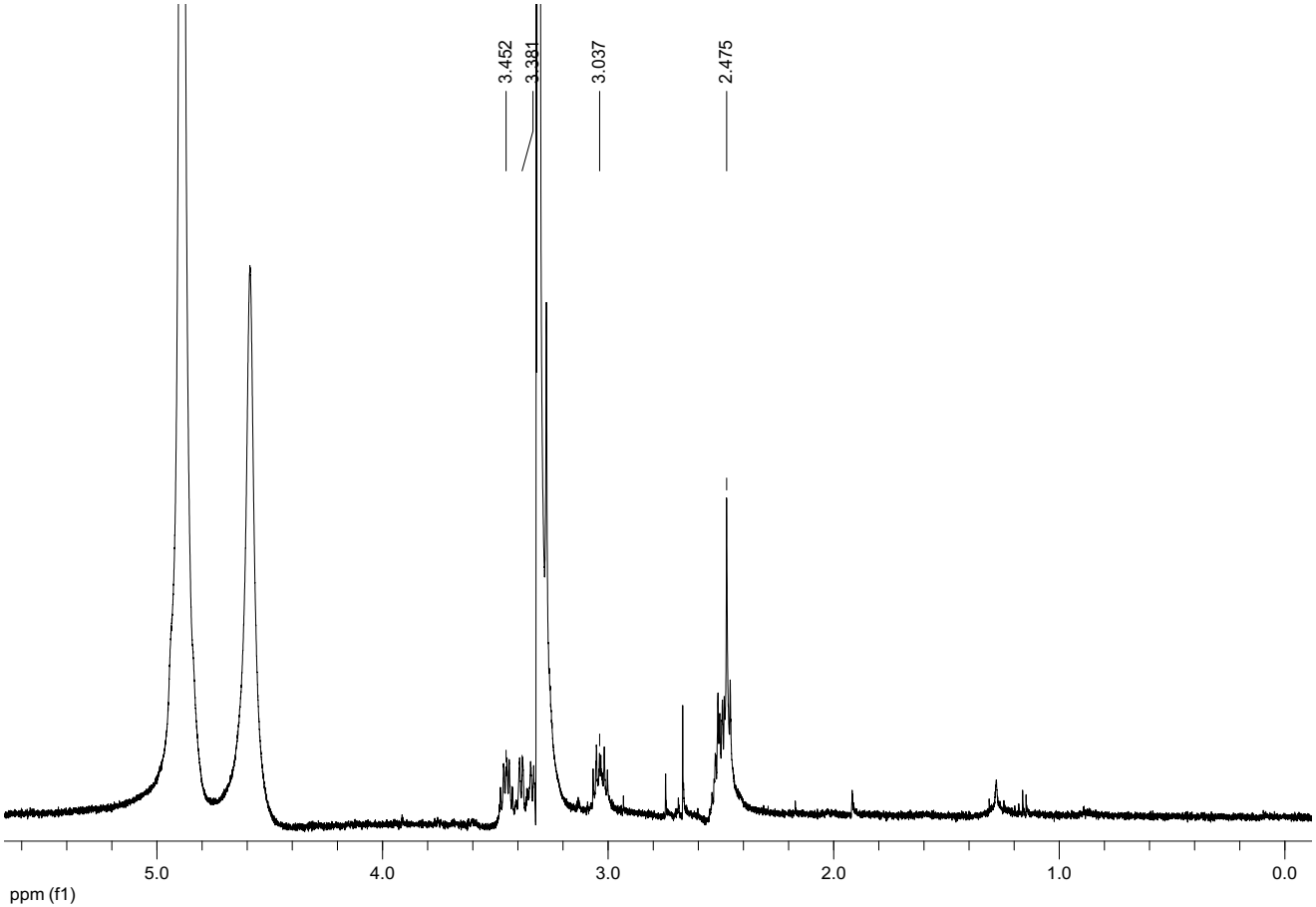

Figure XIV ^{1}H-NMR spectrum of FSC in CD_3OD:D_2O (95/5 w/w).

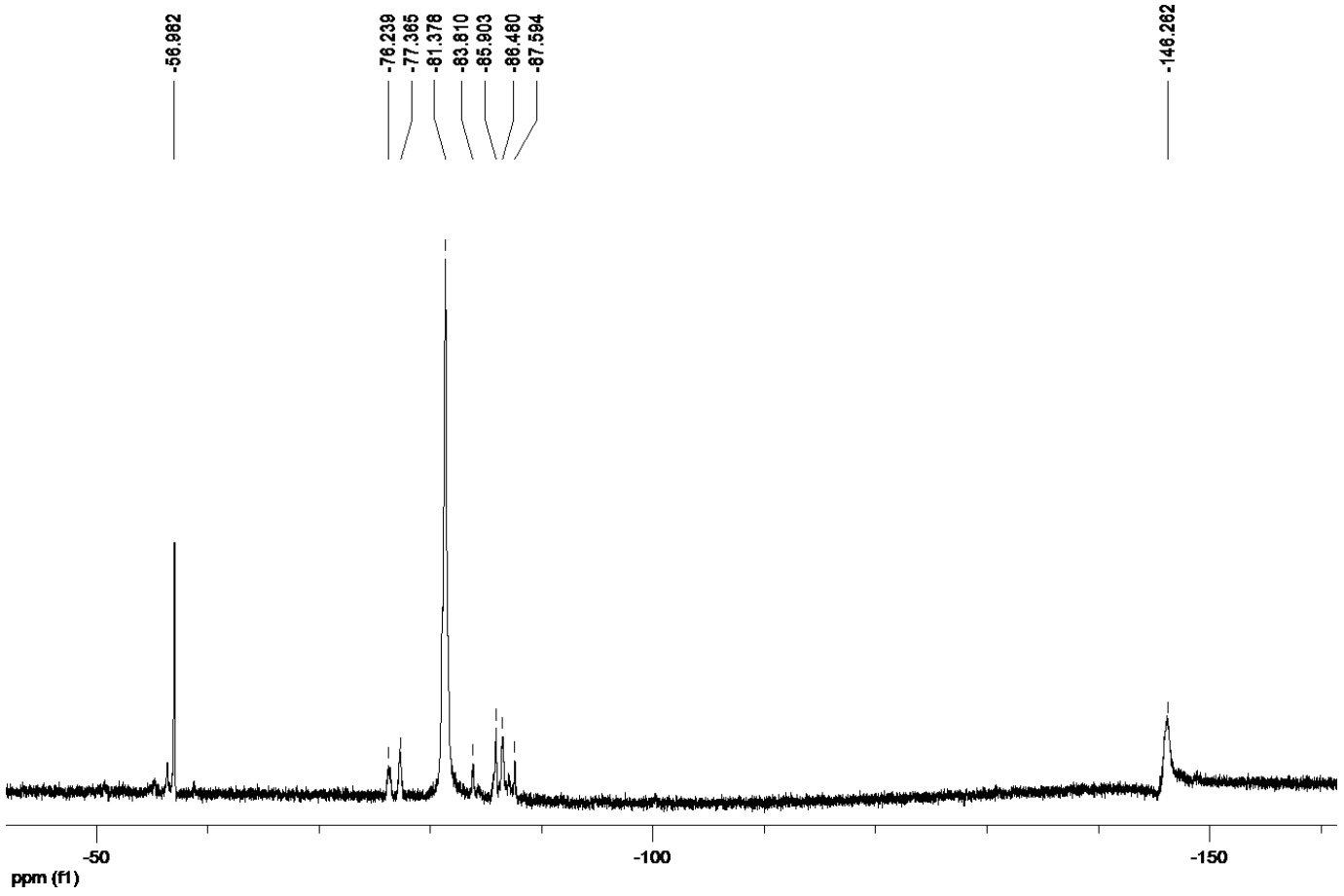

Figure XV ^{19}F-NMR spectrum of FSC in CD_3OD/D_2O (95/5 w/w).